

**NATURAL HYDRATE-BEARING SEDIMENTS:
PHYSICAL PROPERTIES AND CHARACTERIZATION TECHNIQUES**

A Thesis
Presented to
The Academic Faculty

by

Sheng Dai

In Partial Fulfillment
of the Requirements for the Degree
Doctor of Philosophy in the
School of Civil and Environmental Engineering

Georgia Institute of Technology
August 2013

Copyright © Sheng Dai 2013

**NATURAL HYDRATE-BEARING SEDIMENTS:
PHYSICAL PROPERTIES AND CHARACTERIZATION TECHNIQUES**

Approved by:

Dr. J. Carlos Santamarina, Advisor
School of Civil and Environmental
Engineering
Georgia Institute of Technology

Dr. Susan E. Burns
School of Civil and Environmental
Engineering
Georgia Institute of Technology

Dr. J. David Frost
School of Civil and Environmental
Engineering
Georgia Institute of Technology

Dr. Christian Huber
School of Earth and Atmospheric
Sciences
Georgia Institute of Technology

Dr. William Waite
Woods Hole Science Center
U.S. Geological Survey

Date Approved: June 26, 2013

ACKNOWLEDGEMENTS

I would like to thank my advisor, Dr. J. Carlos Santamarina, for giving me such excellent time in my life. I am always amazed by his knowledge, curiosity, patience, and dedication. It is a privilege to spend these years learning from such an exceptional scientist, creative engineer, supportive mentor, and wise human being.

I also like to thank my thesis committee members, Dr. Susan E. Burns, Dr. J. David Frost, and Dr. Christian Huber, for insightful comments and invaluable suggestions. Special thanks to Dr. William F. Waite for his continued encouragement, generous support, and great experiences.

This research was supported by the Chevron Joint Industry Project on Methane Hydrates under contract from the U.S. Department of Energy. Additional funding was provided by the Goizeta Foundation. I am grateful to the funding sources that made my Ph.D. work possible.

Wonderful interactions with members and visitors of Particulate Media Research Laboratory enriched my mind and personal life: Hosung Shin, Changho Lee, Nicolas Espinoza, Jongwon Jung, Harshad Phadnis, Lucio Cruz, Sylvain Cardon, Eunseok Bang, Alessio Savioli, Songhun Chong, Andrea Mezencevova, Aswathy Sivaram, Xingwei Ren, Cuiying Lu, Shahrzad Roshankhah, Liang Lei, Seth Mallett, and Stefanos Athanasopoulos. Special thanks to Douglas Cortes, Jaewon Jang, Cesar Pasten, Seunghee Kim, and Minsu Cha for frequent discussions, to Junbong Jang, Marco Terzariol, and Ethymios Papadopoulos as ‘the best hydrate team’, and to Wei Li, Fengshou Zhang, and Qian Zhao for generous support.

Without unconditional love and sincere support from my wife, Tingting Wang, I could not have completed this work.

TABLE OF CONTENTS

	Page
ACKNOWLEDGEMENTS	IV
LIST OF TABLES	IV
LIST OF FIGURES	V
SUMMARY	XIV
<u>CHAPTER</u>	
1 INTRODUCTION	1
1.1 Motivation	1
1.2 Thesis organization	2
2 THF HYDRATE NUCLEATION IN QUIESCENT AND DYNAMIC CONDITIONS	3
2.1 Introduction	3
2.2 Previous Studies	4
2.3 Experimental Study	5
2.3.1 Experimental devices and configurations	5
2.3.2 Materials - Specimen preparation	7
2.3.3 Experimental procedures	7
2.3.4 Typical temperature signatures	7
2.4 Results and Analyses	9
2.4.1 Heterogeneous hydrate nucleation – Static tests	9
2.4.2 The effect of mechanical vibration on nucleation	11
2.5 Conclusions	16
3 HYDRATE MORPHOLOGY: PHYSICAL PROPERTIES OF SANDS WITH PATCHY HYDRATE SATURATION	17
3.1 Introduction	17

3.2 Hydrate in Porous Media: Patterns	18
3.2.1 Nucleation and Growth	18
3.2.2 Hydrate Occurrence Patterns: Field Evidence	19
3.3 Physical Property Estimation for Patchy Saturation: Methods	23
3.3.1 Upper and Lower Bounds	24
3.3.2 Analytical Models	25
3.3.3 Numerical Simulations	27
3.4 Physical Properties of a Patchy System: Results	28
3.4.1 Bulk Modulus	28
3.4.2 Thermal, Hydraulic and Electrical Conductivities	30
3.5 Discussion: Impact of Hydrate Pore Habit on Physical Properties	33
3.5.1 Compressional P-wave Velocity	33
3.5.2 Hydraulic Conductivity	33
3.6 Conclusions	35
4 WATER RETENTION CURVE FOR HYDRATE-BEARING SEDIMENTS	37
4.1 Introduction	37
4.2 Previous Studies on Water Retention Curve	38
4.3 Methodology – Network Model Simulation	39
4.3.1 Tube population	39
4.3.2 Method #1: Preformed network	40
4.3.3 Method #2: Random growth network	42
4.3.4 Comparison	43
4.4 Results: The Water Retention Curve of Hydrate-Bearing Sediments	44
4.4.1 Hydrate saturation	44
4.4.2 Hydrate pore habit	46
4.4.3 Air entry pressure as a function of hydrate saturation	47
4.5 Discussion	47

4.5.1 Pore size statistics	47
4.5.2 Specimen size and geometry	49
4.5.3 Pore connectivity	52
4.6 Conclusions	53
5 FORMATION HISTORY AND PHYSICAL PROPERTIES OF HYDRATE-BEARING SEDIMENTS: MOUNT ELBERT SITE	55
5.1 Introduction	55
5.2 Hydrate and Permafrost in Alaska North Slope	55
5.2.1 Site Geology	55
5.2.2 Hydrate Formation History	57
5.3 Index Properties and Implications	61
5.4 Core Characterization – Structure of the As-received Sediment	65
5.4.1 Spatial Variability	65
5.4.2 Evolution of Seismic Wave Velocities during Initial Thaw	65
5.5 Geophysical Properties and Stress-Volume Response (Remolded Sediment)	68
5.5.1 S-wave Velocity	69
5.5.2 Dielectric Permittivity	71
5.5.3 Electrical Conductivity	72
5.5.4 Volume Change	74
5.6 Analysis and Discussion	76
5.6.1 Physical Properties – Hydrate Saturation	76
5.6.2 Sand Crushing	77
5.6.3 Fines Migration and Clogging	77
5.7 Conclusions	79
6 SAMPLING HYDRATE-BEARING SEDIMENTS: PRESSURE CORE TECHNOLOGY USING IN THE KRISHNA-GODAVARI BASIN	81

6.1 Introduction	81
6.2. Sampling Disturbance in Hydrate-Free Sediments	82
6.2.1 Sources of sampling disturbance	83
6.2.2 Disturbance evaluation – shear stiffness	84
6.3. Hydrate-Bearing Sediments: Additional Sampling Effects	85
6.3.1 Pore-scale analysis	87
6.3.2 Unloading: Mandel-Cryer effect and secondary hydrate formation	89
6.3.3 Post-sampling creep and aging	92
6.3.4 Testing inside the stability zone at different PT conditions	92
6.3.5 Anomalous hydrate preservation	94
6.4. Discussion: Characterization of Hydrate-Bearing Sediments	95
6.4.1 Sampler design - Plugging	95
6.4.2 Coring speed	96
6.4.3 Pressure core technology	96
6.5. Conclusions	97
7 PRESSURE CORE CHARACTERIZATION TOOLS FOR HYDRATE-BEARING	
SEDIMENTS	99
7.1 Introduction	99
7.2 Pressure Core Technology: Overview	100
7.2.1 Coring and recovery	100
7.2.2 Manipulation	101
7.2.3 Testing and characterization	101
7.2.4 Current situation	101
7.3 GT Pressure Core Characterization Tools (PCCTs)	102
7.3.1 Manipulator MAN	102
7.3.2 Sub-sampling CUT	103

7.3.3 Instrumented Pressure Testing Chamber IPTC	103
7.3.4 Effective Stress Chamber ESC	105
7.3.5 Direct Shear Chamber DSC	107
7.3.6 Sub-sampling Tool for Bio-Studies BIO	108
7.3.7 Controlled Depressurization Chamber CDC	108
7.4 Measurement of Physical Properties: Sensors and Gadgets	109
7.4.1 Tool position control	109
7.4.2 Sensors	110
7.5 Monitoring Dissociation – Gas production	112
7.6 Discussion: Comprehensive Characterization Approach	112
7.7 Conclusions	114
8 SAMPLING EFFECTS ON THE STIFFNESS OF FROZEN SANDS	115
8.1 Introduction	115
8.2. Experimental study	116
8.2.1 Experimental device	116
8.2.2 Specimen preparation	116
8.2.3 Experimental procedure	117
8.2.4 <i>P</i> -wave signatures and data reduction	118
8.3. Experimental results	120
8.3.1 <i>P</i> -wave velocity evolution during loading	120
8.3.2 <i>P</i> -wave velocity evolution during freezing	120
8.3.3 <i>P</i> -wave velocity evolution during unloading	120
8.3.4 Creep of ice-cemented sands after unloading	121
8.3.5 <i>P</i> -wave velocity evolution during thawing	121
8.4. Analyses and discussion	121
8.4.1 Velocity creep of frozen sands	121
8.4.2 Creep of frozen sands following unloading	123

8.4.3 Unloading and reloading rate	124
8.4.4 Effects of stress-cementation history on cemented soils	125
8.4.5 Extension to natural systems	127
8.5. Conclusions	128
9 PORE FLUID SAMPLING FROM HYDRATE-BEARING SEDIMENTS	130
9.1 Introduction	130
9.2 Pore water sampling – Current Technology	131
9.3 Experimental Study	131
9.3.1 Point sampling: Quasi radial flow	132
9.3.2 Cross-section sampling: 1D flow	133
9.4 Analyses and Discussion	135
9.4.1 Radial flow: shape factor	135
9.4.2 Displacement ratio - 1D flow	135
9.4.3 Comparison: displacing versus squeezing methods	139
9.4.4 Required specimen size	142
9.5. Conclusions	142
10 CONCLUSIONS	144
APPENDIX A: CODA WAVE ANALYSIS	148
A1. Introduction	148
A2. Analysis of Seismic Codas	149
A2.1 Method 1: Short-time cross correlation	151
A2.2 Method 2: Time-stretched cross correlation	151
A2.3 Method 3: Frequency-stretched spectra	152
A2.4 Comparison	153
A3. Experimental Study: <i>P</i> -wave Velocity in Dry Sand	154
A3.1 Experiment design	154

A3.2 Test results	155
A4. Analysis	158
A4.1 Velocity-stress response	158
A4.2 Creep in dry sandy specimen	161
A5. Discussion: Underlying Assumptions in Coda Analysis	162
A6. Conclusions	162
APPENDIX B: POROELASTIC MANDEL-CRYER EFFECT	164
APPENDIX C: PT-DEPENDENT METHANE SOLUBILITY IN WATER	168
REFERENCES	171

LIST OF TABLES

	Page
Table 2.1: Physical properties of selected sediments	8
Table 3.1: Hydrate morphologies in natural hydrate-bearing sediments. These data reflect properties of each recovered core only, and may not necessarily represent the properties of entire reservoirs.	21
Table 3.2: Physical properties: upper and lower bound models, assuming idealized arrangements of materials with the highest physical property value (darkest shade) to lowest physical property value (lightest shade), and a measurement direction given by the arrows. Symbol definitions are given in Notes 1 and 2.	24
Table 3.3: Physical properties: analytical models for estimating, rather than bounding, the physical properties of gas hydrate-bearing sediment.	26
Table 3.4: Selected physical properties for two- and three-component mixtures in hydrate-bearing sediment systems (Assumed porosity $n = 0.4$ and mean effective stress $\sigma_v' = 1\text{MPa}$).	31
Table 5.1: Index and engineering properties of Mount Elbert sediment (specimen from depth $z = 620.47\text{-to-}620.62\text{m}$).	62
Table 6.1: Sediment parameters for the poroelastic model used to study the Mandel-Cryer effect in hydrate-bearing sediments.	90
Table 9.1: Assumed physical properties of different types of soils.	141

LIST OF FIGURES

	Page
Figure 2.1: Schematic temperature-time signature corresponding to an exothermic phase transformation during cooling – Labels denote supercooling, induction time, freezing point depression, and equilibrium temperature.	4
Figure 2.2: Experimental configuration: (a) static test and (b) vibration test. Components: 1. Piezoelectric actuator (Model 712A01, PCB Piezotronics, Inc.). 2. Accelerometer (Model 350B04, PCB Piezotronics, Inc.). 3. Nylon coupler. 4. Thermocouple (K-type, precision = 0.1°C). 5. Heat-insulation foam cover. 6. Stainless steel rod.	6
Figure 2.3: Phase transformation. (a) Stability temperature for THF-water mixtures at atmospheric pressure. (b) Typical temperature-time signatures for tap water, THF solution with excess water (90H ₂ O:10THF), stoichiometric mixture 100% hydrate (81H ₂ O:19THF), and THF solution with excess THF (40H ₂ O:60THF).	10
Figure 2.4: Effects of minerals on nucleation.	11
Figure 2.5: Experimental results in tripartite: (a) water to ice and (b) stoichiometric THF-water to hydrate transition. Induction times are represented by symbols: in (a) crosses are results of $t_{ind} < 2500s$ and circles are results of $t_{ind} > 2500s$; in (b) crosses are results of $t_{ind} < 5000s$ and circles are results of $t_{ind} > 5000s$.	13
Figure 2.6: Experimental results: Induction time t_{ind} versus peak acceleration a . Cases: (a) tap water and (b) stoichiometric mixture (81H ₂ O:19THF) 100% hydrate. Discrete points are experimental results obtained with mechanical vibrations. As a reference, the mean and standard deviation values of 16 specimens without vibration are shown as solid and dashed lines.	14
Figure 2.7: Molecular scale analogue: mass, spring, and viscous dissipater subjected to base excitation. Normalized maximum relative displacement as a function of excitation frequency.	15
Figure 3.1: Hydrate morphologies in natural sediments – Field evidence and ψ -boundaries. In response to a combination of sediment particle size and effective stress, hydrate formation occurs in one of three general morphologies: Environments with relatively large sediment grains and high effective stress can host pore-filling hydrates (Upper inset);	

in contrast, hydrates forming in fine-grained sediment with low effective stress can displace sediment grains in all directions and create hydrate nodules or chunks (Lower inset). Between these two extremes, hydrate formation responds to variations in the local stress, displacing sediment grains in the directions of the smallest stress to form hydrate lenses and veins (Middle inset). All data are based on core analysis and do not necessarily reflect reservoir properties (Refer to Table 3.1 for details).

20

Figure 3.2: Bulk modulus K : bounds, analytical models, and numerical simulations. Filled circles show numerical simulation results for a fixed hydrate saturation (either $S_h=0.2$ or 0.8) but different number of patches. KT: Kuster-Toksoz model; SC: self-consistent model. Numbers 2 and 3 after each model designate 2- and 3-component systems. The 2-component model bounds are significantly tighter than three-component bounds, a result that can be exploited when geologic conditions suggest 2-component patchy hydrate saturations can be expected rather than 3-component homogeneous hydrate distributions. Refer to Table 3.2 for material parameters and Table 3.3 and 3.4 for mathematical expressions.

29

Figure 3.3: Conductivities versus the number of hydrate patches for a sandy specimen with porosity $n=0.4$ and hydrate saturation $S_h=0.2$. Dots are numerical results and dashed lines are trends. The patch size decreases as the number of patches increases to retain a constant hydrate saturation. The upper and lower endmember property values are given at the top and bottom right corner of each plot. Refer to Table 3.4 for material parameters

32

Figure 3.4: Self-consistent versus pore-habit specific models: predicted dependence of physical properties on gas hydrate saturation. (Top) Compressional, P-wave velocity: P-wave velocity increases rapidly even at very low hydrate saturations when hydrate forms at sediment grain contacts. When hydrate forms away from grain contacts (C, D), the velocity increases more rapidly at high hydrate saturation when hydrate begins bridging between multiple sediment grains across a pore or fully hydrate-saturated patches become large and numerous enough to begin interacting (E). Hydrate contacts sediment grains and can no longer be considered purely part of the pore fluid above $S_h \approx 25-40\%$. (Bottom) Normalized hydraulic conductivity relative to the hydrate-free $S_h = 0$ state: homogeneous hydrate distributions including pore-filling (H_1) or grain coating (H_2) hydrates versus patchy hydrate distributions with disk- (P_1), sphere- (P_2), or needle-shaped (P_3) hydrates. Homogeneous curves H_1 and H_2 are calculated from [Kleinberg *et al.*, 2003]. Patchy distribution curves P_1 , P_2 , and P_3 are calculated from Table 4 [Berryman, 1995; Pozdniakov and Tsang, 2004].

34

- Figure 4.1: Total tube population. Histogram of tube size: randomly generated lognormal distribution ($\mu_{ln} = 10\mu\text{m}$, $\sigma_{ln} = 0.4$, the total number of tubes is 4802). 40
- Figure 4.2: Network model simulation. (a) Preformed network: realization of a 50×50 square network using the tube population shown in Figure 4.1; tubes are drawn with line thickness linearly proportional to pore radius. (b) Trapping algorithms and resulting water retention curves using the preformed network: the defending phase in tube-1 is displaced in the “loose trapping” algorithm but it remains trapped when the “tight trapping” algorithm is used. (c) Random network growth: starting from the left boundary, gas invades the largest pore where air entry pressure is the lowest; once a tube becomes gas-invaded (solid lines), new tubes are randomly selected from the total tube population and are connected to the newly gas-invaded tube. Invasion and growth continue until all tubes in the population have been attached; thereafter, invasion is completed by displacing water from the largest to the smallest tubes. 41
- Figure 4.3: Water retention curve using the 2D preformed network with connectivity $cn = 4$; histograms of “available” connectivity as de-watering progresses are superimposed on the figure. 43
- Figure 4.4: Water retention curves for sediments with different hydrate saturations S_h . (a) Change in pore size distribution as a function of hydrate saturation assuming that the hydrate mass fills the largest pores first. (b) Computed water retention curves using preformed 2D networks ($cn = 4$). 45
- Figure 4.5: Water retention curves as a function of hydrate saturation S_h (Method: preformed 2D networks where hydrate forms in the largest pores). Continuous trends show the fitted van Genuchten model $vG(P_0, m)$, where the reference pressure P_0 reflects the air entry pressure and the m -parameter captures the sensitivity of changes in capillary pressure P_c to changes in water saturation S_w . 46
- Figure 4.6: The effect of hydrate morphology on the water retention curve. Identical tube networks (Method: preformed network - refer to Figure 2a). The same hydrate saturation $S_h = 25\%$ is satisfied with five different pore habits: (a) Hydrate forms in either the largest or the smallest tubes. (b) Patchy hydrate saturation with different patch size (P1, P3, and P5) that preferentially nucleate at the largest pores. (c) Corresponding soil water characteristic curves with fitted van Genuchten model parameters. 48
- Figure 4.7: Effect of hydrate saturation S_h on the air entry pressure of hydrate-bearing sediments P_0^{HBS} . Preformed network simulation results (dots)

- and fitted predictive model (solid line). Note: there are 6 different network realizations in each case; hydrate forms in largest pores. 49
- Figure 4.8: The effect of pore size statistics on the water retention curve (Method: preformed network – hydrate saturation $S_h = 0\%$). (a) Lognormal pore size distributions with identical mean μ but different standard deviations σ_{ln} . The inset shows the corresponding density curves. (b) Network model simulation results (markers) and fitted van Genuchten model (lines). 50
- Figure 4.9: The effect of network size and length-to-width ratio L/B on the ‘measured’ water retention curve (Method: preformed network – hydrate saturation $S_h = 0\%$). (a) Water retention curves for different size networks with the same length-to-width ratio L/B = 1. (b) Water retention curves computed for the same tube population of 4802 tubes but arranged in different network geometries or L/B ratios. 51
- Figure 4.10: Effect of tube connectivity cn on network model simulations (Note: refer to Figure 1 for the tube population – Hydrate saturation $S_h = 25\%$). (a) Water retention curve using the 2D preformed network with connectivity $cn = 4$; histograms of connectivity as de-watering progresses. (b) Water retention curves obtained using the random growth network method. Results for the 2D preformed network with $cn = 4$ are superimposed for comparison (refer to Figure 4.3). 52
- Figure 5.1: Geological history at Mount Elbert site and hydrate stability zone GHSZ. Data compiled from the literature include: ground surface elevation, stratigraphy, surface temperature, and the base of the ice-bearing permafrost BIPF. The gas hydrate stability zone is computed and superimposed on the figure (assumptions and relevant expressions can be found in the text). Time is shown in logarithmic scale in unit of thousand years [k.a.]. 59
- Figure 5.2: Pore size dependent shift in the phase boundary and in situ pressure and temperature profile at the Mt. Elbert site. Trends computed for silt and sands (same trend as for the bulk fluid "F"), kaolin "K" ($e_{100} = 0.89$, $C_c = 0.29$, $S_s = 10\text{m}^2/\text{g}$), illite "I" ($e_{100} = 2.05$, $C_c = 0.82$, $S_s = 70\text{m}^2/\text{g}$), and montmorillonite "M" ($e_{100} = 3.06$, $C_c = 1.15$, $S_s = 300\text{m}^2/\text{g}$). In terms of specific surface, the tested specimen corresponds to "K"; therefore, pore size had only a minor effect restricting the thickness of the hydrate stability zone. 60
- Figure 5.3: Grain surface texture (Note: scales are not uniform). (a, b) High relief, abrupt angular features and fine cracks indicate ongoing crushing. (c) Craters and cavities associated to chemical weathering. (d) Fine subparallel (1), sharp (2) fractures, and well abraded stylus of possibly heavy minerals (3) [Mahaney, 2002]. (e) Crack⁽¹⁾, sharp

cut⁽²⁾ and overwhelmed v-shape percussions on the surface of the grain indicate intensive collision [Krinsley and Doornkamp, 1973; Mahaney, 2002]. (f) Precipitation, the sharp features of the original broken face in the lower left of the micrograph has been dulled by precipitation.

64

Figure 5.4: Spatial variability characterization of undisturbed sediment. (a) X-ray image taken for the as-received frozen sediment – Only the longitudinal central band is shown to highlight features without edge effects. (b) Longitudinal electrical resistance profiles gathered at four locations after thawing the sediment.

66

Figure 5.5: Evolution of geophysical parameters during thawing of the as-received frozen sediment. (a) Temperature. (b) P-wave velocity. (c) S-wave velocity. (d) Inferred frozen sediment length L_f over initial core length L with respect to time during thawing; both P- and S-wave velocities are used to invert for L_f .

67

Figure 5.6: Evolution of S-wave signatures gathered for the specimen saturated with 19THF:81H₂O. (a) Without hydrate at the end of each loading and unloading step. (b) During hydrate formation to reach $S_{hyd}=1.0$ ($\sigma_v'=0.45\text{MPa}$). (c) During hydrate dissociation (at constant vertical stress $\sigma_v'=1\text{MPa}$).

70

Figure 5.7: Mount Elbert sediment mixed with 100% water during loading and unloading: Evolution of void ratio e , shear wave velocity V_s , real permittivity κ' , and electrical conductivity σ_{el} .

71

Figure 5.8: Mount Elbert sediment mixed with 100% water during loading and unloading: Evolution of void ratio e , shear wave velocity V_s , real permittivity κ' , and electrical conductivity σ_{el} .

72

Figure 5.9: Mount Elbert sediment with 19THF:81H₂O pore fluid: Evolution of void ratio e , shear wave velocity V_s , real permittivity κ' , and electrical conductivity σ_{el} during loading, hydrate formation ($S_{hyd} = 1.0$) and dissociation. The interpretation of electrical parameters κ' and σ_{el} for the unfrozen sediment must take into consideration the presence of THF in the pore fluid (compare to Fig.4.6).

73

Figure 5.10: Real permittivity spectra. Data shown for water, THF solutions, and sediment with and without hydrate.

74

Figure 5.11: Vertical strain for sediments mixed with 57THF:43H₂O pore fluid (circles) and 19THF:81H₂O pore fluid (triangles) during hydrate formation and dissociation. H_0 is the height of sediment at the beginning of each formation or dissociation state.

75

Figure 5.12: Data summary: (a, b) Permittivity and conductivity as a function of

- porosity and hydrate saturation. (c) S-wave velocity as a function of vertical effective stress σ_v' and hydrate saturation S_{hyd} . Symbols are data points. Lines correspond to fitted models. 78
- Figure 6.1: The stress-strain path during sampling. Cores experience excavation unloading (0→1) and wall shear (1→2); volumetric (shown) and shear strains are unavoidable (Note: CSL = critical state line; NCL = normal consolidation line; σ_{res} = residual stress mobilized during expansion against the sampling tube). 83
- Figure 6.2: Sampling disturbance and sediment type. Note: * values computed from G_{max} assuming specimen density $\rho = 2000 \text{ kg/m}^3$; ** Computed from V_p assuming $V_p/V_s = 1.5$. 86
- Figure 6.3: Sampling hydrate-bearing sediments. (a) In situ. (b, c) Unloading effective stress and induced shear in pressure cores. (d) The additional consequences of water pressure release in standard core. 88
- Figure 6.4: Vertical stress relaxation and pore pressure variation. (a) Poroelastic modeling: unloading $\Delta\sigma$ of a cylindrical specimen under zero-lateral strain conditions. Ambient water pressure is constantly u_0 . (b) Unloading induced pore pressure distribution as a function of radial distance $\rho = x/R$ and time $\tau = tc_v/R^2$. (c) Peak pore pressure drop $\Delta u_{max}/\Delta\sigma$ as a function of the coring speed $v_{coring} = (c_v/R)$. 90
- Figure 6.5: Secondary hydrate formation during coring. X-ray tomography (processed after Geotek) of hydrate-bearing sediments recovered from the Krishna-Godavari Basin offshore India during the 2006 National Gas Hydrate Program (NGHP). The long hydrate lense across the diameter at the boundary of this percussion core can result from secondary hydrate formation during sampling. 91
- Figure 6.6: Stiffness creep after unloading (from 50kPa to 1kPa) for specimens with different ice saturations S_{ice} . Experimental data (markers) are fitted with an exponential decay model (lines). 93
- Figure 6.7: Effects of changes in pressure and temperature on hydrate saturation. The hydrate saturation within stability zone increases with decreasing temperature and increasing pressure. The change in hydrate saturation due to a 1K decrease in temperature is approximately the same as produced by a 20MPa increase in pressure. 94
- Figure 7.1: Pressure core manipulation. (a) The manipulator MAN couples with the storage chamber and fluid pressures are equalized at the target pressure p_0 before opening the ball valve. (b) The manipulator captures the core and transfers it into the temporary storage chamber. (c) Ball valves are closed and the depressurized storage chamber is

separated. (d) The selected characterization tool is coupled to the manipulator and is pressurized to p_0 . (e) Ball valves are opened and the core is pushed into the characterization tool; stand-alone characterization tools may be detached after retrieving the rest of the core and closing valves. Note: the cutter tool CUT is shown in panes d&e; it is attached in series to cut core to any desired length to meet tool requirements (for stand-alone ESC, DSC, CDP, and Bio tools). 104

Figure 7.2: Schematic diagrams of characterization chambers. (a) IPTC instrumented pressure testing chamber with P-T control. (b) ESC effective stress chamber with σ' -P-T control. (c) DSC direct shear chamber with σ' - τ -P-T control. (d) CDP controlled depressurization chamber for sediment preservation and gas production. (e) BIO sampler for multiple bio-reactor chambers. Scale: the outside diameter of the large ball valve shown in all devices is OD = 220 mm. 106

Figure 7.3: Flexible wall boundary condition. Lateral effective stress can be independently applied through a flexible wall membrane gadget (ID = 63.5mm, H = 150mm). This device allows the implementation of triaxial test conditions, and prevents preferential flow paths along the interface for fluid conductivity studies. 107

Figure 7.4: Tool Control. The displacement of sensors, subsampling tools and drills are controlled under pressure using a screw-based positioning system where the driver advances along the threaded guide while pushing the tool rod (shown in green). Transducers at the tip of the rod are wired through the central hole in the tool rod. 110

Figure 7.5: Measurement tools and sensors. (a) Bender elements for *S*-wave generation and detection. (b) Piezocrystals for *P*-waves. (c) Penetrometer for strength measurement. (d) Pore fluid sampler. (e) Electrical needle probe for resistivity profiling. (f) Thermocouple instrumented tip. (g) Strain gauge for thermal conductivity determination (TPS – NETL; [Rosenbaum *et al.*, 2007]). 111

Figure 7.6: Monitored gas production tests using IPTC: (a) Evolutions of pressure, temperature, electrical resistivity, and produced gas (Krishna-Godavari Basin, [Yun *et al.*, 2010]); (b) Typical wave signatures during gas production: P-wave signatures eventually fade out after gas production; S-waves detect the evolution of the skeleton shear stiffness during hydrate dissociation and gas production (Ulleung Basin, [Yun *et al.*, 2011]). 112

Figure 8.1: Experimental configuration: spring-loaded self-reactive oedometer cell equipped with piezopads (P_P) and a thermocouple (T_c). 117

Figure 8.2: Cascade of selected *P*-wave signatures gathered during various

- experimental stages (Specimen: initial water content $w\%=5$). 118
- Figure 8.3: Coda wave analysis. Illustration using two consecutive P-wave signatures gathered for the specimen with $S_{ice} = 0.06$ during the creep stage. While there is no measurable difference in first arrivals, wave codas can be used to detect minute velocity changes. 119
- Figure 8.4: Evolution of the P-wave velocity during each experimental stage: (a) loading (at temperature $T=20^{\circ}\text{C}$); (b) freezing (at effective stress $\sigma_v' = 600\text{kPa}$); (c) unloading (at temperature $T= -10^{\circ}\text{C}$); (d) thawing (at effective stress $\sigma_v' = 1\text{kPa}$). 122
- Figure 8.5: Evolution of P-wave velocity during creep. (a) P-wave velocities for specimens with different ice saturation during creep following unloading from $\sigma_v = 50\text{kPa}$ to $\sigma_v = 1\text{kPa}$ at constant temperature $T = -10^{\circ}\text{C}$ (Dots represent experimental results and lines are the fitted model). (b) Viscoelastoplastic model for frozen soils. 124
- Figure 8.6: The effect of loading and unloading rate on the stiffness of partially frozen sands. (a) Evolution of P-wave velocities for sands with different ice saturation S_{ice} during unloading (from $\sigma_v = 600\text{kPa}$ to $\sigma_v = 1\text{kPa}$) and reloading (from $\sigma_v = 1\text{kPa}$ to $\sigma_v = 600\text{kPa}$). (b) Schematic illustration of the effect of unloading rate on ice cementation. 126
- Figure 8.7: The effect of stress change rate on the stiffness of partially frozen soils during loading and unloading. 127
- Figure 9.1: Radial flow in point sampling. (a) Experimental configuration of radial flow in point sampling method. Tap water saturated fine sands (Ottawa F110) immersed in brine. Pore water is extracted under constant flow rate q ; meanwhile, the electrical conductance of sampled pore water is monitored. (b) Electrical conductance of sampled pore water with and without using sealing o-ring. 133
- Figure 9.2: 1D flow in cross-sectional sampling using displacement method. (a) Experimental configuration. (b) Pore fluid displacement ratio: relative amount of pore fluid displaced by oil and gas for different types of soils. 134
- Figure 9.3: Inversion of hydraulic conductivity from point water sampling: the shape factor α . (a) Specimen geometry and (b) numerical results of the shape factor α as a function of core geometry $\lambda = L/D$ and relative pore fluid outlet area $\zeta = A_{out}/A_{core}$. 136
- Figure 9.4: Network model simulation – displacement ratio. (a) Pore fluid displacement patterns in terms of capillary force C and viscous force M . Higher viscosity of invading fluid enhances sediment pore fluid

recovery. Note: 30x30 network with mean tube radius $\mu(r) = 10\mu\text{m}$ and standard deviation $\sigma_{(\ln(r/\mu\text{m}))} = 0.4$. (b) Comparison of experimental and network simulation results on pore fluid displacement by forced oil invasion.

138

Figure 9.5: Pore fluid sampling methods versus soil type: underlying physical properties. (a) Relative recoverable pore fluid volume by displacement (disp) and squeezing (sqz) methods for different soils (Note: refer to Table 1 for soil physical properties; stress used in the squeezing method is assumed $\sigma = 1\text{MPa}$; pore fluid replacement ratio used in the displacement method is assumed $R_r = 0.5$). (b) Recoverable water content using displacement (horizontal dashed lines) and squeezing (solid slopes, under varying stress conditions) methods.

140

SUMMARY

An extensive amount of natural gas trapped in the subsurface is found as methane hydrate. A fundamental understanding of natural hydrate-bearing sediments is required to engineer production strategies and to assess the risks hydrates pose to global climate change and large-scale seafloor destabilization. This thesis reports fundamental studies on hydrate nucleation, morphology and the evolution of unsaturation during dissociation, followed by additional studies on sampling and pressure core testing.

Hydrate nucleation is favored on mineral surfaces and it is often triggered by mechanical vibration. Continued hydrate crystal growth within sediments is governed by capillary and skeletal forces; hence, the characteristic particle size d_{10} and the sediment burial depth determine hydrate morphologies in natural sediments. In aged hydrate-bearing sand, Ostwald ripening leads to patchy hydrate formation; the stiffness approaches to the lower bound at low hydrate saturation and the upper bound at high hydrate saturation. Hydrate saturation and pore habit alter the pore size variability and interconnectivity, and change the water retention curve in hydrate-bearing sediments.

The physical properties of hydrate-bearing sediments are determined by the state of stress, porosity, and hydrate saturation. Furthermore, hydrate stability requires sampling, handling, and testing under in situ pressure, temperature, and stress conditions. Therefore, the laboratory characterization of natural hydrate-bearing sediments faces inherent sampling disturbances caused by changes in stress and strain as well as transient pressure and temperature changes that affect hydrate stability. While pressure core technology offers unprecedented opportunities for the study of hydrate-bearing sediments, careful data interpretation must recognize its inherent limitations.

CHAPTER 1

INTRODUCTION

1.1 Motivation

Gas hydrates are solid crystalline compounds where gases are encapsulated by hydrogen-bonded water molecules. Natural gas hydrates physically resemble ice but require low temperature and high pressure to be stable. Such stability conditions constrain gas hydrates occurrence to submarine sediments and permafrost regions [Kvenvolden, 1988]. The amount of methane trapped in gas hydrate is estimated to be $\sim 3 \times 10^{15} \text{ m}^3$ [Boswell and Collett, 2011].

Gas hydrates are a potential energy resource [Boswell, 2009; Collett, 2002], can contribute to climate change [Archer, 2007; Ruppel and Pohlman, 2008], and can cause large-scale seafloor instabilities [Grozic, 2010; Hornbach et al., 2007; Kvalstad et al., 2005]. Unwanted hydrate formation in pipes prevents flow during hydrocarbon recovery [Sloan et al., 2009]. Hydrate formation can be used for hydrogen storage [Koh et al., 2009], CO₂ sequestration [Jung et al., 2010], and efficient geological storage seals [Tohidi et al., 2010]. Earlier research on gas hydrates focused on pure hydrate crystals [Sloan and Koh, 2008]; the focus has shifted in recent years to hydrates in sediments [Waite et al., 2009].

The purpose of this study is to gain a fundamental understanding of hydrate-bearing sediments in the natural environment, and to develop unprecedented devices to characterize natural hydrate-bearing sediments under in situ pressure, temperature, and stress conditions.

1.2 Thesis organization

The research reported in this thesis is contained in the following nine chapters organized around three main themes:

I. Fundamental properties of hydrate-bearing sediments.

- Chapter 2 documents the study of heterogeneous hydrate nucleation on mineral surfaces and the role of mechanical agitation.
- Chapter 3 investigates the effect of hydrate morphologies in natural sediments on physical properties with emphasis on patchy hydrate saturation in sands.
- Chapter 4 uses network model simulations to study the water retention curve of hydrate-bearing sediments as a function of hydrate saturation.

II. Natural systems.

- Chapter 5 reports an in depth analysis of sub-permafrost hydrate formation at Mount Elbert (Alaska North Slope) followed by a comprehensive laboratory study of a specimen recovered from hydrate stability zone at this site.
- Chapter 6 explores sampling effects on natural hydrate-bearing sediments, and the advantages of pressure core technology. Examples are based on the study of marine hydrate-bearing sediments conducted at the Krishna-Godavari Basin.

III. Characterization techniques for hydrate-bearing sediments.

- Chapter 7 documents a set of high pressure chambers developed to manipulate, subsample, and characterize hydrate-bearing sediments under in situ conditions.
- Chapter 8 uses coda wave analysis to characterize sampling-induced stiffness loss and decementation in frozen soils as an analogue for hydrate-bearing sediments.
- Chapter 9 highlights underlying physical processes during pore water sampling and reports the development of new methodologies and devices compatible with current pressure core technology to sample pore fluids without causing hydrate dissociation.

Finally, Chapter 10 summarizes salient conclusions from this study.

CHAPTER 2

THE HYDRATE NUCLEATION IN QUIESCENT AND DYNAMIC CONDITIONS

Static tests were conducted by J.Y. Lee (2007) and are revisited here as part of a comprehensive study of hydrate nucleation in sediments.

2.1 Introduction

The nucleation of a new phase is the initial step in water freezing, hydrate formation, and salt precipitation. The spontaneous formation of an ordered crystalline lattice from a disordered phase is a random process. In fact, a system can be taken inside the solid phase equilibrium conditions without experiencing phase transformation; such is the case of supercooling. During this metastable state, small crystallites nucleate and immediately break apart. Stochastic nuclei formation results in random induction times. Continued crystal growth starts when nuclei exceed a critical size [Mullin, 2001]. During phase transformation, the equilibrium temperature can be depressed by ionic concentration, charged particles, or capillary effects. Figure 2.1 shows a typical temperature signature for a fluid that undergoes exothermic phase transition during cooling; supercooling, induction time, and equilibrium temperature depression are shown.

Gas hydrate nucleation may take days in quiescent conditions [Sloan and Fleyfel, 1991]. While thermodynamic equilibrium conditions can be accurately predicted [Skovborg *et al.*, 1993; Sloan and Koh, 2008], the kinetics of hydrate formation are affected by mineral surface characteristics, impurities, and mechanical agitations.

The inherent stochastic characteristics of hydrate nucleation are investigated in this study. Experiments include different sediments and externally imposed vibrations. A review of previous studies is presented first.

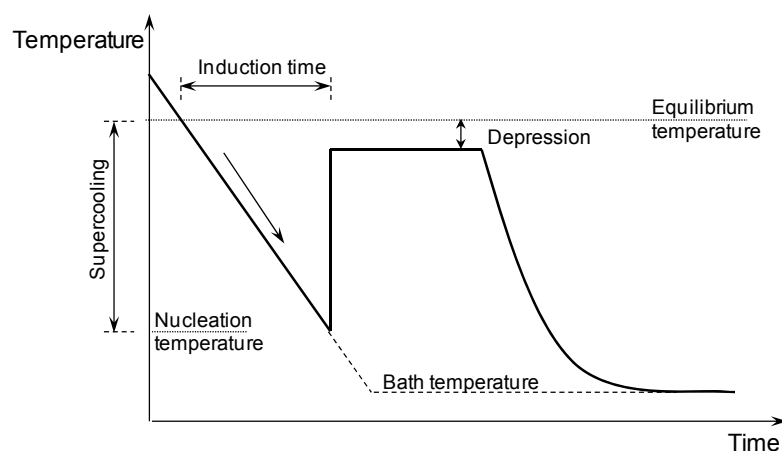


Figure 2.1. Schematic temperature-time signature corresponding to an exothermic phase transformation during cooling – Labels denote supercooling, induction time, freezing point depression, and equilibrium temperature.

2.2 Previous Studies

Nucleation is affected by thermal history, the type of solution, the presence and type of impurities, and agitation. These are reviewed next.

(1) Thermal history of the solution: The molecular structure of water that was previously part of hydrate may not be completely disordered when the PT conditions remain near the stability field. This memory effect reduces induction times for hydrate re-formation [Vysniauskas and Bishnoi, 1983]. During transformation, an order of magnitude increase in the cooling rate lowers the mean nucleation temperature by 0.6 to 2°C [Hobbs, 1974].

(2) Physical properties of the solution: Viscosity, the amount of available mass [Young and Cross, 1911], and salt concentration affect nucleation and crystal growth [Englezos and Hall, 1994; Sloan and Koh, 2008]. In particular, dissolved salts lower the activity of water through strong coulombic attraction as compared to the weaker hydrogen or Van der Waals bonds in hydrate structures; lower activity delays nucleation. Other biological and polymeric inhibitors effectively hinder nucleation [Al-Adel et al., 2008; Lin et al., 2004].

(3) Impurities: The presence of impurities favors heterogeneous nucleation, and reduces both the induction time and the degree of supercooling as a function of particle surface characteristics [*Cha et al.*, 1988; *Englezos and Hall*, 1994; *Riestenberg et al.*, 2003; *Ting and McCabe*, 1934]. On the contrary, small pore sizes shift the stability field to higher pressure or lower temperature [*Clennell et al.*, 1999; *Fletcher*, 1958; *Handa and Stupin*, 1992; *Husowitz and Talanquer*, 2004; *Kwon et al.*, 2008; *Østergaard et al.*, 2002; *Restagno et al.*, 2000].

(4) Mechanical agitation: Experiments show that stirring, shaking, or shocking can trigger nucleation in a supersaturated fluid [*Mullin*, 2001; *Mullin and Raven*, 1962; *Skovborg et al.*, 1993; *Young*, 1911; *Young and Cross*, 1911]. Similarly, mechanical stimuli facilitate ice nucleation and gas hydrate formation [*Barrer and Edge*, 1967; *Skovborg et al.*, 1993; *Sloan and Fleyfel*, 1991; *Tajima et al.*, 2004]. Experimental results for other systems show that the nucleation rate and the morphology of precipitates are affected by stirring conditions and rate [*Akkermans et al.*, 2006; *Liang et al.*, 2004; *Ting and McCabe*, 1934]. The underlying molecular-scale mechanisms remain unclear.

2.3 Experimental Study

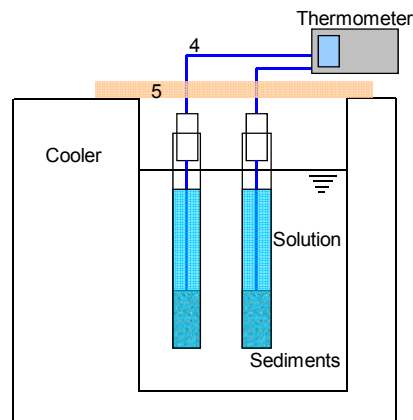
Two experimental studies are conducted to investigate the effect of minerals on THF (tetrahydrofuran) hydrate nucleation under quiescent conditions, and to identify the characteristics of mechanical agitation that favor ice and THF hydrate formation. THF provides accurate control on hydrate concentration, overcomes diffusion-control transport, and nucleates at atmospheric pressure. Devices and test procedures are described first.

2.3.1 Experimental devices and configurations

Figure 2.2 illustrates the experimental configurations used for the two studies.

Temperature is controlled using a high-precision cooler and measured using a smooth bar K-type thermocouple (precision of $\sim 0.1^{\circ}\text{C}$). In dynamic tests (Figure 2.2b), external vibrations are supplied through a stainless steel rod coupled to a piezoelectric actuator (Model 712A01, PCB Piezotronics, Inc.). Vibration frequency and amplitude are controlled through the power supply and the rod vibration is measured using a collinearly mounted accelerometer (Model 350B04, PCB Piezotronics, Inc.). The vibration frequency explored in this study ranges from 800Hz to 7000Hz.

(a)



(b)

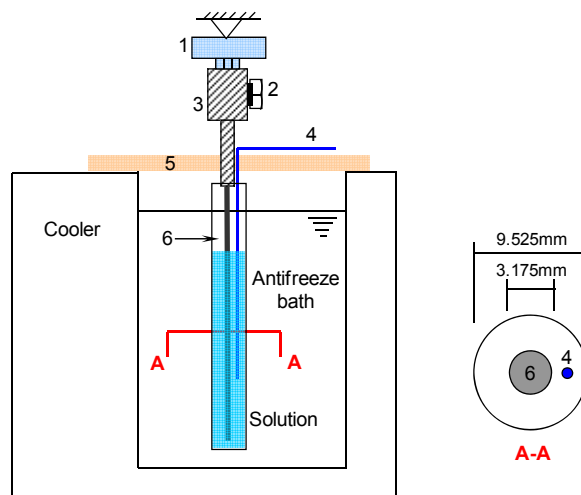


Figure 2.2. Experimental configuration: (a) static test and (b) vibration test. Components: 1. Piezoelectric actuator (Model 712A01, PCB Piezotronics, Inc.). 2. Accelerometer (Model 350B04, PCB Piezotronics, Inc.). 3. Nylon coupler. 4. Thermocouple (K-type, precision = 0.1°C). 5. Heat-insulation foam cover. 6. Stainless steel rod.

2.3.2 Materials - Specimen preparation

Dynamic tests involve either 10ml deionized water (ice formation) or 10ml 81H₂O:19THF stoichiometric solution (100% hydrate formation).

Specimens for static tests consist of 20ml 81H₂O:19THF solution (stoichiometric solution – 100% hydrate) and 5g of soils. Table 2.1 summarizes the main properties of the selected soils. The randomly-shaped RP2 kaolinite is smaller than the hexagonal shaped SA1. Crushed silt is an angular, low specific surface silt. Precipitated silt consists of silt-size aggregations with extensive inter-particle pore networks and high specific surface. The irregularly shaped GCC particles are bulkier than the very uniform, rice-shaped PCC particles.

The selected soil is added to the solution, shaken vigorously, and left to rest in the sealed cylinder for 1~2 hours to allow for sedimentation. A thin layer of oil is added to cover THF solution specimens immediately after mixing to prevent THF evaporation during testing. Each test starts with a freshly prepared specimen to avoid contamination or memory effects.

2.3.3 Experimental procedures

Prepared test cylinders are immersed into a cooling bath with a constant temperature of -5°C and sealed. In dynamic tests, the oscillatory vibration with preselected frequency and amplitude is applied immediately after the cylinder is submerged in the cooler. Bath and cylinder temperatures are monitored to detect phase transformation.

2.3.4 Typical temperature signatures

The phase transformation temperature at the THF hydrate boundary depends on the relative amount of water and THF (Figure 2.3a). At atmospheric pressure, the equilibrium temperature of 81H₂O:19THF solution is ~-4.5°C. Typical temperature-time

Table 2.1. Physical properties of selected sediments

	Kaolinite (SA1)	Kaolinite (RP2)	Precipitated silt (PS)	Crushed silt (CS)	Ground CaCO ₃ (GCC)	Precipitated CaCO ₃ (PCC)
Specific gravity, G_s	2.6	2.6	2.08	2.65	2.71	2.71
Mean grain size, d_{50} [μm]	1.1	0.36	20	20	12	1
pH	6.5	4.66	7	7	8.76	9.87
Specific surface, S_s [m^2/g]	36	29	120	0.113	1.8	9.9
Liquid limit, LL	43	78	-	-	28	52
Sphericity, S	0.7	0.7	0.9	0.9	0.8	0.2
Roundness, R	0.1	0.3	0.7	0.1	0.5	0.9

signatures of deionized water, excess water THF solution (90H₂O:10THF), stoichiometric mixture (81H₂O:19THF), and excess THF solution (40H₂O:60THF) are shown in Figure 2.3b. The induction time in these signatures varies from 3000s (water) to more than 6000s (excess water solution). Supercooling reaches -7.5°C (stoichiometric solution). The exothermic peak readily seen in all cases marks the beginning of the transformation. All reactions reach the equilibrium temperature. The excess water solution exhibits the exothermic peak for hydrate formation followed by the peak for ice formation.

2.4 Results and Analyses

2.4.1 Heterogeneous hydrate nucleation – Static tests

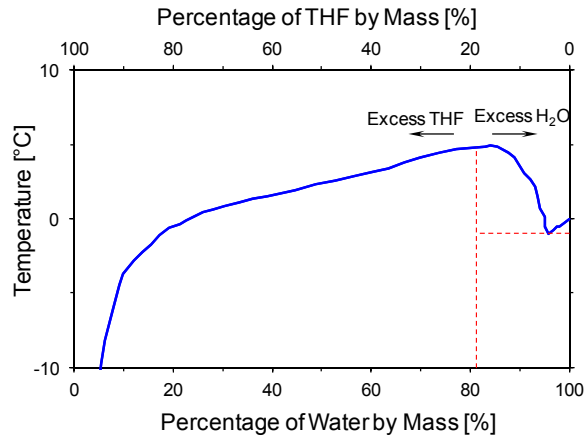
A total of 40 static tests were completed as part of this study. Results are summarized in Figure 2.4. The presence of minerals facilitates nucleation, except in the case of precipitated calcium carbonate PCC. Industrial precipitated mineral (PCC and PS) are less effective at nucleating hydrates than their crushed counterparts (GCC and CS); they also exhibit higher water-mineral contact angle.

Mineral surfaces lower the thermal agitation of water molecules, and prompt their alignment; hence, mineral surfaces that more closely mimic the hydrate crystal structure are more efficient nucleators [Blackwell, 1999; Park and Sposito, 2003; Turnbull and Vonnegut, 1952]. The number of water molecules per unit volume next to mineral surfaces n_w ($1/m^3$) can be estimated in terms of porosity n and specific surface S_s (m^2/g):

$$n_w = \frac{S_s(1-n)G_s\rho_w}{(l_{water})^2} \quad (2.1)$$

where G_s is specific gravity of minerals, ρ_w is water density, and l_{water} is the characteristic size of a water molecule. Experimental results in Figure 2.4 do not show clear benefits

(a)



(b)

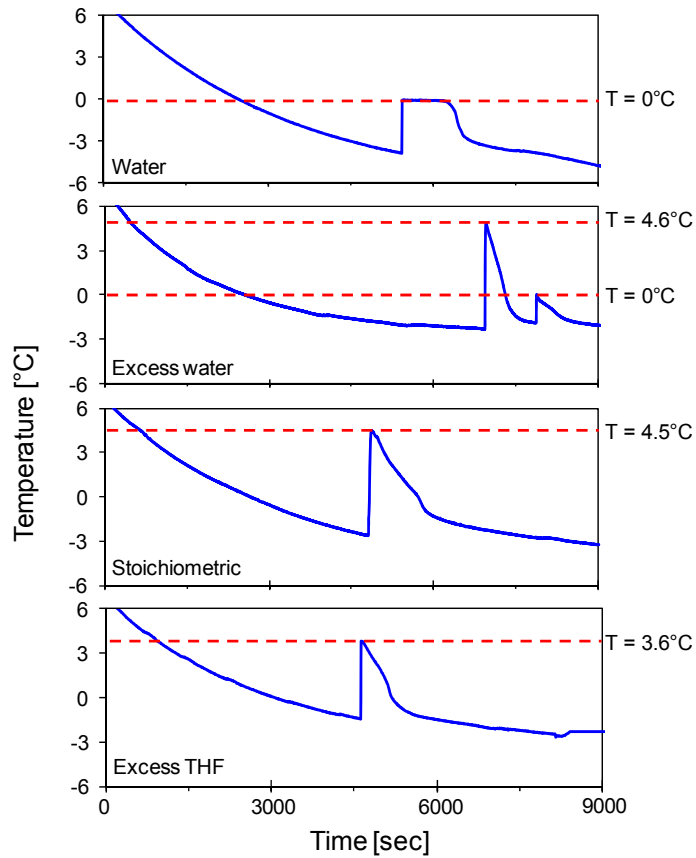


Figure 2.3. Phase transformation. (a) Stability temperature for THF-water mixtures at atmospheric pressure. (b) Typical temperature-time signatures for tap water, THF solution with excess water (90H₂O:10THF), stoichiometric mixture 100% hydrate (81H₂O:19THF), and THF solution with excess THF (40H₂O:60THF).

from specific surface (highest for the two kaolinite clays). Hence, mineral-water interaction associated to mineral surface characteristics must be more important than specific surface. In fact, the rate of nucleation has been linked to the Gibbs free energy ΔG^* , which can be linked to contact and interfacial tension [Hobbs, 1974].

Sediment pores can also affect nucleation kinetics in various ways, particularly as pore sizes become smaller than 10nm [Clennell *et al.*, 1999; Handa and Stupin, 1992; Jang, 2011; Kwon *et al.*, 2008; Østergaard *et al.*, 2002]: small pores restrict the embryo size, capillary suction in mixed fluid conditions hinders nucleation, water activity is reduced in nanometer-sized pores. Pore sizes in this study are 100nm or larger and exert minimal effects on nucleation.

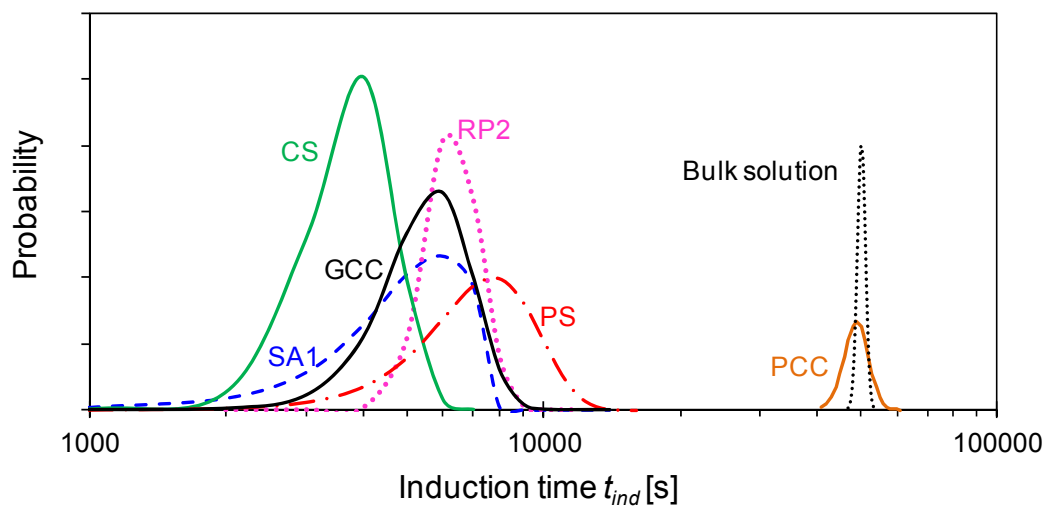


Figure 2.4. Effects of minerals on nucleation.

2.4.2 The effect of mechanical vibration on nucleation

Measured induction times for water-to-ice and THF solution-to-hydrate formation under agitation are shown on tripartite plots in Figure 2.5. Results in both cases suggest that an acceleration threshold is a better discriminator of nucleation than vibration

frequency or amplitude, or vibration velocity (within the vibration frequency explored here, i.e., from 800Hz to 7000Hz - nucleation under mechanical agitation beyond this frequency range needs further work to validate).

Experimental results are replotted in terms of induction time versus peak acceleration in Figure 2.6. The solid line represents the mean induction time $\mu(t_{ind})$ and dashed lines represent the one standard deviation $\pm\sigma(t_{ind})$ band in induction times measured for specimens without vibration as the control group. Histograms for thresholded data clearly show that external vibrations facilitate nucleation when they exceed $a \sim 10\text{m/s}^2$ (Figure 2.6). Yet, induction time data remain variable, that is, mechanical vibration does not suppress nucleation randomness.

Several hypotheses have been advanced to explain the role of agitation on nucleation. Some suggest that mechanical agitation enhances nucleation by altering incipient nuclei to favor crystallization sites [*Melia and Moffitt, 1964; Mullin and Raven, 1962*]. Others consider that mechanical agitation causes transient inhomogeneous energy distribution and high energy regions favor nucleation [*Mullin, 2001*].

At the molecular scale, agitation must cause enough relative displacement to facilitate the formation of a new structure, i.e., nucleation. Let's idealize molecular scale interactions as a damped, single degree of freedom system with a linear spring k , mass m , and dashpot η . The motion that the second molecular layer experiences $y_{m(t)}$ is related to the motion imposed on the first layer $y_{b(t)} = A\cos(\omega t)$ as

$$y_{m(t)} = H * y_{b(t)}, \quad (2.2)$$

where the transfer function H represents the intermolecular response function. The equation of motion follows Newton's second law:

$$m \frac{\partial^2 y_{m(t)}}{\partial t^2} + \eta \frac{\partial (y_{m(t)} - y_{b(t)})}{\partial t} + k(y_{m(t)} - y_{b(t)}) = 0. \quad (2.3)$$

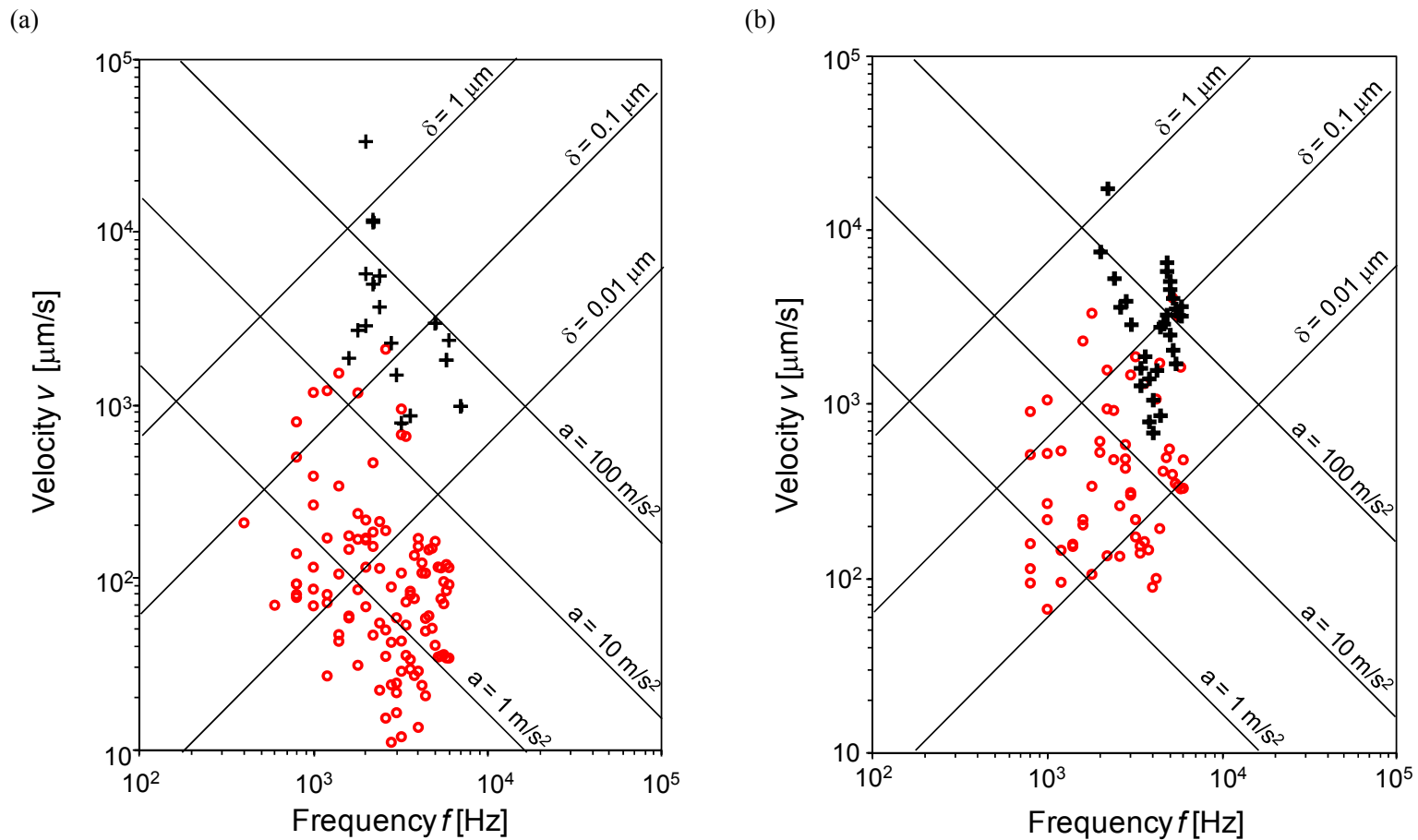
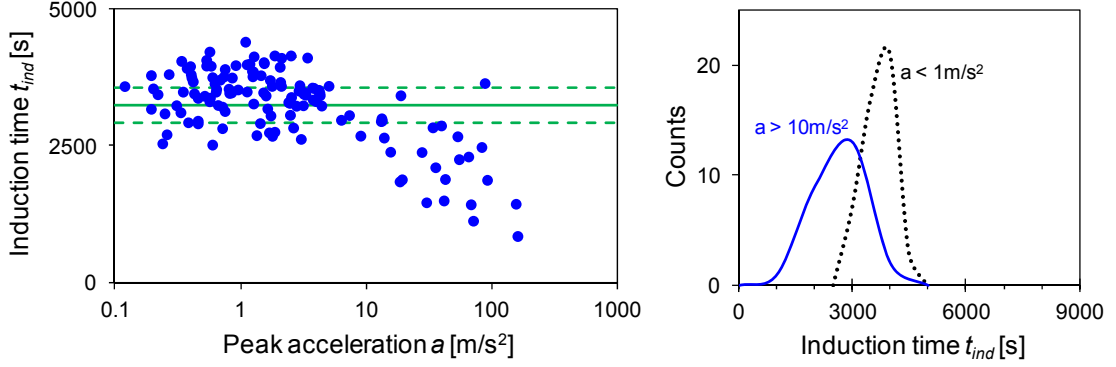


Figure 2.5. Experimental results in tripartite: (a) water to ice and (b) stoichiometric THF-water to hydrate transition. Induction times are represented by symbols: in (a) crosses are results of $t_{ind} < 2500\text{s}$ and circles are results of $t_{ind} > 2500\text{s}$; in (b) crosses are results of $t_{ind} < 5000\text{s}$ and circles are results of $t_{ind} > 5000\text{s}$.

(a) Water to ice



(b) Stoichiometric H₂O-THF mixture to THF hydrate

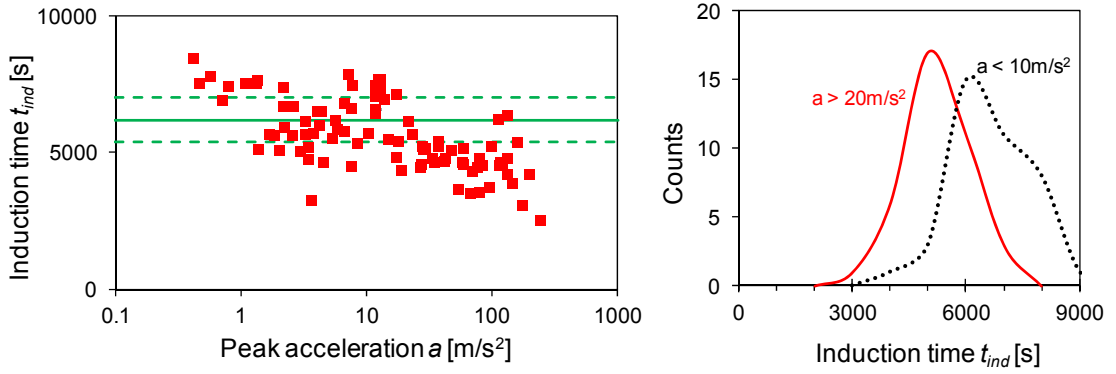


Figure 2.6. Experimental results: Induction time t_{ind} versus peak acceleration a . Cases: (a) tap water and (b) stoichiometric mixture (81H₂O:19THF) 100% hydrate. Discrete points are experimental results obtained with mechanical vibrations. As a reference, the mean and standard deviation values of 16 specimens without vibration are shown as solid and dashed lines.

The combination of Equations 2.2 and 2.3 renders:

$$H = \frac{\omega\eta - k}{\omega^2 m + \omega\eta - k}. \quad (2.4)$$

Thus, the maximum relative displacement δ becomes

$$\delta = \left| y_{m(t)} - y_{b(t)} \right|_{\max} = \left| (H-1)y_{b(t)} \right|_{\max} = \frac{A}{1 + 2\zeta \left(\frac{\omega_r}{\omega} \right) - \left(\frac{\omega_r}{\omega} \right)^2} \quad (2.5)$$

where the resonant frequency is $\omega_r = \sqrt{k/m}$ and the damping ratio is $\zeta = \eta/(2\sqrt{km})$. This equation suggests that: (1) the maximum relative displacement δ approaches the maximum excitation amplitude A at high frequencies $\omega \rightarrow \infty$ where inertia prevails; (2) it is affected by viscous damping η at intermediate frequencies; and (3) it is dominated by the inter-molecular springiness k at low frequencies when $\delta \rightarrow 0$ as $\omega \rightarrow 0$.

Excitation frequencies in this study are much lower than molecular resonance/relaxation frequencies, $\omega/\omega_r \ll 1$. The maximum relative displacement δ/A at low excitation frequencies scales with ω^2 ; this is in agreement with experimental results in Figure 5 that show acceleration $a = A\omega^2$ as the decisive vibration characteristic.

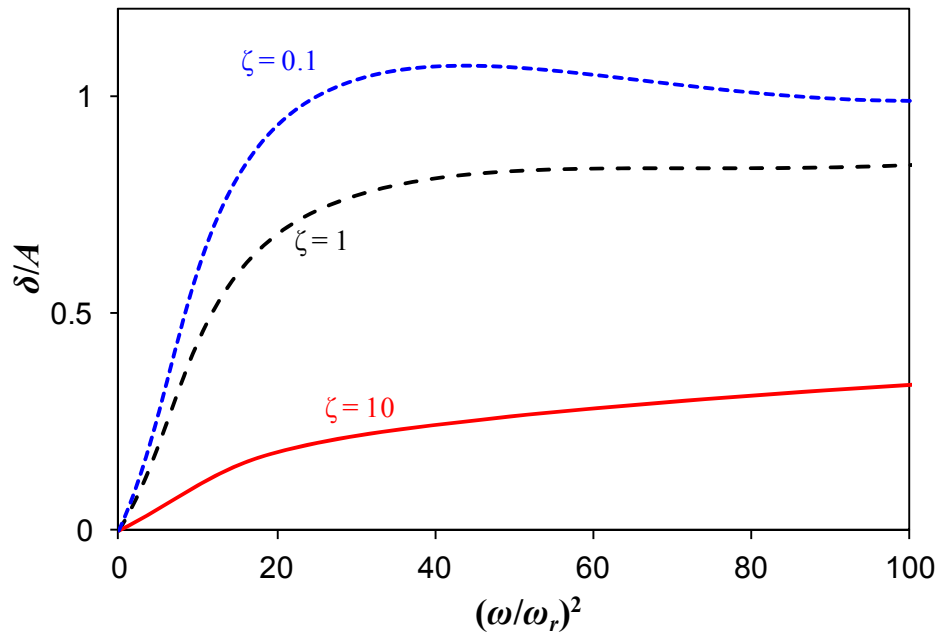


Figure 2.7. Molecular scale analogue: mass, spring, and viscous dissipation. Normalized maximum relative displacement between the first and second molecules subjected to base excitation as a function of excitation frequency.

2.5 Conclusions

Solid phase hydrate formation exhibits induction time, supercooling, and transformation temperature depression. Nucleation is inherently stochastic and experimental results should be expressed in statistical form.

Nucleation is favored in the presence of most minerals. Mineral surface properties affect the induction time and the degree of supercooling, but do not change the equilibrium temperature during phase transformation. Mineralogy and fluid-mineral interaction (i.e., contact angle and interfacial tension) are more important than particle size and sediment porosity.

Mechanical vibration facilitates nucleation. The tripartite analysis of experimental results reveals that acceleration is a better discriminator of nucleation than vibration frequency or amplitude, or vibration velocity.

Experimental results suggest that nucleation is prompted when the imposed acceleration exceeds $\sim 10\text{m/s}^2$. Relative molecular displacement emerges as the underlying mechanism. Mechanical vibration does not suppress the inherent stochastic nature of nucleation. Similarly, boundary layer shear and pore-scale turbulence in steady state flow conditions can favor nucleation.

CHAPTER 3

HYDRATE MORPHOLOGY: PHYSICAL PROPERTIES OF SANDS WITH PATCHY HYDRATE SATURATION

3.1 Introduction

Engineering protocols and stability analyses needed for safe gas production from hydrate-bearing sediments require accurate information about the sediment's physical properties and their dependence on hydrate volume fraction and spatial distribution. Prior to the early 1980's, methane gas hydrate was assumed to be uniformly distributed wherever pressure and temperature conditions were appropriate [Milkov, 2004; Trofimuk *et al.*, 1973]. Subsequent studies have revealed a heterogeneous global distribution, due in part to the importance of advective transport in supplying sufficient methane for hydrate formation [Buffett and Archer, 2004; Gornitz and Fung, 1994; McIver, 1981; Wood and Jung, 2008], as well as spatially-varying sediment properties such as grain size and porosity [Clennell *et al.*, 1999; Waite *et al.*, 2009].

Connections between the sediment type, burial conditions, and resulting hydrate distributions are becoming more apparent as the inventory of high-resolution images of recovered hydrate-bearing cores increases. We have taken advantage of X-ray computed tomography [Holland *et al.*, 2008; Kneafsey, 2010], micro-CT [Jin *et al.*, 2006; Kerkar *et al.*, 2009], and magnetic resonance [Ersland *et al.*, 2010; Kleinberg *et al.*, 2003; Stevens *et al.*, 2008] to explore hydrate occurrence patterns in all types of natural sediments, and present a first-order physical model to analyze these patterns in terms of environmental conditions and sediment characteristics. Focusing on high value, energy resource environments, we then estimate a suite of physical properties for hydrate-bearing sands, containing patches of 100% hydrate-saturated sand embedded in water-

filled sand.

3.2 Hydrate in Porous Media: Patterns

3.2.1 Nucleation and Growth

Hydrate nucleation is favored at the water-gas interface in water-limited systems [Kleinberg *et al.*, 2003; Tohidi *et al.*, 2001; Waite *et al.*, 2004] and on mineral surfaces in the absence of free gas due to the reduced thermal activity and spatial distribution of water molecules in the vicinity of mineral surfaces [Dominguez *et al.*, 2000; Page and Sear, 2006]. Under stable pressure and temperature conditions, molecules continuously jump from one phase to the other in hydrate-water or hydrate-gas systems, and a minimum crystal size d_{cr} of several nanometers must be reached to ensure a stable nucleus for gas-hydrate growth [Lee, 2007]. Eventually, stable nuclei grow into the pore space between sediment grains. Continued molecular transfer across phases can gradually change the spatial hydrate distribution in sediments, concentrating hydrate into fewer, larger crystals [Myerson, 2002]. This “Ostwald-ripening” phenomenon occurs because the methane concentration is higher around smaller hydrate crystals according to the Gibbs-Thompson effect [Henry *et al.*, 1999; Kwon *et al.*, 2008] and diffusive transport develops from the higher methane concentrations surrounding smaller crystals toward larger crystals.

Eventually, hydrate growth becomes constrained by the mineral grains. Further growth takes place by either invading neighboring pores or displacing particles to enlarge the occupied pores. Whether growth occurs in a grain-displacing or pore-filling manner depends on the balance between the local effective stress and the capillary pressure developed by the hydrate mass. At equilibrium, the pressure in the hydrate phase u_h must balance the pressure in the water phase u_w and the effective stress acting on the grain skeleton σ' for a large interface:

$$u_h = u_w + \sigma' . \quad (3.1)$$

In addition, pressures in the hydrate u_h and water u_w phases are related through Laplace's equation [Clennell *et al.*, 1999; Coussy, 2011]

$$(u_h - u_w) = \frac{4\gamma_{hw} \cos \theta}{d_{th}} , \quad (3.2)$$

where the contact angle is assumed here to be $\theta = 0^\circ$, and the hydrate-water interfacial tension is $\gamma_{hw} = 0.032 - 0.039$ N/m [Anderson *et al.*, 2003; Uchida *et al.*, 1999]. The pore throat diameter d_{th} is determined by the fine sediment fraction, taken here to be the finest 10th percentile in the grain size distribution. The pore throat diameter is $d_{th} \cong (\sqrt{2} - 1)d_{10}$ for simple cubic packing. These equations are combined to define a dimensionless parameter:

$$\psi = \frac{\left(\frac{4\gamma_{hw}}{d_{th}}\right)}{\sigma'} = \frac{4\gamma_{hw}}{(\sqrt{2} - 1)d_{10}\sigma'} \cong \frac{10\gamma_{hw}}{d_{10}\sigma'} , \quad (3.3)$$

which reflects the relative balance between capillarity and effective stress. When $\psi > 1$, capillarity prevails and hydrate can displace particles more readily than invade pore throats; thus, we anticipate that fine-grained soils (small d_{10}) under low effective stress σ' are prone to grain-displacement and segregated hydrate formation. Conversely, $\psi < 1$ corresponds to coarse-grained sediments (large d_{10}) subjected to high effective stress σ' , and hydrate growth will fill and invade existing pores rather than displace grains. Therefore, Ostwald ripening in coarse-grained sediments will promote patchy hydrate distributions, whereby hydrate-filled sediment patches ($S_h = 100\%$) are embedded in a hydrate-free sediment ($S_h = 0\%$).

3.2.2 Hydrate Occurrence Patterns: Field Evidence

Reported hydrate morphologies in natural hydrate-bearing sediments are

summarized in Table 3.1, together with reservoir location, core depth, and sediment characteristics. Figure 3.1 shows the same data plotted in terms of vertical effective stress σ_v' versus effective grain size d_{10} . The vertical effective stress is calculated using the sediment depth and an assumed sediment density of 2000 kg/m^3 . The effective grain size d_{10} is estimated from reported grain size distributions and sediment descriptions.

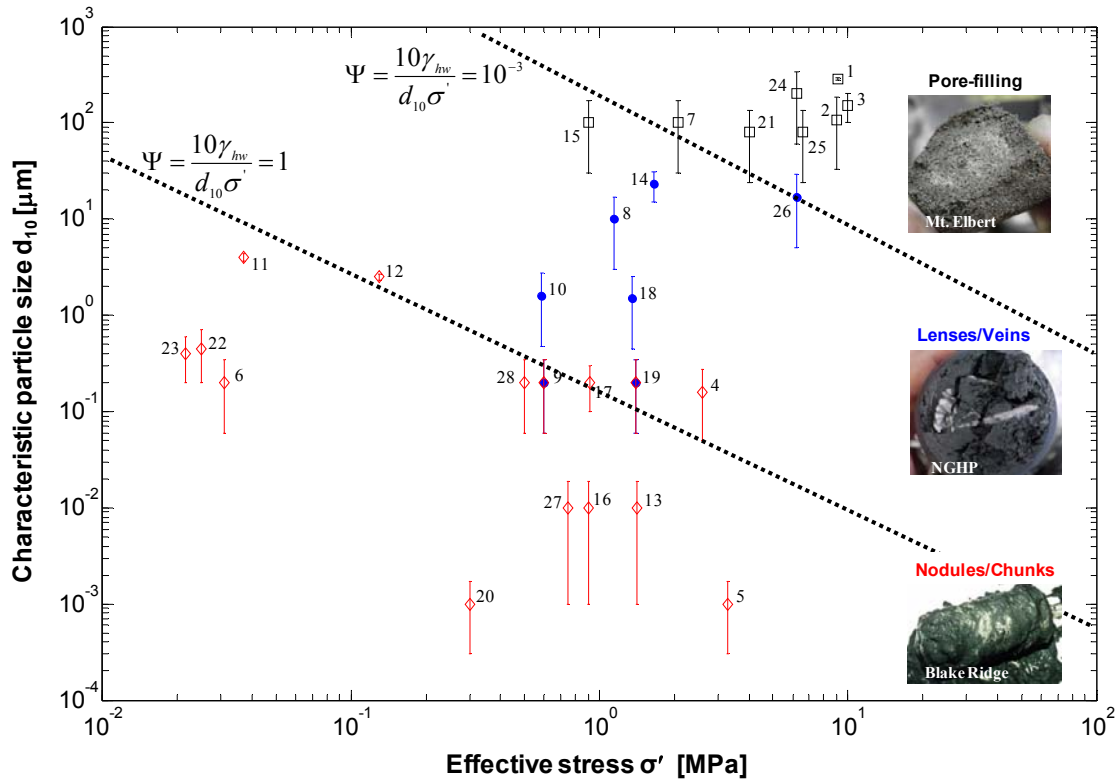


Figure 3.1 Hydrate morphologies in natural sediments – Field evidence and ψ -boundaries. In response to a combination of sediment particle size and effective stress, hydrate formation occurs in one of three general morphologies: Environments with relatively large sediment grains and high effective stress can host pore-filling hydrates (Upper inset); in contrast, hydrates forming in fine-grained sediment with low effective stress can displace sediment grains in all directions and create hydrate nodules or chunks (Lower inset). Between these two extremes, hydrate formation responds to variations in the local stress, displacing sediment grains in the directions of the smallest stress to form hydrate lenses and veins (Middle inset). All data are based on core analysis and do not necessarily reflect reservoir properties (Refer to Table 3.1 for details).

Table 3.1 Hydrate morphologies in natural hydrate-bearing sediments. These data reflect properties of each recovered core only, and may not necessarily represent the properties of entire reservoirs.

Location	No.	Depth [mbsf]	Water depth [m]	Hydrate morphology	Sediment description	Index properties *	d ₁₀ [μm]		Typical values	Ref.
							Mean	s.dev.		
Mallik	1	913.7	913.7	pore filling	granular/pebbles (max 1cm)	d ₁₀ =275.9-292.9μm (at 912.3m)	285	8.5		a,b
	2	903	903	pore filling	medium-grained sand	d ₁₀ =108.4μm (at 908.3m)	108.4	76.02		a,b
	3	892.8-1088.1	990.45	pore filling	medium/fine sands	d ₅₀ =149.9-502.5μm	150	50	fine/medium sands: 0.06-0.6mm	a,b
Blake Ridge	4	259	3058.1	nodules	nanofossil-rich clay	d ₅₀ =1.6 μm	0.16	0.11		c, d
	5	330	3100.1	chunks	55%Illite+45%Smectite		0.001	0.0007	Smectite: ~1nm	c, d
Nankai Trough	6	3.09	2781.59	nodules/chunks	soft clay (39.2% clay)	LL=68; PL=24	0.2	0.14	Kaolinite: ~0.1-1μm	e, f
	7	207.8-260	1178.9	pore filling	sandy sediments		100	70.13	fine/medium sands: 0.06-0.6mm	g
	8	90-140	4799.3	veins	60% sand/granules +40% silt		10	7.01	silt: 2-60μm	h
NGHP	9	60	1300	veins(nodules?)	fine grained clay minerals	S _s =87-94 m ² /g; LL=73-75; PL=34-36	0.2	0.14	Kaolinite: ~0.1-1μm	i, j
Cascadia Margin	10	58.44	1107.44	veins		φ ₁₀ =9.28; φ ₅₀ =6.08	1.6	1.12		k
	11	3.7	678.2	nodules	soft clay sediments	φ ₅₀ =5.7; S=1.2; Sk=-0.81(at 3.59m)	4	0.3		l, m
	12	13.05	687.55	nodules		φ ₅₀ =4.05; S=0.95; Sk=-0.58	2.5	0.2		m, n
Offshore Peru	13	141	3961	nodules	diatomaceous muds (44%Illite)		0.01	0.01	Illite: ~10-100nm	o, p
Okushiri Ridge	14	165.6	5235.6	nodules	diatomaceous muds	φ ₁₀ =5-6	23	8		p, q
	15	88.3-97.9	2715.7	pore filling	Sandy sediments		100	70.13	fine/medium sands: 0.06-0.6mm	r
	16	88.3-97.9	2715.7	nodule	diatom-bearing clays, silty clay	LL=113-143 (at 83.75-189.9m, 799A)	0.01	0.01	Illite: ~10-100nm	r, s
	17	91.07	2661.67	nodule	abundant diatoms	75% sand+15% silt +10%clay	0.2	0.1	Kaolinite: ~0.1-1μm	r

Ulleung Basin	18	136	2100	veins/lenses	microfossile, clay	$d_{50}=3.041 \mu\text{m};$ $d_{10}=1.5 \mu\text{m}$	1.5	1.05		t
	19	140	2218	vein and nodule		18%clay+82%silt $S_s=71$ (at 141m)	0.2	0.14	Kaolinite: $\sim 0.1-1 \mu\text{m}$	u, v
Orca Basin, GOM	20	20-40	2425	nodules	smectite dominant clay	LL=83; PL=31	0.001	0.0007	Smectite $\sim 1\text{nm}$	w, x, y
Alaminos Canyon, GOM	21	~ 400	~ 3130	pore filling	fine sands		80	56.10	fine sands: 60-200 μm	z
Sea of Okhotsk	22	2.3-2.7	~ 840	nodules	20.42% clay	$\phi_{50}=6.13; S=1.73; Sk=1.4;$ $K=2.16$	0.45	0.25		aa, ab
	23	1.65-2.65	~ 670	nodules/veins	23.4% clay	$\phi_{50}=6.35; S=1.70;$ $Sk=1.31; K=2.09$	0.4	0.2		aa, ab
Mt. Elbert	24	619.9	619.9	pore filling	fine quartz sand	$d_{10}=\sim 0.2\text{mm}$ (at 618.1m)	200	140.26		ac, ad
	25	661	661	pore filling	fine-grained quarts	$d_{10}=\sim 0.08\text{mm}$ (at 662.4m)	80	56.10		ac, ad
	26	620	620	vein	silty sand	$d_{10}=0.017\text{mm}$	17	11.92		ae
Atwater Valley	27	0-158	1370	nodules	clay	$S_s=94.2-143.1 \text{ m}^2/\text{g}$	0.01	0.01	Illite: $\sim 10-100\text{nm}$	af
Hydrate Ridge	28	5-106	945.5	nodules	clay	$d_{50}=6 \mu\text{m}; d_{10}=\sim 0.2\text{mm}$	0.2	0.14		ag

Note: 1. Properties: *LL*: liquid limit; *PL*: plastic limit; *S_s*: specific surface; ϕ : the *phi* scale of particle size; *S*: sorting; *Sk*: skewness; *K*: kurtosis;
2. The mean values of d_{10} are chosen either based on reported data or from typical particle sizes listed in the Notes column;
3. The s. dev. (standard deviation) is computed as $s.d.[X] = \text{Mean} \times \sqrt{e^{0.4} - 1}$, since most natural sediments present log-normal distributions with standard deviation $N(\sigma^2)=0.4 \pm 0.2$ (Phadnis and Santamarina, 2011).

References: a) Uchida et al. [2000]; b) Kulenkampff and Spangenberg [2005]; c) Matsumoto et al. [2000]; d) Collett and Wendlandt [2000]; e) Winters [2000a]; f) Winters [2000b]; g) Uchida et al. [2004]; h) Taira et al. [1991]; i) Yun et al. [2010]; j) Collett et al. [2008]; k) Winters et al. [2008]; l) Hovland et al. [1995]; m) Camerlenghi et al. [1995]; n) Westbrook et al. [1994]; o) von Huene et al. [1987]; p) Kvenvolden and Kastner [1990]; q) Hill and Marsters [1990]; r) Tamaki et al. [1990]; s) Holler [1992]; t) Yun et al. [2011]; u) Kim et al. [2011]; v) Kwon et al. [2011]; w) Pflaum et al. [1985]; x) Thayer et al. [1986]; y) Bryant et al. [1986]; z) Boswell et al. [2009]; aa) Luan et al. [2008]; ab) Dang et al. [2010]; ac) Stern et al. [2011]; ad) Winters et al. [2011]; ae) Dai et al. [2011]; af) Yun et al. [2006]; ag) Tan et al. [2006].

Observations show that naturally occurring hydrate exhibits three general morphologies: pore-fill, lenses/veins, and nodules/chunks [Collett *et al.*, 2009; Holland *et al.*, 2008]. As shown in Figure 1, pore-filling hydrate morphology corresponds to deep, coarse-grained sediments for which $\psi < 10^{-3}$. Hydrate forms in nodules and chunks when hydrate crystals can grow by displacing particles in every direction in an entirely capillarity dominated regime where $\psi > 1$. At intermediate conditions, $10^{-3} < \psi < 1$, hydrate growth is capillarity controlled but grain displacement is preferentially aligned normal to the local minimum principal stress σ_3' and leads to lens formation [Cook *et al.*, 2008; Daigle and Dugan, 2010; Shin and Santamarina, 2011].

3.3 Physical Property Estimation for Patchy Saturation: Methods

The physical properties of hydrate-bearing sediments depend on the spatial distribution of gas hydrate, which is generally not known a priori. Observations summarized in Figure 3.1 allow us to constrain the range of possible morphologies, and thereby tighten realistic upper and lower bounds for physical property values.

In particular, pore-filling conditions ($\psi < 10^{-3}$) and Ostwald ripening combine to generate “patchy hydrate saturation” in mature hydrate-bearing coarse-grained sediments. From a modeling perspective, patchy saturation is a two-component combination of hydrate-saturated sand patches ($S_h = 100\%$) embedded in water-saturated, hydrate-free sediment ($S_h = 0\%$), rather than a three-component system (either mineral-hydrate-water or mineral-hydrate-gas). In the following sections, we use analytical models and numerical simulations to estimate core-scale physical properties of patchy hydrate-bearing sediments, and demonstrate the benefits of utilizing the two-component nature of the patchy hydrate distribution to provide a tighter range of physical property estimates than can be obtained for a three-component system. Note that logging and seismic



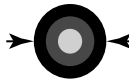
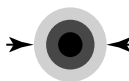
investigations operate at lower resolution [Shankar and Riedel, 2011] and are less sensitive to hydrate morphology [Knight and Nolen-Hoeksema, 1990; Li et al., 2001]; instead, they reflect larger lithologic-scale heterogeneities (reviewed in [Waite et al., 2009]).

3.3.1 Upper and Lower Bounds

Upper and lower bounds can be computed for a given physical property by assuming end-member arrangements of the components (Table 3.2). The parallel and series configurations, also known as the Voigt and Reuss models, are easily calculated but are broader than necessary. Tighter bounds are computed assuming the shell-like arrangement of individual components described by [Hashin and Shtrikman, 1962; Hashin and Shtrikman, 1963], and illustrated in Table 3.2. Hashin-Shtrikman bounds apply to hydraulic, thermal, and electrical conductivities, electrical permittivity, magnetic permeability, and both bulk and shear moduli.

Table 3.2 Physical properties: upper and lower bound models, assuming idealized arrangements of materials with the highest physical property value (darkest shade) to lowest physical property value (lightest shade), and a measurement direction given by the arrows. Symbol definitions are given in Notes 1 and 2.

(a) General expressions

Voigt (Parallel) ^a		Upper	$X = \sum f_i x_i$	T1
Reuss (Series) ^a		Lower	$X = (\sum f_i / x_i)^{-1}$	T2
Hashin-		Upper	$X = x_{\max} + \frac{\xi A_{\max}}{1 - \alpha_{\max} A_{\max}}$	T3
Shtrikman ^b		Lower	$X = x_{\min} + \frac{\xi A_{\min}}{1 - \alpha_{\min} A_{\min}}$	T4

Note: 1. X – bulk property of the mixture; x_i – physical property of the i^{th} constituent; f_i - volume fraction of the i^{th} constituent;

2. $A_{\max, \min} = \sum \frac{f_i}{\alpha_{\max, \min} + \xi / (x_i - x_{\max, \min})}$, see Table 3b for α and ξ .

(b) Property-dependent α and ξ parameters, to be substituted into the expressions for X and $A_{\max,\min}$ from Table 3a. As in Table 3a, x_{\max} and x_{\min} are the maximum and minimum physical property values, respectively, for the components in the mixture.

Properties	α		ξ
	<i>max</i>	<i>min</i>	
Hydraulic conductivity k_H ^{c,d}			
Thermal conductivity λ ^e			
Electrical conductivity σ ^e	$\alpha_{\max} = \frac{1}{3x_{\max}}$	$\alpha_{\min} = \frac{1}{3x_{\min}}$	$\xi=1$
Magnetic permeability μ ^e			
Dielectric permittivity ϵ_r ^e			
Bulk Modulus K ^b	$\alpha_{\max} = \frac{3}{3K_{\max} + 4G_{\max}}$	$\alpha_{\min} = \frac{3}{3K_{\min} + 4G_{\min}}$	$\xi=1$
Shear Modulus G ^b	$\alpha_{\max} = \frac{3(K_{\max} + 2G_{\max})}{5G_{\max}(3K_{\max} + 4G_{\max})}$	$\alpha_{\min} = \frac{3(K_{\min} + 2G_{\min})}{5G_{\min}(3K_{\min} + 4G_{\min})}$	$\xi=0.5$

References: ^a Mavko et al. [1998]; ^b Hashin and Shtrikman [1962, 1963]; ^c Zimmermann and Bodvarsson [1995]; ^d Zimmermann et al. [1991]; ^e Harter and Knudby [2004].

3.3.2 Analytical Models

Effective medium models can be used to estimate physical properties of mixtures when their spatial configuration is known (Table 3.3). The Kuster-Toksöz effective medium model estimates effective properties of a combined medium with known host and patch properties, and it can account for patch shape, e.g., spherical, needle-like, and disk-shaped cracks [Berryman, 1995; Kuster and Toksöz, 1974]. The model converges to the Hashin-Shtrikman upper or lower bounds for spherical patches. Due to the asymmetric nature of this model, results depend on the material selected to be either the patch or the host. In contrast, the self-consistent model is symmetric, meaning all components in the system are considered to be patchy inclusions, and the numerical results are the same regardless of which material is defined as the patch, and which is defined as the host [Berryman, 1980]. The bulk and shear moduli must be iteratively

Table 3.3 Physical properties: analytical models for estimating, rather than bounding, the physical properties of gas hydrate-bearing sediment.

(a) Analytic estimates

Kuster-Toksoz ^a	$(K_{KT} - K_m) \frac{K_m + 4G_m/3}{K_{KT} + 4G_m/3} = \sum f_i (K_i - K_m) P_{m,i}$	T5
	$(G_{KT} - G_m) \frac{G_m + 4\zeta_m/3}{G_{KT} + 4\zeta_m/3} = \sum f_i (G_i - G_m) Q_{m,i}$	T6
Self-consistent ^b	$0 = \sum f_i (X_i - X) Z_{SC,i}$	T7

Note: 1. X is the estimated bulk property of the mixture;

2. The terms $P_{m,i}$, $Q_{m,i}$, and $Z_{SC,i}$ depend on the patch shapes and physical properties, as expressed in Table 3.3b.

(b) Property-dependent α and ξ parameters, to be substituted into the expressions for X and $A_{max,min}$ from Table 3.2a. As in Table 3.2a, x_{max} and x_{min} are the maximum and minimum physical property values, respectively, for the components in the mixture.

	Spherical	Needle	Disk ²
Conductivity ¹ $Z_{SC,i} =$	$\frac{1}{X_i + 2X_m}$	$\frac{1}{9} \left(\frac{1}{X_m} + \frac{4}{X_i + X_m} \right)$	$\frac{1}{9} \left(\frac{1}{X_i} + \frac{2}{X_m} \right)$
Bulk Modulus $Z_{SC,i}$ or $P_{m,i} =$	$\frac{K_m + 4G_m/3}{K_i + 4G_m/3}$	$\frac{K_m + G_m + G_i/3}{K_i + G_m + G_i/3}$	$\frac{K_m + 4G_i/3}{K_i + 4G_i/3}$
Shear Modulus ³ $Z_{SC,i}$ or $Q_{m,i} =$	$\frac{G_m + \zeta_m}{G_i + \zeta_m}$	$\frac{1}{5} \left(\frac{4G_m}{G_i + G_m} + 2 \frac{G_m + \mathcal{G}_m}{G_i + \mathcal{G}_m} + \frac{K_i + 4G_m/3}{K_i + G_m + G_i/3} \right)$	$\frac{G_m + \zeta_i}{G_i + \zeta_i}$

Notes: 1. Appropriate for the conductivity, permeability, and permittivity properties listed in Table 3.3(b). Though Berryman [1995] does not recommend this approach for hydraulic conductivity, equivalent relations have been derived specifically for hydraulic conductivity by Pozdniakov and Tang [2004].

2. Because of the $1/X_i$ term, the disk approximation is calculated in Fig. 4.b with a hydrate patch conductivity of $X_i = (1 \times 10^{-5}) \cdot X_{hydrate-free\ patch}$, rather than setting $X_i = 0$.

$$3. \zeta_m = \frac{G_m}{6} \frac{9K_m + 8G_m}{K_m + 2G_m}, \quad \zeta_i = \frac{G_i}{6} \frac{9K_i + 8G_i}{K_i + 2G_i}, \quad \mathcal{G}_m = G_m \frac{3K_m + G_m}{3K_m + 7G_m}, \quad \mathcal{G}_i = G_i \frac{3K_i + G_i}{3K_i + 7G_i}.$$

4. References: ^a Kuster and Toksoz [1974]; ^b Berryman [1980]; ^c Berryman [1995].

solved in this model, but other properties are computed directly, including conductivity, permeability, and permittivity (see Table 2.3). These analytical models address first order quasi-static effects, and are well-suited for providing a unified approach for estimating a suite of physical properties even in cases where only basic field data are available.

More specialized physical property treatments of patchy-saturated rocks (e.g., [Quintal *et al.*, 2011; Vogelaar *et al.*, 2010]) generally deal with gas patches embedded within fluid-saturated media, where both gas-filled and water-fill patches have identical shear stiffness (or shear wave velocity). This uniform shear stiffness simplification cannot be applied to hydrate-filled patches where solid hydrate significantly enhances the stiffness of hydrate-filled sediment. Our low-frequency models do not consider dispersion due to either viscous losses or polarization effects [Asami, 2005].

3.3.3 Numerical Simulations

Numerical simulations allow us to capture conditions beyond the assumptions made in analytical models. In this study, simulations were implemented in COMSOL Multiphysics. We use cylindrical specimens (radius $R = 0.05\text{m}$ and height $H = 0.2\text{m}$) containing spherical hydrate-saturated sand patches. The number of patches varies from 1 to 200 while the specimen's hydrate saturation is held constant ($S_h = 0.2$). Several realizations of randomly distributed patches are generated for a given number of hydrate patches. The properties of hydrate-saturated sand patches and hydrate-free sand matrix listed in Table 3.4 are used as inputs to the numerical model.

The 3D numerical model is meshed using tetrahedral element, and the number of elements increases with the number of patches, varying from $\sim 10,000$ to $\sim 300,000$. To compute moduli, the cylindrical specimen is loaded with an isotropic stress σ_i and the bulk modulus K is calculated as $K = \Delta\sigma_i / \Delta\varepsilon_v$, where $\Delta\varepsilon_v$ is the computed volumetric strain increment for a change in isotropic stress $\Delta\sigma_i$. When computing conductivities, the cylindrical specimen is surrounded by non-conductive lateral boundaries. A longitudinal

gradient is then imposed to generate the flux appropriate to the type of conductivity being considered. Conductivities are calculated as the ratio between the computed flux and the applied gradient.

A complementary set of simulations is conducted for 20% hydrate-free sand patches embedded in a hydrate-saturated sand host (i.e., $S_h = 80\%$).

3.4 Physical Properties of a Patchy System: Results

We use the analytical models and numerical simulations described above to estimate the physical properties of hydrate-bearing sands with patchy-hydrate saturation. Table 3.4 lists the physical property values selected for these computations. These values correspond to hydrate-bearing sands with porosity $n = 0.4$ and effective stress $\sigma' = 1$ MPa.

3.4.1 Bulk Modulus

Upper and lower bounds provide quick estimates to assess the plausibility of measured values. Parallel, series, and Hashin-Shtrikman bounds are shown in Figure 3.2 for the bulk modulus K of hydrate-bearing sands, either assuming a three-component system (i.e., mineral, hydrate, and water) or a two-component patchy mixture (i.e., patches with $S_h = 100\%$ and sand with $S_h = 0\%$). The patchy saturation assumption significantly reduces the gap between upper and lower bounds because it removes the effect of extreme values for single components, such as the null shear stiffness of water in a series configuration, or the high stiffness of quartz for a parallel arrangement (Table 3.4).

Numerical simulations (solid dots in Figure 3.2) are obtained by assuming the host medium and inclusions are linearly elastic (values listed in Table 3.4). The numerically computed bulk modulus for hydrate-bearing sediments approaches the lower bound when the global hydrate saturation is low ($S_h < \sim 20\%$) and the upper bound when the global hydrate saturation is high ($S_h > \sim 80\%$). Moduli calculated from laboratory

velocity measurements for various types of sediments containing THF hydrate reveal similar trends over a range of hydrate saturations [Lee *et al.*, 2010a].

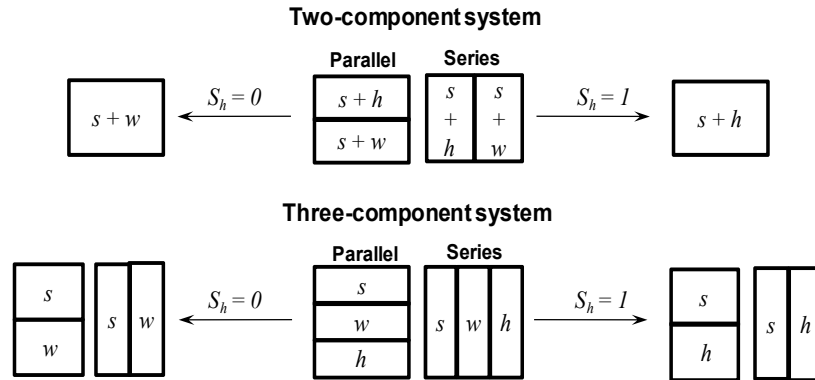
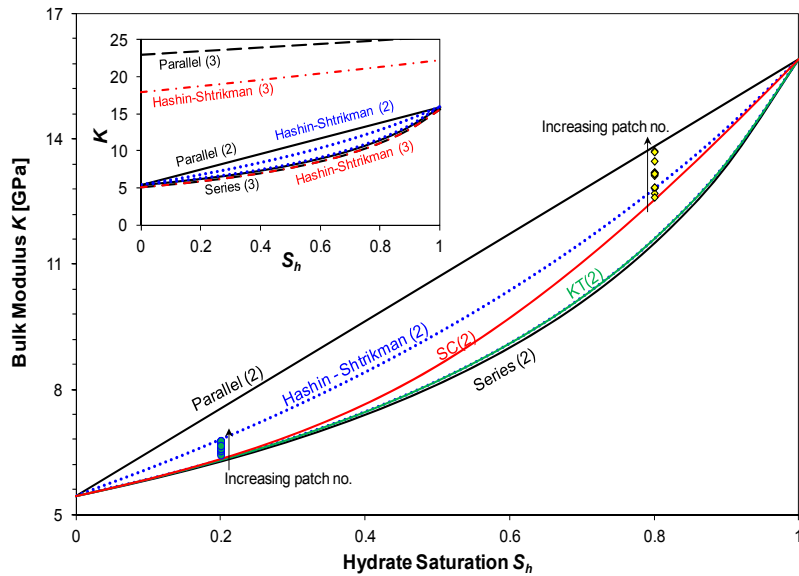


Figure 3.2 Bulk modulus K : bounds, analytical models, and numerical simulations. Filled circles show numerical simulation results for a fixed hydrate saturation (either $S_h = 0.2$ or 0.8) but different number of patches. KT: Kuster-Toksoz model; SC: self-consistent model. Numbers 2 and 3 after each model designate 2- and 3-component systems. The 2-component model bounds are significantly tighter than three-component bounds, a result that can be exploited when geologic conditions suggest 2-component patchy hydrate saturations can be expected rather than 3-component homogeneous hydrate distributions. Refer to Table 3.2 for material parameters and Table 3.3 and 3.4 for mathematical expressions.

Numerical results show the increase in bulk stiffness of hydrate-bearing sediments with the number of hydrate-saturated patches for a given hydrate saturation (Figure 3.2). This result reflects interaction among patches as the number of patches increases and their relative distance becomes less than two times the patch size. Grain-based discrete-element simulations confirm that strong force chains form between large, hydrate-saturated sand patches [Jung *et al.*, 2012]. Because the geometric distribution of patches in cylindrical specimens deviates from Hashin-Shtrikman assumptions, some numerical results fall outside the Hashin-Shtrikman bounds but remain within the series and parallel bounds.

The Kuster-Toksöz effective media model compares well with finite-element simulation results only when the patch concentration is low because the Kuster-Toksöz approach inherently disregards the collaborative coupling among inclusions, or patches, within the host material (see also [Mavko and Mukerji, 1998]). The self-consistent model, in which all constituents are considered inclusions and there is no set host material, outperforms the Kuster-Toksöz model even at higher hydrate-patch concentrations [Berryman, 1980], in agreement with Figure 3.2.

3.4.2 Thermal, Hydraulic and Electrical Conductivities

Conduction phenomena are mathematically equivalent. Therefore, the thermal, hydraulic, and electrical conductivities are estimated using the same analytical models (Table 3.3), inserting the appropriate physical parameters for the property of interest (Table 3.4).

Figure 3.3 shows that thermal, hydraulic, and electrical conductivities increase with the number of hydrate patches for a given hydrate saturation. Though measurable, this effect is small relative to the conductivity difference between hydrate-saturated patches and hydrate-free sediment, which is shown on the right side of each plot in Figure 3.3. At a fixed hydrate saturation, a single large patch inside the cylindrical specimen

Table 3.4 Selected physical properties for two- and three-component mixtures in hydrate-bearing sediment systems (Assumed porosity $n = 0.4$ and mean effective stress $\sigma_v' = 1\text{MPa}$).

Property	Three-component Mixture			Two-component Mixture	
	Quartz	Seawater	Hydrate	Sediment+Seawater ($S_h=0\%$)	Sediment+Hydrate ($S_h=100\%$)
Mass density ρ [g/cm ³]	2.65	1.02-1.05	0.93	1.99	1.962
Poisson's ratio ν [-]	0.17	0.5	0.33 ^a	0.15±0.05 ^b	0.3±0.05 ^{b,c}
Shear wave velocity V_s [m/s]	4120 ^p	0	1960 ^d	392 ^e	1881 ^e
Compressional wave velocity V_p [m/s]	6040 ^p	1500 ^p	3770 ^d	1829	3065
Bulk Modulus, K [GPa]	36.6 ^p	2.25 ^p	8.41 ^p	5.44 ^r	15.9 ^r
Shear Modulus, G [GPa]	31.2 ^q	0 ^p	3.54 ^p	0.27 ^r	7.3 ^r
Drained Young's Mod. $E_{drained}$ [GPa]	72	2.2	8.4 ^a	0.7	18.05
Thermal Conductivity λ [W/m/K]	7.7-8.4 ^f	0.56 ^g -0.58 ^h	0.5-0.58 ^{c,i,j}	3.7 ^j	4.5 ^j
Heat Capacity C [J/kg/K]	730	4200 ^h	1980-2080 ^{a,d,f,m}	2118	1270
Hydraulic conductivity k_H [mm/s]	0	n/a	0	0.1	0
Electrical conductivity σ_e [S/m]	0	5	0	1.15 ^e	0 ^e
Permittivity ϵ_r [-]	4.2	80	7	33 ^e	5 ^e

^a Sloan and Koh [2008] (Methane hydrate); ^b Yun et al. [2005] (drained, skeleton, small strain); ^c Lee et al. [2010] (Methane hydrate, 263K); ^d Helgerud et al. [1999] (Methane hydrate, 5MPa, 273K); ^e Santamarina and Ruppel [2010]; ^f Revil [2000]; ^g Kaye and Laby [2008] (273K); ^h Weast [1987] (273K); ⁱ Waite et al. [2005] (THF hydrate, 261K); ^j Cortes et al. [2009] (THF hydrate, 261K); ^k Huang and Fan [2004]; ^l Handa et al. [1984]; ^m Handa [1986] (Methane hydrate); ^p Waite et al. [2009]; ^q Peselnick et al. [1967]; ^r Computed values.

mimics the series (or Reuss) configuration. The size of each patch decreases when the number of patches increases at a fixed hydrate saturation and conduction improves as more flow paths become available.

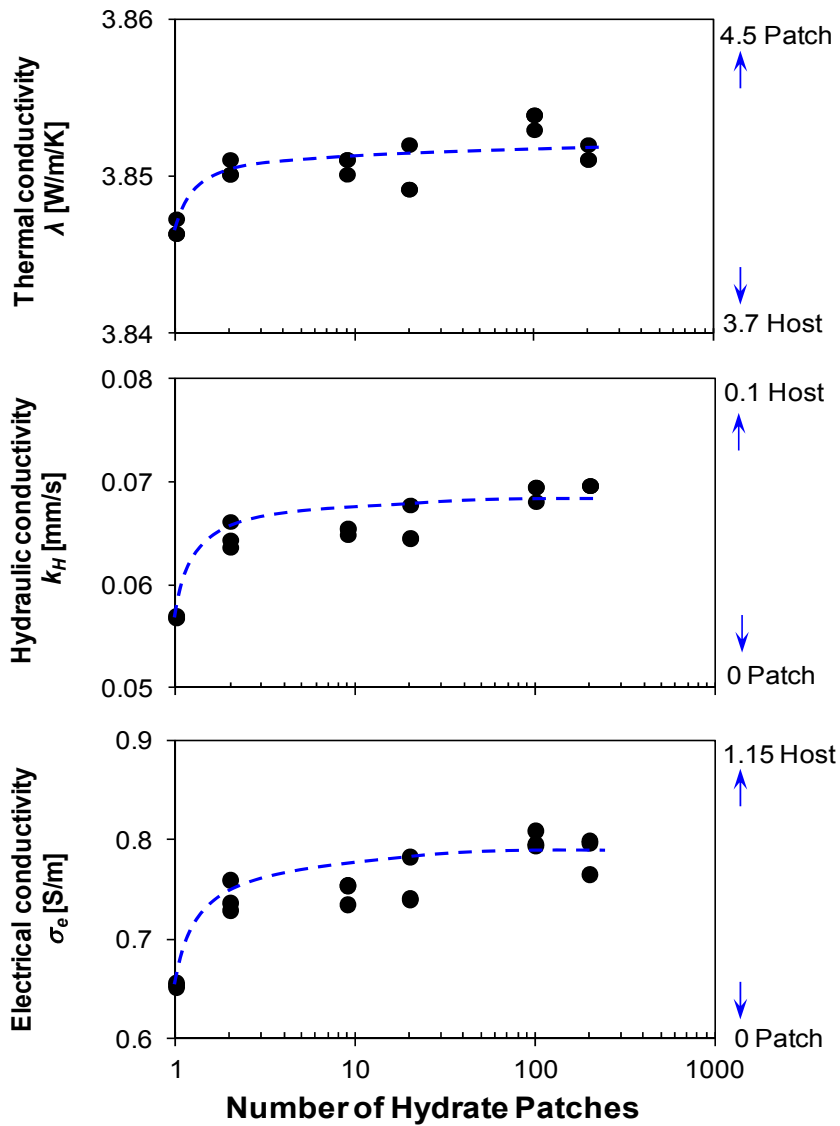


Figure 3.3 Conductivities versus the number of hydrate patches for a sandy specimen with porosity $n = 0.4$ and hydrate saturation $S_h = 0.2$. Dots are numerical results and dashed lines are trends. The patch size decreases as the number of patches increases to retain a constant hydrate saturation. The upper and lower endmember property values are given at the top and bottom right corner of each plot. Refer to Table 3.4 for material parameters

3.5 Discussion: Impact of Hydrate Pore Habit on Physical Properties

3.5.1 Compressional P-wave Velocity

Figure 3.4 shows trends with hydrate saturation for various growth patterns. A small amount of hydrate can dramatically increase the sediment stiffness, and hence the P-wave velocity, in “cementing systems” that form under water-limited conditions (cases A and B). This dramatic increase occurs because water, as the wetting phase, collects at intergranular contacts in water-limited systems. When this water converts to hydrate, the new solid phase dramatically stiffens contacts, increasing the P-wave velocity even with only a small hydrate saturation. In contrast, there is no significant velocity increase at low hydrate saturations when hydrate nucleates either in the pore fluid (C) or on a sediment-grain surface and forms away from grain contacts (D). Between $S_h \approx 25\text{-}40\%$, enough hydrate forms to transition the pore nucleation case (C) to the structure-building case (D) as hydrate begins contacting more than one sediment grain within a pore and the velocity begins increasing rapidly with increasing hydrate saturation. The rapid stiffness increase in patchy distributions when hydrate saturation exceeds 30-40% results from increased patch size and enhanced interactions between patches (case E). This rapid increase has also been observed experimentally [Berge *et al.*, 1999; Yun *et al.*, 2007; Yun *et al.*, 2005]. Cases A, B, C, and D are calculated using the formulation in [Dvorkin *et al.*, 2003] (equations also provided in [Mavko and Mukerji, 1998]), while the trend for patchy saturation (E) is based on the self-consistent model (refer to Figure 3.2).

3.5.2 Hydraulic Conductivity

Pore-filling hydrate leaves thin flow pathways which significantly reduce hydraulic conductivity (Fig. 4b, curve H₁). More conductive, larger diameter flow paths exist in grain-coating hydrate (curve H₂) [Kleinberg *et al.*, 2003; Spangenberg, 2001]. Flow is effectively cut off in both of these homogeneous distribution cases by $S_h = 80\%$.

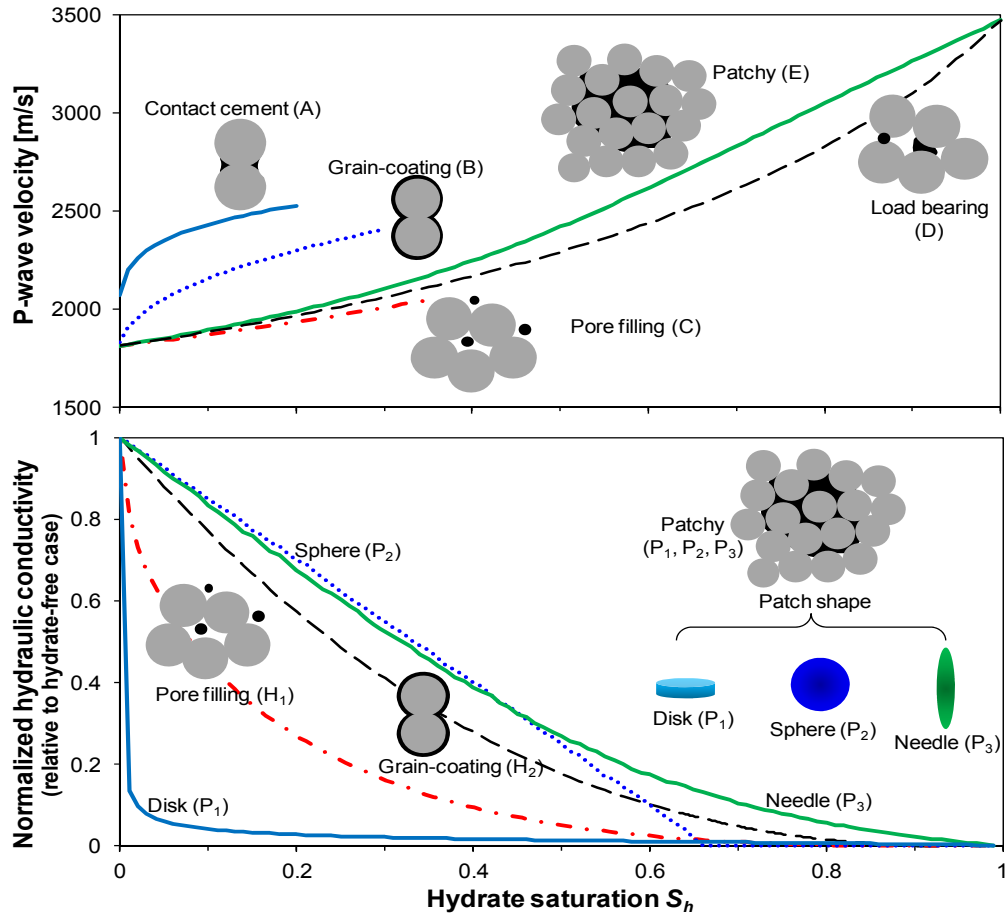


Figure 3.4 Self-consistent versus pore-habit specific models: predicted dependence of physical properties on gas hydrate saturation. (Top) Compressional, P-wave velocity: P-wave velocity increases rapidly even at very low hydrate saturations when hydrate forms at sediment grain contacts. When hydrate forms away from grain contacts (C, D), the velocity increases more rapidly at high hydrate saturation when hydrate begins bridging between multiple sediment grains across a pore or fully hydrate-saturated patches become large and numerous enough to begin interacting (E). Hydrate contacts sediment grains and can no longer be considered purely part of the pore fluid above $S_h \approx 25\text{-}40\%$. (Bottom) Normalized hydraulic conductivity relative to the hydrate-free $S_h = 0$ state: homogeneous hydrate distributions including pore-filling (H_1) or grain coating (H_2) hydrates versus patchy hydrate distributions with disk- (P_1), sphere- (P_2), or needle-shaped (P_3) hydrates. Homogeneous curves H_1 and H_2 are calculated from [Kleinberg *et al.*, 2003]. Patchy distribution curves P_1 , P_2 , and P_3 are calculated from Table 4 [Berryman, 1995; Pozdniakov and Tsang, 2004].

Concentrating hydrate into spherical or needle-shaped hydrate saturated patches leave hydrate-free sections; hence, spherical and needle-shaped patches are less disruptive to fluid flow than homogeneous hydrate distributions (curves P_2 and P_3). Disk-

shaped patches aligned normal to flow can cause extreme flow-blocking conditions even at low hydrate saturations (curve P₁). Conversely, high patch aspect ratio in the flow direction lowers the impact of non-conductive patches on global conductivity [Xia and Thorpe, 1988]. Spherical patches exhibit a conductivity cutoff at a percolation threshold $S_{hd} = 2/3$; for higher hydrate saturation, the needle-shaped patch in the self-consistent model (i.e., curve P₃) may better represent field conditions [Berryman, 1995].

The analysis based on patchy saturation can also be applied to natural hydrate-bearing fines where lenses or chunks are made of 100% segregated hydrate, with the caveat that anisotropy can control such systems. Conductivities can become patch shape- and orientation- dependant, as has been observed in recent gas hydrate logging studies in fine-grained sediments [Cook *et al.*, 2008; Lee and Collett, 2009].

3.6 Conclusions

The lithologically-determined and spatially-varying hydraulic conductivity in sediments control advective methane transport and the reservoir-scale heterogeneous hydrate distribution [Nimblett and Ruppel, 2003; Weinberger and Brown, 2006]. Yet, hydrate morphology at the meso-scale is inherently controlled by the state of effective stress σ' and the grain size of the finer fraction of the sediment d_{10} . Therefore, the meso-scale hydrate morphology can be anticipated from burial depth and sediment type.

Heterogeneous hydrate distributions can be grouped into (1) capillarity-controlled grain-displacing nodules and chunks in fine-grained sediments at low effective stress, (2) lenses and veins in fine-grained sediments at intermediate effective stress where capillarity and effective stress affect growth, and (3) patchy saturation in coarse sands at high effective stress where the granular skeleton remains unaltered during hydrate growth.

Hydrate-bearing sands are of particular interest as an energy resource. Accounting

for patchy saturation, hydrate-bearing sands can be analyzed as a two-component system made of hydrate-saturated sand patches ($S_h = 100\%$) embedded in hydrate-free sand ($S_h = 0\%$). This morphology can be exploited to tighten the bounds of potential physical property values relative to bounds obtained by assuming homogeneous multi-component mixtures of mineral-hydrate-gas or mineral-hydrate-gas-water.

The bulk stiffness of patchy hydrate-bearing sands approaches the lower Voigt-Reuss bound at low hydrate saturations and the upper bound at high saturations due to the mechanical interaction between hydrate-saturated patches. The self-consistent model tracks this shift from the lower-bound to the upper-bound with increasing hydrate saturation, unlike many morphology-specific models that tend to follow either the lower or upper-bound over the entire saturation range.

Patchy hydrate saturation is generally less disruptive to bulk conductivities than homogeneously distributed hydrates. Smaller patches increase flow tortuosity but have lower possibility of extreme flow-blocking conditions. An increased patch slenderness in the fluid flow direction decreases the impact of patches on the global sediment conductivity.

CHAPTER 4

WATER RETENTION CURVE FOR HYDRATE-BEARING SEDIMENTS

4.1 Introduction

The development of governing equations for unsaturated sediments has centered on the saturation-dependant capillary pressure, which is known as the water retention curve, soil water characteristic curve, soil suction curve, soil-moisture retention curve, capillary pressure curve, or suction vs. volumetric water content curve [*Brady and Weil, 2007; Fredlund and Rahardjo, 1993a; Kovács, 2011; Lu and Likos, 2004; Marshall et al., 1996; Williams, 1982*].

The water retention curve of a soil is inherently determined by pore scale characteristics including pore shape, size distribution, interconnectivity and spatial distribution, fluids and interfacial tension, mineral type, and fluid-mineral interactions captured in the contact angle and its hysteresis [*Aubertin et al., 2003; Burger and Shackelford, 2001; Francisca and Arduino, 2007; Miller et al., 2002; Mitchell and Soga, 2005; Olson and Daniel, 1981*].

The water retention curve is causally linked to physical properties of unsaturated sediments such as relative permeability [*Assouline, 2001; Campbell, 1974; Fischer and Celia, 1999; Fredlund et al., 1994; Mualem, 1986; Vogel and Cislserova, 1988*], storage and field capacity [*Assouline, 2001; Brady and Weil, 2007*], shear strength [*Fredlund et al., 1996; Öberg and Sällfors, 1997; Vanapalli and Fredlund, 2000; Vanapalli et al., 1996*], stiffness and volume change [*Delage et al., 1998; Fredlund and Rahardjo, 1993b; Gens and Alonso, 1992; Pedarla et al., 2012*]. Therefore, most numerical codes for coupled processes in unsaturated sediments are anchored on the water retention curve,

including CODE-BRIGHT [*Olivella et al.*, 1994] and TOUGH+HYDRATE [*Moridis et al.*, 2008].

The water retention curve is measured by applying a pressure difference between the two fluids involved, either by vacuum, excess pressure, controlled suction or relative humidity. The volume fraction of either the wetting or the non-wetting fluid is measured at equilibrium for each capillary pressure (see detailed reviews in [*Barbour*, 1998; *Fredlund and Rahardjo*, 1993a; *Looney and Falta*, 2000; *Ridley and Wray*, 1996]). The determination of the water retention curve for hydrate-bearing sediments must involve high fluid pressure and low temperature to prevent hydrate dissociation. Hydrate stability challenges the experimental determination of saturation-dependent capillarity in hydrate-bearing sediments. While numerical simulation results show that the evolution of the reservoir is strongly linked to the water retention curve [*Kimoto et al.*, 2007; *Sanchez and Santamarina*, 2010], the air entry pressure is simply assumed to be constant regardless of hydrate saturation [*Hong and Pooladi-Darvish*, 2005; *Kimoto et al.*, 2007; *Moridis et al.*, 2011; *Moridis and Sloan*, 2007; *Reagan and Moridis*, 2008; *Uddin et al.*, 2011].

The purpose of this study is to develop guidelines for the selection of the water retention curve for hydrate-bearing sediments and to estimate its evolution during dissociation. A review of previous studies on the water retention curve follows.

4.2 Previous Studies on Water Retention Curve

The water retention curve has been extensively studied using experimental, analytical, and numerical methods since the early 1900's. Recent developments consider compressible porous media [*Nuth and Laloui*, 2008; *Parent et al.*, 2007; *Stange and Horn*, 2005] and fractal structures [*Ghanbarian-Alavijeh and Hunt*, 2012; *Huang et al.*, 2006; *Perrier et al.*, 1996; *Tyler and Wheatcraft*, 1989].

The water retention curve has been correlated to sediment characteristics such as

grain size distribution [Arya and Paris, 1981; Aubertin et al., 2003; Chiu et al., 2012; Haverkamp and Parlange, 1986; Kovács, 2011; Stange and Horn, 2005; Zapata et al., 2000]. Regression analyses have linked the water retention curve to several properties of sediment grains and pores [Arthur et al., 2012; Assouline, 2006; Cosby et al., 1984; Elsenbeer, 2001; Ghanbarian-Alavijeh et al., 2010; Parent et al., 2007; Rawls et al., 1991; Tietje and Tapkenhinrichs, 1993; Wagner et al., 2001; Walczak et al., 2006].

Measured suction-saturation curves are relatively smooth and can be fitted with simple function of two or three parameters that typically capture the air entry pressure and the slope, that is the sensitivity of changes in saturation to changes in capillary pressure [Brooks and Corey, 1964; Corey, 1954; Farrell and Larson, 1972; Fredlund and Xing, 1994; Gardner, 1958; Kosugi, 1994; Lu and Likos, 2004; van Genuchten, 1980].

4.3 Methodology – Network Model Simulation

Network model simulations inherently combine pore-scale phenomena to predict the macroscale sediment response [Al-Kharusi and Blunt, 2007; Jang et al., 2011; Lenormand, 1989]. Network models have been used to study the water retention curve [Fischer and Celia, 1999; Peat et al., 2000; Vogel, 2000]. In this study, we use two network model algorithms, preformed network and random growth network, to investigate the water retention curve for hydrate-bearing sediments. This section introduces tube population characteristics, followed by a description of the algorithms including their advantages and disadvantages.

4.3.1 Tube population

The sediment porous network is represented as a lattice structure consisting of tubes with identical length L_t and varying radius r_p . Tubes are connected at zero-volume nodes; hence, the specimen pore volume is the sum of the volume of tubes $V_t = \Sigma(\pi r_p^2 L_t)$.

The number of tubes connected at a node is the pore connectivity cn , which reflects the topology of the porous network.

Mercury intrusion porosimetry data show that natural sediments exhibit a lognormal distribution in pore size with standard deviation $\sigma_{\ln(rp/1\mu m)} = 0.4 \pm 0.2$ [Phadnis and Santamarina, 2011]. In this study, pore radii are randomly generated to satisfy a lognormal distribution. Figure 4.1 shows a histogram of tube sizes for a population of 4802 tubes with a mean pore size $\mu = 10\mu m$ and standard deviation $\sigma_{\ln(rp/\mu m)} = 0.4$.

We note that the upper and lower bounds of the water retention curve can be obtained by invading all tubes arranged in series forming a single line from smallest to largest (upper bound), or in parallel (lower bound - Figure 4.2b).

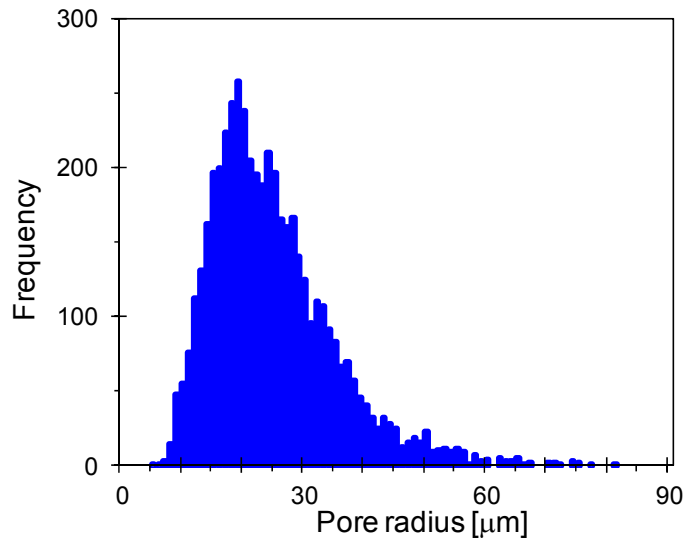


Figure 4.1. Total tube population. Histogram of tube size: randomly generated lognormal distribution ($\mu_n = 10\mu m$, $\sigma_n = 0.4$, the total number of tubes is 4802).

4.3.2 Method #1: Preformed network

Preformed networks are realized before fluid invasion starts. We use a 2D square network, $cn = 4$, formed with a predefined tube population (Note: there are 4802 tubes in 50×50 square networks used to generate most figures in this study). The network is fully

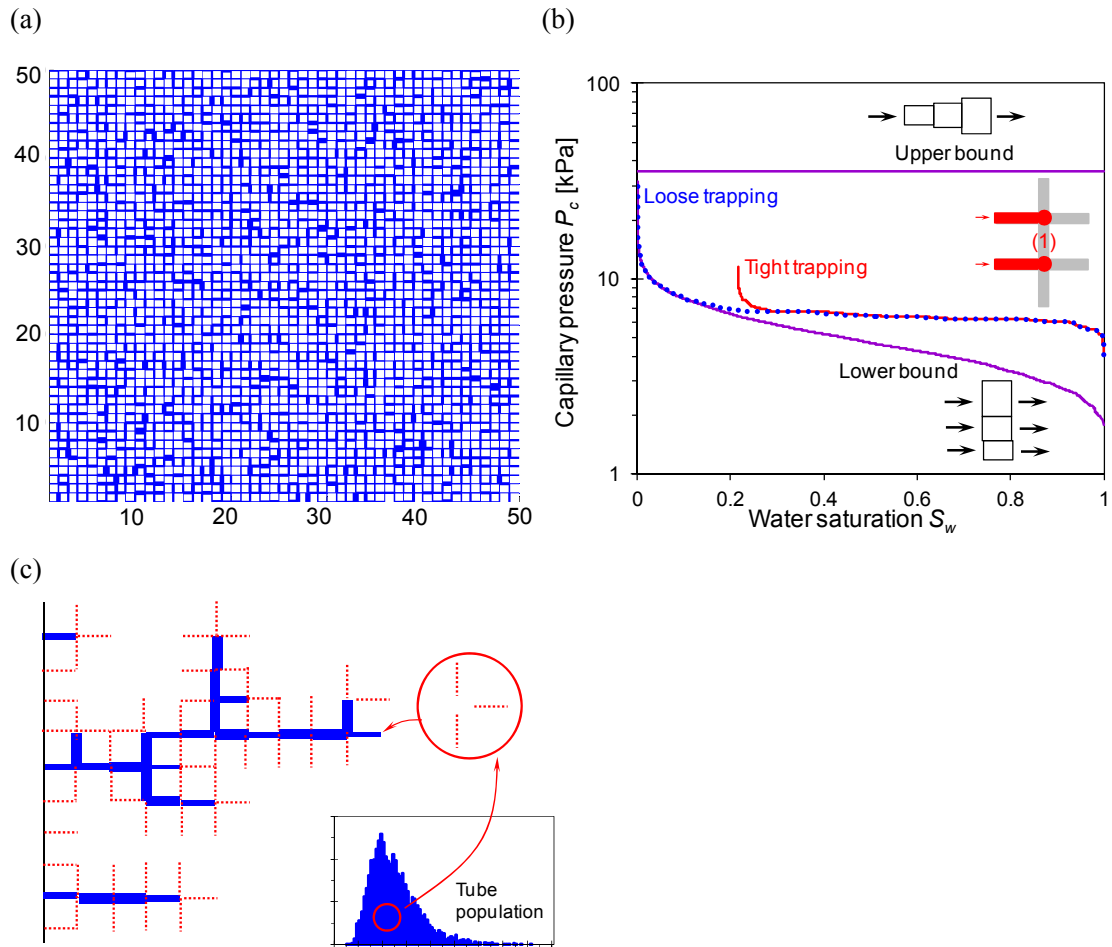


Figure 4.2. Network model simulation. (a) Preformed network: realization of a 50×50 square network using the tube population shown in Figure 4.1; tubes are drawn with line thickness linearly proportional to pore radius. (b) Trapping algorithms and resulting water retention curves using the preformed network: the defending phase in tube-1 is displaced in the “loose trapping” algorithm but it remains trapped when the “tight trapping” algorithm is used. (c) Random network growth: starting from the left boundary, gas invades the largest pore where air entry pressure is the lowest; once a tube becomes gas-invaded (solid lines), new tubes are randomly selected from the total tube population and are connected to the newly gas-invaded tube. Invasion and growth continue until all tubes in the population have been attached; thereafter, invasion is completed by displacing water from the largest to the smallest tubes.

water-saturated and gas invasion is forced from the left boundary. The right boundary is free-draining and there is no fluid flow across the top and bottom boundaries. Air invades the largest tube first as it generates the lowest air entry pressure $P_c = 2T_s \cos \theta / r_p$, where

the air-water interfacial tension is $T_s = 0.072\text{N/m}$ and contact angle is assumed $\theta = 0^\circ$ for a perfectly wetting system. All tubes exposed to the gas phase are potential candidates for further gas invasion. Air invasion displaces water and reduces the water saturation to $S_w = 1 - V_{in} / V_t$, where V_{in} is the volume of gas-invaded tubes and V_t is the total tube volume of the network. These steps are repeated to eventually define the variation in capillary pressure P_c and water saturation S_w .

Two algorithmic decisions affect the results. First, gas invasion after percolation is systematically conducted from the largest to the smallest remaining water-saturated tubes. Second, water trapped in a tube between two air-invaded nodes is resolved by either (Figure 2b): “loose trapping” where the water drains out of the tube during air invasion, or “tight trapping” where trapped water remains trapped. Water displacement and trapping in real systems falls in between these two extreme cases. These two extreme conditions render similar water retention curves for water saturations $S_w > \sim 0.3$. The tight trapping algorithm results in residual water saturation $S_r \approx 0.2$. The loose trapping algorithm is considered for the rest of this study as thermodynamic equilibrium eventually leads to the evaporation of trapped water at a given suction.

4.3.3 Method #2: Random growth network

In the random growth network algorithm, the tube network is extended every time the gas phase reaches a new node. This method begins with a set of randomly sampled tubes to represent those tubes on the left boundary of the preformed network (Note: 50 tubes in this study). Gas invasion starts at the largest tube. Immediately, a set of $cn-1$ new tubes are randomly selected from the remaining tube population and connected to this gas-invaded tube, where cn is the selected pore connectivity. These steps are repeated until no tubes remain from the original population. Then, networked tubes that are still water saturated are invaded from the largest to the smallest to complete the calculation of the capillary pressure P_c versus water saturation S_w trend. Figure 4.2c illustrates the

random growth network method, in which the solid lines represent gas-invaded tubes and the dashed lines are gas-attached tubes randomly sampled from the tube.

4.3.4 Comparison

The random growth network algorithm fails to capture water trapping mechanism, but avoids searching all geometrically connected tubes after each step of gas invasion; thus, it is much more efficient than the preformed network algorithm in computing the water retention curve.

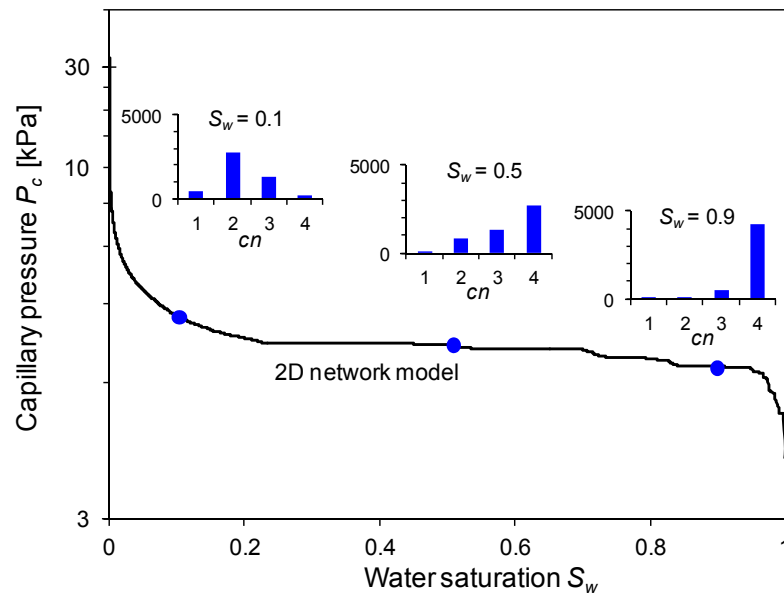


Figure 4.3. Water retention curve using the 2D preformed network with connectivity $cn = 4$; histograms of “available” connectivity as de-watering progresses are superimposed on the figure.

Random growth leads to disconnected paths and a constant “available coordination” throughout the desaturation process. In fact, the “available” connectivity in a preformed network gradually decreases with gas invasion, as shown in Figure 4.3. But differences between these two algorithms diminish as pore size variability increases and invasion localization prevails. The main advantages of the random growth network

method are computational efficiency and the freedom to explore higher connectivity networks relevant to 3D porous systems.

4.4 Results: The Water Retention Curve of Hydrate-Bearing Sediments

4.4.1 Hydrate saturation

Hydrate growth in sediment pores occupies pore space, shuts flow paths, and alters the water retention curve. As hydrate growth is inhibited in smaller pores, hydrates tend to fill the largest tubes first [Clennell *et al.*, 1999; Malinverno, 2010]. Sediments with four hydrate saturations are considered here ($S_h = 0, 0.25, 0.5,$ and 0.75). Figure 4a shows corresponding pore size histograms.

Water retention curves for sediments with different hydrate saturations are obtained using the preformed network method ($cn = 4$ - Figure 4b). The resulting capillarity-saturation curves shift to higher air entry values as hydrate saturation increases: the presence of hydrates in large pores forces gas to pass through smaller hydrate-free pores and thus require higher capillary pressure. Network results show that the porous systems reaches shut-off conditions as the hydrate saturation approaches $S_h \sim 0.8$.

Trends can be quantitatively described using the van Genuchten model [1980] to capture the dependence of capillary pressure P_c on water saturation S_w

$$P_c = P_0 \left[\left(\frac{S_w - S_r}{1 - S_r} \right)^{\frac{1}{m}} - 1 \right]^{-m}, \quad (4.1)$$

where P_0 reflects the air entry value, m captures the sensitivity of water saturation S_w to capillarity P_c , and S_r is the residual water saturation. Water retention curves in Figure 5 are fitted by adjusting P_0 and m -values (for $S_r = 0$). Results show that the air entry pressure P_0 increases with hydrate saturation. The m -value remains relatively constant

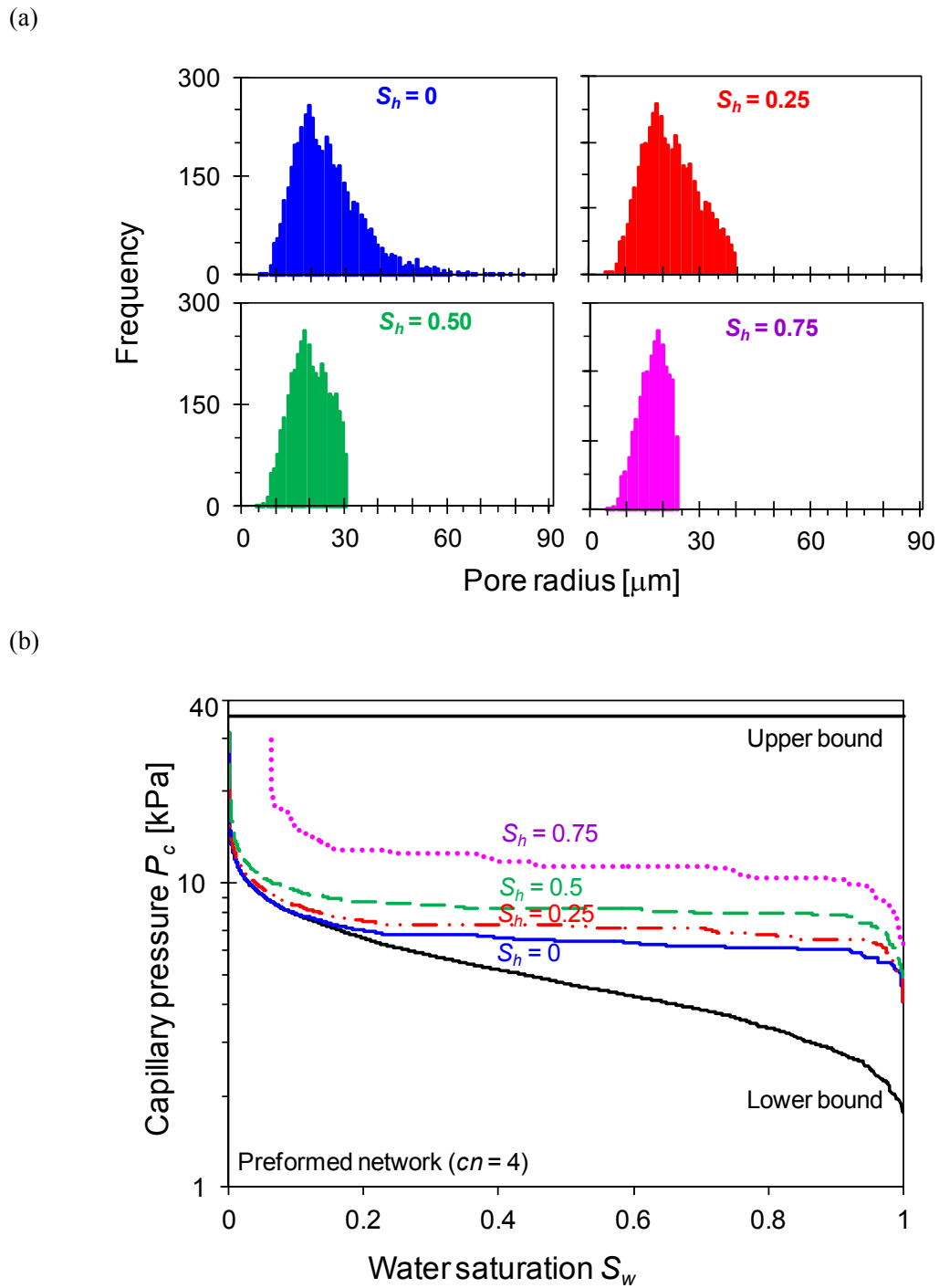


Figure 4.4. Water retention curves for sediments with different hydrate saturations S_h . (a) Change in pore size distribution as a function of hydrate saturation assuming that the hydrate mass fills the largest pores first. (b) Computed water retention curves using preformed 2D networks ($cn = 4$).

until hydrate saturations exceed $S_h > 0.5$, assuming that hydrate fills the largest pores first. Once the m -value is known, the Brooks-Corey [1964] and van Genuchten [1980] models can be used to compute the relative permeabilities of water and gas.

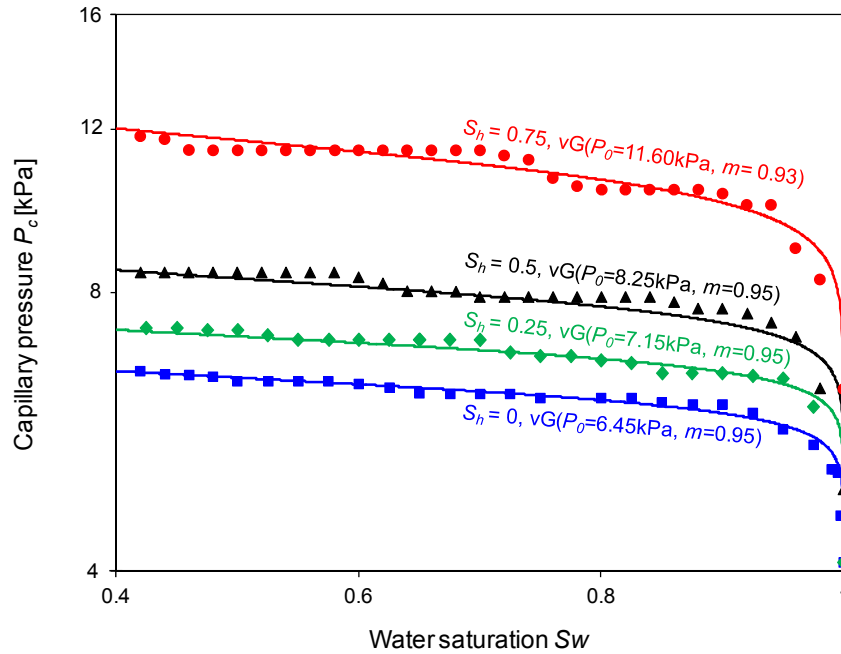


Figure 4.5. Water retention curves as a function of hydrate saturation S_h (Method: preformed 2D networks where hydrate forms in the largest pores). Continuous trends show the fitted van Genuchten model $vG(P_0, m)$, where the reference pressure P_0 reflects the air entry pressure and the m -parameter captures the sensitivity of changes in capillary pressure P_c to changes in water saturation S_w .

4.4.2 Hydrate pore habit

The effect of pore habit on the water retention curve is studied next for sediments with identical hydrate saturation $S_h = 0.25$ but different hydrate spatial distributions. Two extreme conditions are modeled, whereby hydrate fills the largest tubes or the smallest tubes albeit not physically possible (Figure 4.6a). Three other realizations assume patchy hydrate formation [Dai *et al.*, 2012], whereby hydrate nucleates in the largest tubes and grows into neighboring tubes within a 1-grid, 3-grid, or 5-grid distance (see $P1$, $P3$, and

P_0 in Figure 4.6b).

Computed water retention curves shown in Figure 4.6c are fitted with the van Genuchten model. Results in Figure 4.6d show that hydrate morphology affects both the air entry pressure P_0 and the m -value. The upper trend corresponds to the case when disseminated hydrate fills the largest tubes. The larger the patch size, the lower the air entry pressure P_0 , as many relatively large tubes still remain hydrate-free in the network.

4.4.3 Air entry pressure as a function of hydrate saturation

Preferential hydrate nucleation in large pores increases the air entry pressure in hydrate-bearing sediments. The dependency of air entry pressure P_0^{HBS} on hydrate saturation S_h is studied using 6 realizations. Results plotted in Figure 4.7 are fitted with the following power function:

$$\text{for } S_h < 0.8, \quad \frac{P_0^{HBS}}{P_0^{HF}} = \left(\frac{0.8}{0.8 - S_h} \right)^{0.25}, \quad (4.2)$$

where P_0^{HF} is the air entry pressure for hydrate-free sediments. The value of 0.8 captures the porosity shut off to flow when $S_h > 0.8$ (refer to Figure 4.4). Pressure normalization with respect to the hydrate-free network extends the validity of this trend to a wide range of sediments with pore size variability $\sigma_{\ln r} \approx 0.4$.

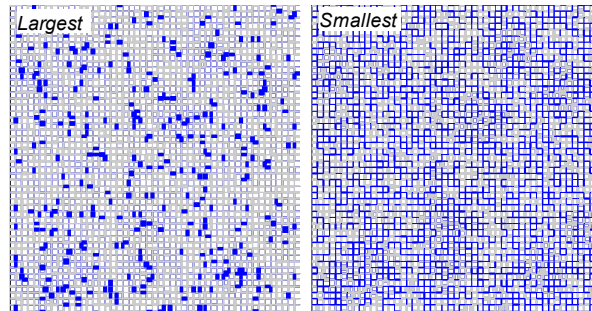
4.5 Discussion

Numerical algorithms developed for this study allow us to explore other soil parameters, specimen size and geometry. The latter affects both numerical studies as well as the experimental determination of the water retention curve.

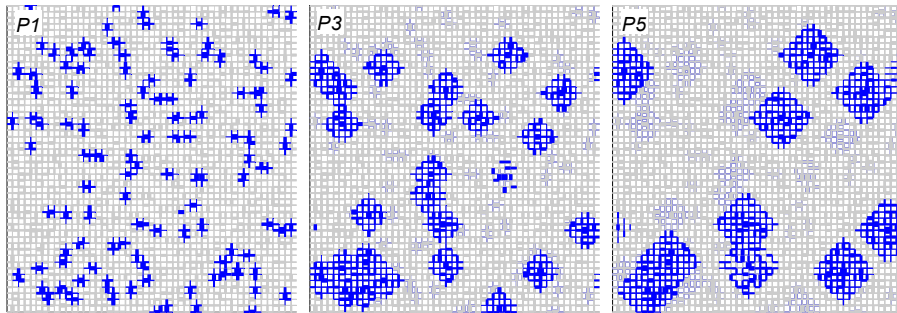
4.5.1 Pore size statistics

The effect of pore size variability on the water retention curve is explored using three sets of lognormally distributed pore with identical mean pore size but different

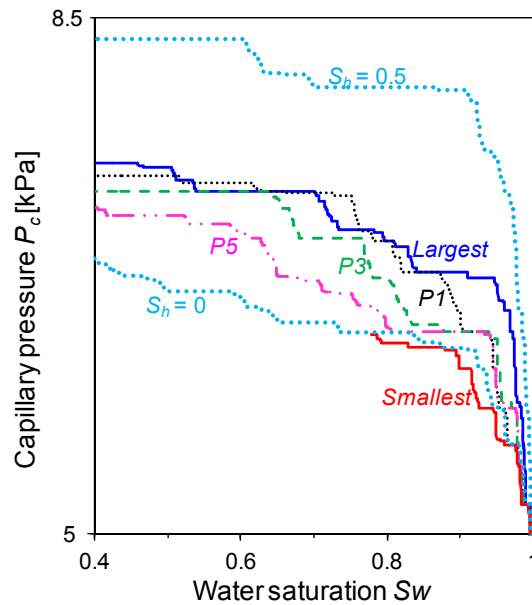
(a)



(b)



(c)



Morphology	van Genuchten model		
	P_0	m	
$S_h = 0\%$	8.30	0.95	
$S_h = 25\%$	Largest	7.24	0.95
	P1	7.22	0.96
	P3	7.09	0.95
	P5	6.86	0.94
Smallest	6.68	0.94	
$S_h = 50\%$	6.52	0.95	

Figure 4.6. The effect of hydrate morphology on the water retention curve. Identical tube networks (Method: preformed network - refer to Figure 2a). The same hydrate saturation $S_h = 25\%$ is satisfied with five different pore habits: (a) Hydrate forms in either the largest or the smallest tubes. (b) Patchy hydrate saturation with different patch size (P1, P3, and P5) that preferentially nucleate at the largest pores. (c) Corresponding soil water characteristic curves with fitted van Genuchten model parameters.

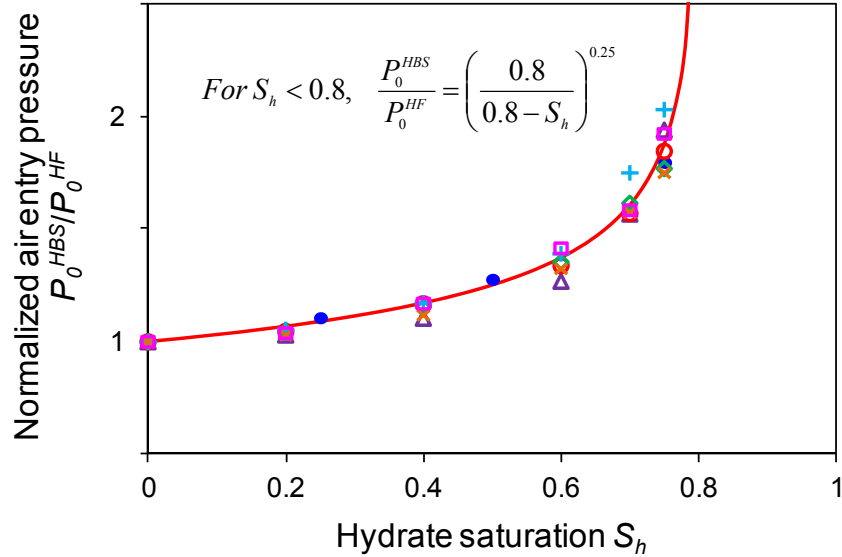


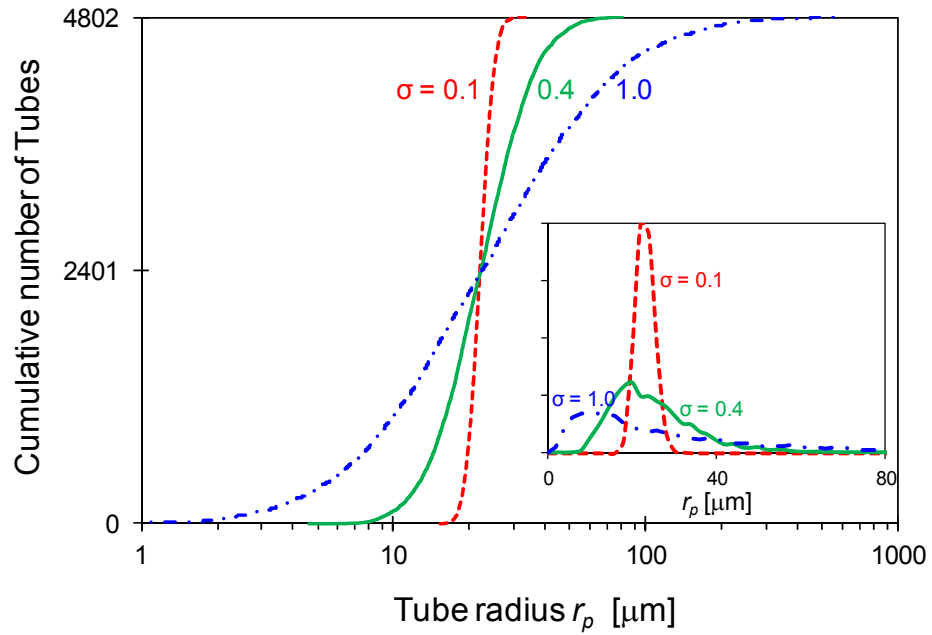
Figure 4.7. Effect of hydrate saturation S_h on the air entry pressure of hydrate-bearing sediments P_0^{HBS} . Preformed network simulation results (dots) and fitted predictive model (solid line). Note: there are 6 different network realizations in each case; hydrate forms in largest pores.

standard deviation (Figure 4.8a). Water retention curves in Figure 4.8b show that a larger variation in sediment pore size reduces both the air entry pressure P_0 and the m -value. The capillary pressure $P_c = 2T_s/r$ at water saturation $S_w = 0.9$ corresponds to the mean pore size r_μ approximately. In other words, the pressure required for the initiation of decisive water depletion is determined by the sediment mean pore size.

4.5.2 Specimen size and geometry

The experimental determination of the water retention curve in the laboratory involves small specimens. Up-scaling and geometric effects are numerically explored herein. Figure 4.9a shows computed water retention curves for different preformed network sizes. The variance in air entry pressure P_0 reduces with increasing network size; differences in water retention curve diminish as water depletion progresses beyond $S_w < 0.7$. On the other hand, water retention curves for networks with identical total number of

(a)



(b)

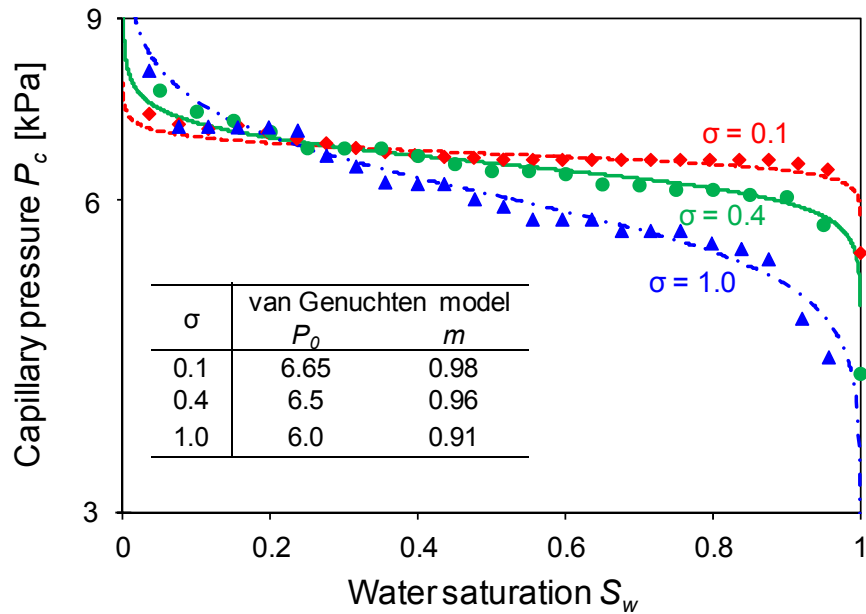


Figure 4.8. The effect of pore size statistics on the water retention curve (Method: preformed network – hydrate saturation $S_h = 0\%$). (a) Lognormal pore size distributions with identical mean μ but different standard deviations σ_{ln} . The inset shows the corresponding density curves. (b) Network model simulation results (markers) and fitted van Genuchten model (lines).

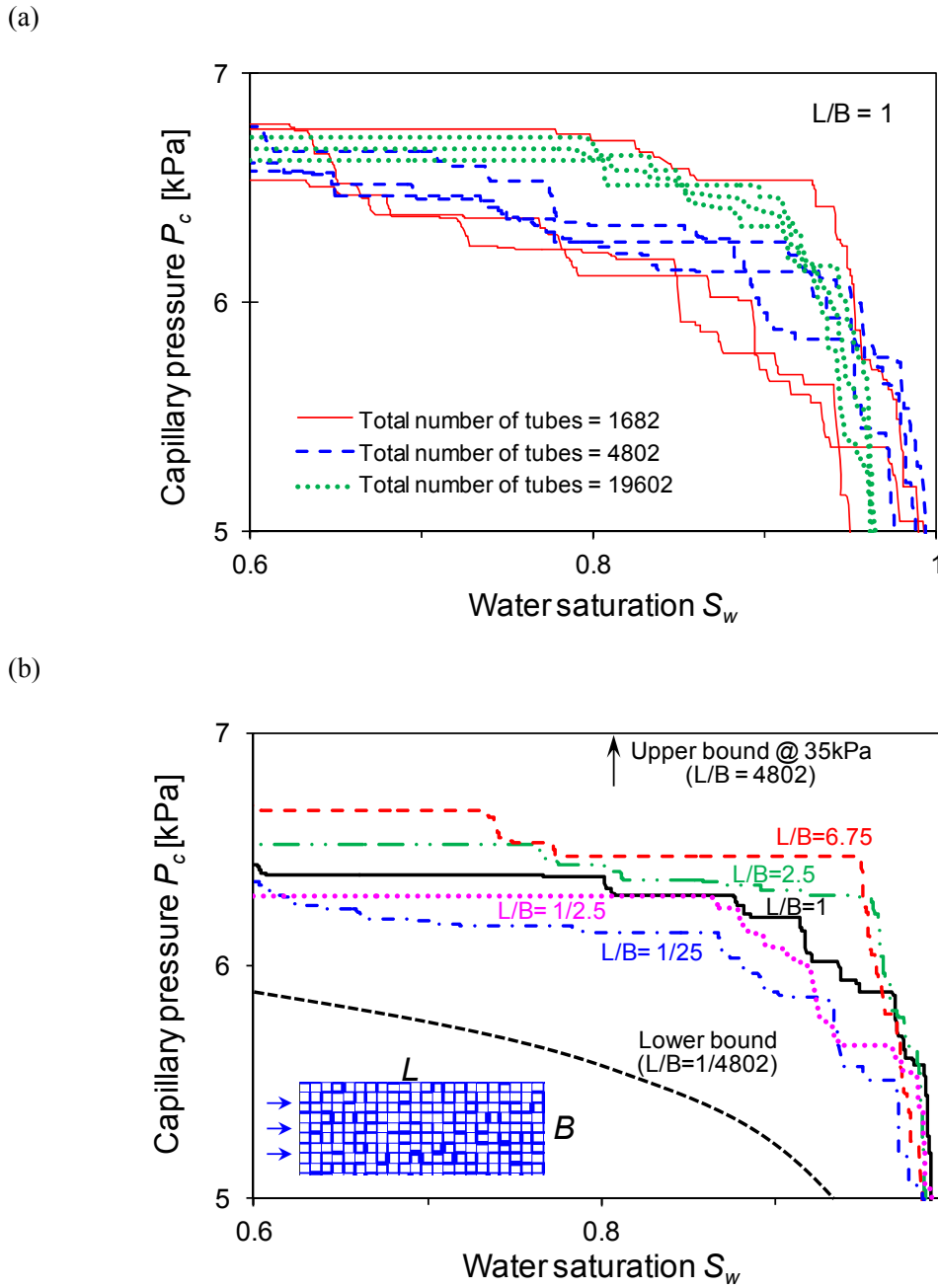


Figure 4.9. The effect of network size and length-to-width ratio L/B on the ‘measured’ water retention curve (Method: preformed network – hydrate saturation $S_h = 0\%$). (a) Water retention curves for different size networks with the same length-to-width ratio $L/B = 1$. (b) Water retention curves computed for the same tube population of 4802 tubes but arranged in different network geometries or L/B ratios.

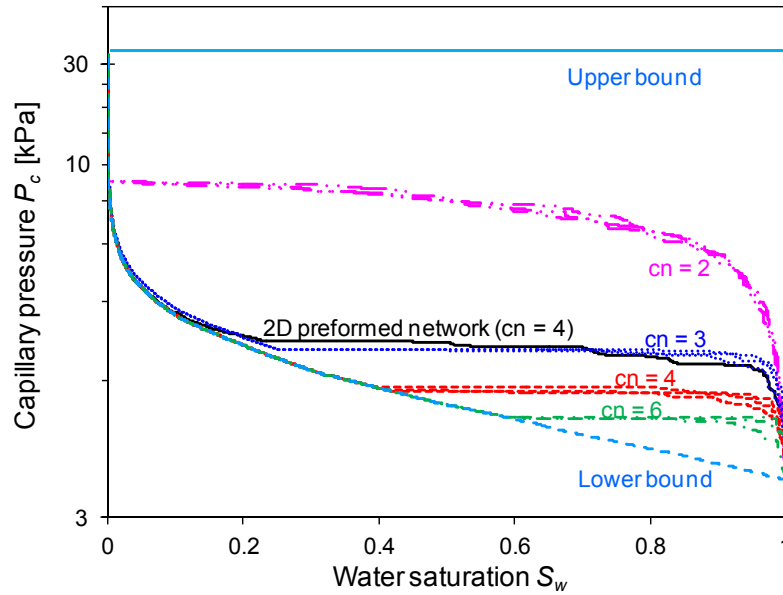


Figure 4.10. Effect of tube connectivity cn on network model simulations (Note: refer to Figure 1 for the tube population – Hydrate saturation $S_h = 25\%$). (a) Water retention curve using the 2D preformed network with connectivity $cn = 4$; histograms of connectivity as de-watering progresses. (b) Water retention curves obtained using the random growth network method. Results for the 2D preformed network with $cn = 4$ are superimposed for comparison (refer to Figure 4.3).

tubes (10000) but different length-to-width ratio L/B show distinct differences in both air entry pressure P_0 and slope m -value (Figure 4.9b): as L/B decreases, specimens become wide and short, and the water retention curve tends to the lower bound parallel configuration; conversely, long and narrow configurations with high L/B produced water retention curves that approach the upper bound series configuration. Therefore, laboratory measured water retention curves should be applied with caution to reservoirs, since experimentally determined water retention curves can be biased by specimen size and geometry.

4.5.3 Pore connectivity

Pore connectivity higher than $cn = 4$ can be observed in 3D porous networks. Various coordinations are simulated using the random growth network. Results obtained

from the random growth network algorithm with a fixed connectivity $cn = 3$ agree well with the preformed 2D network algorithm with $cn = 4$ (Figure 4.10 – refer to “available coordination” in Figure 4.3). Water retention curves exhibit lower air entry pressure but almost the same m -value as the pore coordination increases.

4.6 Conclusions

The water retention curve captures the variation of capillary pressure with water saturation, and it is inherently determined by sediment pore size variability and interconnectivity. The water retention curve plays a central role in the analysis of unsaturated hydrate-bearing sediments during reservoir simulation.

Network model simulations can be used to investigate the water retention curve for hydrate-bearing sediments. The preformed network model can employ different water trapping algorithms to capture residual water saturation and gas percolation. The random growth network can efficiently replicate high order tube connectivity and provides quick estimates of the water retention curve.

Hydrate distribution affects both the air entry pressure P_c and slope. In particular, patchy hydrate distribution renders lower air entry pressure than distributed hydrate saturation. The air entry pressure P_0 increases with hydrate saturation S_h , yet, the slope of the water retention curve remains relatively constant at low hydrate saturations $S_h < 0.5$.

The air entry pressure of hydrate-bearing sediments P_0^{HBS} can be estimated from the air entry pressure of hydrate-free sediments P_0^{HF} as a power function of hydrate saturation. The 0.25 exponent indicates a relatively low effect at low hydrate saturations.

Higher variation in sediment pore size distribution lowers the air entry value P_0 but steepens the curve. Decisive water displacement starts when the capillary pressure exceeds the capillary pressure for the mean pore size. Preferential hydrate nucleation in large pores alters the sediment water retention curve. Percolating flow paths shut off

when hydrate saturation approaches $S_h \sim 80\%$.

The specimen size and geometry affect the measured capillary pressure, especially at high water saturation $S_w > 0.7$. Therefore, experimentally determined water retention curves in the laboratory should be applied to reservoir scale with caution.

The results are relevant to mixed fluid conditions in a wide range of sediments including those that have experienced diagenesis, bio-clogging, or mineral precipitation.

CHAPTER 5

FORMATION HISTORY AND PHYSICAL PROPERTIES OF HYDRATE-BEARING SEDIMENTS: MOUNT ELBERT SITE

5.1 Introduction

Pressure and temperature constrain the formation of gas hydrates to permafrost regions and marine sediments in continental margins [Kvenvolden and Lorenson, 2001]. This manuscript documents a study of hydrate-bearing sediments in permafrost. The site is about 400 km north of the Arctic Circle on the coastal plain of Alaska North Slope [Hunter *et al.*, 2011]. First, we investigate the local geology and the formation history of the permafrost and hydrate phase. Then we report results of a comprehensive experimental characterization study conducted on a single specimen recovered during the 2007 drilling expedition (BPXA-DOE-USGS Mount Elbert Gas Hydrate Stratigraphic Test Well); parameters include index properties, geotechnical and geophysical characteristics obtained for the “undisturbed” sample, and subsequent remolded specimens with and without THF hydrate. Finally, we explore potential implications related to gas production.

5.2 Hydrate and Permafrost in Alaska North Slope

5.2.1 Site Geology

The sediments at the Alaska North Slope are grouped into Franklinian, Ellesmerian and Brookian sequences in relation to tectonic episodes and lithologic characteristics [Grantz *et al.*, 1975; Lerand, 1973]. The Franklinian sequence consists of metamorphosed clastic and carbonate rocks [Reiser *et al.*, 1978]. The Ellesmerian

sequence records the northward retreat of the coast line and the shallow-marine and nonmarine clastic sedimentation [Collett *et al.*, 1988]. And the Brookian sequence records a series of tectonic events: uplift of the Brook Range, subsidence of the Colville trough, and the formation of the Barrow arch caused by the northward downwarping of the Colville trough [Bird, 1999; Collett *et al.*, 1988; Grantz *et al.*, 1979]. Currently, the Barrow arch is approximately parallel to the present shoreline and controls the occurrence of numerous oil and gas fields including the Milne Point Unit [Collett *et al.*, 1988; Grantz *et al.*, 1975]. Gas hydrate prospects at Milne Point Unit are found in the sand layers of the fluvial-deltaic Sagavanirktok Formation within the Brookian sequence. This complex formation includes structural compartmentalization and faults that may serve as gas migration pathways from deeper hydrocarbon reservoirs [Casavant *et al.*, 2004; Hennes, 2004; Hunter *et al.*, 2005].

The stratigraphy at the Mount Elbert well exhibits a stacked sequence of fluvial, deltaic and nearshore marine sands with interbedded layers of both terrestrial and marine shales [Rose *et al.*, 2011]. Gas hydrates are found in two primary horizons at the Mount Elbert well. The C unit consists of 16 meters of gas hydrate-bearing sands (depth: ~650m to ~666m), and the shallower D unit which consists of 14 meters of gas hydrate-bearing sands (depth: ~614m to ~628m). The sediment tested in this study was recovered from the D unit. Both layers have relatively high hydrate saturation ranging from $S_{hyd} = 0.6$ -to- 0.75 ; this estimate is based on analyses of well log data [Lee and Collett, 2011] and pore water geochemistry [Torres *et al.*, 2011].

Isotopic compositional analysis shows the coexistence of thermogenic and biogenic gases at the Alaska North Slope [Collett *et al.*, 1988; Lorenson *et al.*, 2008; Valin and Collett, 1992]. This points to two general scenarios for gas hydrate formation. One theory assumes that a pre-existing gas reservoir was converted into hydrate after favorable changes in temperature and pressure. The other suggests that gas migrated upwards into the stability zone and then formed hydrate. In particular, biogenic and/or

deeper thermogenic free gases may have migrated upward through Eileen fault [Carman and Hardwick, 1983; Lorensen et al., 2008; Masterson et al., 2001]. Various sealing and trapping mechanisms have been proposed, such as structured fault closures [Collett et al., 1988; Hunter et al., 2005], low permeability marine siltstone layers [Collett et al., 1993; Collett et al., 1988; Collett et al., 1990], permafrost [Downey, 1984; Jamison et al., 1980; Pratt, 1979], previously formed hydrate itself [Hunter et al., 2005], or concentrated deposits of peat or coal seams [Pratt, 1979].

5.2.2 Hydrate Formation History

We combine various sources of information to reconstruct the evolution of the stratigraphy, ground surface, base of the ice-bearing permafrost, and potential gas hydrate stability zone at the Mount Elbert region. Data sources include: (1) logging data gathered for the Mount Elbert well, (2) stratigraphic and geologic information from the Alaska North Slope [Bird, 1981; 1999; Collett et al., 1988; Frederiksen et al., 1998; Inks et al., 2008; Reimnitz et al., 1972; Valin and Collett, 1992], and (3) information on permafrost and ground-surface temperature [Brigham and Miller, 1983; BujakResearchInternational, 2008; Elias and Matthews Jr, 2002; Kaufman et al., 2004; Matheus et al., 2003; Parrish et al., 1987; Spicer and Chapman, 1990; Wolfe, 1980; 1994; Wolfe and Upchurch, 1987]. We make the following assumptions:

- Continuous permafrost starts when the mean annual ground surface temperature is lower than -5°C [Brown, 1970]. Thereafter, we place the base of the ice-bearing permafrost BIPF following Lunardini [1995] and Osterkamp and Gosink [1991].
- The temperature at the BIPF is assumed to be -1°C , based on both logging data ($-1\pm 0.5^{\circ}\text{C}$, [Lachenbruch et al., 1982]) and salt concentration (12.7g/L, reported later in this manuscript) which induces a -0.8°C freezing point depression [Andersland and Ladanyi, 2004].
- The temperature within the permafrost increases with depth above the BIPF

following a linear geothermal gradient of 1.64 °C/100m [Lachenbruch *et al.*, 1982]. Centennial fluctuations of the surface temperature can cause an anomalous temperature profile in the upper 160 meters at Prudhoe Bay [Lachenbruch *et al.*, 1982].

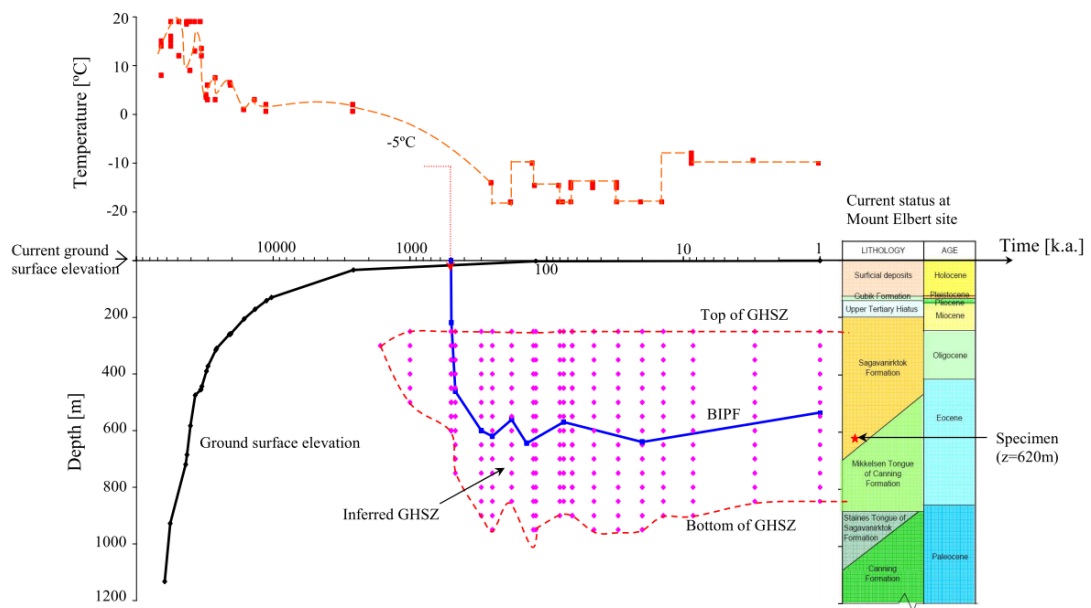
- The temperature beneath the BIPF is computed assuming that oscillations in the depth of the permafrost have a period much longer than the thermal diffusion time. Thus, we assume a time-constant, linear geothermal gradient below the permafrost (3.56°C/100m – from logging data in [Collett *et al.*, 2008b]; corroborated with data at other wells in the Alaska North Slope - refer to [Collett *et al.*, 1993; Collett *et al.*, 1988; Lachenbruch *et al.*, 1982].

- The fluid pressure is hydrostatic and the water table is assumed at the ground surface. This assumption is based on the proximity of the Mount Elbert site to the coast line, evidence of hydrate formation before the permafrost (to be shown later in this section), and confirmatory fluid pressure data found in [Collett *et al.*, 1993].

- The methane hydrate stability zone is computed with the pressure-temperature conditions assumed above. We use the equation by Sloan and Koh [2008] to compute the phase boundary for pure methane gas hydrate, but we modify it to fit data points generated using the HWHYD software; for temperature higher than 0 °C, the equation is $P[\text{kPa}] = \exp(40.234 - 8860/T[\text{K}])$. The effect of salt concentration on methane hydrate stability is also considered in this computation following Sloan and Koh [2008].

The computed depth-time evolution for hydrate and permafrost are summarized in Figure 5.1. These results indicate that current hydrate-bearing sediments could have formed almost a million years before the onset of permafrost at Mount Elbert. The hydrate stability zone thickened as the base of the permafrost deepened. In fact, the permafrost invaded the pre-existing gas hydrate zone; therefore, ice and hydrate may coexist throughout the superposition depth. These results are compatible with hydrate formation sustained by the upwards migration of deep thermogenic gases, which became trapped together with shallower biogenic gases within the current gas hydrate stability

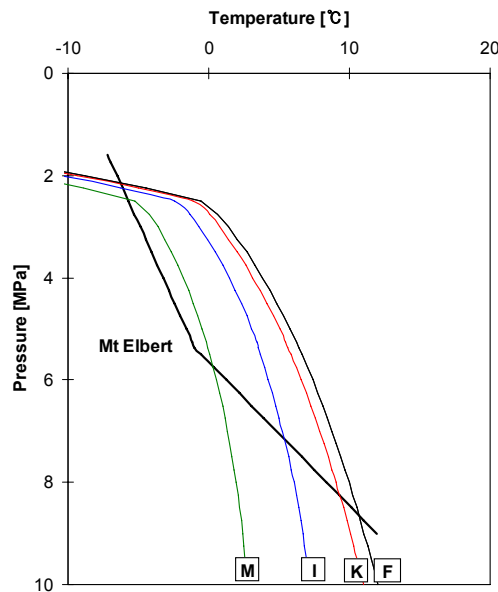
zone and converted into hydrate as ground-surface cooled in the Pleistocene epoch. Pre-existing free gas and high-conductivity faults can explain the high hydrate saturation found at the North Slope.



We can anticipate that preferential hydrate accumulation in the coarse-grained C and D units is due to either advective flow favored through the more permeable coarse grained layers (methane transport dissolved in water), or gas invasion due to the low capillary entry pressures in coarse-grained layers with low fines content (methane transport in gas phase).

Could pore size shift pressure-temperature PT stability conditions in layers with high fines content and explain the absence of hydrate in these layers? We explore this

situation taking into consideration the pressure-temperature conditions in Figure 5.1. The void ratio with depth is computed using the standard 1D consolidation theory $e = e_{100} + C_c \times \log(\sigma'/\text{kPa})$ where e_{100} and C_c are sediment-dependent parameters [Burland, 1990]. Pore size d_{pore} depends on void ratio and specific surface S_s and can be estimated as $d_{pore} = \alpha \times e / (S_s \times \rho)$ where ρ is the mineral mass density and α varies from $\alpha = 2$ for parallel face-to-face configuration to $\alpha = 6.2$ for edge-to-face aggregation of platy particles. Finally, the equilibrium temperature shift ΔT_{dep} due to pore size is computed for cylindrical pores as $\Delta T_{dep} = -2\gamma_w m_h T_{bulk} / d_{pore} \rho h_0 L_f$ [Kwon *et al.*, 2008]. Stability boundaries are shown in Figure 5.2 for Mount Elbert PT conditions and for sediment parameters that correspond to silt or sand sediments (same trend as for the bulk fluid "F"), kaolin "K", illite "I", and montmorillonite "M". The specific surface measured for the Mount Elbert specimen is similar to the specific surface for kaolinite; therefore, pore size had only a minor effect restricting the thickness of the hydrate stability zone.



5.3 Index Properties and Implications

The specimen studied herein was recovered from the D unit at a depth between 620.47m and 620.62m. This depth is below the permafrost but within the hydrate stability zone. Index properties are discussed next; a summary of all parameters is presented in Table 1.

The measured gravimetric water content $\omega_c = 26.9\%$ (oven-dried method-ASTM D2216) can be used to estimate a lower bound of the porosity $n = G_s \times \omega_c / (1 + G_s \times \omega_c) = 0.42$ by assuming complete water saturation. The aqueous extraction method was adopted to recover the pore fluid from the specimen [Rhoades, 1982]. This extracted pore fluid has pH = 7.4 (non-bleeding type narrow range pH strips-ASTM D4972), and electrical conductivity $\sigma_{pf} = 1.9S/m$ measured at 20°C using a Network Analyzer HP-8752A (for comparison, $\sigma_{pf} \approx 10^{-3}S/m$ in fresh water and $\sigma_{pf} \approx 4.2S/m$ in seawater at 20°C). The total dissolved salts TDS in the pore fluid can be estimated from the measured electrical conductivity to be TDS = 12.7g/L (empirical relationship $\sigma_{pf} = 0.15TDS$, where σ_{pf} is in mS/m and TDS in mg/L – as reported in [Santamarina et al., 2001]).

The grain size distribution indicates a poorly sorted silty-sand (sieve analysis-ASTM D421, and hydrometer-D422): median grain size $D_{50} = 0.07mm$, coefficient of uniformity $C_u = 4.79$, and coefficient of curvature $C_{cur} = 1.84$. The fine fraction is 56% by mass (passes through sieve #200, i.e $d < 75\mu m$). The specific surface is $11.3m^2/g$ (methylene blue method – value in the range of kaolinite clay). The high fraction of fine particles and relatively high specific surface hinder fluid conduction and hydrate accumulation, and affect the sediment stiffness and strength.

Compositional EDX (Energy-dispersive X-ray spectroscopy) analysis shows that silicon (61.3%), tantalum (12.3%), aluminum (11.9%), and oxygen (9.7%) are the major components. This composition is roughly consistent with the reported mineralogy: quartz= 81~83%, plagioclase= 4~7%, pyrite= 1~2%, K-spar= 1%, chloride= 3%, kaolinite= 2%, and illite= 3% ([Winters et al., 2011] - details in Table 5.1). Composition

Table 5.1. Index and engineering properties of Mount Elbert sediment (specimen from depth z= 620.47-to-620.62m)

Index properties	This study		Other depths *	
	Values	Device/Technique	¹ Z=619.47-619.49m; ² Z=620.32-620.46m; ³ Z=623.16-623.23m; ⁴ Z=623.56-623.58m	
Median diameter D_{50}	0.07 mm	Sieve and hydrometer [ASTM D421, D422]	¹ 0.074; ³ 0.061	
Coefficient of uniformity C_u	4.8		¹ 10; ³ 20.56	
Coefficient of curvature C_{cur}	1.8		¹ 2.68; ³ 2.11	
Passing sieve #200	56 %		¹ 50%; ³ 61%	
Roundness R	0.47	Leica MZ6 stereomicroscope [Krumbein and Sloss, 1963; Santamarina et al., 2001]		
Sphericity S	0.62			
Specific surface S_s	11.3 m ² /g	Methylene blue [Santamarina et al., 2002]		
Specific gravity G_s	2.67	Pycnometer [ASTM D854]		
Maximum void ratio e_{max}	1.10	[ASTM D4254]		
	1.01~1.07 ⁺			
Composition/Mineralogy	Si=61% Ta=12% Al=12% O=10% K=1.5% Mg=1.0% other=2.3%	Hitachi S-3500 SEM, EDX	² Quartz=83% Plagioclase=4% Pyrite=2% K-spar=1% Chlorite=3% Kaolinite=2% Illite=3%	⁴ Quartz=81% Plagioclase=7% Pyrite=1% K-spar=1% Chlorite=3% Kaolinite=2% Illite=3%
Porosity n	0.42 (as received)		¹ 42.6; ³ 43	
Initial void ratio e_0	0.72 (as received)		¹ 0.74; ³ 0.75	
pH	7.4	Non-bleeding pH strip [ASTM D4972, Rhoades, 1982]		
Electrical conductivity of pore fluid σ_{pf}	1.9 S/m	High frequency network analyzer at 1GHz (HP8752A)		
Total dissolved salts in pore fluid	12.7 g/L	Computed from σ_{pf}		
Engineering properties (no hydrate)				
Compression index C_c	0.07	Oedometer	-	
Swelling index C_s	0.006		-	
V_s at 1kPa means stress: α	35.36	Bender element in oedometer cell		
Sensitivity of V_s to σ_v : β	0.295			
Constant volume friction angle ϕ_{cv}	35°±2° [#]			
	34° ⁺			
Permeability	1.2~3.5×10 ⁵ md	Computed from Hazen's equation based on D_{10}	² 2100 md (to air at 4.03MPa) ⁴ 1370 md (to air at 4.03MPa)	

Note: * [Winters et al., 2011].

⁺ estimated using relations in Cho et al., [2006].

[#] simplified procedure in Santamarina and Cho, [2001].

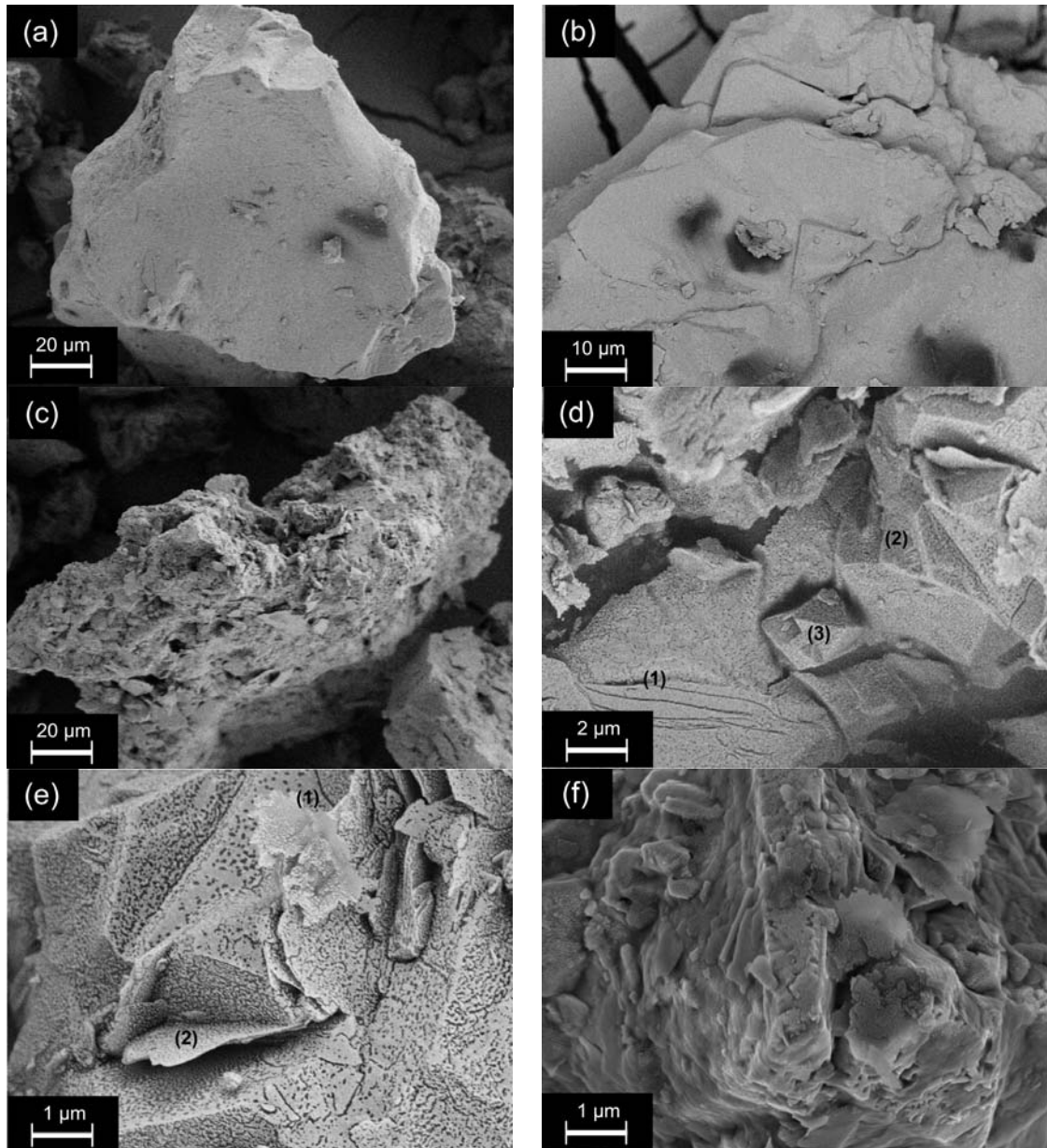
and mineralogy are in agreement with the measured value of specific gravity $G_s = 2.67$ (pycnometer, ASTM D854).

Particle size, shape, and surface texture reflect grain composition and formation history, and determine the sediment mechanical behavior. The grain surface texture was observed using a scanning electron microscope (Hitachi S-3500). Representative grain surface textures are shown in Figure 3. Most grains have medium to high relief, abrupt edges, and v-shaped percussions that suggest intensive collisions and crushing. V-shaped percussion fractures are also present in glacial grains, especially when grains are emplaced by fast moving wet-based glaciers; however, dominant micro-textures obtained in glacial grains are missing in these sediments, in particular there is no evidence of sub-parallel grooves, conchoidal fractures, edge rounding, linear and curved troughs, and multiple adhering particles [Kransley and Doornkamp, 1973; Mahaney, 2002; Mahaney and Kalm, 1996]. Sphericity S and roundness R were visually determined using a stereomicroscope (Leica MZ6- chart in [Krumbein and Sloss, 1963]); mean values are $S = 0.62$ and $R = 0.47$. We can conclude on the bases of observed and missing features that the tested specimen agrees with the fluvial-deltaic origin of gas hydrate-bearing sediments at Mount Elbert, and have not experienced glacial entrainment.

The loosest packing density was obtained by funneling dry sediment to obtain the maximum void ratio $e_{max} = 1.10$ and porosity $n_{max} = 0.52$ (ASTM D4254). Particle shape data are used to obtain a second estimation of the maximum void $e_{max} = 1.01\sim 1.07$ which is roughly in agreement with the measured value. The shape-based estimate of the minimum void ratio $e_{min} = 0.64\sim 0.68$ could not be experimentally confirmed due to the limited amount of sediments [Cho *et al.*, 2006].

Large strain shear strength involves particle rotation and contact slippage, which are affected by particle shape. Published correlations and measured grain shape parameters S and R allow us to estimate the constant volume friction angle $\psi_{cv} = 34^\circ$ (data in Table 1 - [Cho *et al.*, 2006]); this angle approximately agrees with the value

measured using the angle of repose method $\psi_{cv} = (35 \pm 2)^\circ$ (simplified procedure in [Santamarina and Cho, 2001]).



5.4 Core Characterization – Structure of the As-received Sediment

The core was sealed and frozen as soon as it was recovered from the Mount Elbert test well (diameter ~70mm, length 80mm). The sample arrived at our laboratory in a frozen state at standard pressure (1atm). While depressurization and freezing alter the fabric, the as-received state still captures meso-scale features that are lost after thawing and remolding.

The specimen was gradually covered by a protective wax layer without causing thawing. By using standard gravimetric and volumetric measurements, we obtained the initial void ratio of the specimen $e_0 = 0.72$ (ASTM D2216), which corresponds to an initial porosity $n_0 = 0.42$, in agreement with the lower bound estimate based on water content.

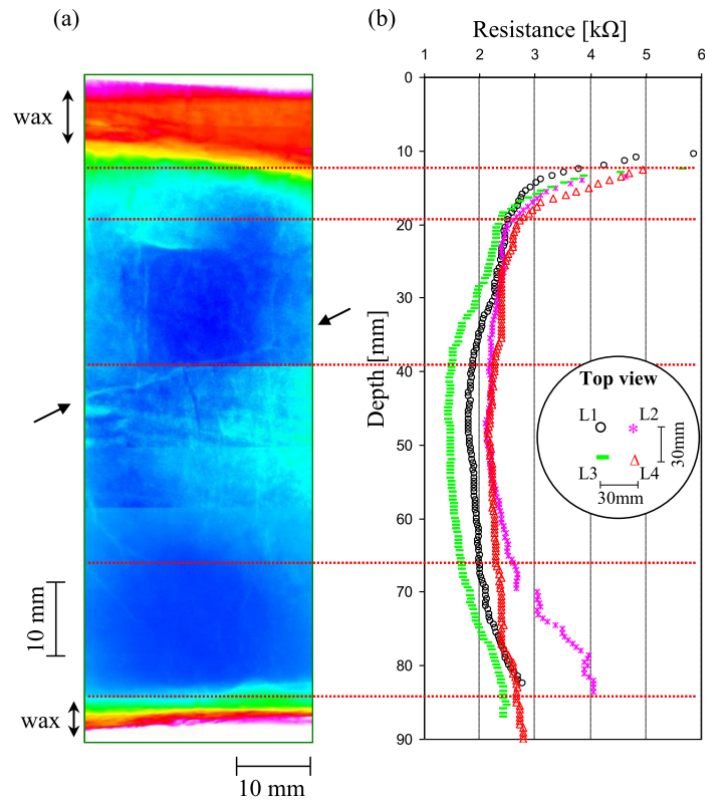
5.4.1 Spatial Variability

We used two methods to assess the spatial variability of the core: X-ray images (frozen state - Dage XD7600NT) and the electrical needle probe technique (thawed specimen within the wax shell - [Cho *et al.*, 2004]).

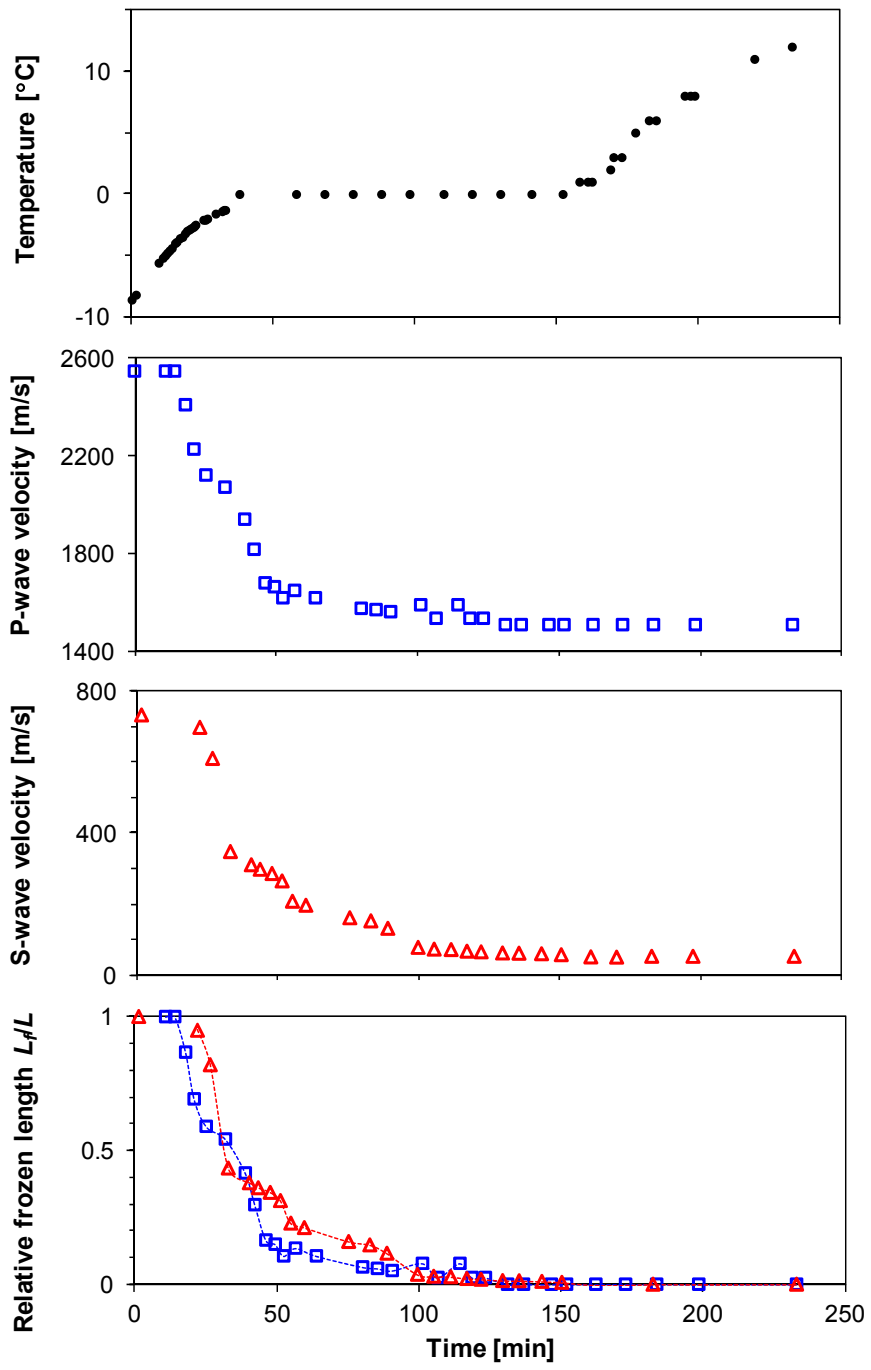
The color variation in the X-ray image (see 2D slice in Figure 5a) and oscillations in electrical resistance profiles (Figure 4b) represent variance in sediment porosity and/or composition. Both resistance profiles and X-ray images show relatively lower porosity in the upper and lower zones than in the center of this specimen. There is no clear evidence of pre-existing hydrate lenses in the X-ray image as fluids migrated after depressurization; only faint traces of discontinuities remain (see arrows in Figure 4a).

5.4.2 Evolution of Seismic Wave Velocities during Initial Thaw

Frozen pore fluid has minimal effect on X-ray absorption in soils, but a pronounced effect on acoustic velocities and electrical properties [Lee *et al.*, 2007]. Therefore, we monitored the evolution of temperature, P-wave and S-wave velocities



during the first thawing of the as-received specimen. Results plotted in Figure 5 highlight the great impact frozen fluids exert on the stiffness of sediments without external stress: propagation velocities in the frozen sediment are $V_p = 2550\text{m/s}$ and $V_s = 734\text{m/s}$ and fall to $V_p = 1500\text{m/s}$ and $V_s = 50\text{m/s}$ after complete thawing (Note: the velocity of sound in degassed water is $V_p \approx 1480\text{m/s}$, and it experiences a pronounced decrease in the presence of gas, e.g., a 35% decrease in V_p is observed for a volume fraction of gas as low as 10^{-4}). Wave velocities measured after thawing the specimen indicate that this sediment is fully water saturated and not-cemented. Complete water saturation could imply that this specimen did not contain hydrate in situ.



The measured P-wave and S-wave velocities are length-averaged values and integrate the travel time through frozen and thawed regions. We invert for the “remnant frozen length” using the travel times for both P and S propagations and the velocities for the frozen condition ($V_p = 2550\text{m/s}$ and $V_s = 734\text{m/s}$) and the unfrozen state ($V_p = 1500\text{m/s}$ and $V_s = 50\text{m/s}$). Results in Figure 5.5d show that the frozen length shortens while the temperature measured at the center of the core remains constant at the water-ice phase boundary. The end of thawing, i.e., when the inferred frozen length reaches zero, coincides with the increase in the core temperature above zero degrees. These results show that the complementary use of P- and S-wave propagation provides insightful information that can be used to characterize and delineate permafrost sediments and to monitor thawing or dissociation such as during gas production from hydrate-bearing sediments. We have applied similar techniques to monitor the depressurization of pressure cores gathered from hydrate bearing sediments in the Krishna-Godavari basin (India) and the Ulleung basin (East Sea); high attenuation hinders P-wave propagation soon after dissociation starts and free gas emerges.

5.5 Geophysical Properties and Stress-Volume Response (Remolded Sediment)

The stress-volume response was studied using an instrumented oedometer cell which houses shear wave transducers, a dielectric probe for complex permittivity measurement, and a K-type thermocouple. The remolded sediment was mixed with three different pore fluids: (1) deionized water, (2) a 57:43 THF-water solution to obtain 50% hydrate saturation $S_{hyd} = 0.5$ with excess THF to avoid freezing, and (3) a 19:81 THF-water solution to reach $S_{hyd} = 1.0$ after phase transformation. Standard consolidation test procedures (ASTM D2435) were followed for the specimen mixed with deionized water, while hydrate formation and dissociation stages were imposed after each consolidation step in specimens mixed with THF solutions. Additional details can be found in similar

studies by *Yun et al.*, [2007] and *Lee et al.*, [2008]; a detailed discussion on the use of THF as hydrate former is presented in *Lee et al.*, [2007].

5.5.1 S-wave Velocity

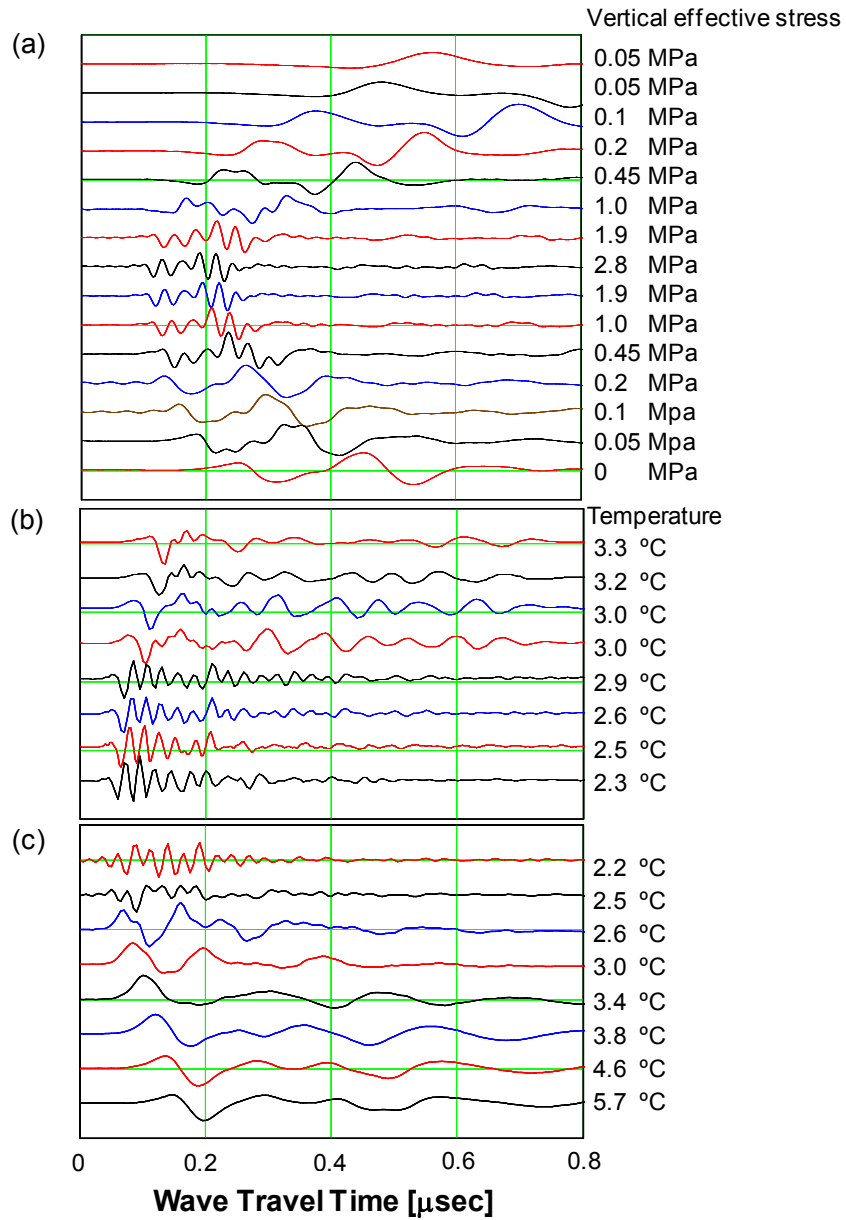
A selection of S-wave signatures is presented in Figure 6. Signatures gathered for the specimen without hydrate at the end of each consolidation step (Figure 5.6a) show that the S-wave velocity increases with the increase in effective stress, demonstrating the critical role of effective stress on the stiffness of uncemented sediments. The impact of hydrate formation and dissociation on the stiffness of hydrate-bearing sediments under a certain effective stress is highlighted by signatures in Figures 5.6b and 6c where hydrate formation leads to a pronounced increase in S-wave velocity.

Shear wave velocities for sediments with and without hydrate are shown in Figures 5.7b, 5.8b, and 5.9b. Results confirm that shear wave velocity is controlled by vertical effective stress in sediments without hydrate (Figure 5.7b). When a Hertzian-type model is employed, the vertically propagating shear wave velocity in uncemented sediments loaded under zero-lateral strain condition can be expressed as:

$$V_s = \alpha \left(\frac{\sigma'_v}{kPa} \right)^\beta \quad (5.1)$$

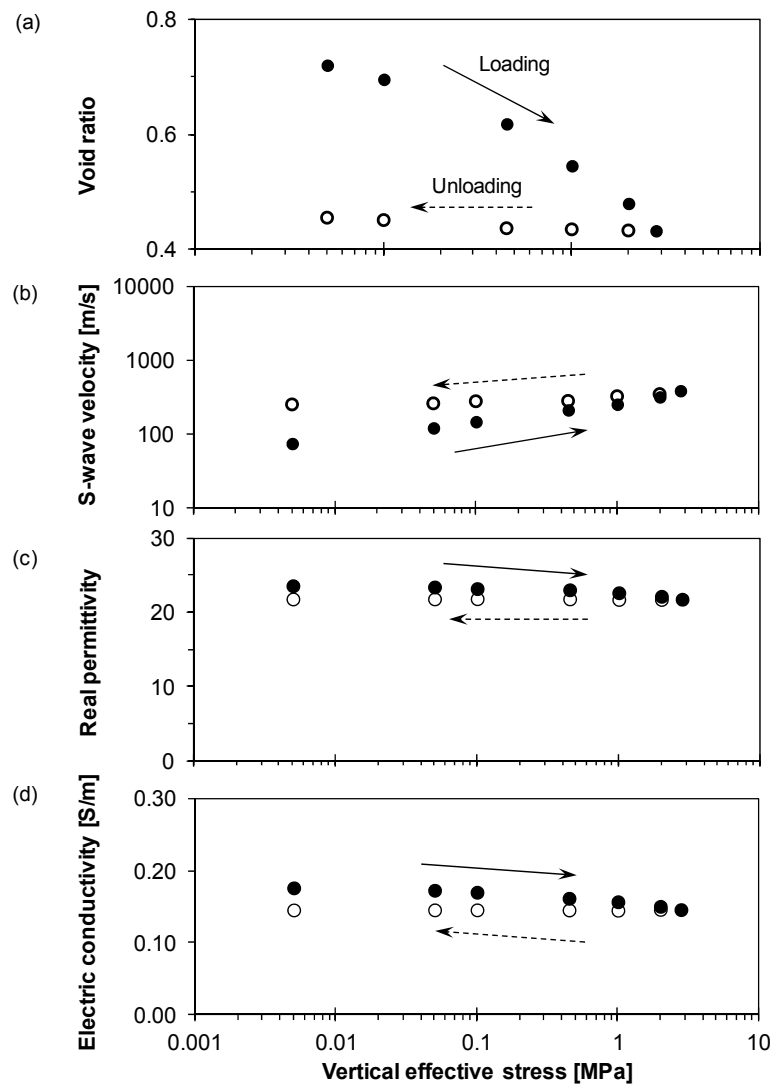
where, the α -factor denotes V_s at 1kPa vertical effective stress, and the β -exponent captures the sensitivity of shear wave velocity to effective stress. Experimental observations indicate that α and β parameters depend on packing, fabric, and the type of intergranular contacts (for detailed information, refer to [*Santamarina et al.*, 2001]). For this Mount Elbert sediment, the fitted values $\alpha = 40.8$ m/s and $\beta = 0.25$ ($r^2 = 0.94$) point to a sediment stiffness of high sensitivity to the stress state. The shear wave velocity for the sediment with hydrate saturation $S_{hyd} = 0.5$ combines both stress and cementation effects on stiffness (Figure 5.8b). Finally, the sediment with 100% hydrate pore saturation $S_{hyd} = 1.0$, exhibits a stress-independent that ranges from $V_s = 1520$ - 1580 m/s

(Figure 5.9b). Note that the propagation velocity in the as-received frozen specimen was only $V_s = 734\text{m/s}$, suggesting sampling effects.



5.5.2 Dielectric Permittivity

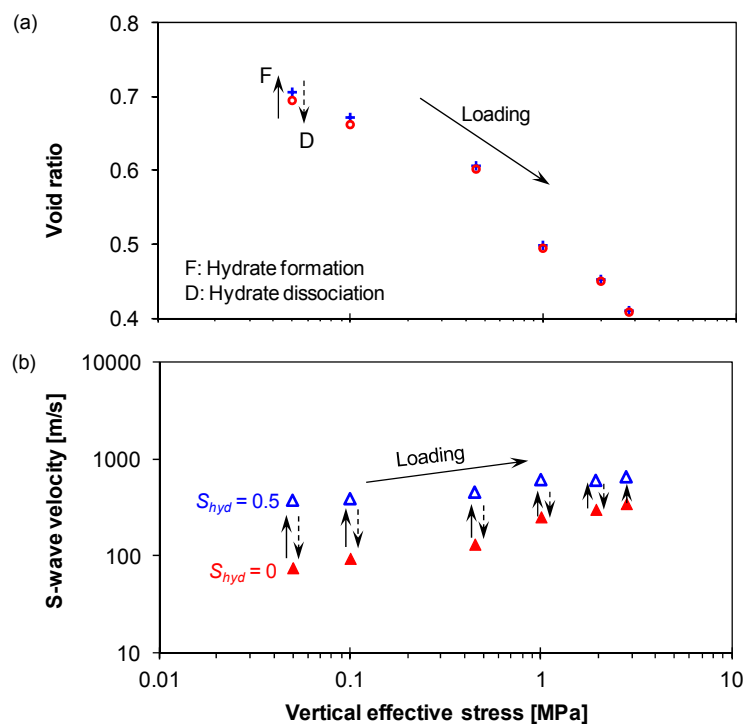
Permittivity spectra in the microwave frequency range for different types of mixtures are shown in Figure 5.10 (gathered using HP-8752A analyzer and dielectric probe). These spectra highlight the governing role of free water orientational polarization, the decrease in real permittivity κ in solutions with THF and in low porosity soil mixtures

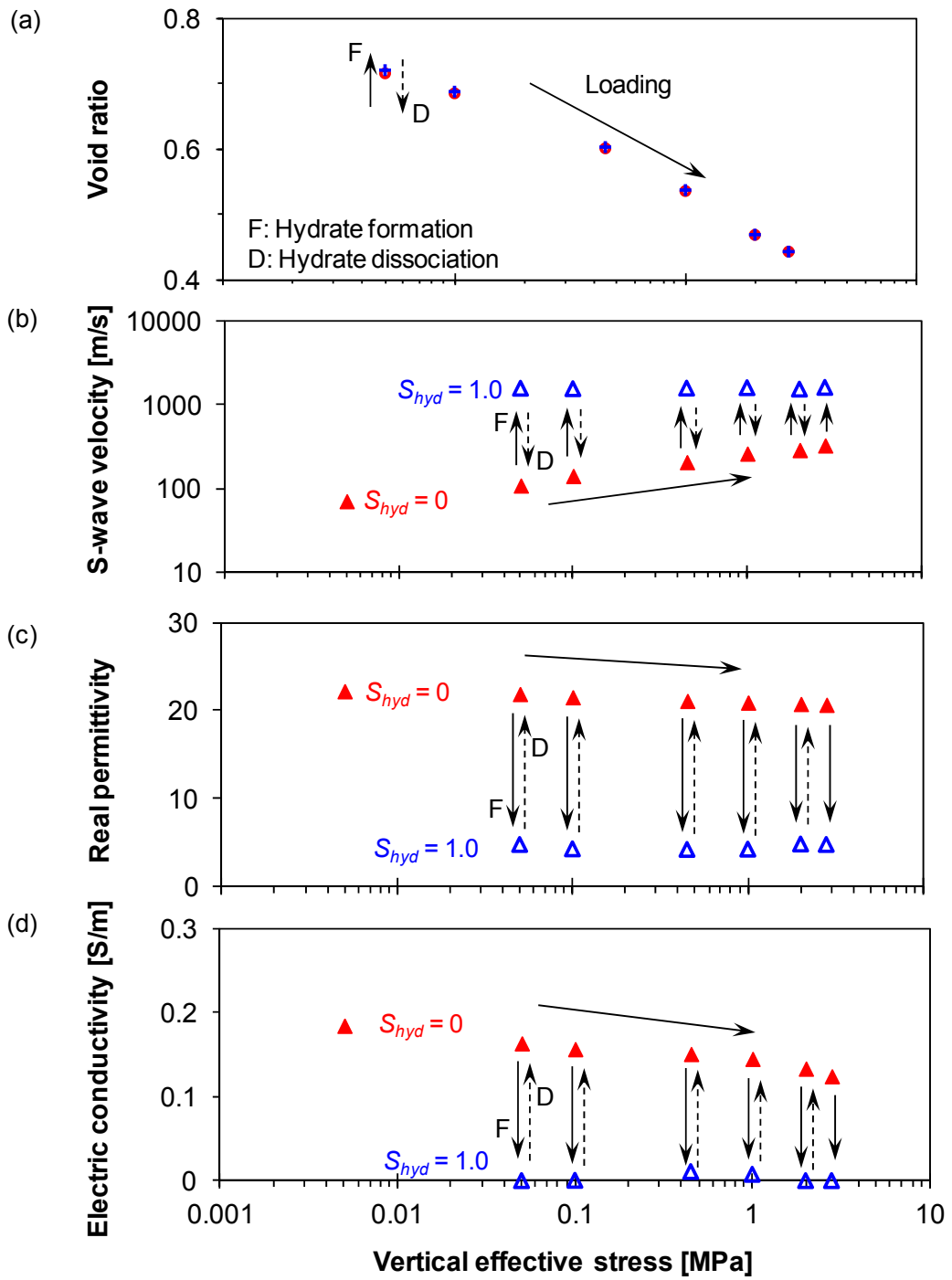


[Santamarina *et al.*, 2001]. The decrease in real permittivity with the increase in effective stress acting on the mixture prepared with deionized water is caused by the decrease in volumetric water fraction during sediment compaction (Figure 5.7c). On the other hand, the decrease in permittivity during hydrate formations reflects the decrease in polarizability as water molecules become part of hydrate cages (see data in Figure 5.9c for the sediment mixed with 19:81 THF-water solution).

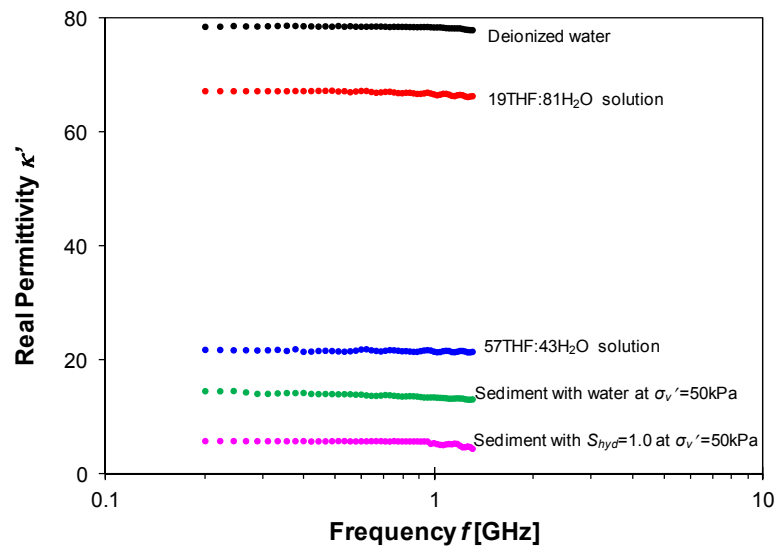
5.5.3 Electrical Conductivity

The pore fluid electrical conductivity σ_{pf} is a measure of ionic concentration and mobility. The sediment electrical conductivity σ_{el} is determined by the pore fluid conductivity and the fluid-filled porosity $n(1-S_{hyd})$. The common role of porosity in permittivity and conductivity explains the similar trends measured for electrical





conductivity and permittivity (Figure 5.7d and 5.9d). These results imply that dielectric permittivity and electrical conductivity are effective indicators of hydrate presence in sediments (Note: electrical parameters for the sediment with 57:43 THF-water solution are not shown since an excess THF mixture is used). However, permittivity is primarily affected by water content while conductivity is also affected by ionic concentration and mobility.

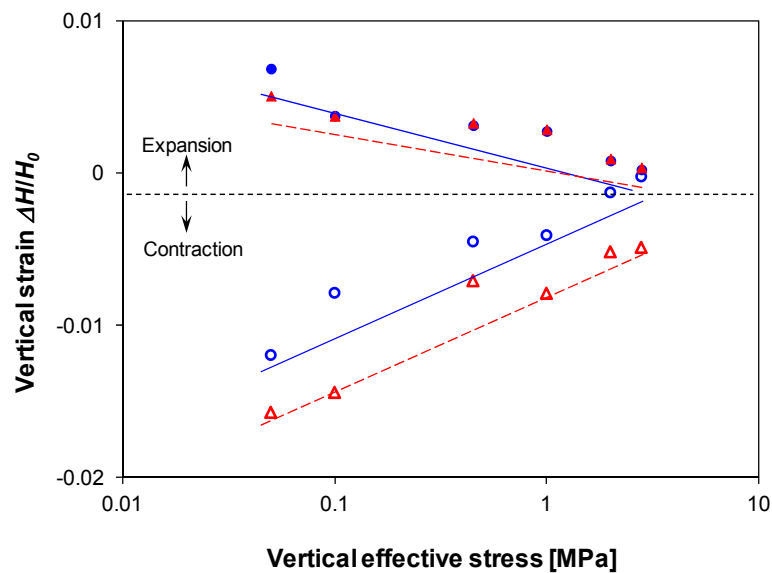


5.5.4 Volume Change

The change in void ratio e with effective stress σ_v' is documented in Figures 5.7a, 5.8a and 5.9a for the three mixtures. Trends are very similar for these mixtures. Compression C_c and swelling C_s indices characterize the mechanical responses in terms of the slopes of the normal consolidation line and the unloading curve on a plot of void ratio vs. the logarithm of vertical effective stress σ_v' . The sediment can be modeled using $C_c = 0.07$ and $C_s = 0.006$; these values correspond to sediments with low compression and expansion properties.

The mixtures with $S_{hyd} = 0.5$ and $S_{hyd} = 1.0$ experience volume change during hydrate formation and dissociation. Changes appear small in Figures 5.8a and 5.9a; data are plotted again in Figure 5.11 but in terms of strain $\varepsilon_z = \Delta H/H_0$, where ΔH is the change in specimen height during phase transformation and H_0 is the specimen height at the beginning of the hydrate formation or dissociation phase. Results in Figure 5.11 clearly show (1) expansion during formation and contraction during dissociation, (2) diminishing volume change with increasing confinement, and (3) slightly higher contraction than expansion; hence, there is residual volume contraction after a formation-dissociation cycle. The last observation suggests that volume expansion during hydrate formation alters the stability of granular columns and leads to skeletal collapse during hydrate dissociation [Lee *et al.*, 2010b].

Figure 1 shows that some sedimentation continued after hydrate formation started about 1.65Ma before present. As hydrate could have prevented sediment compaction, higher volumetric strain could take place in these layers during hydrate dissociation.



5.6 Analysis and Discussion

Experimental results demonstrate that vertical effective stress, porosity, and hydrate saturation are the major controls on the mechanical and geophysical response of hydrate-bearing sediment. Interrelationships among these parameters are explored next. Results obtained in this study are compared with the database of geophysical parameters gathered for hydrate bearing sediments at Georgia Tech, and semi-empirical equations in *Santamarina and Ruppel* [2010].

5.6.1 Physical Properties – Hydrate Saturation

Permittivity: Permittivity values κ at 1 GHz are plotted as a function of porosity and hydrate saturation in Figure 5.12a. We recognize the prevalent role of free water on permittivity and use a robust Complex Refractive Index Method CRIM model to fit the data:

$$\sqrt{\kappa} \approx 2.8 + 6n - 7nS_{hyd} \quad (5.2)$$

Conductivity: The ratio σ_{el}/σ_{pf} between the measured sediment conductivity σ_{el} and the pore fluid conductivity σ_{pf} , is plotted in Figure 5.12b as a function of porosity and hydrate saturation. A simple form of Archie's Law fits the data:

$$\sigma_{el}/\sigma_{pf} = [n(1 - S_{hyd})]^{1.45} \quad (5.3)$$

S-wave velocity: The complete S-wave velocity data set for different hydrate saturations ($S_{hyd} = 0, 0.5, \text{ and } 1.0$) and vertical effective stress levels is summarized in Figure 5.12c. Trends clearly show the transition from stress-controlled to hydrate-controlled stiffness in hydrate-bearing sediments. We fit the data using a theoretical expression initially developed for cemented soils [*Fernandez and Santamarina, 2001*]:

$$V_{hs} = \sqrt{\left(\frac{V_h S_{hyd}^2}{n}\right)^2 \theta + \left[\alpha \left(\frac{\sigma'_{\parallel} + \sigma'_{\perp}}{2kPa}\right)^{\beta}\right]^2} \quad (5.4)$$

where, $\alpha = 40.8$ and $\beta = 0.25$ correspond to the sediment without hydrate (Figure 5.7b),

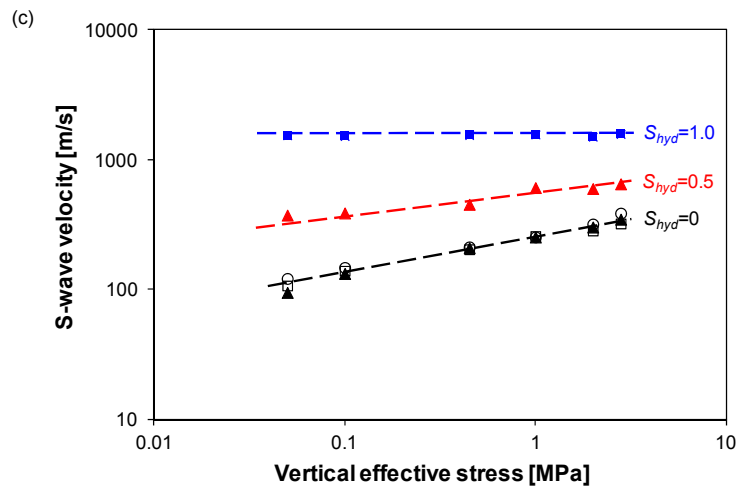
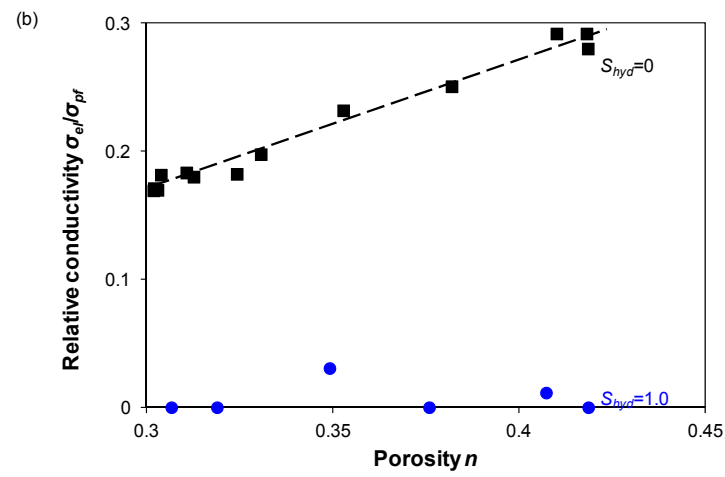
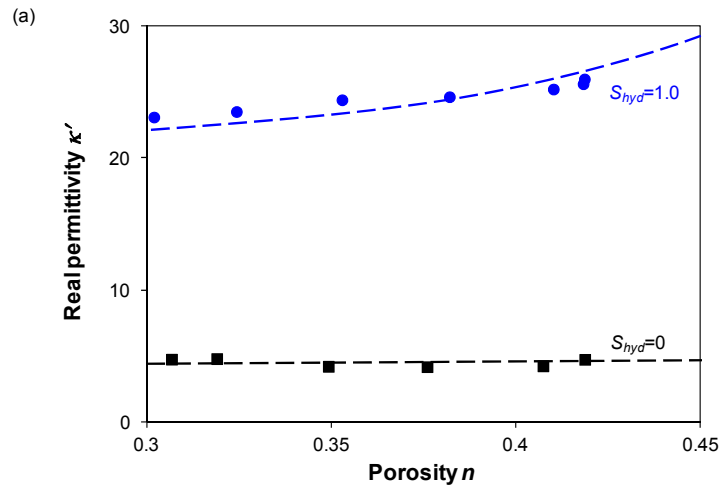
and the fitted parameter $\theta = 0.38$ reflects the hydrate habit in pores [Santamarina and Ruppel, 2010]. While a quantitative interpretation of the factor θ is not yet available, we can advance that $\theta = 0$ for pore filling hydrate and may exceed $\theta = 1.0$ for cementing hydrate.

5.6.2 Sand Crushing

The oedometer cell used in this study is limited to a maximum vertical stress of $\sigma_v' = 2.8\text{MPa}$. Surface features noted in Figure 5.3 may be related to the high effective stress in situ (6-to-7MPa): for a median particle size $D_{50} = 0.07\text{mm}$ and initial void ratio $e_0 = 0.72$, the vertical yield stress at massive grain crushing is estimated to be $\sigma_y \approx 10\text{-to-}20\text{MPa}$ for a 100% quartz sand, yet, some crushing starts at stress levels as low as $\sim 4\text{MPa}$ [Lo and Roy, 1973; McDowell, 1999; Nakata et al., 2001; Yamamuro and Lade, 1996]. Thus, depressurization-driven gas production from deep hydrate-bearing sediments may cause contraction due to sand crushing, in addition to contraction due to hydrate dissociation reported in Figure 5.11.

5.6.3 Fines Migration and Clogging

Fines in the sediment and crushing-generated fines may migrate during gas production. Fines migration is controlled by particle size, the ratio of migrating particle size to pore constriction size, and the spatial variability of the flow velocity field. Experimental results show annular clogging in radial flow when the orifice-to-particle size ratio is smaller than $d_{or}/d_p < 3\text{-}4$ and when seepage velocities exceed threshold values (detailed information and data for single-phase flow can be found in [Valdes and Santamarina, 2006; 2007]). We estimate that the Mount Elbert sediment tested in this study is prone to fines migration and clogging. Proper gas production strategies will be needed to prevent formation damage which may also cause sustained sand production.



5.7 Conclusions

The analysis of published investigations and a systematic laboratory study conducted using undisturbed and remolded specimens from the Mount Elbert well reveal the following observations (note: experimental results presented in this study are based on a single specimen; significant variations should be expected along the sediment column):

The reconstructed stratigraphy, historical ground surface elevation, base of the ice-bearing permafrost, and potential gas hydrate stability zone at the Mount Elbert region suggest that gas invaded/accumulated in coarse-grained layers and converted into hydrate-bearing sediments almost a million years before the permafrost. Any remaining water froze when the permafrost thickened and invaded the hydrate stability zone. Hence ice and hydrate may coexist at certain depths.

Gas invasion and accumulation in coarse-grained layers before pressure-temperature stability conditions help explain the relatively high hydrate saturation found in coarse-grained layers at the Mount Elbert well. High fines content in other layers hindered fluid flow, methane transport and hydrate accumulation. The pore size-dependent shift in the PT phase boundary is not sufficient to impede hydrate formation in these sediments.

Grain surface texture features are consistent with the previously suggested fluvial-deltaic origin of these sediments, without glacial entrainment. The effective stress level corresponds to the onset of crushing. S-wave velocity during the initial thawing of the as-received sediment indicates uncemented granular skeleton. The tested specimen has a high fraction of fines and shows no evidence of hydrate present.

The volumetric strain during dissociation vanishes when the effective stress exceeds 2-to-4 MPa. Therefore, small volumetric strains are expected during gas production at the Mount Elbert well, where the in-situ stress exceeds 6-to-7 MPa. Two possible situations may alter this conclusion: (1) crushing associated to the increase in

effective stress during depressurization-driven production and (2) high in-situ porosity if early hydrate formation prevented densification. Grain crushing may feed fines migration and clogging, which in turn could contribute destabilization and sustained sand production.

The major controls on the mechanical and geophysical properties of hydrate-bearing sediments are effective stress, porosity, and hydrate saturation. Geophysical parameters and established empirical relationships in geomechanics allow us to obtain robust estimates of engineering design parameters for hydrate-bearing sediments. Furthermore, elastic and electromagnetic wave measurements can be employed to characterize and delineate hydrate-bearing/permafrost sediments and to monitor dissociation/thawing processes, during gas production from hydrate-bearing sediments.

CHAPTER 6

SAMPLING HYDRATE-BEARING SEDIMENTS: PRESSURE CORE TECHNOLOGY USING IN THE KRISHNA-GODAVARI BASIN

6.1 Introduction

The 2006 Indian National Gas Hydrate Program Expedition NGHP was conducted to investigate geological and geochemical controls on gas hydrate occurrence offshore of the Indian Peninsula and along the Andaman convergent margin [Collett *et al.*, 2006]. Hydrate saturation estimated from P-wave velocity and electrical resistivity logs vary from $S_h < 5\%$ to as high as $S_h = \sim 80\%$ [Lee and Collett, 2009; Shankar and Riedel, 2011]. The total hydrate-trapped methane gas in India's exclusive economic zone is estimated to be ~ 1.9 trillion cubic meter (TCM) [Sain and Gupta, 2012].

The Krishna-Godavari Basin on the eastern side is a rich marine hydrate reservoir with an estimated methane accumulation of 0.16-0.9TCM [Collett *et al.*, 2008a]. The Krishna-Godavari Basin has experienced initial rifting, carbonate platform development, and finally the deposition of a delta system [Bastia and Nayak, 2006; Krishna *et al.*, 2000]. Sediments in this basin are 4-7km thick with deep layers that date from the Late Carboniferous to recent shallow layers [Bastia and Nayak, 2006; Gupta, 2006; Rao, 2001; Rao and Mani, 1993]. These clay-rich sediments have preferential hydrocarbon accumulations in regions dominated by montmorillonite and kaolinite [Basu, 1990]. Poorly preserved organic matter in Paleocene and Cretaceous sequences has generated gas and gas-condensate [Banerjee *et al.*, 1994]. Most of the methane gas trapped in hydrate is biogenetic. Hydrate formation has caused grain-displacing discontinuities in the form of nodules, veins, and lenses [Rees *et al.*, 2011].

Both conventional and pressure cores were recovered during the 2006 expedition.

The five pressure cores recovered at site NGHP-01-21 were kept at 4°C and 13MPa fluid pressure, and tested three months later using the Instrumented Pressure Testing Chamber (IPTC) [Yun *et al.*, 2010].

The laboratory testing of all natural sediments faces inherent sampling disturbance [Hvorslev, 1949]. This manuscript reviews sampling effects, demonstrates the need for pressure core technology in the study of hydrate-bearing sediments, and analyzes emergent poroelastic and PT phenomena when sampling these formations. Previous studies of sampling effects applicable to near surface sediments are reviewed first.

6.2. Sampling Disturbance in Hydrate-Free Sediments

Sampling affects the mechanical, biological, chemical, mineralogical, and lithologic properties of natural sediments. Cores experience excavation unloading and wall shear induce unavoidable volumetric and shear strains. Figure 6.1 illustrates a conceptual stress-strain path during sampling [Hight *et al.*, 1992; La Rochelle *et al.*, 1980; Ladd and DeGroot, 2003; Landon, 2007; Shogaki and Kaneko, 1994]. In “perfect sampling”, the sample experiences the undrained removal of the deviator stress ($\Delta\sigma = \sigma_v - \sigma_{ho} \rightarrow 0$), followed by an undrained triaxial extension. In “ideal sampling”, the specimen sequentially experiences compression and extension along the centerline and shear strain along sampling tube walls during sampler penetration; finally it experiences undrained shear stress relief during sample extrusion [Baligh, 1985; Baligh *et al.*, 1987; Levadoux and Baligh, 1980].

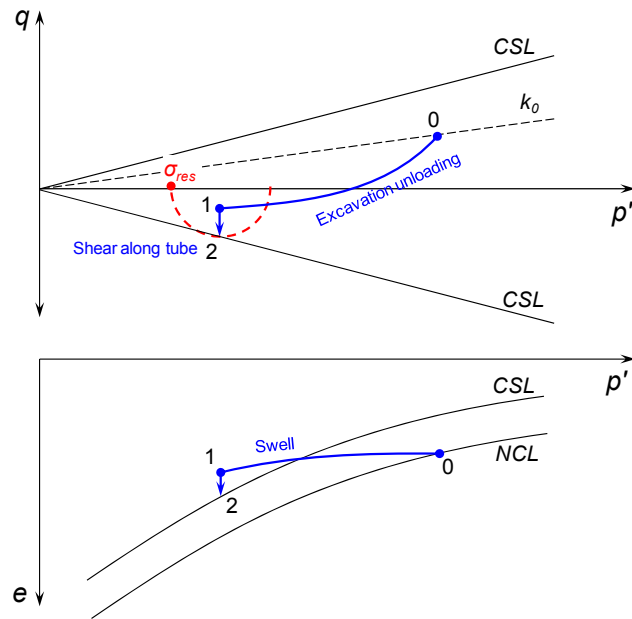


Figure 6.1 The stress-strain path during sampling. Cores experience excavation unloading (0→1) and wall shear (1→2); volumetric (shown) and shear strains are unavoidable (Note: CSL = critical state line; NCL = normal consolidation line; σ_{res} = residual stress mobilized during expansion against the sampling tube).

6.2.1 Sources of sampling disturbance

Several sediment and operational factors account for changes in physical and mechanical properties. These factors are reviewed next.

(1) Drilling or coring cause changes in stress, fluid pressure, and ensuing strains during coring and specimen extraction even before sediments are sampled [Baligh *et al.*, 1987; Cao *et al.*, 2007; Clayton *et al.*, 1998; Li *et al.*, 1997]. The stress caused by the high mud pressure required to circulate the slurry can be more detrimental than the unloading stress induced by drilling and corer penetration [Chung *et al.*, 2004].

(2) Sampling related effects include effective stress relaxation [Chau, 1991; La Rochelle *et al.*, 1980], friction along the sampling tube [Baligh *et al.*, 1987; Chau, 1991; Clayton and Siddique, 1999], deformation due to insufficient rigidity of the sampling tube,

clogged drain hole, and pore pressure variation [Clayton and Siddique, 1999; Safaqah and Riemer, 2006; Siddique et al., 1999].

(3) Storage and transportation the specimen experiences: temperature variation, sampler deformation, vibrations, and drying [Baligh et al., 1987; Shogaki and Kaneko, 1994].

(4) Early stages of testing also impose multiple disturbing steps: sample extrusion [Baligh et al., 1987; Chung et al., 2004; Day, 1990], specimen trimming to the required designed dimensions [Atkinson et al., 1992; Baligh et al., 1987], and specimen installation [Hight et al., 1992].

6.2.2 Disturbance evaluation – shear stiffness

Visual inspection [Hvorslev, 1949; Long, 2003] and radiology (ASTM D4452) provide direct “geometric” evidence of disturbance. Numerous studies have been conducted to measure physical/mechanical changes. Observations include: (1) decrease in undrained shear strength s_u and pre-consolidation stress p_c particularly in soils with low plasticity [Baligh et al., 1987; Long, 2003; Tanaka et al., 2001; Zhang and Lunne, 2002]; (2) increase in volumetric strain ϵ_v , axial strain ϵ_a , and shear strain ϵ_s at peak deviatoric stress [Giao et al., 2004; Hird and Hajj, 1995; Santagata and Germaine, 2005]; smaller sampling strains in over-consolidated clays [Siddique et al., 1999]; (3) decrease in most consolidation parameters in normally consolidated soils, such as compression index c_c , coefficient of volume compressibility m_v , and coefficient of consolidation c_v [Shogaki and Kaneko, 1994]; and (4) pore pressure variation during coring, specimen extrusion, and specimen trimming [Kimura and Saitoh, 1984; Safaqah and Riemer, 2006].

The change in shear stiffness or shear wave velocity from values measured in situ V_F to those measured in the laboratory V_{lab} at the same stress conditions is a good indicator of disturbance [Landon et al., 2007]. The extent of sampling disturbance also depends on soil type [Rinaldi and Santamarina, 2008; Stokoe and Santamarina, 2000;

Tatsuoka and Shibuya, 1991]. Figure 6.2 shows shear wave velocity measured for clays, sands, and cemented soils/rocks both in the field V_F and the laboratory V_{Lab} . It can be observed that:

- Soft clayey or fine-grained sediments can either gain or lose stiffness during sampling.
- Stiff clayey sediments tend to experience smaller sampling induced stiffness changes, suggesting that the fabric of stiff clayey soils can be well preserved.
- Loose sandy coarse-grained soils tend to gain stiffness due to densification.
- Most coarse-grained soils tend to lose stiffness during sampling, probably due to the loss of diagenetic cementation during the sampling of natural coarse-grained materials. In general, coarse-grained sediments with a field velocity $V_F > 150\text{m/s}$ will most likely lose stiffness.
- Cemented soils or rocks ($V_s > 1000\text{m/s}$) are also affected by sampling. But most importantly, sampling bias has the greatest effect on measured parameters: small laboratory specimens do not include joints and faults encountered in the field, hence $V_{lab}/V_F \gg 1$.
- Sampling effects that involve destructuration result in V_{lab}/V_F values that decrease with increasing depth, because of induced fissuring and cracks [Eberhardt *et al.*, 1999].

6.3. Hydrate-Bearing Sediments: Additional Sampling Effects

The sources of sampling disturbance that affect hydrate-free sediments apply to hydrate-bearing sediments as well. However, additional effects are anticipated due to pressure and temperature dependency of hydrate dissolution and dissociation, and its time dependent relaxation. These effects are explored next.

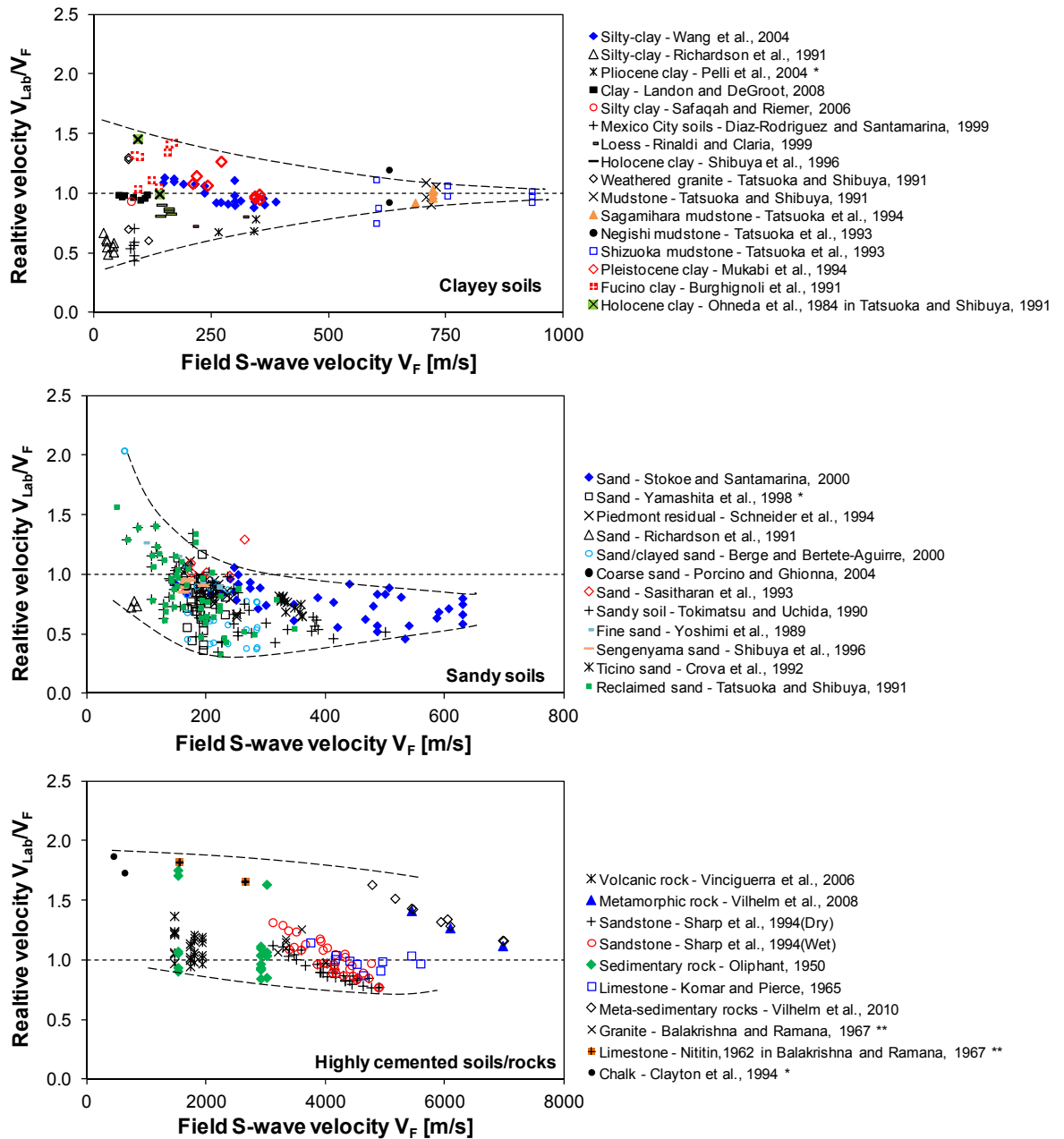


Figure 6.2 Sampling disturbance and sediment type. Note: * values computed from G_{max} assuming specimen density $\rho=2000\text{kg/m}^3$; ** Computed from V_p assuming $V_p/V_s=1.5$.

6.3.1 Pore-scale analysis

In situ hydrate-bearing sediments are subjected to effective stress with temperature and water pressure within the hydrate stability field. Figure 6.3 illustrates a pore-scale analysis of potential sampling effects.

Coring releases effective stress and induces soil skeleton dilation (Figure 6.3b). Tensile strain localization at cemented contacts causes hydrate breakage or debonding, and potential hydrate dissociation. Hydrate crystals under tension may cause local hydrate dissociation due to effective decrease in internal stress [*Jung and Santamarina, 2011*]. Methane hydrate within the stability zone dissociates during cold compaction and ductile deformation of hydrate crystals, and free water is released [*Durham et al., 2003*].

Corer insertion induces shear along walls (Figure 6.3c). Shear straining leads to dilation in dense sediments or contraction in loose sediments. Such volume change and associated pore pressure variation alter hydrate cementation and stability.

Decrease in water pressure produces gas exsolution from the pore fluid followed by hydrate dissociation (Figure 6.3d). Degassing is typically associated with volume expansion, fines migration, sediment fracturing [*Jung et al., 2011; Santamarina and Jang, 2009*], and carbon isotope fractionation of CH₄ [*Wallace et al., 2000*]. Hydrate dissociation releases deionized water leading to pore water freshening and the decrease in salt concentration, which alters interparticle electrical forces and double-layer properties that govern clay [*Santamarina et al., 2001*]. The loss of hydrate crystals decreases sediment stiffness, accompanied by volume contraction [*Lee et al., 2010b*]. Additionally, fast depressurization may also rupture the microbe cells [*Hemmingsen and Hemmingsen, 1980; Park and Clark, 2002*].

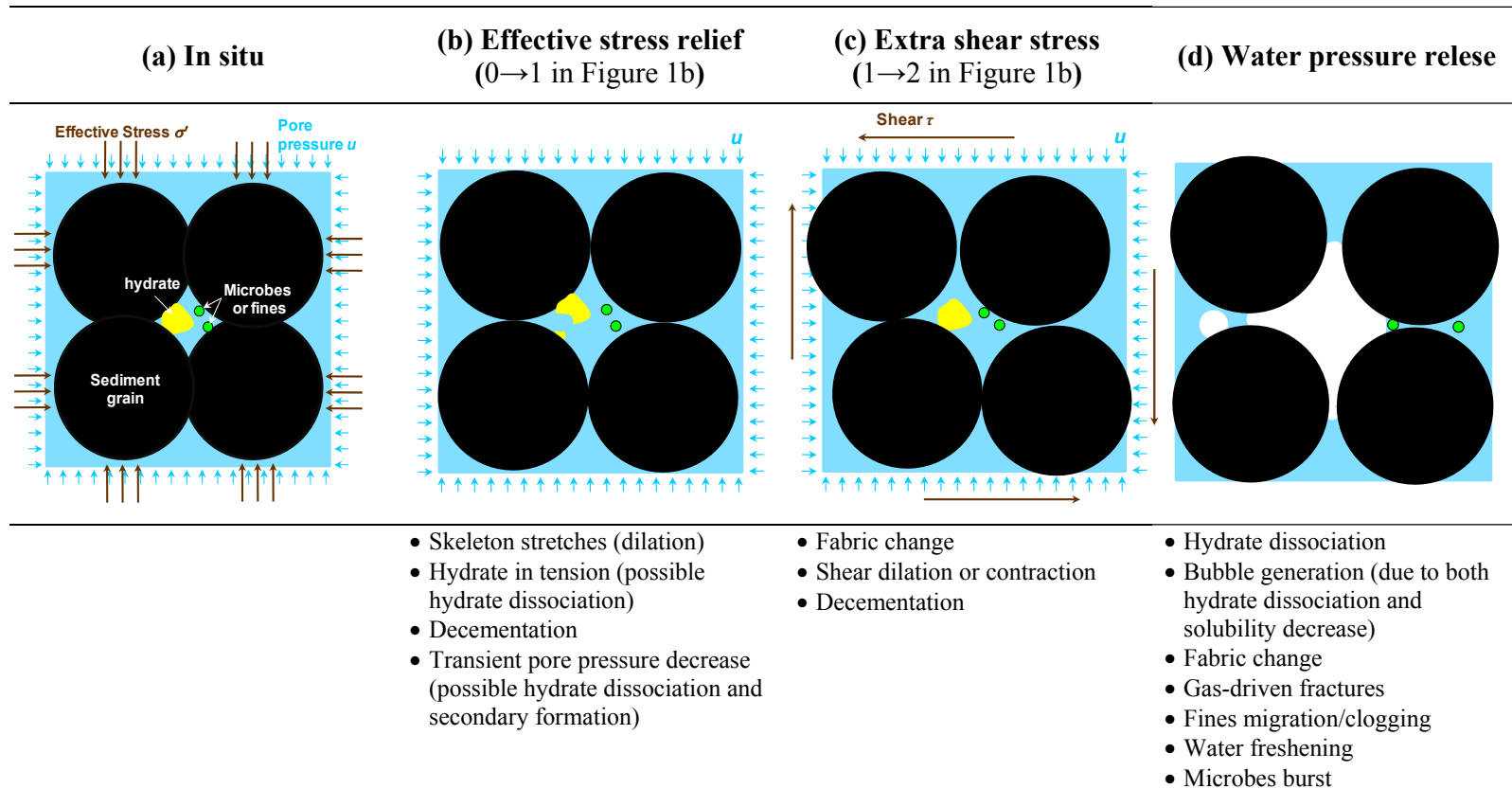


Figure 6.3. Sampling hydrate-bearing sediments. (a) In situ. (b, c) Unloading effective stress and induced shear in pressure cores. (d) The additional consequences of water pressure release in standard core.

6.3.2 Unloading: Poroelastic Mandel-Cryer effect and secondary hydrate formation

The pore pressure response to a sudden stress change is not homogenous throughout the specimen (i.e., Mandel-Cryer effect [Cryer, 1963; Mandel, 1953]). Unloading-induced skeleton rebound during sampling produces a drop in pore pressure [Safaqah and Riemer, 2006], which results in increased water content, particularly at the center of the specimen [Bjerrum, 1973].

Unloading $\Delta\sigma$ induces temporal and spatial variation of pore pressure u (in the form of Laplace transform \tilde{u}) in a cylindrical soil specimen (radius R) under zero lateral strain conditions is (refer to Appendix B for details):

$$\tilde{u} = M \left(1 - \frac{\alpha\eta}{GS} \right) A_1 I_0 \left(r\sqrt{s/c} \right) - \alpha M A_2 \quad (6.1)$$

Numerical inversion of the Laplace transform of this equation [Stehfest, 1970] returns the relative pore pressure decrease ($\Delta u/\Delta\sigma$) in terms of dimensionless radius $\rho = x/R$, where x is the distance from the center of the core, and dimensionless time $\tau = t/(R^2/c_v)$, where c_v is the pore water pressure diffusion coefficient (Figure 6.4b).

At the beginning of unloading, the skeleton rebound is hindered by the stiff pore water, causing pore pressure decrease across the specimen ($\tau = 0$ in Figure 6.4b). The pore pressure at boundaries immediately recovers, creating ‘weakened’ boundaries accompanied by a load transfer to inner zones. This leads to additional pore pressure drop $\Delta u > \Delta\sigma$ towards the center of the specimen ($\rho < 0.7$ and $\tau = 0.01-0.1$ in Figure 6.4b). The maximum pore pressure drop occurs at the center part of the specimen at time $\tau = t/(R^2/c_v) \approx 0.06$. The magnitude of maximum pore pressure drop increases with unloading rate, i.e., coring speed v_{coring} , since slower unloading allows more time for pore water pressure diffusion and homogenization (Figure 6.4c).

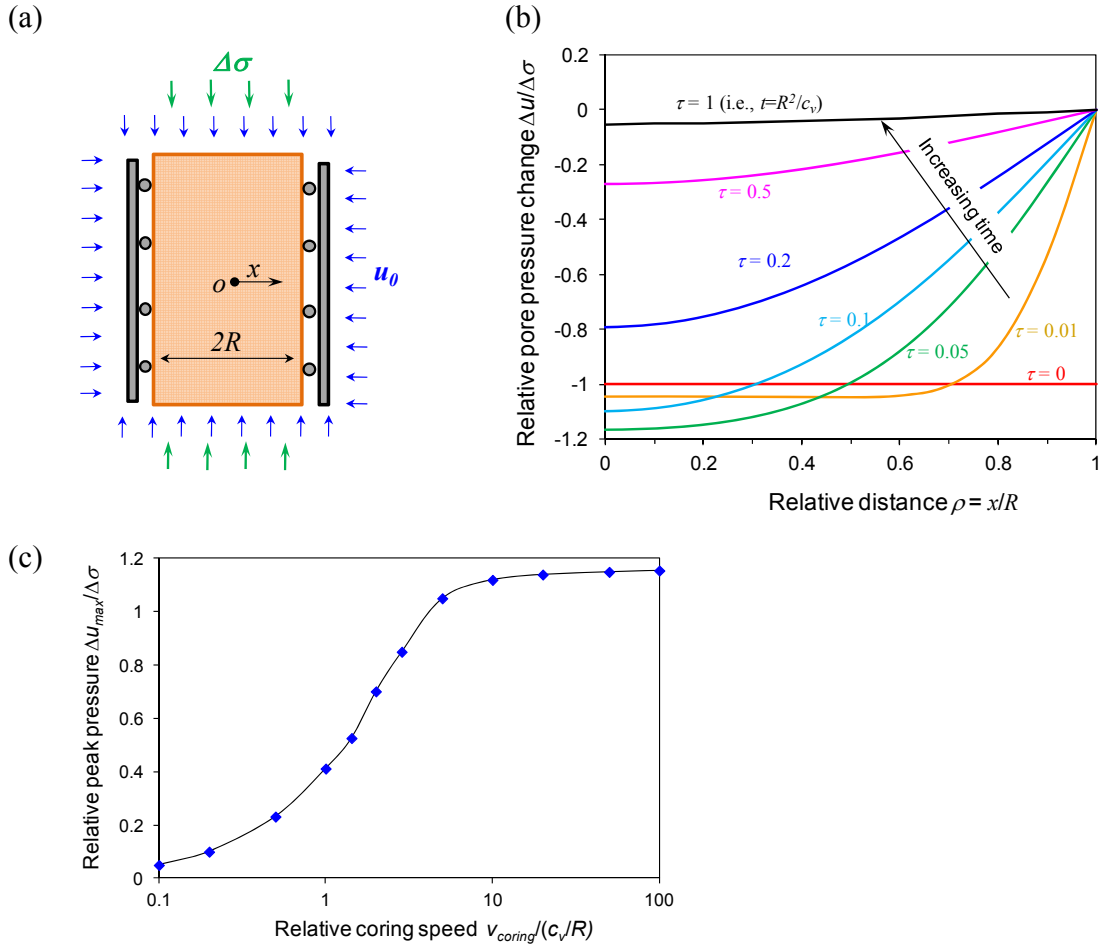


Figure 6.4. Vertical stress relaxation and pore pressure variation. (a) Poroelastic modeling: unloading $\Delta\sigma$ of a cylindrical specimen under zero-lateral strain conditions. Ambient water pressure is constantly u_0 . (b) Unloading induced pore pressure distribution as a function of radial distance $\rho = x/R$ and time $\tau = tc_v/R^2$. (c) Peak pore pressure drop $\Delta u_{max}/\Delta\sigma$ as a function of the coring speed $v_{coring} = (c_v/R)$.

Table 6.1 Sediment parameters for the poroelastic model used to study the Mandel-Cryer effect in hydrate-bearing sediments.

Properties	Unit	Value
Shear modulus, G	MPa	130
Drained Poisson's ratio, ν	-	0.2
Undrained Poisson's ratio, ν_u	-	0.46
Porosity, n	-	0.4
Skempton's coefficient, B	-	0.9
Permeability, k	mD	0.1
Fluid viscosity, μ	Pa·s	0.001

Transient pore pressure decrease can trigger hydrate dissociation, fluid expansion, and a gas-driven diametric fracture. As the pore pressure recovers, secondary hydrate may form. The vertical hydrate lense observed in the X-ray images (Figure 6.5) of hydrate-bearing sediments recovered from the Krishna-Godavari Basin clearly show this sampling effect when using percussion corer (Fugro Pressure Corer). Similar unique hydrate morphology is also observed in fine-grained sediments recovered from Ulleung Basin, where spiral hydrate lenses form as the rotary corer (HYACE) advances [Yun *et al.*, 2011]. Apparently, the morphology of secondary formed hydrates reflects the stress path imposed on the specimen by coring and sampling (refer to [Skovborg *et al.*, 1993; Sloan and Fleyfel, 1991; Tajima *et al.*, 2004] and Chapter 2).

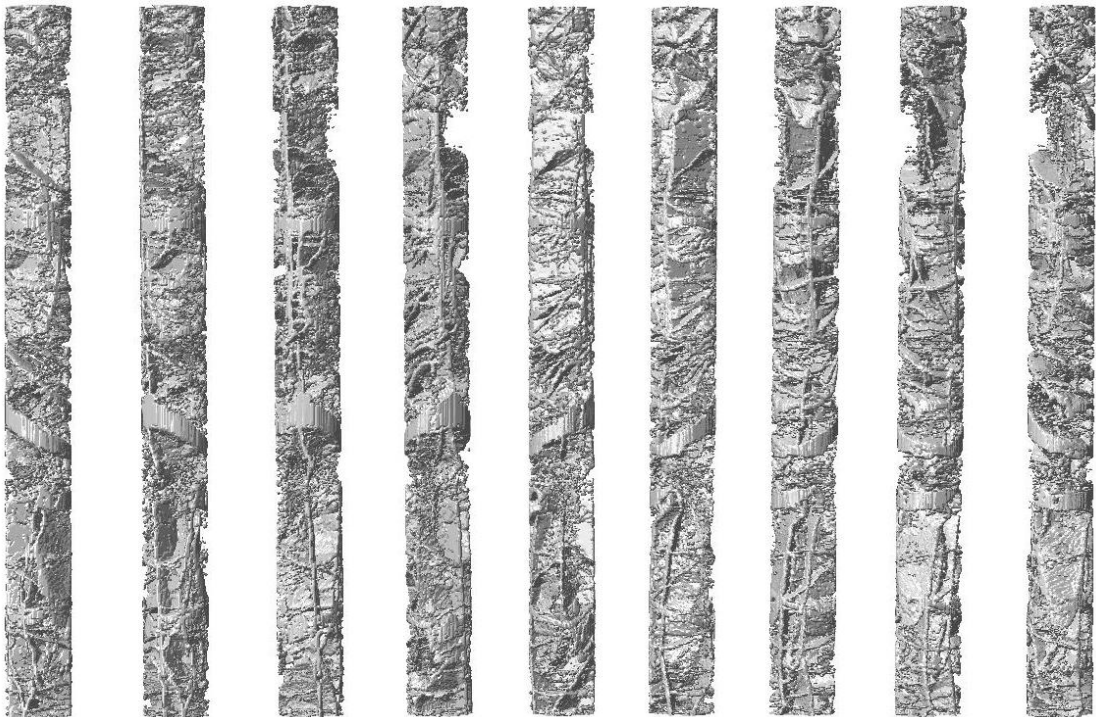


Figure 6.5. Secondary hydrate formation during coring. X-ray tomography (processed after Geotek) of hydrate-bearing sediments recovered from the Krishna-Godavari Basin offshore India during the 2006 National Gas Hydrate Program (NGHP). It is estimated that the long hydrate lense across the diameter of this percussion core resulted from secondary hydrate formation during sampling.

6.3.3 Post-sampling creep and aging

The post-sampling stiffness evolution in frozen fine sands with different ice saturations ($S_{ice} = 0.15, 0.3, \text{ and } 0.52$) is experimentally studied as an analogue for hydrate-bearing sediments (refer to Chapter 8). The P-wave velocity of specimens after unloading (from 50kPa to 1kPa) decreases with time $V_{(t)}$ following an exponential trend (Figure 6.6):

$$V_{(t)} = V_0 - \Delta V (1 - e^{-\alpha t}) \quad (6.2)$$

where V_0 is the initial velocity, ΔV is the total velocity loss at infinite time, and $t_{ch} = 1/\alpha$ is the characteristic time for the stiffness creep. This relaxation time is $t_{ch} \approx 10$ minutes for all specimens in this study. Such a short period suggests inevitable stiffness loss in hydrate-bearing sediments after sampling because most relaxation effects will have finished even before the core reaches the drill rig.

Note that the compressive strength of methane hydrate is more than 20 times stronger than that of water ice under identical temperature and strain rate conditions [Durham *et al.*, 2003], but their tensile and adhesive strength are similar [Jung and Santamarina, 2011]. Therefore, stiffness loss of hydrate-bearing sediments after unloading is expected to be comparable with results obtained with ice shown here. The ductile behavior of hydrate (ice) may favor load transfer (from the hydrate mass to the soil skeleton) during hydrate formation and sedimentation.

6.3.4 Testing inside the stability zone at different PT conditions

Recovered hydrate-bearing sediments experience P-T changes, even when they are kept within the stability field using pressure core technology. Methane solubility in water in the presence of methane hydrate decreases with increasing pressure and decreasing temperature. The isochoric analysis of the variation in hydrate saturation due to P-T changes indicates that the decrease in methane solubility caused by a 1K decrease

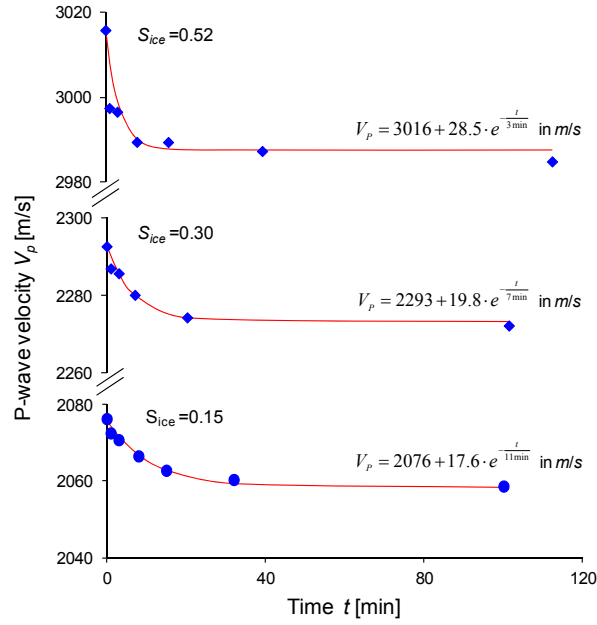


Figure 6.6. Stiffness creep after unloading (from 50kPa to 1kPa) for specimens with different ice saturations S_{ice} . Experimental data (markers) are fitted with an exponential decay model (lines).

in temperature is approximately equivalent to the increase induced by a 20MPa pressure drop (see details in Appendix C). In other words, a simultaneous decrease in both pressure and temperature with a gradient $\partial P/\partial T \approx 20MPa/K$ (dash line in Figure 6.7) will not alter methane solubility or hydrate saturation. As temperature prevails, the change in hydrate saturation ΔS_H can be estimated from the temperature change ΔT as (Appendix C):

$$\Delta S_H = 0.001 \left(\frac{\Delta T}{1K} \right) (1 - S_{H0}) \quad (6.3)$$

where S_{H0} is the initial hydrate saturation.

The change in hydrate saturation within normal P - T working conditions is relatively small, primarily because of the low methane solubility in water. The observations allow testing hydrate-bearing sediments at lower and safer pressures without significant changes in the hydrate mass as long as minor changes in temperature are accommodated.

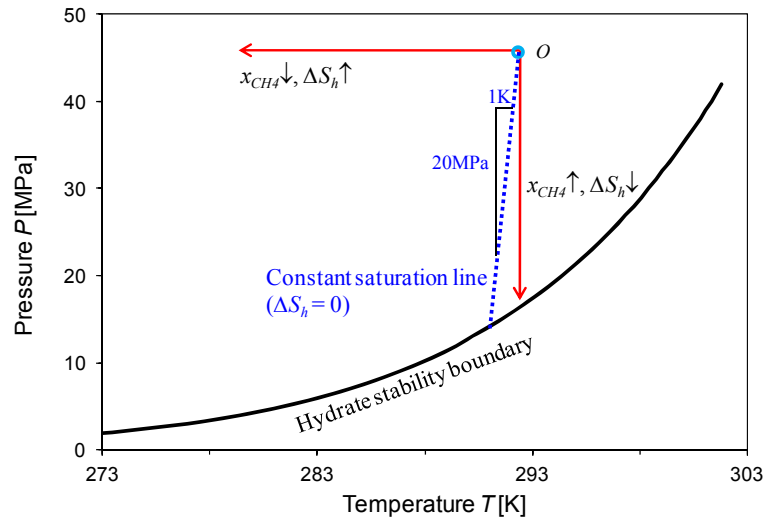


Figure 6.7. Effects of changes in pressure and temperature on hydrate saturation. The hydrate saturation within stability zone increases with decreasing temperature and increasing pressure. The increase in hydrate saturation due to a 1K decrease in temperature is approximately the same as produced by a 20MPa increase in pressure.

6.3.5 Anomalous hydrate preservation

Experiments show that methane hydrate can be temporarily preserved within ice for a short transient outside the stability field but below water freezing temperatures; this is known as hydrate self-preservation or anomalous preservation [Stern *et al.*, 2001; Yakushev and Istomin, 1992]. This anomalous preservation regime extends from 240K to 273K at atmospheric pressure [Iwasaki *et al.*, 2005; Melnikov *et al.*, 2010; Stern *et al.*, 2001]. The lower bound of this regime 240K is the transition temperature from cubic ice I_c to hexagonal ice I_h , where the annealing of stacking occurs [Kuks *et al.*, 2004; Murray and Bertram, 2006]. Hydrate dissociation within this regime undergoes three stages: (1) initial fast hydrate dissociation [Takeya *et al.*, 2001], supercooled water from hydrate dissociation forms a thin film outside the residual hydrate crystals [Melnikov *et al.*, 2009]; (2) the ice shell slows down gas escape, yet is not strong enough to encapsulate stable hydrate; and (3) hydrate dissociation virtually stops when the external ice shell is strong enough to keep inner hydrate stable; gradually, gas molecules can escape by solid-

state diffusion [Davidson *et al.*, 1986; Stern *et al.*, 2000; Takeya *et al.*, 2001; Tse and Klug, 2002].

The ice fraction that renders the maximum volume fraction of hydrate preserved by the ice shell is approximately 50% at 240K but less than 2% at 270K, assuming the tensile strength of ice is $\sigma_t = 2.316 - 0.013(T/^\circ\text{C})$ MPa [Petrovic, 2003].

Several other mechanisms are involved in self-preservation, including: (1) hydrate micro-structure: quenched methane hydrate is noticeably less prone to fracturing or flaking than synthesized methane hydrate [Stern *et al.*, 2001]; (2) the allowed time to re-freeze the supercooled water ranges from tens of hours at 270K to few seconds at 253K, and it is a function of the size of water droplets as well [Melnikov *et al.*, 2009]; (3) the ice cover formed at high degrees of supercooling will be less perfect [Melnikov *et al.*, 2010]; and (4) Ostwald-ripening reduces grain to grain boundaries especially at higher temperatures.

The anomalous preservation of methane hydrate allows for the temporary manipulation and sub-sampling of frozen hydrate-bearing sediments without using high pressure chambers. Note that methane hydrate is stable at $T < -80^\circ\text{C}$ at atmospheric pressure. Therefore, hydrate-bearing sediments can be stored in dry ice or liquid nitrogen at atmospheric pressure.

6.4. Discussion: Characterization of Hydrate-Bearing Sediments

6.4.1 Sampler design - Plugging

The following criteria for sampler design help reduce sampling disturbances, based on previous experimental and numerical studies [Clayton and Siddique, 1999; Clayton *et al.*, 1998; La Rochelle *et al.*, 1980; Lunne *et al.*, 2006]:

- Sharp shoe cutting angle: angle lower than 5°
- Thin sampler wall thickness: wall to radius ratio $t/R < 8\%$

- Low friction along inside and outside corer walls
- Low inside clearance relative to the core radius g/R

The clearance between the liner and the sediment g/R determines the core recovery ratio in “soft” sediments that swell against the liner during insertion. Consequently, there is a trade-off between preventing radial stress relaxation and plugging: smaller clearance g/R minimizes specimen lateral strain, but leads to higher lateral stress on the inner wall and wall friction. It can be shown that a 5cm diameter core can readily plug when trying to insert a 1m-long specimen into the liner.

6.4.2 Coring speed

Coring speed determines the unloading rate (i.e., stiffness loss) and affects the magnitude of transient pore pressure drop (i.e., possible dissociation and secondary hydrate formation). To minimize the transient pore pressure drop, the rate of coring R/v_{coring} should be lower than the rate of pore pressure dissipation R^2/c_v , where c_v is the pore water diffusion coefficient and R is the specimen radius (see also Figure 4c). Therefore, the coring velocity v_{coring} should be:

$$v_{coring} \ll c_v / R, \quad (6.4)$$

Hydrate-bearing sediments in Krishna-Godavari Basin have $c_v \approx 1.2 \times 10^{-4} \text{ m}^2/\text{s}$ [Yun *et al.*, 2010]. Consequently, the coring velocity should be $v_{coring} \leq 28 \text{ cm}/\text{min}$ to allow pore pressure dissipation in a 5cm-diameter core.

6.4.3 Pressure core technology

Pressure core technology allows the manipulation (e.g., coring, transferring, sub-sampling, and testing) of hydrate-bearing sediments while always maintaining in situ pressure and temperature conditions [Santamarina *et al.*, 2012; Schultheiss *et al.*, 2009] (see also Chapter 7). Pressure cores not only preserve hydrates but can also maintain gases, pore water, and host sediments as in situ [Trehu *et al.*, 2006].

Ideal sampling methods should maintain not only pressure and temperature, but also the effective stress throughout core manipulation and testing. Recompression tends to revert sampling disturbances except in brittle soft clays or loose sands [Bjerrum, 1973; Ladd and DeGroot, 2003; Landon, 2007]. Restored effective stress is critical for the measurement of stress-dependent properties such as stiffness and strength in all sediments, including hydrate-bearing sediments.

6.5. Conclusions

Sediment sampling causes unavoidable stress relaxation and strains that can alter the physical and mechanical properties of natural soils. Pressure and temperature changes during sampling can also cause dramatic disturbance to soils from deep hydrocarbon formations such as hydrate-bearing sediments. The main lessons learned from field expeditions including the Krishna-Godavari Basin study are:

Undrained unloading causes a marked transient pore pressure drop at the center of the specimen (i.e., poroelastic Mandel-Cryer effect). The coring speed should $v_{coring} \ll c_v/R$ to avoid undrained conditions. The coring speed for a 5cm-diameter core should not exceed $v_{coring} = 28$ cm/min in fine-grained sediments such as those in the Krishna-Godavari Basin ($c_v = 1.2 \times 10^{-4}$ m²/s).

Transient hydrate dissociation followed by secondary hydrate formation alters hydrate morphology and distribution. X-ray images show longitudinal hydrate lense formation in pressure cores recovered from Krishna-Godavari Basin due to poroelastic sampling artifacts.

Skeleton dilation due to unloading can trigger hydrate dissociation under tension, or hydrate-mineral debonding. This effect is prevented by slow coring/relaxation. The characteristic relaxation time is approximately 10 minutes for all specimens in this study.

Such a short period suggests inevitable stiffness loss in hydrate-bearing sediments after sampling because most relaxation effects will have finished even before the core reaches the drill rig.

The isochoric analysis of the variation in hydrate saturation due to P - T changes shows that the decrease in methane solubility caused by a $1K$ decrease in temperature is approximately offset by the change induced by a $20MPa$ pressure drop. This observation allows testing hydrate-bearing sediments at lower and safer pressures without significant changes in the hydrate mass as long as minor changes in temperature are accommodated.

To minimize sampling disturbances, samplers should have a sharp shoe cutting angle ($<5^\circ$), thin sampler wall thickness ($t/R < 8\%$), low wall friction, and adequate inside clearance relative to the core radius g/R . There is a trade-off between preventing radial stress relaxation and plugging: smaller clearance g/R minimizes specimen lateral strain but leads to higher lateral stress on the inner wall and wall friction. Hence clearance determines plugging and the core recovery ratio in “soft” sediments.

CHAPTER 7

PRESSURE CORE CHARACTERIZATION TOOLS FOR HYDRATE-BEARING SEDIMENTS

The author was primarily involved in the design of (1) the manipulator, (2) the saw cutter, and (3) the retrofitting of the effective stress chamber. This chapter includes all tools. The publication [*Santamarina et al.*, 2012] was co-authored with PhD students J.B. Jang and M. Terzariol at GeorgiaTech. The pressure core characterization tools were successfully deployed to study the natural hydrate-bearing sediments from the Nankai Trough (January 2013), as part of a collaborative research with AIST, JOGMEC, and US Geological Survey. Confidentiality requirements prevent reporting this study within this thesis.

7.1 Introduction

Natural gas hydrates form under high fluid pressure and low temperature, where biogenic or thermogenic gases are available. These requirements delimit the distribution of hydrate bearing sediments to sub-permafrost, deep lakes (theoretical water depth greater than ~390 m) or ocean sediments (theoretical water depth greater than ~320m). Typically, hydrates are found in deeper water columns due to thermal fluctuations, and diffusion near the sediment surface [*Xu and Ruppel*, 1999].

The clathrate or cage-like structure formed by water molecules hinders the repulsion between gas molecules and allows for high gas concentration: there is one molecule of methane every 5.75 molecules of water in CH₄-hydrate, compared to the solubility of methane in water which is in the order of 1-in-750. With such a high methane concentration, natural gas hydrates can become an energy resource and remains a potential source for a potent green-house gas.

Depressurization and/or heating across the phase boundary causes hydrate dissociation. The hydrate volume expands multiple times just to cross the phase boundary; for example there is a 1.3-times expansion under Blake Ridge pressure-temperature P-T conditions, and 4-times expansion in the shallower Hydrate Ridge formation. Rapid volume expansion brings the sediment to failure in low permeability formations, triggering wellbore and even large scale seafloor instabilities.

Dissociation, volume expansion and the ensuing sediment destructuration dramatically affect the ability to characterize hydrate-bearing sediments. Indeed, proper characterization requires coring, recovery, manipulation and testing under P-T conditions within the stability field. Pressure core technology has been advanced to address this need.

7.2 Pressure Core Technology: Overview

7.2.1 Coring and recovery

The development of pressure coring and recovery tools have involved research teams around the world, including initiatives such as the International Ocean Drilling Program and the European Union's Marine Science and Technology Program [*Amann et al.*, 1997; *Dickens et al.*, 2003; *Kvenvolden et al.*, 1983; *Pettigrew*, 1992; *Qin et al.*, 2005; *Schultheiss et al.*, 2009]. Push-piston (clay bearing sediments) and rotary coring (sands with high hydrate saturation) methods have been developed to gather several meter long pressure cores. The core slides inside a plastic liner during coring to facilitate its manipulation after recovery. The in situ fluid pressure is maintained by a ball valve that closes the barrel beyond the core-catcher; the ball valve seal is critical to reliable pressure core recovery. While temperature control is also possible (PTCS - [*Kawasaki et al.*, 2006]), analytical and field results show that the additional complexity of temperature

control is unnecessary as long as the barrel is rapidly cooled once it reaches the surface.

7.2.2 Manipulation

Earlier studies using pressure cores required fast depressurization and stabilization in liquid nitrogen before transferring the core into testing chambers. Such drastic changes in pressure and temperature can be prevented if all operations after recovery are conducted under P-T conditions within the stability field to prevent dissociation. Pressure core manipulation and transfer technology requires a longitudinal positioner/manipulator and ball valves to couple components at equalized pressures (Pressure Core Analysis and Transfer System PCATS - [Schultheiss *et al.*, 2006]).

7.2.3 Testing and characterization

Testing and characterization tools were developed in parallel to manipulation capabilities. Non-contact characterization tools are based on gamma density, X-rays and water-coupled P-waves (Pressure Multi-Sensor Core Logger - [Abegg *et al.*, 2008; Schultheiss *et al.*, 2006]). Contact/invasive tools allow for the assessment of stiffness using P-and S- wave velocities, strength, electrical resistivity profiles and internal core temperature (IPTC - [Yun *et al.*, 2006]); contact measurements require pre-drilling the plastic liner under pressure at the locations where measurements will be conducted. Subsampling capabilities have also been developed for biological studies under in situ P-T conditions (DeepIsoBug - [Parkes *et al.*, 2009]).

7.2.4 Current situation

Other characterization needs have gradually surfaced driven by the enhanced understanding of hydrate bearing sediments, the renewed interest in gas production and related engineering tasks, and the increased reliability of pressure core recovery. Pressure core characterization tools developed at the GeorgiaTech are described next.

7.3 GT Pressure Core Characterization Tools (PCCTs)

Our pressure core characterization system includes both core manipulation tools and characterization chambers. Tools have been selected to obtain complementary information relevant to science and engineering needs, with emphasis on the measurement of parameters used in hydro-thermo-mechanical analyses.

All tools are designed following key guidelines and objectives: simple and robust systems, portable components for fast deployment, modular design for maximum flexibility, standard dimensions and parts for economic construction and maintenance, rust-resistance for seawater environment (all devices are made of stainless steel 316), can hold 35 MPa fluid pressure and operate at 21 MPa, capable to impose effective stress when physical parameters are effective stress dependent, and safe for the monitoring of hydrate dissociation and gas production during controlled depressurization, heating or fluid exchange (such as with liquid CO₂). The modular design implies geometrically compatible chambers and components developed with the same design philosophy; in particular, any two tools/chambers can be readily coupled through an identical flange-clamp system.

7.3.1 Manipulator MAN

The manipulator is a longitudinal positioning system that is used to grab and move the core along the interconnected chambers and valves as needed, always under the required P-T conditions. Figure 7.1 shows the typical operation sequence used to retrieve a specimen from the storage chamber into the manipulator followed by displacing core into a generic test chamber. The geometric analysis of the operation shown in Figure 7.1 reveals that the length of the manipulator L_{man} (with its “temporary storage chamber”) is proportional to the length of the core L_{core} to be manipulated, $L_{\text{man}} \approx 3.5 \cdot L_{\text{core}}$. If an external positioning system is used, the rod must undertake the force due to the fluid pressure and the force required to displace the core; such a design is typically limited by

buckling even when an open ended hollow tube is selected. Our system is designed to handle $L_{\text{core}} = 1.2$ m long cores, uses an internal telescopic screw system (stroke = 2.6m) driven by an external stepper motor, and can position the specimen with sub-milimetric resolution. It is coupled to the 1.3m long temporary storage chamber by means of a dismountable flange-clamp connection. A see-through port is included to confirm the position of the manipulator at any time.

7.3.2 Sub-sampling CUT

The 1.2m long core can be cut into short specimens. Our cutting tool CUT houses either a linear or a ring-shaped saw-blade within a clamp-type chamber. The saw-based cutting ensures clean surfaces and minimizes specimen disturbance. The cutting tool CUT is mounted in series between the manipulator and any other test or storage chamber as needed (Figure 7.1e).

7.3.3 Instrumented Pressure Testing Chamber IPTC

The chamber was developed to measure P&S wave velocities, undrained strength, electrical conductivity, internal core temperature, and to sample fluids (Figure 7.2A - details in [Yun *et al.*, 2006]). This cylindrically-shaped chamber has two sets of four diametrically opposite port pairs. The first pair drills holes (ID = 8mm) in the plastic liner so that contact probes in successive ports can be pushed into the specimen. In characterization mode, the IPTC is coupled to the manipulator on one side and an extension chamber on the other end, and measurements can be conducted at any position along the core length. The eight access ports make the IPTC a versatile chamber for conducting well-monitored production studies in view of reservoir calibration models.

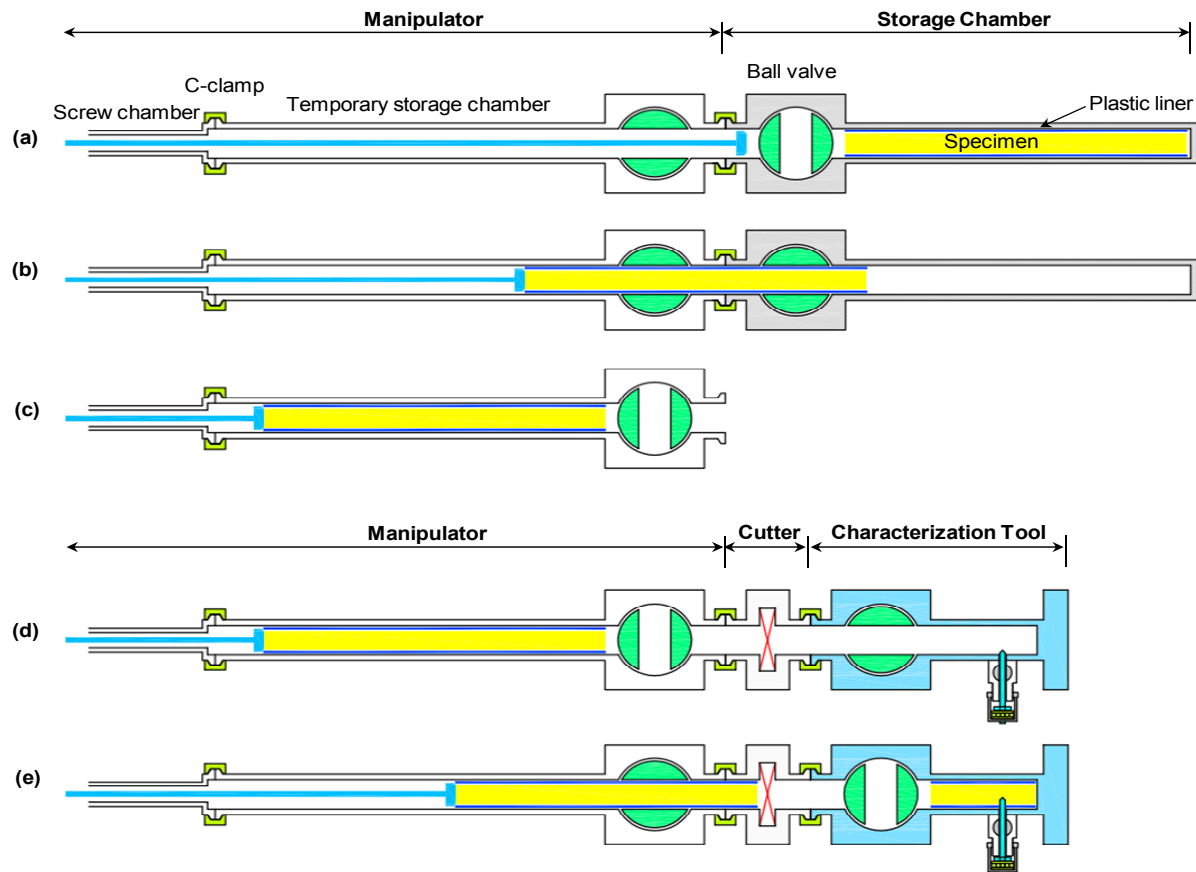


Figure 7.1. Pressure core manipulation. (a) The manipulator MAN couples with the storage chamber and fluid pressures are equalized at the target pressure p_0 before opening the ball valve. (b) The manipulator captures the core and transfers it into the temporary storage chamber. (c) Ball valves are closed and the depressurized storage chamber is separated. (d) The selected characterization tool is coupled to the manipulator and is pressurized to p_0 . (e) Ball valves are opened and the core is pushed into the characterization tool; stand-alone characterization tools may be detached after retrieving the rest of the core and closing valves. Note: the cutter tool CUT is shown in panes d&e; it is attached in series to cut core to any desired length to meet tool requirements (for stand-alone ESC, DSC, CDP, and Bio tools).

7.3.4 Effective Stress Chamber ESC

Pressure cores are recovered and stored at fluid pressure and temperature P-T conditions needed to preserve hydrate. However, physical properties such as stiffness and shear strength are a function of both hydrate saturation and effective stress (Note: the relative relevance of effective stress increases as hydrate saturation decreases).

The effective stress chamber ESC maintains P-T stability conditions and restores the effective stress σ' that the sediment sustains in situ (Figure 7.2b). It was designed and laboratory-tested at Georgia Tech in 2006 under Joint *Oceanographic* Institutions JOI sponsorship, and it was first deployed in the field by the Korean Institute of Geoscience & Mineral Resource KIGAM in collaboration with Geotek during the UBGH1 expedition [Lee *et al.*, 2009a].

The original design was based on a zero-lateral strain boundary condition. We have updated this chamber to accommodate a stress-controlled boundary condition using a jacket (Figure 7.3). The resulting triaxial stress configuration consists of σ_3' applied with the jacket and σ_1' applied by a piston that is advanced through the ball valve and acts directly onto the pressure core. The piston and the base pedestal house the sensors needed for the measurements of physical properties, including stiffness (wave velocities), thermal conductivity, and electrical resistivity.

A salient advantage of the flexible wall configuration is the ability to conduct precise fluid conductivity measurements by preventing the preferential flow along the sediment-steel boundaries in rigid-wall chambers. This chamber is particularly well suited to monitor production studies under in situ effective stress conditions, including the assessment of sediment volume change upon dissociation.

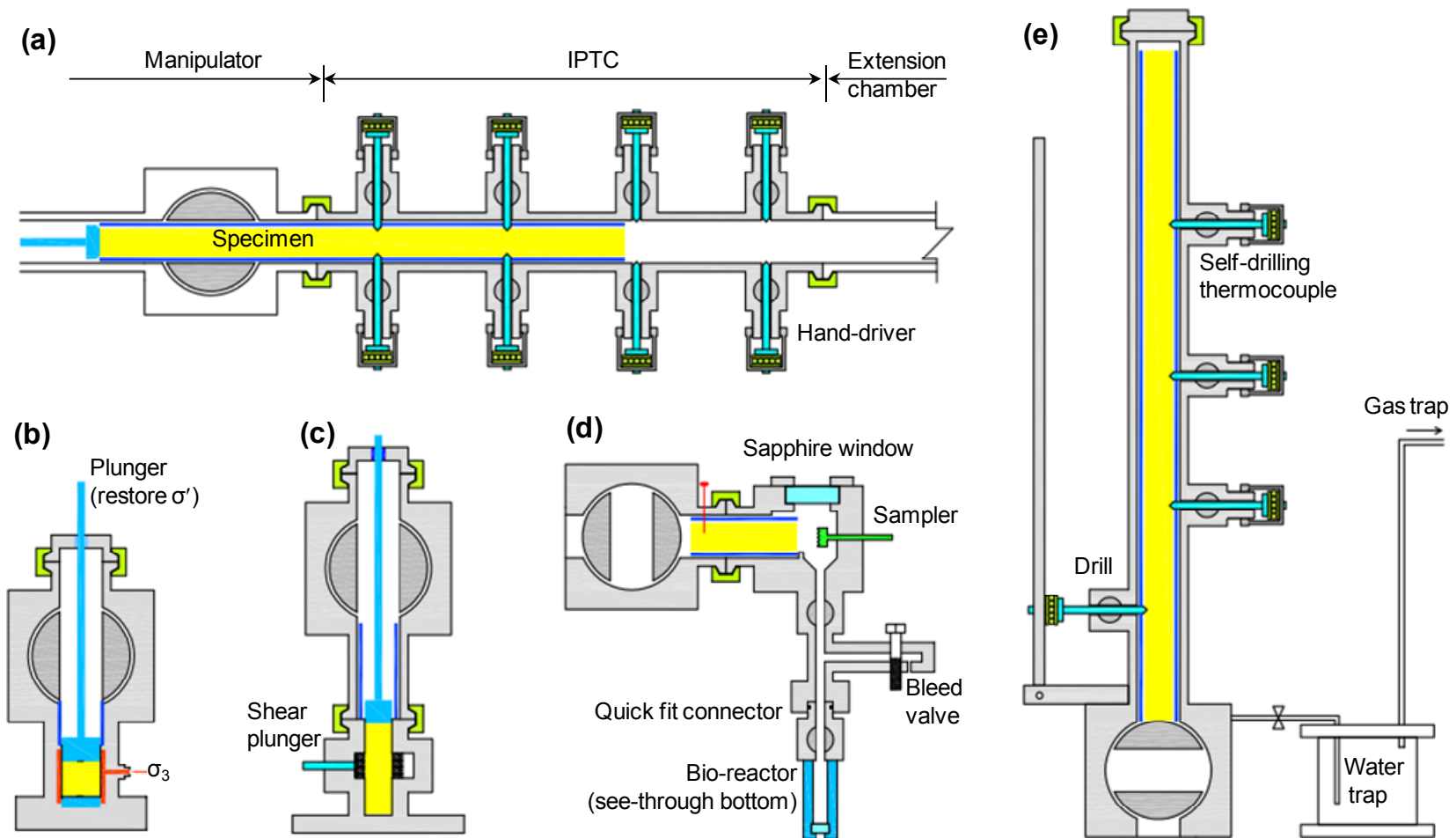


Figure 7.2. Schematic diagrams of characterization chambers. (a) IPTC instrumented pressure testing chamber with P-T control. (b) ESC effective stress chamber with σ' -P-T control. (c) DSC direct shear chamber with σ' - τ -P-T control. (d) CDP controlled depressurization chamber for sediment preservation and gas production. (e) BIO sampler for multiple bio-reactor chambers. Scale: the outside diameter of the large ball valve shown in all devices is OD = 220 mm.

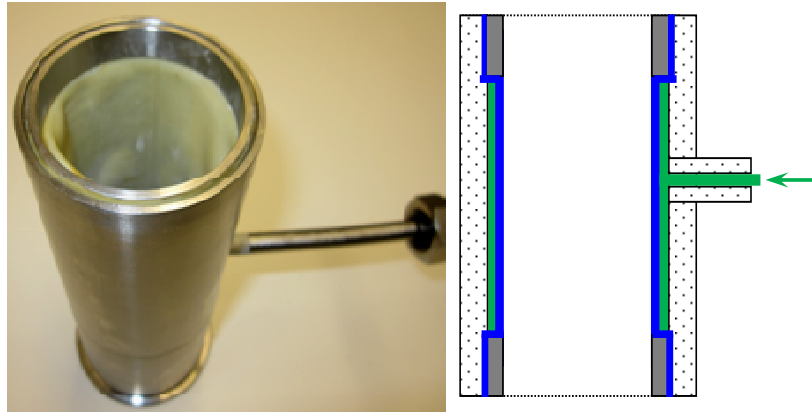


Figure 7.3. Flexible wall boundary condition. Lateral effective stress can be independently applied through a flexible wall membrane gadget (ID = 63.5mm, H = 150mm). This device allows the implementation of triaxial test conditions, and prevents preferential flow paths along the interface for fluid conductivity studies.

7.3.5 Direct Shear Chamber DSC

The shear strength of hydrate-bearing sediments under in situ pressure, temperature and effective stress conditions is a necessary parameter for constitutive models.

Two constraints guided the design of the DSC tool. First, the imperfect boundaries that result when cutting heterogeneous cores under pressure cause stress concentration during vertical loading; thus, we selected a “double direct shear” geometry to cut across the specimen away from end effects. Second, overcutting during coring leaves a gap and the core tends to tilt during shear; then, we adopted a double shear plane configuration to avoid bending action. Consequently, the direct shear chamber consists of a thick wall stainless steel ring that is pushed to shear the central third of the specimen (Figure 7.2c). The DSC includes the piston to restore the overburden stress (self-reacting vertical frame - similar to the ESC), a liner trap to capture the plastic liner before the specimen enters the shear chamber, and a small lateral built-in frame to push the side piston that displaces the ring (Figure 7.2c). The maximum shear displacement is $\delta_{\max} = 15\text{mm}$ so that both peak and residual shear strengths can be determined.

The test sequence includes: (1) shear under in situ vertical overburden stress and P-T conditions, (2) push the ring back to its original position, (3) monitor hydrate dissociation and gas production at constant vertical effective stress and zero-lateral strain boundary conditions, and (4) shear the specimen again to determine the hydrate-free residual shear strength. The complete data set provides strength and volume change data under in situ conditions that are necessary for model calibration, production design and stability analyses.

7.3.6 Sub-sampling Tool for Bio-Studies BIO

The study of bioactivity in deep-water sediments without incurring in depressurization cycles is crucial to the survival of some barophilic microorganisms. The BIO chamber is loaded with a core segment using the manipulator; afterwards, it is detached from the manipulator for all successive procedures (Figure 7.2d). Its operation involves (1) Nitrogen-liquid replacement, (2) core face cleaning and chamber fluid-based sterilization, (3) sub-sampling using a rotary sampling head, and (4) sample release into the bio-reactor that is pre-filled with nurturing solutions (volume = 10 cc). All operations can be observed through a sapphire window. Bio-reactors are readily replaced by closing a system of two ball valves and decoupling the quick connect fitting in between. This device allows the collection of a large number of specimens from a single core segment under in situ hydrostatic pressure.

7.3.7 Controlled Depressurization Chamber CDC

Successful pressure coring operations may produce more pressure cores than can be readily stored. In this case, recovered cores are selectively de-pressurized to conduct further studies under atmospheric pressure. The controlled depressurization chamber is designed to help preserve the core lithology and to gain valuable information during depressurization, with minimal demand on personnel resources. This stand-alone device

has a built-in drilling station to perforate the liner at selected locations in order to reduce the specimen longitudinal expansion. A pressure transducer and a thermocouple monitor the gas P&T conditions inside the chamber. In addition, three self-drilling thermocouples are built-in along the CDC; these are driven into the core to monitor the internal sediment temperature during depressurization. Finally, a 2L water trap and a 55L gas trap are attached in series to the needle valve that controls the rate of depressurization; these traps sit on scales to monitor produced water and gas (Figure 7.2e).

7.4 Measurement of Physical Properties: Sensors and Gadgets

Multiple sensing systems have been developed to characterize the sediment and to determine hydro, thermo, chemo, bio, and mechanical parameters within the chambers, under controlled pressure, temperature, and effective stress conditions as described above. Not all sensors or gadgets are available for all chambers, yet, their deployment in various devices support the comprehensive characterization of natural hydrate-bearing sediments under in situ pressure, temperature, and/or stress conditions, and permit detailed monitoring of gas production tests.

7.4.1 Tool position control

All contact instruments, sensors and drills are mounted on polished rods (diameter $d=7.9\text{mm}$) which are advanced into the specimen using externally controlled screw-based positioning systems to overcome the 1.7 kN force at the maximum working fluid pressure of 35 MPa (Figure 7.4). The hand-operated driver advances along the threaded guide while pushing the tool rod. The ball valve between the threaded guide and the chamber permits replacing tools under pressure (Figure 7.4).

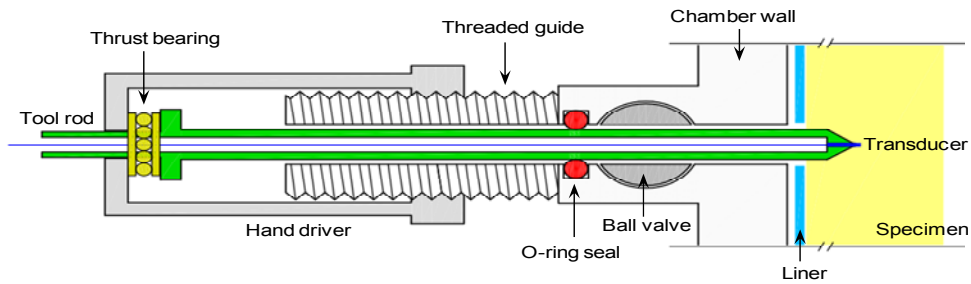


Figure 7.4. Tool Control. The displacement of sensors, subsampling tools and drills are controlled under pressure using a screw-based positioning system where the driver advances along the threaded guide while pushing the tool rod (shown in green). Transducers at the tip of the rod are wired through the central hole in the tool rod.

7.4.2 Sensors

Transducers are mounted at the tip of tool rods and wired through the central bore. Available instruments are shown in Figure 7.5. Small-strain wave velocity measurements employ bender elements for S-waves and pinducers for P-waves (Figures 5a&b – peripheral electronics and test procedures as described in [Lee and Santamarina, 2005a; b]).

While large-strain strength data can be gathered using the direct shear chamber (DSC – Figure 7.2c), we have developed a strength-penetration probe as well (Figure 7.5c). This device determines the sediment strength using a cone-shaped stud equipped with a full-bridge strain gauge inside. The measured tip resistance during probe penetration reflects the sediment undrained shear strength (details in [Yun *et al.*, 2006]).

Fluid conductivity can be determined using the flexible wall system built within the effective stress chamber ESC (Figure 7.2b & 3), and inferred using the fluid sampling tool (Figure 7.5d). This is a self-drilling drainage port with a pressure or volume control flow condition to drive the interstitial fluids out of hydrate-bearing sediment. The pressure difference can be selected to preserve hydrates within stability conditions.

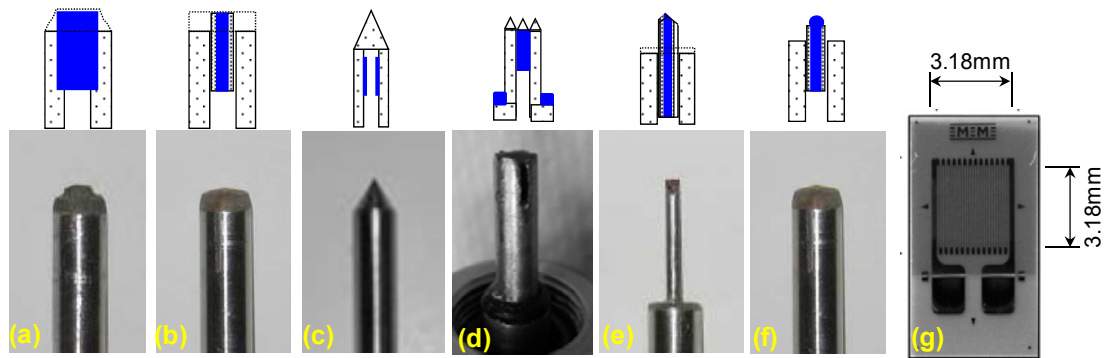


Figure 7.5. Measurement tools and sensors. (a) Bender elements for *S*-wave generation and detection. (b) Piezocrystals for *P*-waves. (c) Penetrometer for strength measurement. (d) Pore fluid sampler. (e) Electrical needle probe for resistivity profiling. (f) Thermocouple instrumented tip. (g) Strain gauge for thermal conductivity determination (TPS – NETL; [Rosenbaum *et al.*, 2007]).

Electrical resistivity is measured using an electrical needle probe that is gradually inserted into the specimen to determine a radial resistivity profile with millimeter-scale spatial resolution (Figure 7.5e – details and measurement procedure in [Cho *et al.*, 2004]). We have also developed a multiple electrode system at the base of the effective stress cell that allows us to conduct a surface-based electrical resistivity tomography within a specimen.

The thermal probe consists of a thermocouple deployed at the tip of a tool rod. When pushed into the sediment, the thermal probe monitors the temperature inside the core (Figure 7.5f). The self-drilling version of this probe, deployed in the controlled depressurization chamber CDC, places the thermocouple inside a hollow drill tip at the end of a tool rod. Internal temperature measurements can be used to monitor phase transitions during controlled gas production studies and to determine thermal conductivity (by inversion for given imposed boundary conditions). In addition, the TPS sensor for thermal conductivity measurements developed at NETL (Figure 7.5g,[Rosenbaum *et al.*, 2007]) can be installed at the tip of tools or on the pedestal of the effective stress and direct shear chambers.

7.5 Monitoring Dissociation – Gas production

All PCCTs chambers allow core-scale gas production tests by either depressurization, heating, or chemical injection (e.g., inhibitors or carbon dioxide). Monitoring data include pressure, temperature, produced gas and water, stiffness (seismic wave velocities), fluid conductivity, and electrical resistivity. Figure 7.6 shows examples of data gathered during the depressurization of natural hydrate-bearing sediments.

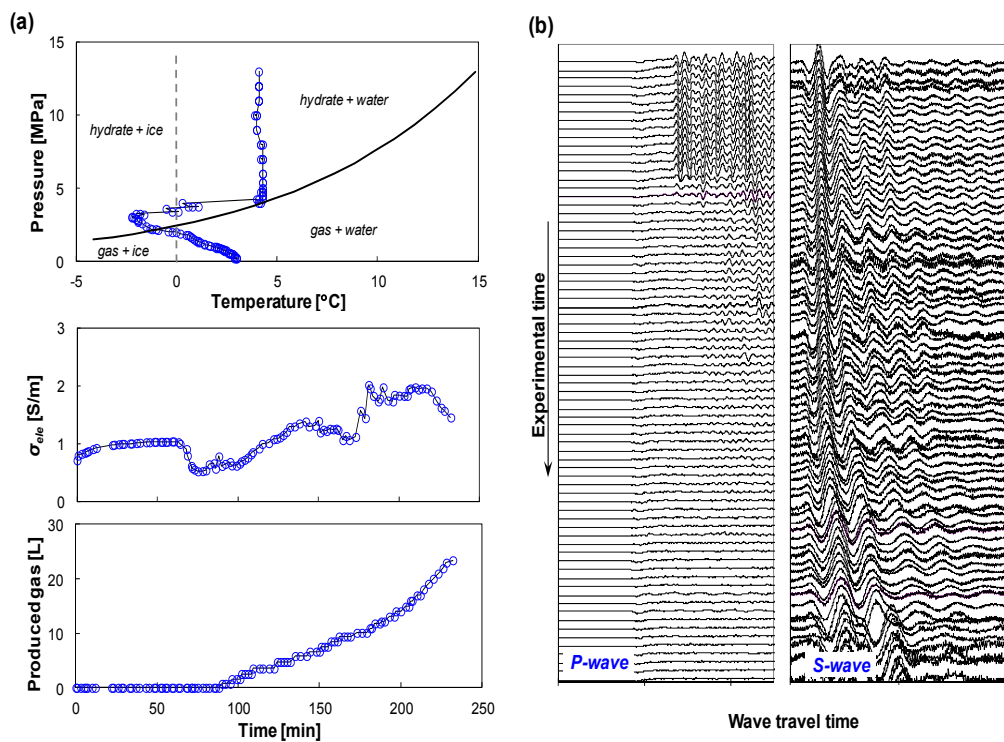


Figure 7.6. Monitored gas production tests using IPTC: (a) Evolutions of pressure, temperature, electrical resistivity, and produced gas (Krishna-Godavari Basin, [Yun *et al.*, 2010]); (b) Typical wave signatures during gas production: P-wave signatures eventually fade out after gas production; S-waves detect the evolution of the skeleton shear stiffness during hydrate dissociation and gas production (Ulleung Basin, [Yun *et al.*, 2011]).

7.6 Discussion: Comprehensive Characterization Approach

Pressure coring, recovery, and testing prevent hydrate dissociation and its catastrophic consequences on sediment structure. However, inherent sampling effects

caused by unavoidable changes in effective stress remain. These changes are quite prominent and include: stress relaxation from lithostatic confinement to virtually no effective stress, the potential for internal fluid pressure drop and local dissociation even when chamber P-T conditions are within the stability field (i.e., a form of poro-elastic Mandel-Cryer effect coupled with phase transition), side friction along the liner, skeleton expansion and the potential for stain-induced decementation.

Clearly, in-situ testing can play an important role in the characterization of hydrate bearing sediments. However, in situ tests face their own technical challenges and interpretation difficulties, including the effect of tool insertion on measured properties.

Based on these observations and field experiences (Gulf of Mexico, Krishna-Godavari Basin, Ullung Basin, and Mount Elbert), the comprehensive characterization of hydrate-bearing sediments should include: (1) detailed analysis of available logging data, (2) pressure core characterization and monitored de-pressurization, (3) index properties (with emphasis on grain size distribution and fines content, specific surface, SEM microphotographs, mineralogy and plasticity, pH and pore fluid ionic concentration), and (4) laboratory tests on reconstituted specimens with synthetic hydrate saturation to determine the behavior of sediments as a function of effective stress and hydrate saturation (including: stiffness, strength, and hydraulic conductivity).

Index properties -analyzed within the framework of accumulated field and laboratory data- provide exceptional information related to hydrate pore habit and morphology, potential sediment properties and production-related information including the possibility of fines migration (Refer to [Waite *et al.*, 2009]for a comprehensive review of hydrate-free sediment properties).

The reconstitution of hydrate bearing sediments is hindered by inherent difficulties in forming methane hydrate from dissolved phase methane. Tetrahydrofuran THF presents important advantages as a proxy hydrate former [Lee, 2007]. First, its complete miscibility in water enables accurate hydrate saturation control and fast hydrate

formation from dissolved phase (i.e., no preferential formation at interparticle contacts). Second, THF hydrate forms at atmospheric pressure and standard geotechnical devices can be used to characterize hydrate bearing sediments.

7.7 Conclusions

Pressure core technology is needed for the proper evaluation of natural hydrate bearing sediments.

The set of pressure core characterization tools PCCTs described in this review allow the manipulation, sub-sampling, and extensive assessment of natural gas hydrate bearing sediments under in situ pressure, temperature, and effective stress conditions.

In addition to pressure core testing, comprehensive characterization programs should include sediment index properties analyzed within the framework of available data for natural hydrate bearing sediments, and tests with remolded specimens with synthetic hydrate.

Pressure core technology can also be deployed to study other gas rich hydrocarbon formations such as deep sea sediments, coal bed methane and gas shales.

CHAPTER 8

SAMPLING EFFECTS ON THE STIFFNESS OF FROZEN SANDS

8.1 Introduction

Most natural soils have experienced some degree of cementation due to diagenesis, salt precipitation, bacterial activity, or ice/hydrate formation. The effect of cementation on soil behavior depends on (i) the amount, type, and pore habit of the cementing agent; (ii) the grain shape, size distribution, and packing density of the host sediment; and (iii) the stress state and stress-cementation histories [*Clough et al.*, 1981; *Consoli et al.*, 2009; *Consoli et al.*, 2010; *Fernandez and Santamarina*, 2001; *Ismail et al.*, 2002; *Khan et al.*, 2006; *Lee et al.*, 2009b; *Rinaldi and Santamarina*, 2008].

Cementation produces a marked increase in stiffness, affects the threshold strain, promotes a dilative tendency upon shear, increases drained and undrained strengths, decreases permeability, and hinders liquefaction [*Acar and El-Tahir*, 1986; *Baig and Picornell*, 1997; *Baxter et al.*, 2011; *DeJong et al.*, 2006; *Delude*, 1997; *Dutton*, 1992; *Lee et al.*, 2009b; *Olague Caballero*, 2008; *Pestana and Salvati*, 2006; *Wang and Leung*, 2008; *Yun and Santamarina*, 2005].

The small-strain stiffness of freshly remolded soils is controlled by the stress state. Interparticle cementation increases the soil skeleton stiffness by increasing the interparticle contact area and enhancing coordination. Sampling-induced strains readily affect cementation. Consequently, post sampling stiffness measurements often show significant differences from field measurements [*Rinaldi and Santamarina*, 2008; *Stokoe and Santamarina*, 2000; *Tatsuoka and Shibuya*, 1991]. Such differences reflect unavoidable sampling effects due to changes in stress and resulting strains during sampling and post-sampling creep.

Limited data are available on sampling effects on the stiffness of frozen ground and hydrate-bearing sediments [Waite *et al.*, 2009]. This study explores the stiffness evolution of frozen sands by monitoring the *P*-wave velocity during loading, freezing, unloading, creep, and ice melting processes. Results are also relevant to sampling and aging effects in other cemented soils such as hydrate-bearing sediments.

8.2. Experimental study

Unsaturated fine sands are subjected to freezing and thawing, and stress under zero-lateral strain boundary conditions in an oedometer cell. The experimental device, materials, and detailed procedures are described next.

8.2.1 Experimental device

A spring-loaded (spring stiffness $K = 306\text{N/mm}$) self-reactive oedometer cell (inside diameter $d_{in} = 69.85\text{mm}$, height $H = 76.2\text{mm}$) is used to impose a relatively constant load under zero-lateral strain boundary conditions during loading, freezing, unloading, creep, and melting steps. Piezopads are mounted on the top and bottom caps of the oedometer cell to measure the vertically propagating *P*-wave velocity across the specimen. A K-type thermocouple (precision of 0.1°C) is placed at the center of the specimen to monitor temperature. Figure 8.1 shows a schematic configuration of the device and sensors.

8.2.2 Specimen preparation

A fine grained, uniform, quartzitic sand is used for this study (Ottawa F110, specific gravity $G_s = 2.65$, mean grain size $D_{50} = 0.12\text{mm}$, maximum and minimum void ratios $e_{max} = 0.848$ and $e_{min} = 0.535$, coefficient of uniformity $C_u = 1.7$, coefficient of curvature $C_c = 0.99$, roundness $R = 0.7$, and sphericity $S = 0.7$). The sand is homogeneously mixed with a pre-determined amount of water to attain a target water

content ($w\% = 2, 5, 10, \text{ and } 20\%$). Finally, the homogeneously mixed, partially saturated sand is scooped into the oedometer cell and tamped uniformly.

Given the small grain size, water forms menisci at interparticle contacts and remains in position by capillarity. Upon freezing, the resulting ice saturation $S_{ice} = V_{ice}/V_{void}$ is estimated to be $S_{ice} = 0.06, 0.15, 0.3, \text{ and } 0.52$ for the different water saturations.

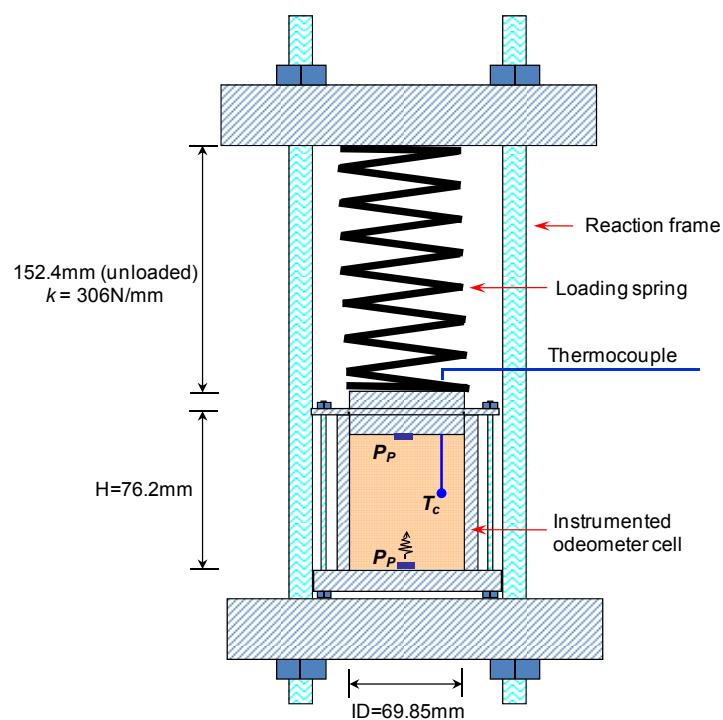


Figure 8.1 Experimental configuration: spring-loaded self-reactive oedometer cell equipped with piezopads (P_P) and a thermocouple (T_C).

8.2.3 Experimental procedure

Each specimen is subjected to five successive stress-temperature stages: (1) gradual loading from $\sigma_v' = 1 \text{ kPa}$ to 600 kPa at constant room temperature $T = 20^\circ\text{C}$; (2) cooling from 20°C to -10°C to trigger ice formation at constant vertical stress $\sigma_v = 600 \text{ kPa}$; (3) vertical stress relaxation from 600 kPa down to 1 kPa at constant temperature $T = -10^\circ\text{C}$; (4) creep at constant vertical stress $\sigma_v = 1 \text{ kPa}$ and temperature $T = -10^\circ\text{C}$; and

finally (5) heating from $T = -10^{\circ}\text{C}$ to room temperature $T = 20^{\circ}\text{C}$ at constant vertical stress $\sigma_v = 1\text{kPa}$. P -wave signals are recorded through all stages.

8.2.4 P -wave signatures and data reduction

A selection of P -wave signatures gathered during the various experimental stages is presented in Figure 8.2.

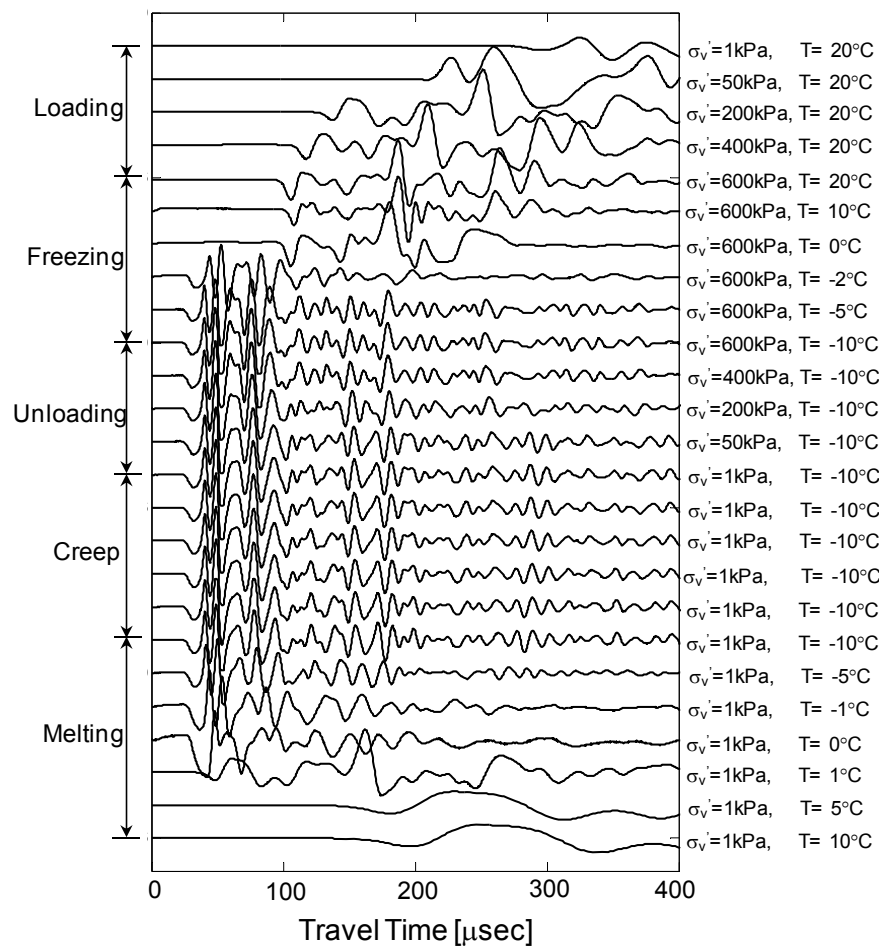


Figure 8.2 Cascade of selected P -wave signatures gathered during various experimental stages (Specimen: initial water content $w\%=5$).

Time shifts in first arrivals during loading, freezing, and thawing stages can be easily distinguished. However, changes in signatures during unloading and subsequent creep are almost indiscernible. The first arrival reflects the fastest path between source and receiver; later coda wave arrivals correspond to longer paths after multiple boundary reflections and internal scattering. Therefore, time shifts between the codas of two consecutive signals are longer and easier to detect than time shifts between first arrivals (as illustrated in Figure 8.3). We use coda wave analysis to determine minute changes in P-wave velocity between two successive signals. Theoretical analyses and details on the use of coda wave analysis can be found in [Dai *et al.*, 2013; Snieder *et al.*, 2002; Wuttke *et al.*, 2012].

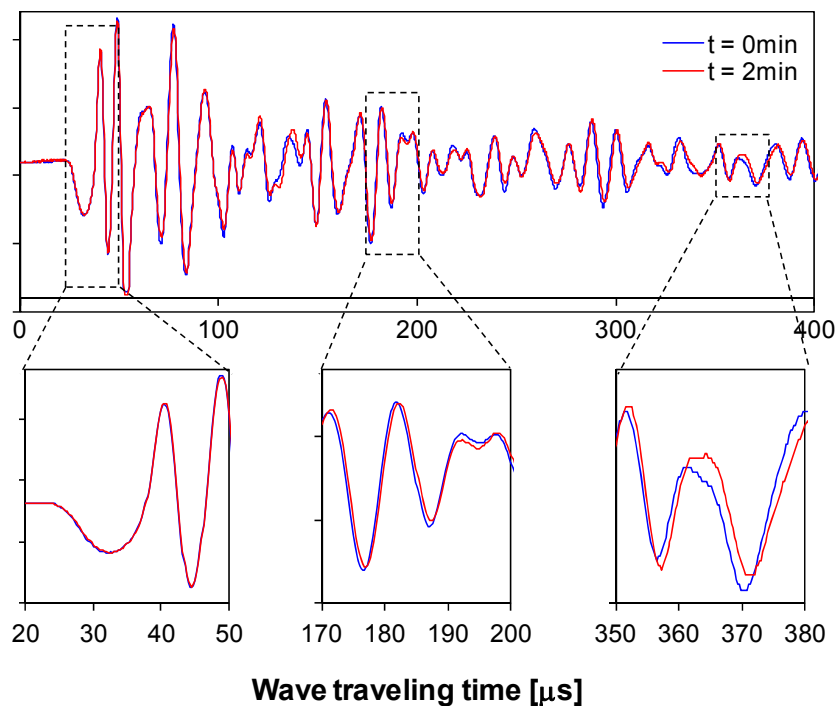


Figure 8.3 Coda wave analysis. Illustration using two consecutive P-wave signatures gathered for the specimen with $S_{ice}=0.06$ during the creep stage. While there is no measurable difference in first arrivals, wave codas can be used to detect minute velocity changes.

8.3. Experimental results

8.3.1 *P*-wave velocity evolution during loading (unfrozen, room temperature)

P-wave velocities during loading at constant room temperature ($T = 20^{\circ}\text{C}$) are very similar for all specimens (Figure 8.4a): the *P*-wave velocity increases with the applied vertical stress following a power equation (i.e., a linear trend in log-log scale), as characterized by Hertzian contact model. Deviation from linearity at low stresses ($<10\text{kPa}$) reflects the role of capillarity on the skeleton stiffness; in particular, the *P*-wave velocity at very low stress (1kPa) slightly increases with decreasing water content (see also [Cho and Santamarina, 2001]).

8.3.2 *P*-wave velocity evolution during freezing (constant vertical stress)

The evolution of *P*-wave velocities during freezing at constant vertical effective stress $\sigma_v = 600\text{kPa}$ are presented in Figure 8.4b. Decisive changes in velocity occur when the temperature measured at the center of specimen approaches the freezing point ($T = 0^{\circ}\text{C}$). The maximum *P*-wave velocity is achieved when all free water freezes and the final velocity is proportional to ice content S_{ice} , i.e., the effect of ice cementation on soil stiffness.

8.3.3 *P*-wave velocity evolution during unloading (frozen, constant temperature)

The applied vertical stress is then reduced from $\sigma_v = 600\text{kPa}$ to 1kPa at constant temperature $T = -10^{\circ}\text{C}$ to study stiffness loss during unloading and relaxation in frozen soils. Unloading is implemented in four stages, holding each load for 10 minutes. No specimen experiences more than 10% velocity loss during unloading, implying strong cementation effects. In particular, specimens with higher ice saturation exhibit a lower stiffness loss. Velocities during unloading are summarized in Figure 8.4c.

8.3.4 Creep of ice-cemented sands after unloading (frozen, constant stress and temperature)

P -wave velocities are monitored for 2 hours after unloading to a nominal stress $\sigma_v = 1\text{kPa}$ and at constant temperature $T = -10^\circ\text{C}$. Measured P -wave velocities show creep in all frozen sands in the form of an exponential decay with time (Figure 8.5b).

8.3.5 P -wave velocity evolution during thawing (constant stress)

Specimens are allowed to warm up to room temperature $T = 20^\circ\text{C}$ at the end of the test. The velocity evolution during thawing, Figure 8.4d, is opposite to the evolution during freezing. Most of the loss in stiffness occurs when the temperature measured at the center of the specimen approaches the melting point $T = 0^\circ\text{C}$ (Note: similar stiffness-temperature responses can also be found in [Andersland and Ladanyi, 2004]). The final velocity at room temperature $T = 20^\circ\text{C}$ and $\sigma_v = 1\text{kPa}$ is lower than the velocity before freezing at $\sigma_v = 600\text{kPa}$, primarily due to differences in confining stress.

8.4. Analyses and discussion

8.4.1 Velocity creep of frozen sands

The decrease in P -wave velocity with time V_t in the frozen sand specimens after unloading follows an exponential trend (fitted to the data in Figure 8.5a),

$$V_t = V_0 - \Delta V(1 - e^{-\alpha t}) \quad (8.1)$$

where V_0 is the initial velocity before unloading, ΔV is the velocity loss at infinite time, and the α -constant captures the characteristic time $1/\alpha$ for velocity decrease. The characteristic time for velocity loss during creep is about 10 minutes for all specimens in this study. This short period suggests that sampling effects are inevitable as specimens cannot be recovered and reloaded fast enough in most onshore and offshore cases. The

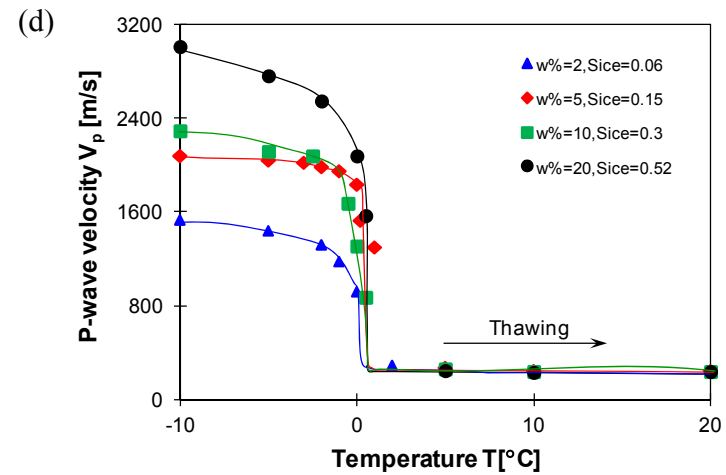
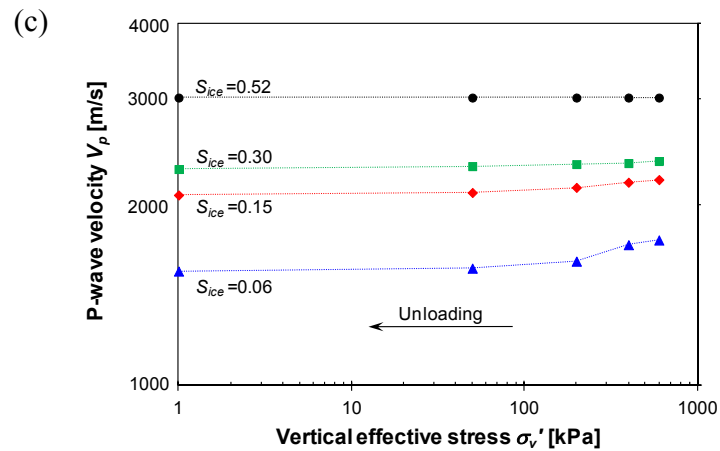
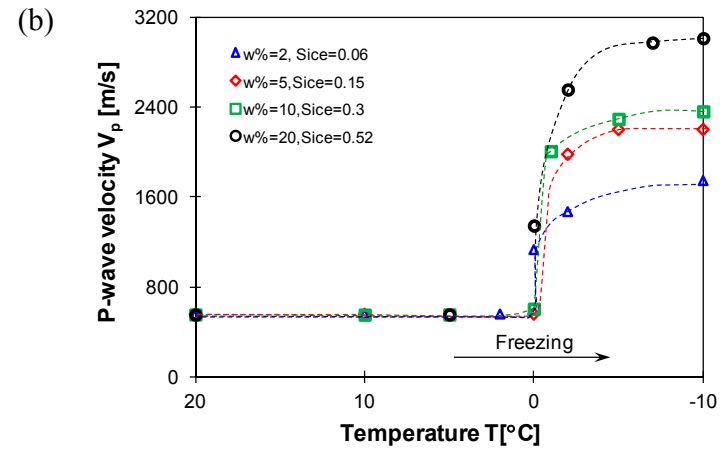
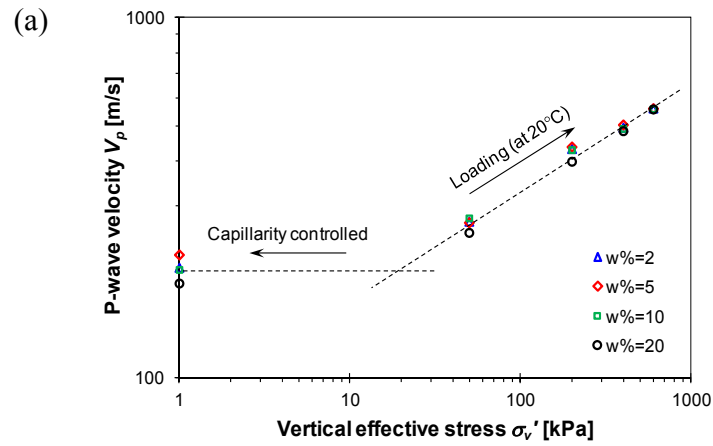


Figure 8.4 Evolution of the P -wave velocity during each experimental stage: (a) loading (at temperature $T=20^\circ\text{C}$); (b) freezing (at effective stress $\sigma_v' = 600\text{ kPa}$); (c) unloading (at temperature $T=-10^\circ\text{C}$); (d) thawing (at effective stress $\sigma_v' = 1\text{ kPa}$).

total velocity loss ΔV due unloading is relative small, about 1% of the initial velocity V_0 for all tested specimens regardless of ice saturation.

8.4.2 Creep of frozen sands following unloading

Quartzitic grains tend to rebound during unloading to $\sigma_v = 1\text{kPa}$, causing tensile strain in the ice mass that formed while the sand skeleton was subjected to high confining stress $\sigma_v = 600\text{kPa}$. However, grain rebound is hindered by the ice tensile strength and creep rate. The granular skeleton tends to stretch during unloading and causes tension in bounded ice. The mineral-ice-mineral system can break either (i) by ice tensile failure ($\sim 2.3\text{MPa}$, [Petrovic, 2003]) when the mineral is hydrophilic, or (ii) by ice-mineral debonding when the mineral is hydrophobic [Jung and Santamarina, 2011]. A lumped parameter model of the frozen soil mass involves an elastic model for the soil skeleton (k_{sk}) and a visco-elastic-plastic model for ice ($k_{ice}-\eta-\sigma_s$), as shown in Figure 8.5b. The external force across a section A with porosity n and ice saturation S_{ice} is taken by both the soil skeleton and the ice component:

$$\begin{aligned}\sigma_{ext} A &= \sigma_{sk(t)} A + \sigma_{ice(t)} n S_{ice} A \\ \sigma_{ice(t)} &= \sigma_{ice}^0 \left[1 - \exp\left(-\frac{k_{ice}}{\eta} t\right) \right] = \sigma_{ice}^0 [1 - \exp(-\alpha t)]\end{aligned}\quad (8.2)$$

where, $\sigma_{sk(t)}$ and $\sigma_{ice(t)}$ are stresses on the soil skeleton and the ice component. The combination of the equilibrium Equation 8.2 with deformation compatibility results in time-dependent deformation:

$$\varepsilon_{ice(t)} = \varepsilon_{sk(t)} = \frac{\sigma_{ext}}{n S_{ice} k_{ice} + k_{sk} [1 - \exp(-\alpha t)]} \quad (8.3)$$

The behavior of this system is stress-rate dependent: unloading frozen sands faster than the ice creep rate ($\dot{\varepsilon}_{ice} \gg \sigma_{ice} / \eta$) can cause ice tensile failure or debonding; on the other hand, slow unloading (e.g., $\dot{\varepsilon}_{ice} \ll \sigma_{ice} / \eta$) allows ice creep and the cemented fabric may be preserved.

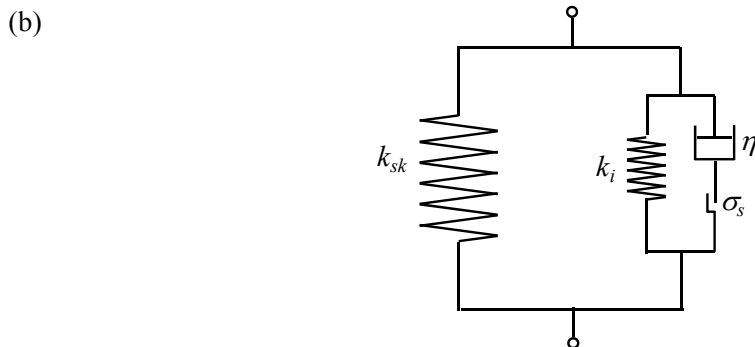
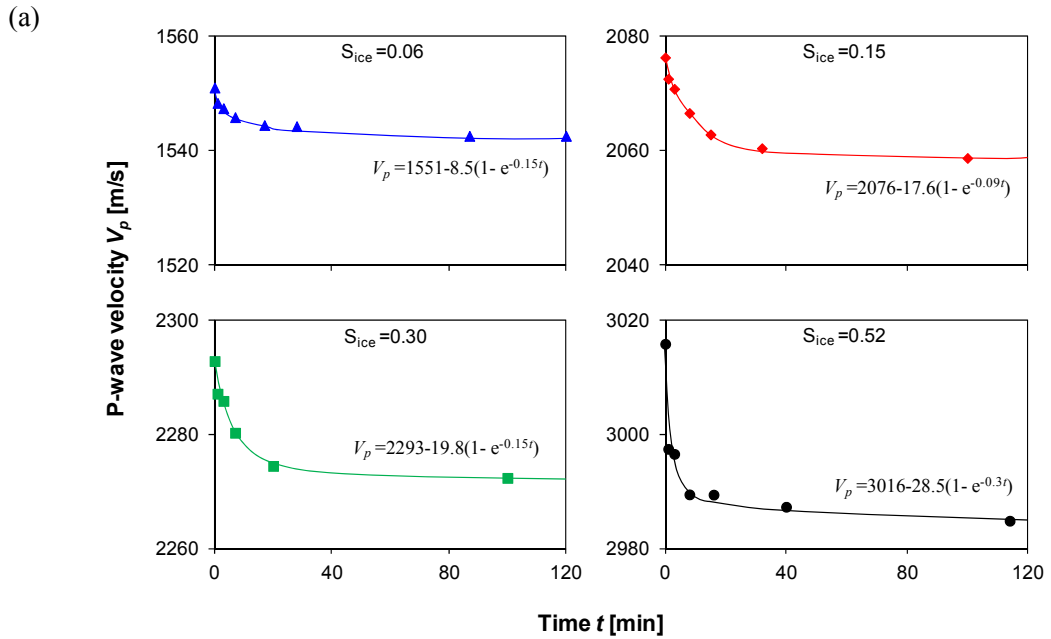


Figure 8.5 Evolution of P-wave velocity during creep. (a) P-wave velocities for specimens with different ice saturation during creep following unloading from $\sigma_v = 50\text{kPa}$ to $\sigma_v = 1\text{kPa}$ at constant temperature $T = -10^\circ\text{C}$ (Dots represent experimental results and lines are the fitted model). (b) Viscoelastoplastic model for frozen soils.

8.4.3 Unloading and reloading rate

Supplementary experiments are conducted to study the effect of unloading/reloading rate on stiffness changes in frozen sands. Frozen specimens with two ice saturations (i.e., $S_{ice} = 0.05$ and 0.30) are kept under constant stress $\sigma_v = 600\text{kPa}$ and temperature $T = -10^\circ\text{C}$ for 24 hours before unloading. Identical specimens are subjected

to both fast (2 minutes) and slow (1 hour) unloading from 600kPa down to 1kPa, and allowed to creep for 2 hours. Then, the specimens are reloaded back to 600kPa within 2 minutes. *P*-wave velocities are monitored continuously during all experimental stages (Figure 8.6).

Fast unloading causes a higher velocity loss than slow unloading as predicted by the model above. Specimens that experienced fast unloading cannot fully recover their initial stiffness after reloading (at least within the first two hours after reloading); on the other hand, specimens subjected to slow unloading recover most of their initial stiffness (Figure 8.6b). Clearly, fast unloading causes either tensile failure or debonding of the cementing ice.

8.4.4 Effects of stress-cementation history on cemented soils

The stress-cementation history has a minor effect on specimen stiffness: loading-before-cementation results in slightly higher stiffness than cementation-before-loading [Fernandez and Santamarina, 2001; Rinaldi and Santamarina, 2008]. However, the behavior of these two cementation histories is distinctly different during unloading.

The stress is undertaken by the soil skeleton when loaded-before-cementation; therefore, the cementing agent experiences tension and may break/debond during unloading (Figure 8.7), and restoring the stress state to its original level cannot fully recover the specimen stiffness. Conversely, both the skeleton and the cement are stressed together when the sediment is cemented-before-loading, and subsequent loading or unloading has minimal effect on cementation. This situation changes when the cement creeps, as in the case of frozen soil: ice creeps and transfers its stress to the granular skeleton. Then, the response to stress changes, and even melting, depends on relative rates.

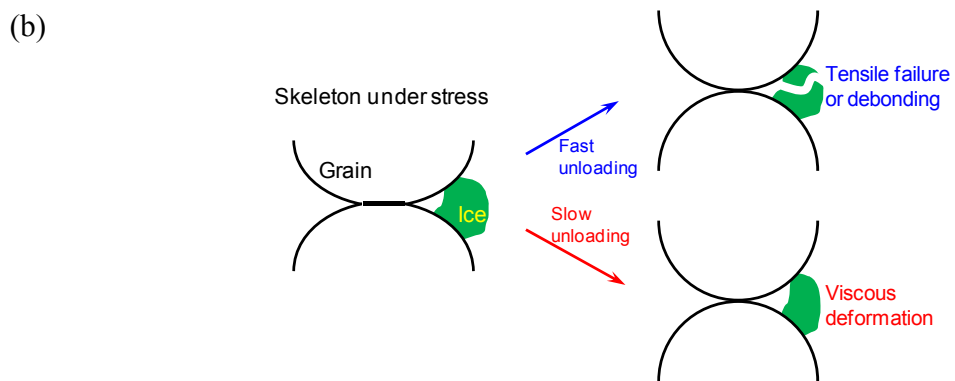
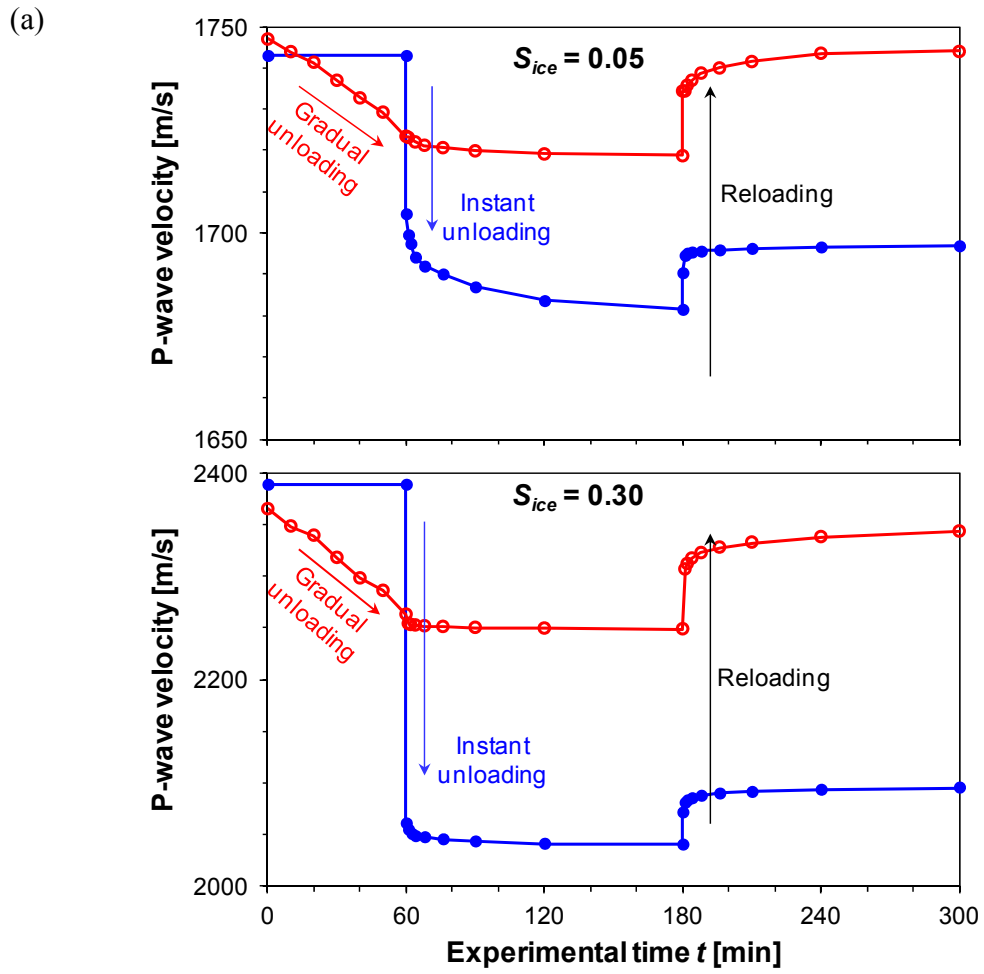


Figure 8.6. The effect of loading and unloading rate on the stiffness of partially frozen sands. (a) Evolution of P-wave velocities for sands with different ice saturation S_{ice} during unloading (from $\sigma_v = 600\text{kPa}$ to $\sigma_v = 1\text{kPa}$) and reloading (from $\sigma_v = 1\text{kPa}$ to $\sigma_v = 600\text{kPa}$). (b) Schematic illustration of the effect of unloading rate on ice cementation.

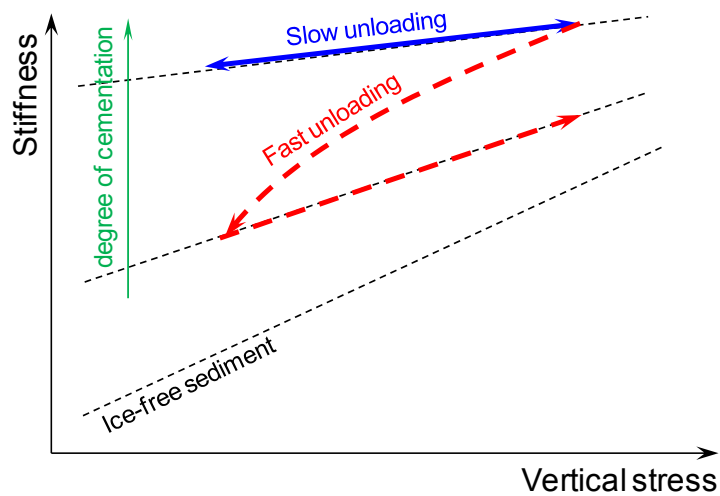


Figure 8.7 The effect of stress change rate on the stiffness of partially frozen soils during loading and unloading.

8.4.5 Extension to natural systems

Cemented soils include frozen soils, hydrate bearing sediments, diagenetically cemented, salt cemented, and bio cemented soils. The stiffness-stress response for all these soils follow a similar trend: starting from cementation governed stiffness at low stress, and gradually changing to stress dependent stiffness at high stress. Cementation can play a dominant role on stiffness even for low cement concentration in most practical cases. This is particularly true when cement formation/precipitation takes place at interparticle contacts such as the freezing of unsaturated soils in this study.

Inherent stress changes during sampling may induce de-cementation and stiffness loss. Cement content, strength, unload-vs.-creep rate will determine the extent of stiffness loss. Cementation loss within the formation, such as ice melting in permafrost, dissociation in hydrate-bearing sediments, or carbonate dissolution due to ground water acidification, may trigger instability in sediments that experienced cementation-before-loading. For instance, hydrates at Mount Elbert (Alaska North Slope) formed before the

completion of sedimentation and hindered subsequent sediment consolidation [Dai *et al.*, 2011]. Hydrate dissociation during gas production will trigger large volume changes in these unconsolidated sediments. High compressibility is expected in other common systems such as reactive fly ash.

8.5. Conclusions

The sampling of cemented soils can cause pronounced disturbance due to stress relaxation, decementation, and post-sampling creep relaxation. These effects were investigated in this study by monitoring the P-wave velocity evolution of frozen soils subjected to various stress and temperature histories. Salient conclusions follow.

The P-wave velocity of frozen soils decreases exponentially with time after unloading. The final velocity loss is about 1% of its initial velocity in all tested cases. The characteristic time for velocity loss during creep is approximately 10 minutes for all specimens with different ice contents. This short period suggests that sampling effects are inevitable as specimens cannot be recovered and reloaded fast enough in most onshore and offshore cases.

The mechanical behavior of frozen sands is stress-rate dependent: unloading faster than ice creep rate can cause ice tensile failure or debonding; slow unloading allows ice creep and the cemented fabric may be preserved. After restoring the initial stress state, specimens that experienced fast unloading cannot fully recover their initial stiffness (in short laboratory times); while specimens subjected to slow unloading recover most of their initial stiffness.

The stiffness of cemented soils is dominated by cementation at low stress, and by confinement at high stress. Cementation can play a dominant role on stiffness in most practical cases, particularly when cement forms at interparticle contacts.

The stiffness of cemented soils is affected by the content, strength, and pore habit

of the cementing agent, the rate of stress change, creep rate, and cementation-loading history.

Results from this study are relevant to sampling disturbance in frozen soils, as well as other natural systems, such as hydrate-bearing sediments, desiccated soils with salt precipitation, and reactive fly ash among others.

CHAPTER 9

PORE FLUID SAMPLING FROM HYDRATE-BEARING SEDIMENTS

9.1 Introduction

The pore fluid in hydrate-bearing sediments can provide critical information about the physical, chemical, and biological conditions within the sediment [Ussler III and Paull, 2001], diagenesis and hydrate stability [Dickens *et al.*, 2007; Lapham *et al.*, 2008; Trehu *et al.*, 2004], and even paleoclimate [Kennett *et al.*, 2000].

Pore fluid sampling from hydrate-bearing sediments is experimentally challenged due to contamination and the need to preserve the hydrate within the stability field at all times: gas hydrate formation excludes dissolved ions, thus hydrate dissociation “freshens” the pore fluid and alters geochemical signatures in the pore fluid. In addition to hydrate dissociation, depressurization changes the solubility of many species, may induce degassing, mineral precipitation, changes in pore water alkalinity and dissolved inorganic carbon DIC concentrations [De Lange *et al.*, 1992; Schrum *et al.*, 2012].

Recent developments in pressure core technology allow coring, transferring, sub-sampling, and testing natural hydrate-bearing sediments while maintaining in situ pressure and temperature conditions at all times [Santamarina *et al.*, 2012; Schultheiss *et al.*, 2006; Yun *et al.*, 2006]. Hence, pressure core technology offers the unprecedented possibility to conduct complete biogeochemical analysis of pore fluids sampled from natural hydrate-bearing sediments without causing hydrate dissociation. This study explores potential pore fluid sampling methodologies compatible with current pressure core technology, and investigates underlying physical processes during pore fluid sampling from natural sediments.

9.2 Pore water sampling – Current Technology

Laboratory methods for pore fluid sampling from sediments are based on either pressure gradient or sediment squeezing. Pressure gradient methods either pull pore fluids by suction (vacuum) or displace fluids out by injecting water or another immiscible fluid, or by osmotic gradients. Syringe-type pore fluid samplers with suction-controlled capabilities allow for high-resolution fluid sampling in soft sediments [*Barbee and Brown*, 1986; *Beck et al.*, 2007; *Berg and McGlathery*, 2001].

Suction filtration samplers can be single-level [*Berg and McGlathery*, 2001; *Howes et al.*, 1985; *Makemson*, 1972; *Nayar et al.*, 2006] or multiple-level samplers [*Bertolin et al.*, 1995; *Montgomery et al.*, 1981; *Sayles et al.*, 1973; *Watson and Frickers*, 1990]. Dialysis samplers or osmosamplers obtain pore fluid by creating an osmotic pressure difference between deionized water and sediment pore fluid [*Hesslein*, 1976; *Jannasch et al.*, 2004; *Seeberg-Elverfeldt et al.*, 2005].

Sediment squeezing expels pore fluids through drainage ports (Note: techniques based on centrifuges combine pressure gradient and squeezing). The squeezing method can minimize pore fluid contact with air [*Kalil and Goldhaber*, 1973]. However, this method may induce several sampling artifacts, such as the destruction of microbial cells and detritus [*Bolliger et al.*, 1992], oxygen contamination [*Loder et al.*, 1978; *Robbins and Gustinis*, 1976], nitrate contamination [*Risgaard-Petersen et al.*, 2006; *Schrum et al.*, 2012], and temperature artifacts [*Bischoff et al.*, 1970; *Fanning and Pilson*, 1971].

9.3 Experimental Study

Pore fluid sampling methods compatible with hydrate-bearing sediments and deployable with pressure core characterization technology are considered next. Two geometric configurations are viable with these tools (refer to Chapter 7): either fluid sampling through a perforation across the plastic liner (point sampling - pressure

gradient), or through the bottom of a disk-shaped specimen (pressure gradient - forced displacement or squeezing). Both configurations are explored next for conditions that favor pressure gradient methods.

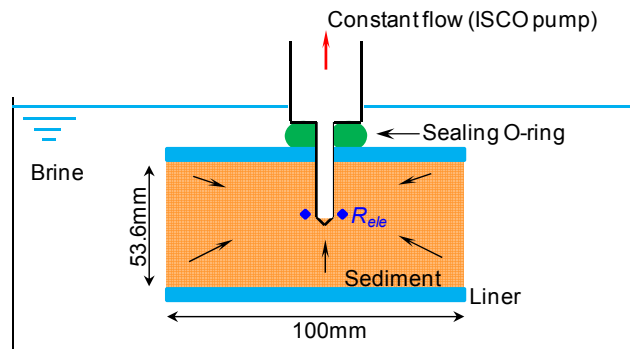
9.3.1 Point sampling: Quasi radial flow

Experimental design. Pressure cores contain hydrate-bearing sediments in plastic liners. The space between the liner and high-pressure steel chambers is filled with salt water. This experiment uses a 100mm long standard liner (ID = 53.6mm, OD = 59.6mm) filled with compacted fine sand (Ottawa F110, $d_{50} = 0.12\text{mm}$) and saturated with tap water. The “specimen” is submerged in a brine filled tank. The electrical conductance is monitored at the sampler tip during pore fluid extraction to detect the arrival of the “contaminating” brine (Figure 9.1a).

A self-drilling type pore fluid sampler is used to penetrate the liner and reach the center of the core. The tube (ID = 3.7mm, OD = 9.5mm) is reamed to OD = 4.7mm for 25mm at the tip; an o-ring (Buna-N, hardness = 75) is mounted on the shoulder (Figure 1a). The sampler is connected to an ISCO pump to impose a precise flow-controlled conditions during extraction ($q = 1, 2, \text{ and } 5\text{ml/min}$). Tests are repeated with and without the sealing o-ring for each extraction rate.

Experimental results. Figure 9.1(b) shows the evolution of electrical conductance at the tip during fluid extraction. The sudden increase in pore fluid conductance indicates brine invasion reaching the sampling tip, i.e., contamination. Tests using the o-ring seal render a larger sampled volume before contamination: 10~15cc without the o-ring and 30~60cc with the o-ring. Clearly, the seal prevents fast contamination through the perforation. When the o-ring is used, lower extraction flow rates lead to a higher amount of sampled pore fluid before contamination. For reference, the specimen contains ~100cc of fresh water, hence, the recovery efficiency is 30-60% for this geometry.

(a)



(b)

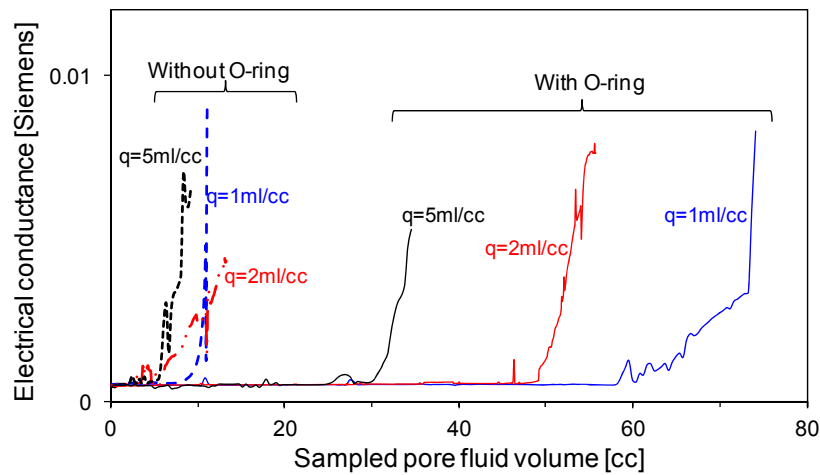


Figure 9.1. Radial flow in point sampling. (a) Experimental configuration of radial flow in point sampling method. Tap water saturated fine sands (Ottawa F110) immersed in brine. Pore water is extracted under constant flow rate q ; meanwhile, the electrical conductance of sampled pore water is monitored. (b) Electrical conductance of sampled pore water with and without using sealing o-ring.

9.3.2 Cross-section sampling: 1D flow

Experimental design. Sediment squeezing and 2D flow can be conducted in the effective stress chamber ESC and in the direct shear chamber DSC (refer to Ch 7). This configuration is tested herein using the fluid displacement method. Coarse sand (Ottawa 70/80) and fine sand (Ottawa F110) with various amounts of clayey fines (Kaolinite SA1) are saturated with tap water and compacted within the plastic liner. Air or oil is forced to

invade the soil specimen to displace the pore fluid. The discharged pore water is collected at the bottom of the specimen (Figure 9.2a).

Experimental results. Let's define the fluid replacement ratio R_r between the volume of recovered pore fluid V_{rec} and the total initial pore fluid volume V_{pf} , that is $R_r = V_{rec}/V_{pf}$. Figure 9.2b shows the measured pore fluid displacement ratio R_r for different types of sediments under various injection pressures. The results vary with soil type and invading fluid. Forced oil invasion advances as a stable front and yields displacement ratios higher than $R_r > 0.85$ for the coarse sand, the fine sand, and the mixture of fine sand with 3% of clay by weight. Even for the specimen of fine sand mixed with 15% clay by weight, the displacement ratios for forced oil exceed $R_r = 0.55$.

Forced gas invasion is prone to fingering and results in significantly lower displacement ratio ($0.3 < R_r < 0.6$). A high pressure difference facilitates pore fluid recovery by preventing early gas fingering, and the replacement ratio increases from ~ 0.3 under $\Delta P = 7\text{kPa}$ to ~ 0.6 under $\Delta P = 70\text{kPa}$.

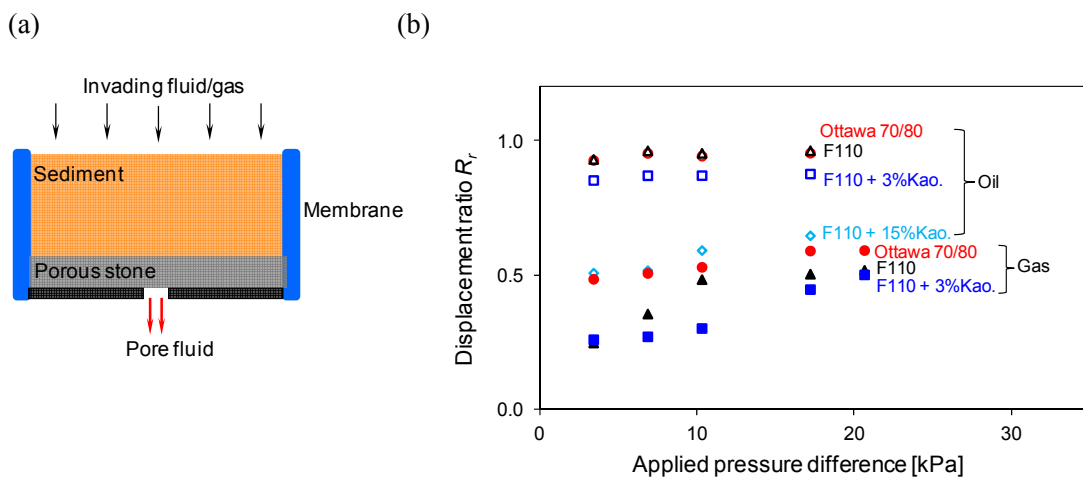


Figure 9.2. 1D flow in cross-sectional sampling using displacement method. (a) Experimental configuration. (b) Pore fluid displacement ratio: relative amount of pore fluid displaced by oil and gas for different types of soils.

9.4 Analyses and Discussion

9.4.1 Radial flow: shape factor

Instrumented pore fluid extraction can be used to estimate the sediment hydraulic conductivity. The geometry of boundary conditions and hydraulic anisotropy affect the pressure field and flow lines. The imposed fluid flux q through a soil specimen with hydraulic conductivity k , cross section area A , and length L under a certain pressure gradient Δu in 1D flow conditions is

$$q = k \frac{A}{L} \frac{\Delta u}{\rho_L g}, \quad (9.1)$$

where ρ_L is the fluid density. Flow in the “point sampling” method is not 1D and Darcy’s law is modified by the dimensionless shape factor α :

$$q = \alpha k \frac{A}{L} \frac{\Delta u}{\rho_L g}, \quad (9.2)$$

Finite element simulations (COMSOL Multiphysics - 3D) are conducted to study the shape factor α as a function of various core length/diameter ratios, $\lambda = L/D$ and the ratio between the area of the flow outlet over the area of the core $\zeta = A_{out}/A_{core}$ (Figure 9.3a, 20,000 to 40,000 elements - Non-conductive lateral boundaries). Figure 9.3b shows the numerically computed shape factor α as a function of core slenderness $\lambda = L/D$ and the relative outlet area $\zeta = A_{out}/A_{core}$. The shape factor approaches $\alpha = 1$ as $\lambda \rightarrow \infty$ and 1D flow prevails.

9.4.2 Displacement ratio - 1D flow

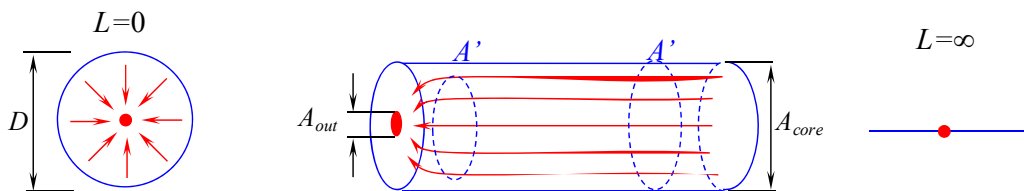
The forced invasion of an immiscible fluid involves capillary and viscous forces. The capillary number C and the viscosity number M can be used to parameterize the invasion process [Lenormand, 1989]:

$$C = \frac{v_{inv} \eta_{max}}{\gamma \cos \theta}$$

$$M = \frac{\eta_{inv}}{\eta_{def}}$$
(9.3)

where v_{inv} is the velocity of the invading fluid, η_{max} is the maximum viscosity of the two fluids, γ and θ are the interfacial tension and contact angle between the two fluids, and η_{inv} and η_{def} are the viscosity of invading and defending fluids.

(a)



(b)

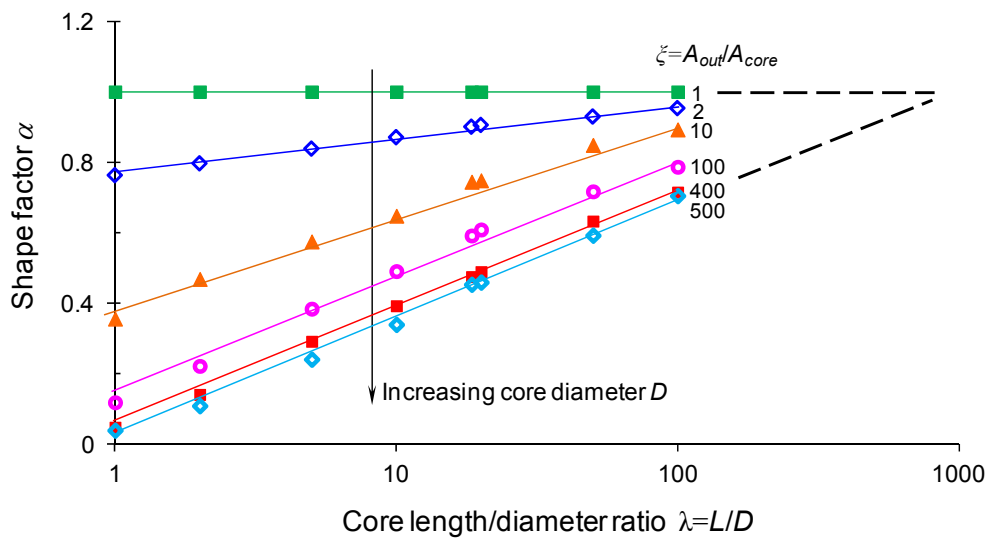


Figure 9.3. Inversion of hydraulic conductivity from point water sampling: the shape factor α . (a) Specimen geometry and (b) numerical results of the shape factor α as a function of core geometry $\lambda = L/D$ and relative pore fluid outlet area $\zeta = A_{out}/A_{core}$.

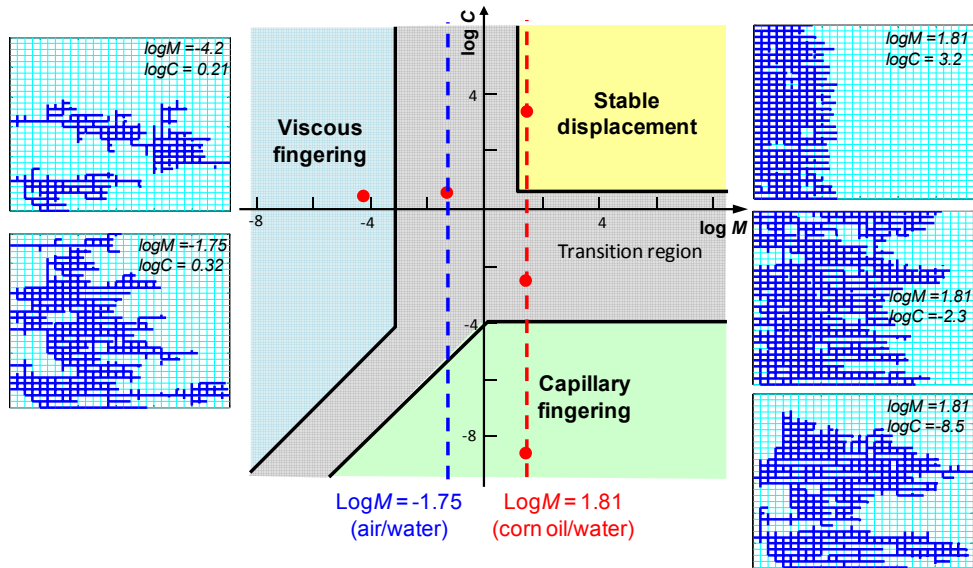
Displacement patterns are investigated using network model simulations taking capillary effects into consideration [Aker *et al.*, 1998; Blunt, 2001; Fatt, 1956]. At the pore scale, Poiseuille flow is modified as:

$$q_{ij} = \frac{\pi r_{ij}^4}{8\eta_{eff} L_{ij}} \left(\Delta P_{ij} - \frac{2\gamma \cos\theta}{r_{ij}} \right), \quad (9.4)$$

where q_{ij} , r_{ij} , L_{ij} , and ΔP_{ij} are the flux, tube radius, tube length, and differential pressure between nodes i and j . The effective viscosity η_{eff} is the volume averaged viscosities of the two fluids ($f_1\eta_1 + f_2\eta_2$) where f_i represents the volume fraction of the i^{th} fluid in the tube and $f_2 = 1 - f_1$. Mixed fluid flow occurs only when $\Delta P_{ij} > 2\gamma \cos\theta / r_{ij}$; flow in tubes filled with a single fluid follows the Poiseuille tube equation. The pressure at each node is computed to satisfy mass conservation at nodes, so that the flux and flow rate in each tube are calculated with known nodal pressures, tube size, and fluid viscosity [Jang, 2011]. The position of menisci is updated at each time step using Equation 9.4.

Figure 9.4a illustrates the invasion patterns in terms of the capillary number C and the viscosity number M . The superimposed network model simulation results apply to pore water displacement by forced air or oil invasion. In these 2D simulations, viscous or capillary fingering results in a pore fluid recovery ratio $R_r < \sim 0.4$; while stable displacement leads to $R_r > 0.8$. It follows from the results that stable displacement requires an invading pore fluid with viscosity $\eta_{inv} > \sim 30\eta_{pf}$ at a velocity $v_{inv} > \sim 10\gamma \cos\theta / \eta_{inv}$. Figure 9.4b shows both numerical and experimental results of pore fluid displacement ratios by forced oil invasion: the invasion velocity of the viscous fluid in the less conductive specimens (F110+10%Kaolinite) may fail to meet the velocity requirement for stable displacement.

(a)



(b)

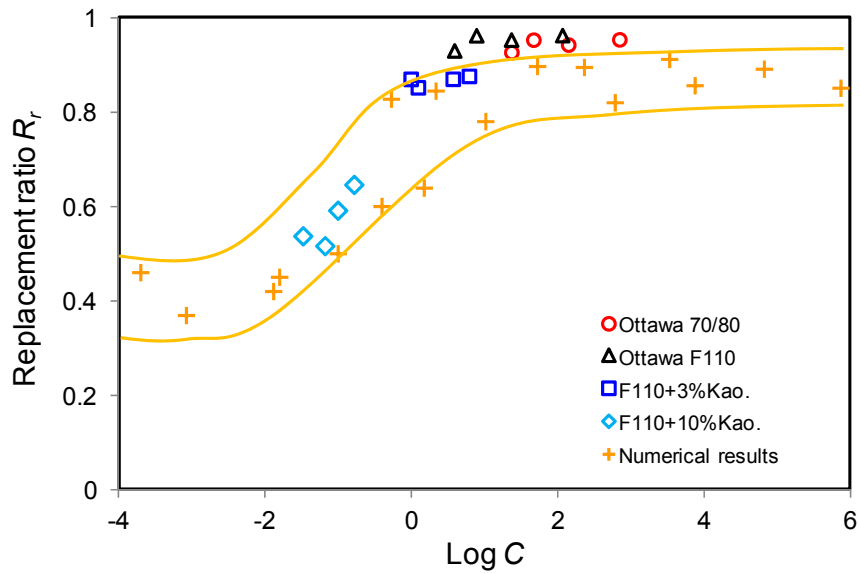


Figure 9.4. Network model simulation – displacement ratio. (a) Pore fluid displacement patterns in terms of capillary force C and viscous force M . Higher viscosity of invading fluid enhances sediment pore fluid recovery. Note: 30x30 network with mean tube radius $\mu_{(r)} = 10\mu\text{m}$ and standard deviation $\sigma_{(\ln(r/\mu\text{m}))} = 0.4$. (b) Comparison of experimental and network simulation results on pore fluid displacement by forced oil invasion.

9.4.3 Comparison: displacing versus squeezing methods

The amount of pore fluid recovered by imposing a pressure gradient and forced invasion depends on the initial soil void ratio e_0 and pore fluid displacement ratio R_r .

$$V_{disp} = V_0 \frac{e_0}{1 + e_0} R_r, \quad (9.5)$$

where V_0 is the initial soil total volume. The volume of pore fluid recovered by squeezing V_{sqz} depends on the sediment stiffness and the applied stress: compressible soft clayey soils require a low squeezing stress, yet very high stresses are needed for dense silts and sands. For a specimen under zero-lateral strain condition (oedometer cell)

$$V_{sqz} = V_0 \frac{C_c}{1 + e_0} \log\left(\frac{\sigma'}{1kPa}\right), \quad (9.6)$$

where, C_c is the soil compression index and σ' is the applied vertical stress. The relative amount of pore fluid that can be recovered using displacing versus squeezing methods is

$$\frac{V_{disp}}{V_{sqz}} = \frac{V_0 \frac{e_0}{1 + e_0} R_r}{V_0 \frac{C_c}{1 + e_0} \log\left(\frac{\sigma'}{1kPa}\right)} = \frac{e_0 R_r}{C_c \log(\sigma'/kPa)}. \quad (9.7)$$

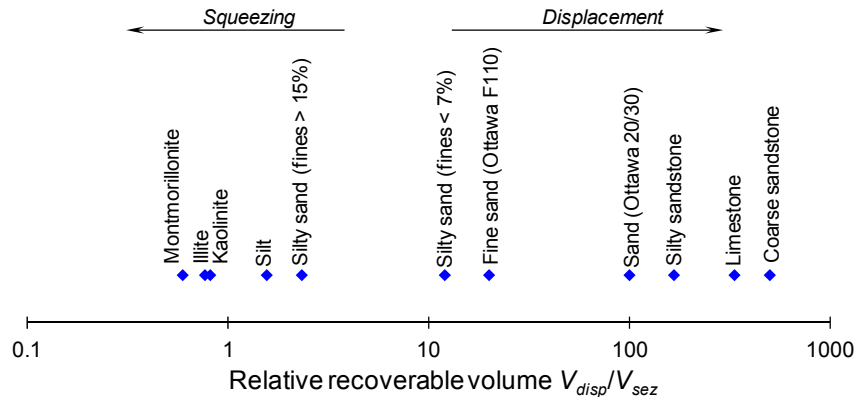
Figure 9.5a shows the relative recoverable volume of pore fluid V_{disp}/V_{sqz} for different types of soils (parameters in Table 9.1).

On the other hand, the relative time for pore fluid sampling using these two methods is

$$\begin{aligned} \frac{t_{disp}}{t_{sqz}} &= \frac{L/v}{L^2/c_v} = \frac{c_v}{vL} \\ &= \frac{1 + e}{0.434 C_c} \frac{\sigma'}{\Delta P} \end{aligned} \quad (9.8)$$

where L is the characteristic length of the specimen, v is the flow velocity during displacement, and c_v is the pore pressure diffusion coefficient.

(a)



(b)

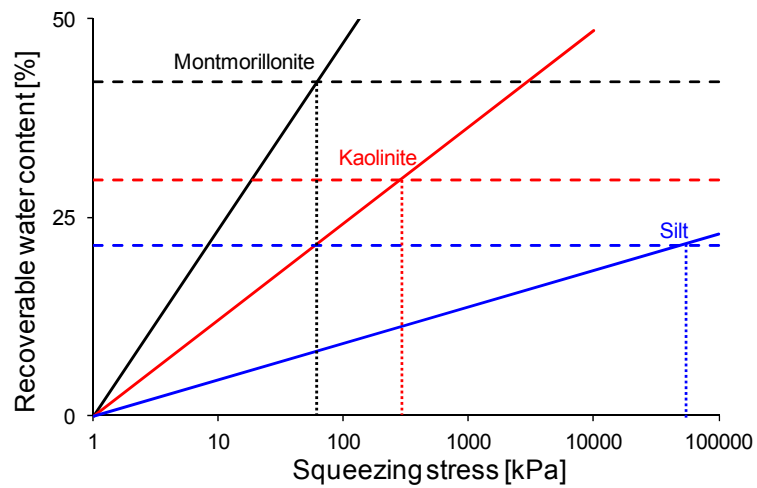


Figure 9.5. Pore fluid sampling methods versus soil type: underlying physical properties. (a) Relative recoverable pore fluid volume by displacement (disp) and squeezing (sqz) methods for different soils (Note: refer to Table 1 for soil physical properties; stress used in the squeezing method is assumed $\sigma' = 1$ MPa; pore fluid replacement ratio used in the displacement method is assumed $R_r = 0.5$). (b) Recoverable water content using displacement (horizontal dashed lines) and squeezing (solid slopes, under varying stress conditions) methods.

Table 9.1. Assumed physical properties of different types of soils.

	Initial porosity e_0 [-]	Void ratio n [-]	Compression index Cc [-]	Porosity at 100kPa e_{100kPa} [-]	Specific surface S_s [m ² /g]	Hydraulic conductivity K [×10 ⁻⁶ cm/s]
Silty sandstone	0.1	0.09	0.0001	0.0998	-	2
Coarse sandstone	0.15	0.13	0.00005	-	-	500
Limestone	0.2	0.17	0.0001	-	-	120
Ottawa 20/30	0.6	0.38	0.001	0.598	0.00314	9000
Ottawa sand F110	0.6	0.38	0.005	0.59	0.01887	5000
Silty sand (fines<7%)	0.65	0.39	0.009	0.632	0.03774	1000
Silty sand (fines>15%)	0.7	0.41	0.05	-	-	80
Silt	0.75	0.43	0.08	0.59	0.1	50
Kaolinite	1.47	0.60	0.3	0.87	15	1
Illite	3.69	0.79	0.8	2.09	80	0.1
Montmorillonite	5.36	0.84	1.5	2.36	600	0.01

9.4.4 Required specimen size

The amount of pore fluid required for geochemical analysis varies: 0.5ml for chloride analyses, 1ml for sulfate, 7ml for dissolved inorganic carbon (DIC), C-13 isotope and alkalinity, and 14ml for ammonium, phosphate, Fe, Mn, Ba, Sr, Li, and O/H isotopes (M. Kastner and R. Colwell – Personal communications). Therefore, a 200cm³ specimen of hydrate-bearing sediments is needed to sample enough uncontaminated pore fluid for a full set of geochemical analyses when using the self-drilling sampler (assuming 30% of pore fluid can be recovered without being contaminated). The 1D configuration requires a specimen of 75cm³ when viscous oil is used with an invading speed $v_{inv} > \sim 10\gamma\cos\theta/\eta_{inv}$.

9.5. Conclusions

Pore fluid sampling from hydrate-bearing sediments is challenged by sampling artifacts and the need to maintain high pressure at all times. This study explored pore fluid sampling methods compatible with current pressure core technology and investigated underlying physical processes during pore fluid sampling from natural sediments.

The selection of sampling method, squeezing versus displacement, also depends on soil physical properties, particularly compressibility C_c and hydraulic conductivity.

An o-ring seal can effectively prevent fast contamination through the perforation in syringe-type self-drilling samplers. The pore fluid recovery efficiency can range between 30% and 60% before contamination for the specimen geometries relevant to pressure core testing. Instrumented pore fluid extraction can be used to estimate the sediment hydraulic conductivity assuming an adequate shape factor α for the flow field. The shape factor α depends on core slenderness $\lambda = L/D$ and the relative outlet area $\zeta =$

A_{out}/A_{core} .

The displacement pattern of forced invasion of an immiscible fluid is governed by the capillary number C and the viscosity number M . Both experimental and network model simulation results show that fingering renders low pore water displacement ratio $R_r < \sim 0.4$. Stable displacement using a viscous fluid $\eta_{inv} > \sim 30\eta_{pf}$ results in high displacement ratios $R_r > 0.8$.

Both the self-drilling sampler and pore fluid displacement methods can be implemented within current pressure core characterization tools PCCTs to sample pore fluid from natural hydrate-bearing sediments without causing hydrate dissociation.

CHAPTER 10

CONCLUSIONS

The purpose of this research was to gain a fundamental understanding of hydrate-bearing sediments in the natural environment and to develop unprecedented devices to characterize natural hydrate-bearing sediments under in situ pressure, temperature, and effective stress conditions. The scope of this work has included: hydrate nucleation, hydrate growth in natural sediments, water retention curve in hydrate-bearing sediments, natural hydrate-bearing sediments in permafrost and marine settings, and the design and deployment of pressure core technology. The main conclusions from this study follow.

Hydrate nucleation.

- Nucleation is favored by the presence of most minerals. Mineralogy and fluid-mineral interaction are more important than particle size and sediment porosity.
- Nucleation is prompted by mechanical agitation (without suppressing the inherent stochastic nature of nucleation).
- Acceleration is a better discriminator of nucleation than vibration frequency or amplitude, or vibration velocity.
- Relative molecular displacement emerges as the underlying mechanism for agitation triggered nucleation.

Hydrate growth in natural sediments.

- Hydrate morphology at the meso-scale is inherently controlled by the state of effective stress σ' and the grain size of the finer fraction of the sediment d_{10} .
- Heterogeneous hydrate distribution is inherent in natural sediments. Capillarity-controlled grain-displacing nodules and chunks form in fine-grained sediments at low effective stress. Lenses and veins emerge in fine-grained sediments at intermediate effective stress where capillarity and effective stress affect growth.

Patchy saturation prevails in coarse sands at high effective stress where the granular skeleton remains unaltered during hydrate growth.

- The bulk stiffness of patchy hydrate-bearing sands approaches the lower bound at low hydrate saturations, but it tends towards the upper bound at high saturations due to the mechanical interaction between hydrate-saturated patches.
- Patchy hydrate saturation is generally less disruptive to bulk conductivities than homogeneously distributed hydrates. An increased patch size or slenderness in the fluid flow direction decreases the impact of patches on the global sediment hydraulic conductivity.

Water retention curve for hydrate-bearing sediments.

- The water retention curve captures the variation of capillary pressure with water saturation, and it is inherently determined by sediment pore size variability and interconnectivity.
- The air entry pressure P_0 increases with hydrate saturation S_h and can be estimated from the air entry pressure of hydrate-free sediments P_0^{HF} as a power function of hydrate saturation.
- Hydrate morphology affects the air entry value P_0 and curve slope m -value. In particular, patchy hydrate distribution renders lower air entry pressure than distributed hydrate saturation.
- Higher variation in sediment pore size distribution lowers the air entry value P_0 but steepens the curve.
- The specimen size and geometry affect the measured capillary pressure, especially at high water saturation $S_w > 0.7$.

Natural Hydrate-bearing sediments.

- In both permafrost and marine settings, the major controls on the mechanical and geophysical properties of hydrate-bearing sediments are effective stress, porosity, and hydrate saturation.

- Elastic and electromagnetic waves provide complementary information for characterization and process monitoring of hydrate-bearing and/or permafrost sediments.
- The formation of gas hydrate before the completion of sedimentation may have hindered further sediment compaction at the Mount Elbert site.
- Coring natural sediments faces inherent sampling disturbance, as observed in the Krishna-Godavari Basin.
- Skeleton expansion during unloading can trigger hydrate dissociation under tension, hydrate-mineral debonding, and stiffness loss.
- Undrained unloading can cause a marked pore pressure drop towards the center of the specimen (Mandel-Cryer effect), resulting in transient hydrate destabilization.
- Sampling induced secondary hydrate formation alters hydrate morphology and physical properties of natural hydrate-bearing sediments.

Pressure core technology.

- Pressure core technology is needed for the proper evaluation of natural hydrate-bearing sediments. Pressure core characterization tools PCCTs developed at GeorgiaTech allows the manipulation, sub-sampling, and extensive assessment of natural hydrate-bearing sediments under in situ pressure, temperature, and effective stress conditions.
- Restored effective stress is needed for measuring stress-dependent properties of hydrate-bearing sediments such as stiffness and strength. The effective stress chamber ESC has a triaxial stress condition. The flexible wall configuration allows precise fluid conductivity measurements by preventing the preferential flow along the sediment-steel boundaries in rigid-wall chambers. This chamber is particularly well suited to monitor production studies under in situ effective stress conditions, including the assessment of sediment volume change upon dissociation.

- Pore fluid sampling from hydrate-bearing sediments is challenged by sampling artifacts and the need to maintain high pressure during pore fluid extraction.
- The selection of squeezing versus displacement is affected by soil physical properties, particularly sediment compressibility and fluid conductivity.
- Pressure and flow rate measurements during pore fluid sampling allows for the simultaneous inversion of specimen hydraulic properties.
- Self-drilling point samplers and pore fluid displacement methods can be implemented within current pressure core characterization tools PCCTs to sample pore fluid from natural hydrate-bearing sediments without causing hydrate dissociation.

APPENDIX A: CODA WAVE ANALYSIS

A1. Introduction

The characterization of natural soils is inherently challenging due to their particulate nature and the effect of the measurement process on measured properties. Small-strain measurements using elastic waves provide valuable soil information without altering the soil fabric; examples include small-strain stiffness and attenuation, spatial variability, and soil changes during internal or boundary-imposed processes.

A salient problem in wave measurements is the determination of the first arrival in wave fields. Recommended criteria vary for different experimental configurations (Examples for bender element tests can be found in: [Arroyo *et al.*, 2006; Lee and Santamarina, 2005a; Youn *et al.*, 2008]). Furthermore, changes in first arrivals can often fall below detection limits when monitoring phenomena such as diagenesis, creep, and aging.

On the other hand, the signal tail or “coda” captures multiple scattered and reflected waves that arrive after the fastest wave front [Aki, 1969; Aki and Chouet, 1975; Snieder, 2006]. These later wave fronts have travelled longer paths and accumulated larger time shifts. Therefore, coda analysis or coda wave interferometry may provide process information even when changes in first arrivals are below resolution. Coda wave analysis has been used to evaluate slight changes in fields, such as earthquake engineering, volcano monitoring, fault movement, and material characterization [Gret, 2004; Otheim *et al.*, 2011; Schurr *et al.*, 2011; Shapiro *et al.*, 2005; Snieder, 2006; Snieder *et al.*, 2002; Wuttke *et al.*, 2012].

This study identifies and compares algorithms for basic coda wave analysis, highlights underlying assumptions in coda interpretation, and demonstrates the methodology using experimental data gathered to assess the stiffness evolution of a

uniform quartzitic sand specimen during loading, creep, and unloading processes. Eventually, the enhanced signal processing methodology provides new insight into soil behavior.

A2. Analysis of Seismic Codas

The concept of coda wave analysis is introduced herein. For clarity, the “sampling interval” Δt is the time separation between two contiguous discrete values in a digital signal, and a “time window” is a signal segment between two predefined times.

Consider two consecutive P-wave signals A and B obtained for a sandy specimen under isotropic confinement, the first one at $67.6kPa$ ($9.8psi$) and the second one at $68.9kPa$ ($10psi$) (Figure 1a). The time for the first arrival t_D is identical in both signals ($t_D \approx 200\mu s$), yet time windows taken between 1800-to-2200 μs (i.e., 9 to 11 times the travel time for the first arrival t_D) and 3600-to-4000 μs (i.e., 18 to 20 times t_D) show that coda waves accumulate time shifts.

The time delay for a given “event” in the two signals increases linearly with travel distance l , i.e., with the event time $t = l/V$, as shown in Figure 1b. The slope of the trend in Figure 1b is $\theta = \Delta t/t$. For a velocity change from V_A to $V_B = V_A + \Delta V$,

$$\theta = \frac{\Delta t}{t_A} = \frac{t_A - t_B}{t_A} = \frac{\frac{l}{V_A} - \frac{l}{V_B}}{\frac{l}{V_A}} = \frac{V_B - V_A}{V_B} \cong \frac{\Delta V}{\bar{V}} \quad (A1)$$

where the average velocity is $\bar{V} = (V_A + V_B)/2$. Equation 1 shows that the slope of time lags θ is equal to the relative change in velocity $\Delta V/\bar{V}$ between signals A and B.

It follows from Equation A1 that a certain event at time t_A in signal A appears at a stretched time $t_B = t_A(1+\theta)$ in signal B. Thus, the slope θ is herein referred to as the “stretching factor”. Three different methods to determine the stretching factor θ are presented next.

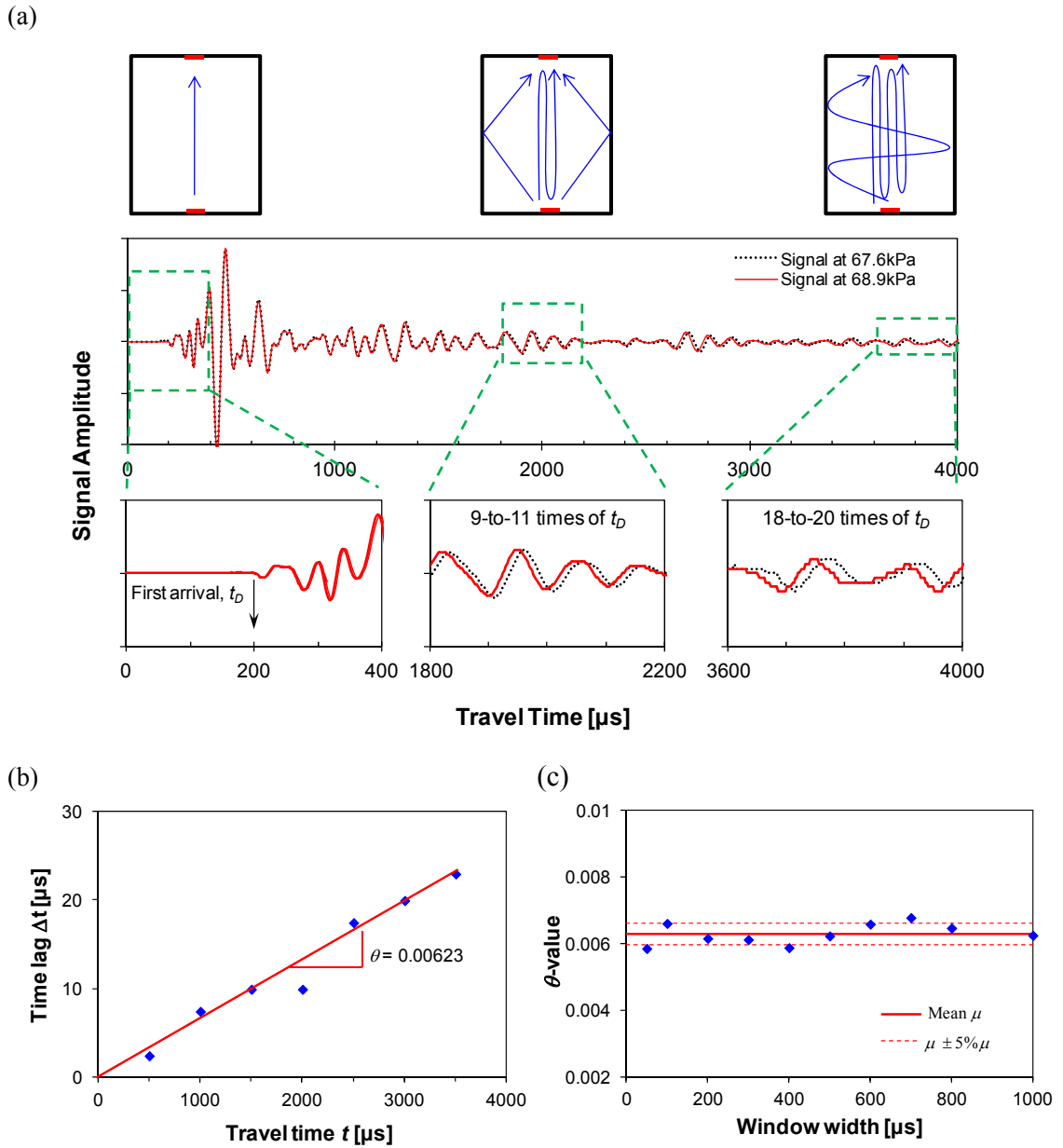


Figure A1. Schematic illustration of seismic coda analysis. (a) The first arrival of a wave signature reflects the fastest wave pathway (Fermat's principle). Events that have experienced multiple reflections arrive later in the coda. Therefore, codas accumulate differences in propagation velocity. (b) The time lag Δt between two signals increases almost linearly with propagation time t . The slope θ is the stretching factor. (c) The value of θ varies slightly with window width in time-windowed cross correlations. Differences in θ values attributable to the window width are mostly within 5%.

A2.1 Method 1: Short-time cross correlation

Short-time windows are extracted from the full signals A and B, and the relative time lag Δt between the windowed signals is determined by cross correlation [Snieder *et al.*, 2002; Wuttke *et al.*, 2012]. Multiple time lags are obtained by repeating ‘time windowing and cross correlation’ at different positions along the signals. The time lag Δt determined for each window position is plotted versus the window central time t_w to determine θ (Figure A1b). Window width and superposition must be selected a priori. Computed θ values vary slightly with window width (Figure A1c).

A2.2 Method 2: Time-stretched cross correlation

The linear increase in time lag Δt with travel time t for corresponding events in signals A and B implies that waveforms can overlap by linearly stretching the time scale of the faster one, say signal B [Sens-Schönfelder and Wegler, 2006]. The procedure consists of four steps: (1) select a value of θ ; (2) time-stretch the faster signal B using $t_B = t_A(1+\theta)$; (3) compute the cross correlation between the full-length signals, i.e., the original signal A and the stretched signal B; (4) repeat step 1 to 3 for other θ values. The sought value of θ is the one that renders the highest cross correlation (Figure A2a). Note that time-stretching requires re-sampling: new signal values at all times t_i are obtained by interpolating between stretched signal values that fall immediately above and below t_i (we use linear interpolation).

Signal amplitudes decrease with time, thus, cross correlation values are biased by the earlier higher energy events in the signals. This bias is overcome by pre-dividing both signals A and B by the same exponential amplifier (dash dot line in Figure A2a) to yield signals with constant energy content in time (Figure A2b): the signal value x_i at time t_i is amplified by a factor $e^{\alpha t_i}$ where α is constant for all t_i and equal for both signals.

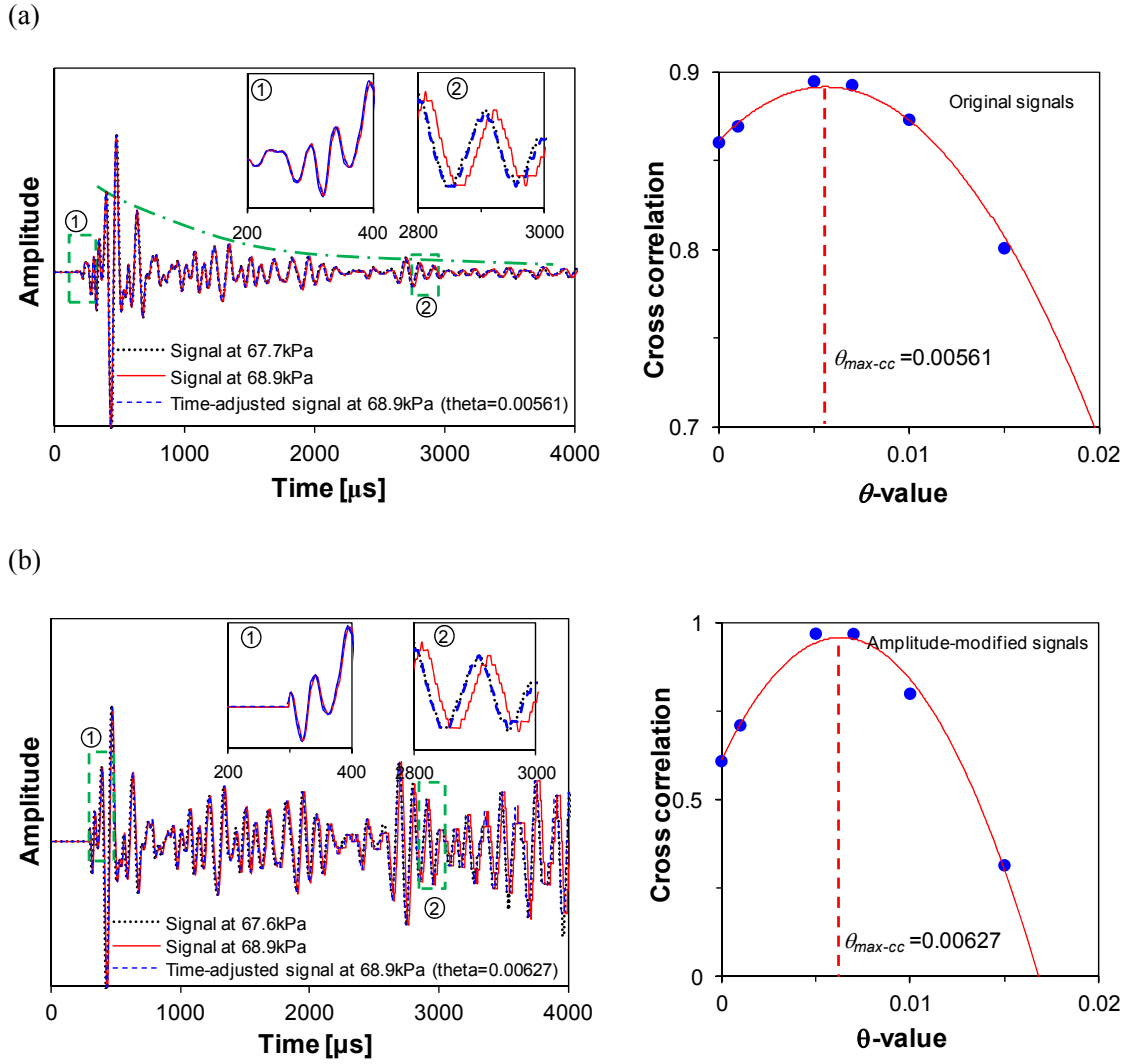


Figure A2. Time-stretched cross correlation: full-signal based determination of the stretching factor θ in the time domain. (a) Computations using original signals. (b) Both signals are exponentially amplified (dash dot line in Figure 2a) to obtain constant energy content in time before computing the cross correlation: the signal value x_i at time t_i is amplified by a factor $e^{\alpha t_i}$ where α is constant for all t_i and equal for both signals. Inserts show amplified signal windows (noted as “1” and “2”).

A2.3 Method 3: Frequency-stretched spectra

Two signals A and B with a linear increase in time lag can be regarded as the same signal but sampled with two different sampling intervals: signal A using Δt and signal B with $(1 \pm \theta)\Delta t$. In other words, their amplitudes are identical when the discrete

time $t_A=i\cdot\Delta t$ equals $t_B=i\cdot[(1\pm\theta)\Delta t]$, where i is an integer. Therefore, in frequency domain the spectral magnitude for signal A at frequency $\omega_A=2\pi u/(N\cdot\Delta t)$ equals that for signal B at $\omega_B=2\pi u/[N\cdot(1\pm\theta)\Delta t]$, where the integer u is the frequency counter and N is the number of discrete points in the sampled signal. Then, the stretching coefficient can be determined in the frequency domain as follows: (1) compute the frequency spectrum for both signals A and B; (2) linearly stretch the spectrum of the slower signal until both spectra match best (cross correlation – Note: this requires interpolation to compute stretched spectral values at frequencies ω_u); (3) the sought value of θ is the one that corresponds to the best match between the two spectra. Results are shown in Figure A3 for the same signal pair used earlier.

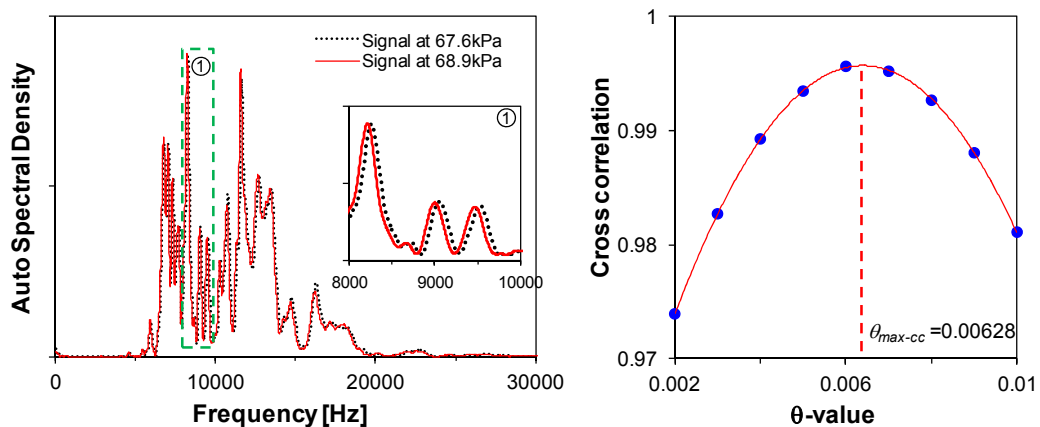


Figure A3. Stretched spectra: full-signal based determination of the stretching factor θ in the frequency domain.

A2.4 Comparison

Values in Figures A1, A2, and A3 were obtained for the same signal pair. The computed stretching factors are (a) short-time cross correlation $\theta = 0.00623$ ($\pm 5\%$ for different window widths), (b) amplitude-adjusted time-stretched cross correlation $\theta = 0.00627$, and (c) cross correlation of the frequency-stretched spectra $\theta = 0.00628$. From

Equation 1, the stretching factor is $\theta = \Delta V/V$, hence, θ -values measured in this example indicate that a 0.6% velocity change has taken place in the medium between signals A and B (i.e., a 1.4kPa isotropic stress increase).

A3. Experimental Study: *P*-wave Velocity in Dry Sand

The purpose of this experimental study is to explore the potential of coda wave analysis in detecting very small velocity changes. We study two cases: velocity changes due to small changes in effective stress and the more challenging case of velocity changes during creep-aging.

A3.1 Experiment design

Specimen. A cylindrical soil specimen (radius $R = 17.5\text{mm}$ and height $H = 74.4\text{mm}$) is confined by a latex membrane and subjected to isotropic stress in a triaxial chamber (Figure A4). The soil selected for this study is Ottawa-20/30 sand (quartzitic; median grain size $d_{50} = 0.72\text{mm}$; coefficient of uniformity $C_u = 1.2$; roundness $R = 0.9$; sphericity $S = 0.9$; packing $e_{max/min} = 0.742/0.502$).

Testing procedure. The load history involves three stages. (1) Loading: the confining stress is gradually increased from 0kPa until 68.9kPa, in 1.4kPa steps (note that the confining stress is actually measured in PSI and converted into kPa; the loading is increased from 0psi to 10psi, in 0.2psi steps). (2) Creep: the applied confining stress is held constant at 68.9kPa for approximately 8 hours. (3) Unloading: the confining stress is gradually decreased back to 0kPa in (-)1.4kPa steps.

Wave propagation. Piezopads are installed on the caps of the sample to monitor the evolution of *P*-wave velocity in the sand. Received wave signals are recorded at each loading step and periodically during creep.

Data reduction. The “reference” first arrival travel time is determined for the signal gathered at isotropic confinement $\sigma = 34.5\text{kPa}$ in this study, where the first-arrival

is very clear. All other travel times are referred to this one through consecutive stretching coefficients $t_B = t_A(1+\theta)$, as discussed earlier.

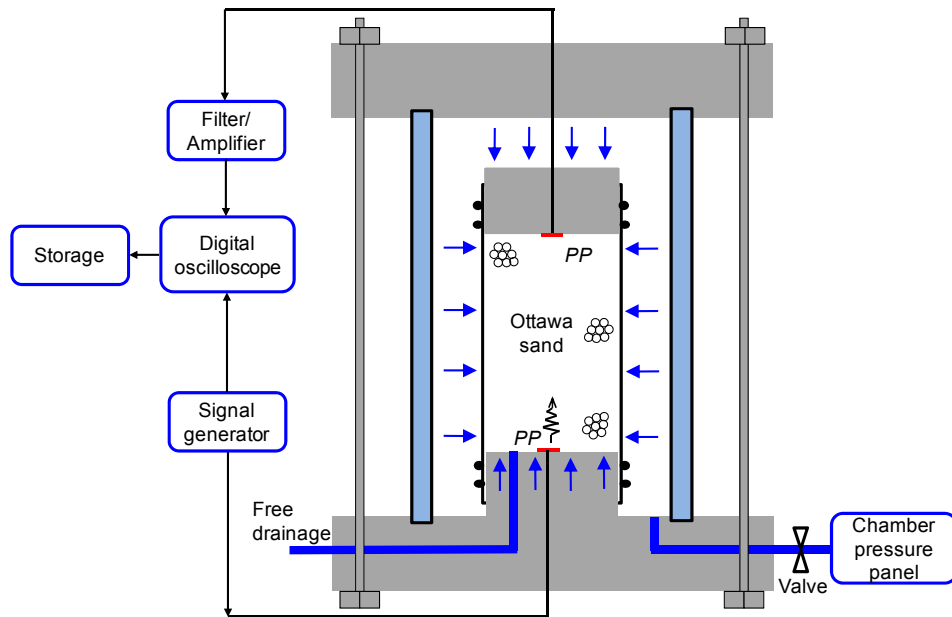


Figure A4. Experimental configuration. Stiffness evolution in uniform quartzitic dry sand subjected to isotropic gas confinement (as illustrated in arrows). *P*-waves are generated and detected using piezopads (*PP*).

A3.2 Test results

The complete cascade of 110 signals recorded during loading, creep, and unloading stages is shown in Figure A5. The horizontal axis shows the wave travel time and the vertical axis shows the waveforms cascading in chronological sequence from the beginning of the test until the end. Signal amplitude is captured with gray intensity: white denotes waveform peaks and black troughs. Travel times shorten during loading and creep. Particularly during creep, differences in first arrival times cannot be visually distinguished (In fact, they may be smaller than the sampling interval $\Delta t = 0.25\mu\text{s}$). However, codas show clear time shifts of peaks and troughs, even during the creep stage.

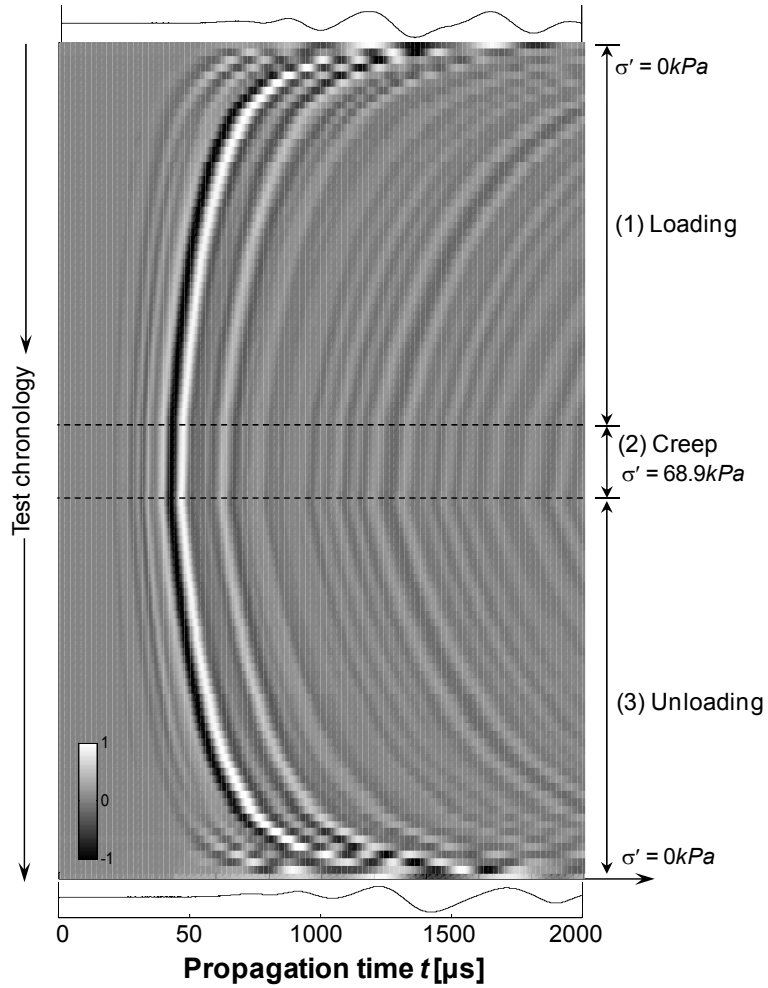


Figure A5. Cascade of received wave signals (in total 110 waveforms; the first and last signals are shown at the top and bottom of the signal cascade). The signal amplitude is illustrated in gray intensity, where white represents peaks and black troughs. (1) Loading from self weight $\sigma' = 0kPa$ to $\sigma' = 68.9kPa$ in $\Delta\sigma' = 1.4kPa$ (0.2psi) increments. (2) Creep at constant confining pressure ($\sigma' = 68.9kPa$). (3) Unloading from $P = 68.9kPa$ to self weight in $\Delta\sigma' = -1.4kPa$ drops. Notice the increasing gradient of peaks and troughs in wave codas recorded during the creep stage.

Figure A6 shows computed θ values for all consecutive signals using the short-time cross correlation method. Computed P -wave velocities during the three experimental stages are then presented in Figure A7a. The initial P -wave velocity of the specimen under self weight is $110.0m/s$. Velocity increases with confining stress to reach $292.2m/s$ at $68.9kPa$, and decreases during unloading to a final value of $119.0m/s$. Figure

A7b shows the time-lapse velocity change for the Ottawa sand specimen during creep under constant isotropic confinement $\sigma' = 68.9\text{kPa}$ (Note: velocity plotted in high resolution). The increase in velocity due to creep is $\Delta V_P \approx 1.5\%$ within 8 hours of monitoring, and velocity changes as small as $\Delta V/V < 0.1\%$ are detected between consecutive signals.

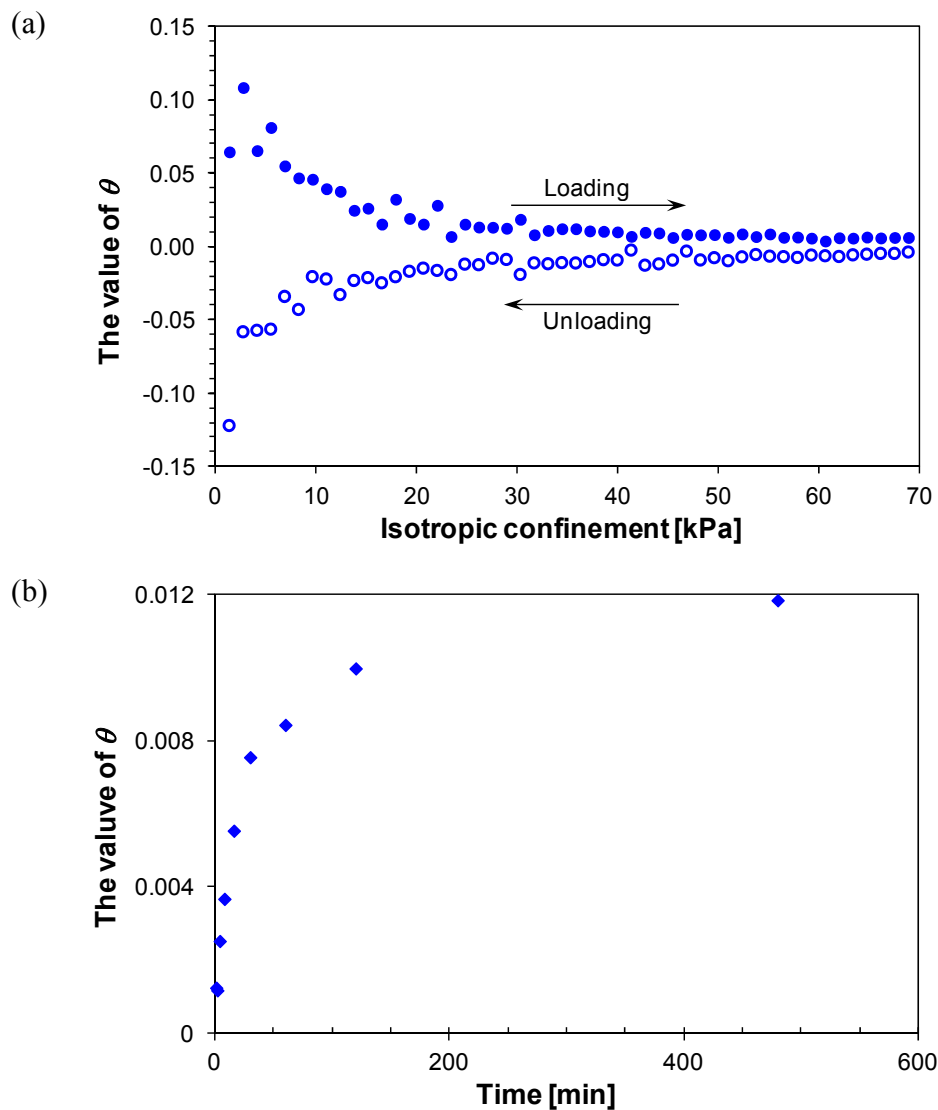


Figure A6. Computed θ values (a) during loading and unloading, and (b) during creep.

A4. Analysis

A4.1 Velocity-stress response

The velocity-stress power relationship. A power-type Hertzian relationship adequately captures velocity-stress in soils [Santamarina *et al.*, 2001]:

$$V = \alpha \left(\frac{\sigma'}{\sigma'_{ref}} \right)^\beta \quad (A2)$$

where α is the soil wave velocity when σ' equals the reference effective stress σ'_{ref} , and β reflects the dependency of velocity on effective stress σ' in the direction of wave propagation. Wave velocities measured at $\sigma' > 10kPa$ are well fitted with Equation 2 ($\alpha = 93.0m/s$ and $\beta = 0.27$ during loading, and $\alpha = 98.0m/s$ and $\beta = 0.26$ during unloading). Stiffness hysteresis in quartzitic sands subjected to isotropic loading is easily missed in standard visual signal interpretation. However, this is clearly seen in the coda-based data plotted in Figure 7a. This hysteresis behavior may possibly due to slight changes in fabric and/or interparticle contact behavior.

Self weight effect. Measured velocities at lower confinement stresses (i.e., $< \sim 10kPa$ in this study) deviate from the velocity-stress power relationship. This is because soil self weight induces an inhomogeneous stress distribution inside of the specimen that has not been captured in the velocity-stress relationship.

At zero confinement ($\sigma'_c = 0$), the vertical effective stress in the sediment increases linearly with depth due to self weight, from $\sigma'_z = \sigma'_{cap}$ (top cap at $z = 0$) to $\sigma'_z = \sigma'_{cap} + \gamma_s H$ at the bottom of the specimen (height H and unit weight γ_s). This stress field must be accounted for during the analysis of P -wave velocity data obtained at very low confining stress. Travel time is an integral of slowness $1/V(z)$ along the specimen height H ,

$$t = \int_0^H \frac{dz}{\alpha \left(\frac{\sigma'_z}{\sigma'_{ref}} \right)^\beta} = \int_0^H \frac{dz}{\alpha \left(\frac{\sigma'_0 + \sigma'_{cap} + \gamma_s z}{\sigma'_{ref}} \right)^\beta} = \frac{1}{\alpha \gamma_s (1 - \beta)} \left[\left(\frac{\sigma'_0 + \sigma'_{cap} + \gamma_s H}{\sigma'_{ref}} \right)^{1-\beta} - \left(\frac{\sigma'_0 + \sigma'_{cap}}{\sigma'_{ref}} \right)^{1-\beta} \right]$$

(A3)

where σ'_0 is the applied isotropic confining stress. Travel times determined using coda analysis are plotted as a function of isotropic confining stress in Figure 8. We concluded that when self weight is accounted for at low confining stress, the power velocity-stress relation (Equation A2) properly reproduces the complete data set (compare Figures A7a and A8).

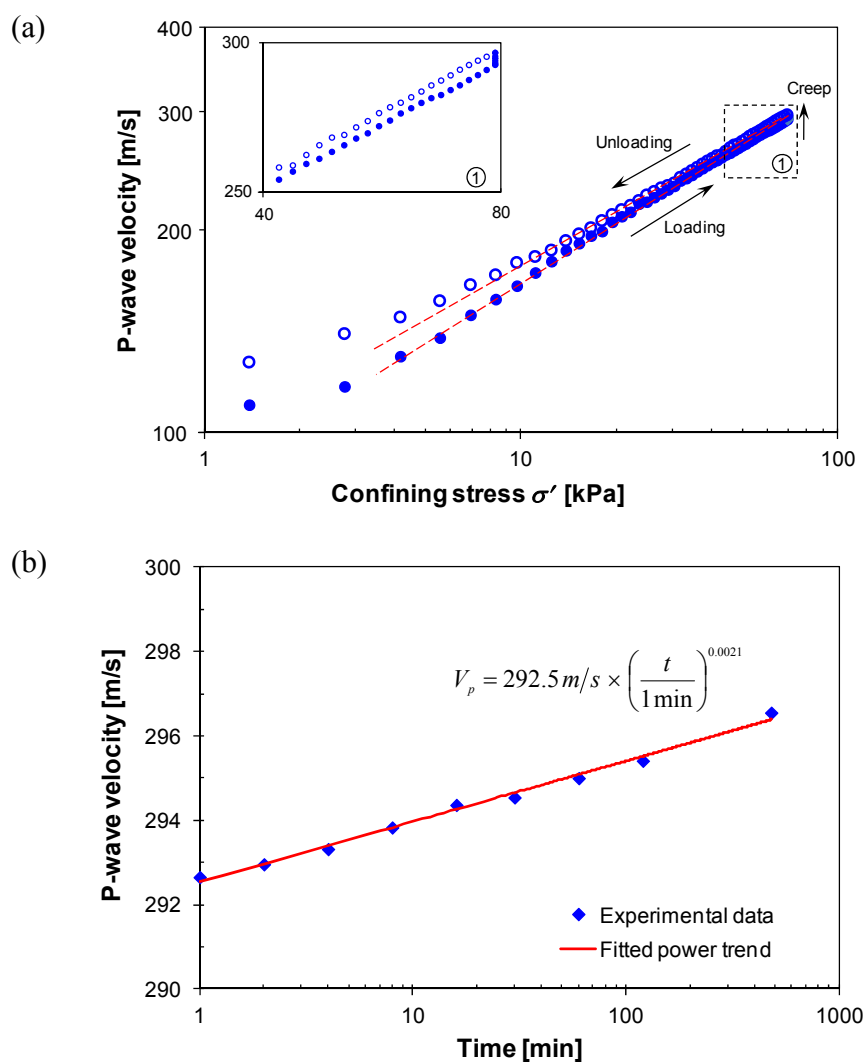


Figure A7. *P*-wave velocity evolution (a) as a function of applied confining stress σ' during loading (solids) and unloading (circles) stages; the insert amplifies changes in stiffness due to creep during sustained loading $\sigma' = 68.9\text{kPa}$; (b) as a function of time during creep (diamonds) at constant confining stress $\sigma' = 68.9\text{kPa}$.

If self weight is neglected, predicted travel times t_p are much longer than measured times- t_m at low confinement (Figure A8). For a given sediment with parameters α and β , the ratio t_p/t_m is a function of the ratio between self weight and confining stress, $\gamma_s H/(\sigma'_0 + \sigma_{cap})$. From Equation A3,

$$\frac{t_p}{t_m} = \frac{\frac{\gamma_s H}{\sigma'_0 + \sigma_{cap}}(1-\beta)}{\left(1 + \frac{\gamma_s H}{\sigma'_0 + \sigma_{cap}}\right)^{1-\beta} - 1} \quad (\text{A4})$$

For $\beta = 0.25$, the error in travel time due to self weight is less than 1% when $(\sigma'_0 + \sigma_{cap})/(\gamma_s H) > 10$. In other words, the effect of self weight on soil stiffness can be negligible when the confining stress is at least 10 times larger.

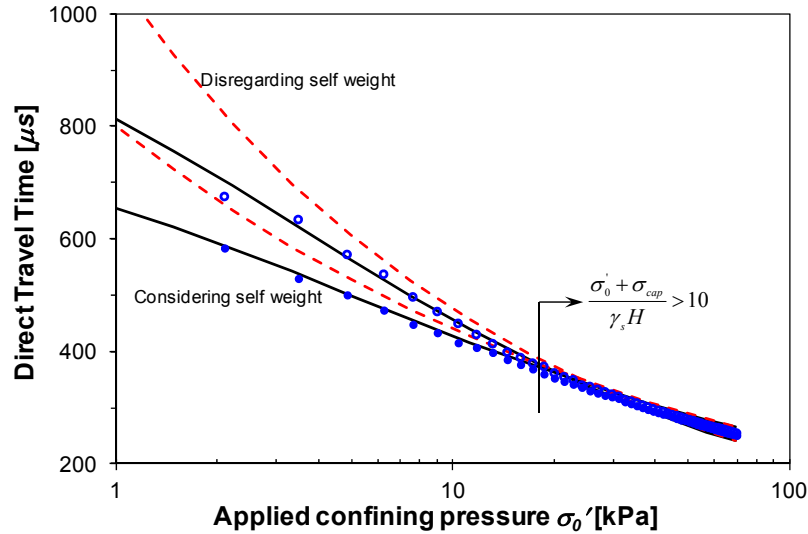


Figure 8 Predicted (solid lines: considering the self weight effect; dashed lines: disregarding the self weight effect) vs. measured (dots) direct travel time as a function of applied confining pressure σ'_0 . Accounting for self-weight requires time integration along the specimen.

Velocity-stress parameter β and the stretching factor θ . The stretching factor θ between two consecutive signals gathered at stresses σ'_A and σ'_B reflects the stress-dependent velocity change. Indeed, combining Equations A1 and A2 yields

$$\theta = 1 - \left(\frac{\sigma'_B}{\sigma'_A} \right)^\beta \quad (\text{A5})$$

This result anticipates the ability of coda waves to resolve changes in mean stress smaller than 1% in uncemented sands (assumes $\theta = 0.001$ and $\beta = 0.25$).

A4.2 Creep in dry sandy specimen

Computed wave velocities in the sand specimen tested during the creep stage follow a power law with time (Figure 7b):

$$V_p = a \left(\frac{t}{t_{ref}} \right)^b = 292.5 \left(\frac{t}{1 \text{ min}} \right)^{0.0021} \quad (\text{A6})$$

where the parameter a is the P -wave velocity under constant confinement at the reference time t_{ref} (in this case $t_{ref} = 1 \text{ min}$), and the exponent b reflects the rate of creep-dependent stiffening. Both a and b are experimentally determined parameters, and are inherently governed by confining conditions and sediment characteristics.

The creep strain rate $\dot{\varepsilon}$ of a particulate medium at constant effective stress is a function of stress σ' and time t [Mitchell and Soga, 2005; Singh and Mitchell, 1968]:

$$\dot{\varepsilon} = k \left[\frac{\sigma'}{\sigma'_{ref}} \right]^m \left[\frac{t_{ref}}{t} \right]^n \quad (\text{A7})$$

where k , m , and n are sediment-dependent parameters, and σ'_{ref} and t_{ref} are the reference stress and time. At the particle level, the tangential normal stiffness E_T in a Hertzian system can be related to the axial strain ε_Z as (simple cubic packing - [Cascente and Santamarina, 1996; Richart et al., 1970]):

$$E_T = \frac{G_m}{1 - \nu_m} \varepsilon_Z^{1/2} \quad (\text{A8})$$

where G_m and ν_m are the shear modulus and Poisson's ratio of the material that makes the grains. The strain at time t is obtained by integrating Equation 7, and it is replaced in Equation 8 to obtain a general expression for the evolution of velocity during soil creep

as a function of stress σ' and time t :

$$V_P = \sqrt{\frac{E}{\rho}} = \sqrt{\frac{G_m}{\rho(1-\nu_m)}} \left(\frac{k \cdot t_{ref}}{1-n} \right)^{\frac{1}{4}} \left(\frac{\sigma'}{\sigma_{ref}} \right)^{\frac{m}{4}} \left(\frac{t}{t_{ref}} \right)^{\frac{1-n}{4}} \quad (A9)$$

Most soils have an n value that ranges between 0.75 and 1 ([Singh and Mitchell, 1968]; lower values reported in [Campanella and Vaid, 1974; Singh and Mitchell, 1969]). The fitted n value for the quartzitic sand tested in this study is $n = 0.9916$ (compare equations A6 and A9), indicating a slow velocity change with time under a confinement of 68.9kPa.

A5. Discussion: Underlying Assumptions in Coda Analysis

Basic coda analysis presumes that changes in the medium cause identical proportional velocity changes $\Delta V/V$ on all wave paths and propagation modes. In particular, P - and S -wave velocities must be equally affected by the process, i.e., V_P/V_S remains constant and θ values for P and S components are identical $\theta_P = \theta_S$. This condition applies to dry or unsaturated soils. In saturated soils, the P -wave velocity is primarily controlled by the fluid bulk modulus; thus, only a minor increase in $\Delta V_P/V_{P_0}$ takes place during loading while the change in $\Delta V_S/V_{S_0}$ can be large.

We highlight that basic coda analysis reveals the relative stretching factor between two waveforms. An absolute wave travel time is required as reference value to determine velocity and velocity changes. Typically, the waveform with the clearest first arrival is selected to determine the reference travel time.

A6. Conclusions

Slight velocity changes in a soil specimen that cause undetectable changes in the first arrival may be measured using coda wave analysis. Values smaller than $\Delta V/V <$

0.1% were detected in this study.

The proportional change in velocity is mathematically equal to the stretching factor $\theta = \Delta V/V$. There are robust signal processing algorithms to determine the stretching factor θ between consecutive signals. They involve the cross correlation of either (1) short-time windows, (2) time-stretched signals, or (3) frequency-stretched spectra.

Basic coda wave analysis applies to systems with homogeneous velocity changes and constant V_p/V_s ratio. This is the case in dry and partially saturated soils.

The high velocity resolution attained with coda wave analysis allows for the determination of wave velocities during small stress changes, creep, diagenesis, and aging, where subtle contact-level processes can only be detected by high resolution signal interpretation. Coda wave analysis can resolve a $\Delta\sigma'/\sigma' < 1\%$ change in mean effective stress.

Self weight induces an inhomogeneous stress distribution inside of a specimen. Data reduction must consider gravity effects when the boundary effective stress is less than 10 times the gravity-induced stress.

In agreement with existing creep models, experimental results show that velocity increases during soil creep under constant confinement and follows a power law as a function of time. The exponent can be readily measured using coda wave analysis even when stable quartzitic sands are tested for relatively short duration.

APPENDIX B: POROELASTIC MANDEL-CRYER EFFECT

The theory of poroelasticity originates from 1D soil consolidation [Terzaghi, 1923], then extends to 3D consolidation by considering Darcy's law and fluid-solid coupling [Biot, 1941], pore pressure coefficients [Skempton, 1954], undrained Poisson's ratio of bulk materials [Rice and Cleary, 1976], and coupled poroviscoelastic theory [Abousleiman et al., 1996]. Refer to [Detournay and Cheng, 1993] for an comprehensive review on the development of poroelasticity theory.

Governing equations: A set of governing equations of isotropic poroelastic materials in Cartesian coordinates can be described as follow [Abousleiman and Kanj, 2004; Biot, 1941; Cui and Abousleiman, 2001; Detournay and Cheng, 1993; Kanj and Abousleiman, 2004; Rice and Cleary, 1976]:

- Stress-strain response:

$$\sigma_{ij} = 2G\varepsilon_{ij} + \lambda\varepsilon_v\sigma_{ij} - \alpha\delta_{ij}u \quad (B1)$$

- Pore pressure-volumetric strain relationship:

$$u = M(\zeta - \alpha\varepsilon_v) \quad (B2)$$

- Equilibrium equations (for a cylindrical specimen):

$$\begin{cases} \frac{\partial\sigma_{rr}}{\partial r} + \frac{1}{r}\frac{\partial\sigma_{r\theta}}{\partial\theta} + \frac{\sigma_{rr} - \sigma_{\theta\theta}}{r} = 0 \\ \frac{\partial\sigma_{r\theta}}{\partial r} + \frac{1}{r}\frac{\partial\sigma_{\theta\theta}}{\partial\theta} + 2\frac{\sigma_{r\theta}}{r} = 0 \end{cases} = 0 \quad (B3)$$

- Strain-displacement (kinematic) relationship:

$$\varepsilon_{ij} = \frac{w_{i,j} + w_{j,i}}{2} \quad (B4)$$

- Fluid continuity:

$$\frac{\partial\zeta}{\partial t} + \frac{k}{\mu}\nabla^2 u = 0 \quad (B5)$$

- Darcy's law:

$$q_i = -\frac{k}{\mu} u_{,i} \quad (\text{B6})$$

These equations (B1-B6) can be manipulated to obtain new equations in terms of pore fluid change, which is intimately related with pore pressure:

$$\nabla^2 \left(\zeta - \frac{GS}{\eta} \varepsilon \right) = 0 \quad (\text{B7})$$

$$\frac{\partial \zeta}{\partial t} - c(\nabla^2 \zeta) = 0 \quad (\text{B8})$$

where, S is the storage coefficient of the saturated porous media; η is the poroelastic stress coefficient; and c is the diffusivity coefficient. All these parameters, including the Biot's effective stress coefficient M , are functions of material properties [Detournay and Cheng, 1993; Kanj and Abousleiman, 2004]:

$$\alpha = \frac{3(v_u - \nu)}{B(1 - 2\nu)(1 + \nu_u)} \quad (\text{B9})$$

$$S = \frac{\alpha^2(1 - \nu_u)(1 - 2\nu)^2}{2G(1 - \nu)(\nu_u - \nu)} \quad (\text{B10})$$

$$\eta = \frac{\alpha(1 - 2\nu)}{2(1 - \nu)} \quad (\text{B11})$$

$$M = \frac{2G(\nu_u - \nu)}{\alpha^2(1 - 2\nu)(1 - 2\nu_u)} \quad (\text{B12})$$

$$c = \frac{2kG(1 - \nu)(\nu_u - \nu)^2}{\mu\alpha^2(1 - \nu_u)(1 - 2\nu)} = \frac{k}{\mu} \frac{1}{S} \quad (\text{B13})$$

Model description: Here we investigate the pore pressure variation in a cylindrical water-saturated specimen (with radius R) after instant effective stress relaxation while maintaining neighboring water pressure constant, simulating the stress conditions of pressure core sampling. This specimen is initially subjected to a pore pressure of u_0 and a vertical effective stress of $\Delta\sigma$ under zero lateral strain conditions. Thus, vertical stress relaxation on this specimen resembles a uniaxial tension test. Therefore, the boundary conditions (i.e., at $r = R$, where r is the distance

from the center of the specimen) are

$$\begin{cases} \sigma_{rr}|_R = 0 \\ u|_R = u_0 \\ \sigma_{r\theta} = \sigma_{rz} = 0 \end{cases} \quad (\text{B14})$$

Moreover, symmetry in geometry and stress conditions gives

$$\begin{cases} \sigma_{r\theta} = \sigma_{\theta z} = 0 \\ \gamma_{r\theta} = \gamma_{\theta z} = 0 \end{cases} \quad (\text{B15})$$

Therefore, equations B8 can be expressed for a cylindrical specimen with above-mentioned conditions as

$$\frac{\partial \zeta}{\partial t} - c \left(\frac{\partial^2 \zeta}{\partial r^2} + \frac{1}{r} \frac{\partial \zeta}{\partial r} \right) = 0 \quad (\text{B16})$$

the Laplace transform of which is

$$\frac{d^2 \tilde{\zeta}}{dr^2} + \frac{1}{r} \frac{d\tilde{\zeta}}{dr} - \frac{s}{c} \tilde{\zeta} = 0 \quad (\text{B17})$$

where $\tilde{}$ denotes the Laplace transform, and s is the Laplace transform parameter [Carslaw and Jaeger, 1959]. Thus, the partial differential equation (B14) is turned into an ordinary differential equation (B17) in Laplace form with a solution as:

$$\tilde{\zeta} = A_1 I_0(r\sqrt{s/c}) \quad (\text{B17})$$

where, A_1 is an arbitrary function of s ; I_0 is the modified Bessel function of the first kind of order zero. Similarly, equation B7 can be manipulated in this way together with other governing equations (B1 and B3) and boundary conditions (Equation B14) to yield

$$\tilde{u} = M \left(1 - \frac{\alpha\eta}{GS} \right) A_1 I_0(r\sqrt{s/c}) - \alpha M A_2 \quad (\text{B18})$$

where,

$$A_1 = \frac{2\eta(1-\nu)(1-\nu_u)}{GD} \left[\frac{\eta(1-\nu)(1+\nu_u)}{\nu_u - \nu} \tilde{u}_o - \frac{\Delta\tilde{\sigma}}{2} \right],$$

$$A_2 = I_0(r\sqrt{s/c}) \frac{(1-\nu)(1-2\nu_u)}{GD} \left[\frac{4\eta I_1(r\sqrt{s/c})}{r\sqrt{s/c} I_0(r\sqrt{s/c})} \tilde{u}_o - \frac{\Delta\tilde{\sigma}}{2} \right],$$

$$D = (1-\nu)(1+\nu_u) I_0(r\sqrt{s/c}) - 4(\nu_u - \nu) \frac{I_1(r\sqrt{s/c})}{r\sqrt{s/c}}.$$

APPENDIX C: PT-DEPENDENT METHANE SOLUBILITY IN WATER

The following analysis assumes (1) a closed system with constant volume, i.e., isochoric analysis; (2) properties of hydrate (e.g., cage occupancy) existed before PT change remains unchanged afterward; (3) properties of newly crystallized hydrate depend on final PT conditions. Therefore, here we focus on the changes in the methane saturated liquid phase, in which the ratio of the molecular numbers (in mole) of water M_{H_2O} , methane M_{CH_4} , and sodium chloride M_{NaCl} before PT change is:

$$M_{H_2O} : M_{CH_4} : M_{NaCl} = \frac{1kg}{18.0153g/mol} : x_{CH_4} \times 1kg : 0.6mol = 55.508 : \left(\frac{x_{CH_4}}{mol/kg} \right) : 0.6 \quad (C1)$$

where x_{CH_4} is the methane solubility (unit: mol/kg) in water with the presence of methane hydrate. This value as a function of pressure P (in MPa) and temperature T (in K) is obtained by surface fitting of data generated by Duan's model [Duan and Mao, 2006; Duan et al., 1992; Sun and Duan, 2005; 2007]:

$$x_{CH_4} = a_{00} + a_{10}P + a_{01}T + a_{20}P^2 + a_{11}PT + a_{02}T^2 + a_{30}P^3 + a_{21}P^2T + a_{12}PT^2 + a_{03}T^3 \quad (C2)$$

The fitting coefficient for fresh water are $a_{00} = -9.1888E+1$; $a_{10} = -4.7606E-2$; $a_{01} = 1.0235$; $a_{20} = -1.6949E-5$; $a_{11} = 3.6239E-4$; $a_{02} = -3.8107E-3$; $a_{30} = -3.6663E-9$; $a_{21} = 6.6497E-8$; $a_{12} = -6.9339E-7$; $a_{03} = 4.7447E-6$; and for seawater are $a_{00} = -8.4258E+1$; $a_{10} = -4.9049E-2$; $a_{01} = 9.4112E-1$; $a_{20} = -1.9999E-5$; $a_{11} = 3.7414E-4$; $a_{02} = -3.5135E-3$; $a_{30} = -4.2837E-9$; $a_{21} = 7.8354E-8$; $a_{12} = -7.1714E-7$; $a_{03} = 4.3864E-6$.

Decreasing pressure increases methane solubility in water with the presence of methane hydrate. Freed methane gas may combine with water molecules and form hydrate within the hydrate stability zone. However, mass conservation suggests the total number of methane (M_{CH_4}) and water (M_{H_2O}) molecules before and after PT change are identical:

$$\begin{cases} x_{CH_4} \times 1kg = M_{CH_4}^H + M_{CH_4}^L \\ 55.508mol = M_{H_2O}^H + M_{H_2O}^L \end{cases} \quad (C3)$$

where, superscripts H represents newly nucleated hydrate phase and L for liquid phase.

Meanwhile, the ratio between methane and water molecules in the liquid phase is determined by methane solubility after PT change x_{CH_4}' (unit: mol/kg):

$$\frac{M_{CH_4}^L}{M_{H_2O}^L} = \frac{x_{CH_4}' \times 1kg}{55.508mol} \quad (C4)$$

And this ratio in the hydrate phase is governed by the stoichiometric composition of newly nucleated hydrate:

$$\frac{M_{CH_4}^H}{M_{H_2O}^H} = \frac{2\theta_1 + 6\theta_2}{46} \quad (C5)$$

where θ_1 and θ_2 are the fractional occupancy of methane molecules in small and large cages. There values can be computed as:

$$\theta_i = C_i f / (1 + \sum C_i f), \quad i = 1, 2. \quad (C6)$$

where C_i is the temperature (unit: K) dependent Langmuir constant of methane in i -type cavity [Sun and Duan, 2007]; f is the fugacity of methane in hydrate phase which is governed by pressure and temperature state [Duan et al., 1992].

The combination of Equations B3, B4, and B5 renders the number (in *mole*) of methane in newly formed hydrate phase as a function of final PT state:

$$M_{CH_4}^H = \frac{(2\theta_1 + 6\theta_2) \times 55.508mol \times (x_{CH_4} - x_{CH_4}') \times 1kg}{(2\theta_1 + 6\theta_2) \times 55.508mol - 46x_{CH_4}' \times 1kg} = f(P, T) \quad (C7)$$

Thus, the volume (unit: cc) of the newly crystallized hydrate is:

$$V_H = \frac{M_{CH_4}^H}{2\theta_1 + 6\theta_2} \times N_A \times V_{cell} \quad (C8)$$

where N_A is the Avogadro's number $N_A = 60.23 \times 10^{23} \text{ mol}^{-1}$; V_{cell} is the volume of a unit sl methane hydrate cell $V_{cell} = (12 \times 10^{-8})^3 \text{ cc}$ [Sloan and Koh, 2008].

Also, the volume of the liquid phase after PT change can be computed as [Duan and Mao, 2006]:

$$V_L = \frac{18.0153M_{H_2O}^L + 58.443 \times 0.6}{\rho_w} + x_{CH_4}' \overline{V}_{CH_4} \quad (C9)$$

where $M_{H_2O}^L$ is the number of water molecules (in mole) in liquid phase after PT change, the value of which can also be computed through Equations B3, B4, and B5; ρ_w is the water density as a function of temperature and salinity (Here we use the empirical equation from [McCutcheon *et al.*, 1993]); \overline{V}_{CH_4} is the partial molar volume of methane (refer to [Sun and Mohanty, 2006] for detailed calculation).

Finally, the hydrate saturation after PT change S_H can be determined as:

$$S_H = S_{H_0} + (1 - S_{H_0}) \frac{V_H}{V_H + V_L} \quad (C10)$$

REFERENCES

- Abegg, F., H. J. Hohnberg, T. Pape, G. Bohrmann, and J. Freitag (2008), Development and application of pressure-core-sampling systems for the investigation of gas- and gas-hydrate-bearing sediments, *Deep Sea Research Part I: Oceanographic Research Papers*, 55(11), 1590-1599.
- Abousleiman, Y., A. H. D. Cheng, C. Jiang, and J. C. Roegiers (1996), Poroviscoelastic analysis of borehole and cylinder problems, *Acta Mechanica*, 119(1), 199-219.
- Abousleiman, Y. N., and M. Y. Kanj (2004), The generalized Lamé problem-Part II: applications in poromechanics, *Transactions of the ASME*, 71, 180-189.
- Acar, Y. B., and E.-T. A. El-Tahir (1986), Low strain dynamic properties of artificially cemented sand, *Journal of Geotechnical Engineering*, 112(11), 1001-1015.
- Aker, E., K. J. MÅløy, A. Hansen, and G. G. Batrouni (1998), A two-dimensional network simulator for two-phase flow in porous media, *Transport in Porous Media*, 32(2), 163-186.
- Aki, K. (1969), Analysis of the seismic coda of local earthquakes as scattered waves, *Journal of Geophysical Research*, 74(2), 615-631.
- Aki, K., and B. Chouet (1975), Origin of coda waves: Source, attenuation, and scattering effects, *Journal of Geophysical Research*, 80(23), 3322-3342.
- Akkermans, C., P. Venema, S. Rogers, A. van der Goot, R. Boom, and E. van der Linden (2006), Shear Pulses Nucleate Fibril Aggregation, *Food Biophysics*, 1(3), 144-150.
- Al-Adel, S., J. A. G. Dick, R. El-Ghafari, and P. Servio (2008), The effect of biological and polymeric inhibitors on methane gas hydrate growth kinetics, *Fluid Phase Equilibria*, 267(1), 92-98.
- Al-Kharusi, A. S., and M. J. Blunt (2007), Network extraction from sandstone and carbonate pore space images, *Journal of Petroleum Science and Engineering*, 56(4), 219-231.
- Amann, H., H. J. Hohnberg, and R. Reinelt (1997), HYACE - a novel autoclave coring equipment for systematic offshore gashydrate sampling *Rep.*, 37-49 pp, Technische Univ. Berlin (Germany). Inst. fuer Schiffs- und Meerestechnik, Fachgebiet Maritime Technik.
- Andersland, O. B., and B. Ladanyi (2004), *Frozen ground engineering*, 2nd ed., John Wiley & Sons, Inc.
- Anderson, R., M. Llamedo, B. Tohidi, and R. W. Burgass (2003), Experimental measurement of methane and carbon dioxide clathrate hydrate equilibria in mesoporous silica, *The Journal of Physical Chemistry B*, 107(15), 3507-3514.
- Archer, D. (2007), Methane hydrate stability and anthropogenic climate change, *Biogeosciences Discussions*, 4(2), 993-1057.
- Arroyo, M., D. Muir Wood, P. D. Greening, L. Medina, and J. Rio (2006), Effects of sample size on bender-based axial G (sub 0) measurements, *Geotechnique*, 56(1), 39-52.
- Arthur, E., P. Moldrup, P. Schjønning, and L. W. de Jonge (2012), Linking Particle and Pore Size Distribution Parameters to Soil Gas Transport Properties, *Soil Science*

- Society of America Journal*, 76(1), 18-27.
- Arya, L. M., and J. F. Paris (1981), A physicoempirical model to predict the soil moisture characteristic from particle-size distribution and bulk density data, *Soil Science Society of America Journal*, 45(6), 1023-1030.
- Asami, K. (2005), Simulation of dielectric relaxation in periodic binary systems of complex geometry, *Journal of Colloid and Interface Science*, 292(1), 228-235.
- Assouline, S. (2001), A model for soil relative hydraulic conductivity based on the water retention characteristic curve, *Water Resources Research*, 37(2), 265-271.
- Assouline, S. (2006), Modeling the Relationship between Soil Bulk Density and the Water Retention Curve Contribution of the Agricultural Research Organization, Institute of Soil, Water and Environmental Sciences, Bet Dagan, Israel, No. 607/05, *Vadose Zone J.*, 5(2), 554-563.
- Atkinson, J. H., M. A. Allman, and R. J. Boese (1992), Influence of laboratory sample preparation procedures on the strength and stiffness of intact Bothkennar soil recovered using the Laval sampler, *Geotechnique*, 42(2), 349-354.
- Aubertin, M., M. Mbonimpa, B. Bussi re, and R. P. Chapuis (2003), A model to predict the water retention curve from basic geotechnical properties, *Canadian Geotechnical Journal*, 40(6), 1104-1122.
- Baig, S., and M. Picornell (1997), Low strain shear moduli of cemented sands, *Journal of Geotechnical & Geoenvironmental Engineering*, 123(6), 540.
- Baligh, M. M. (1985), Strain Path Method, *Journal of Geotechnical & Geoenvironmental Engineering*, 111(9).
- Baligh, M. M., A. S. Azzouz, and C. T. Chin (1987), Disturbances due to 'ideal' tube sampling, *Journal of Geotechnical Engineering*, 113(7), 739-757.
- Banerjee, V., A. K. Mittal, K. Agarwal, A. K. Uniyal, and K. Chandra (1994), Carbon isotope geochemistry of petroleum-associated gases in Krishna-Godavari Basin, India, *Organic Geochemistry*, 21(3-4), 373-382.
- Barbee, G., and K. Brown (1986), Comparison Between Suction and Free-Drainage Soil Solution Samplers¹, *Soil science*, 141(2), 149-154.
- Barbour, S. L. (1998), Nineteenth Canadian Geotechnical Colloquium: The soil-water characteristic curve: a historical perspective, *Canadian Geotechnical Journal*, 35(5), 873-894.
- Barrer, R. M., and A. V. J. Edge (1967), Gas Hydrates Containing Argon, Krypton and Xenon: Kinetics and Energetics of Formation and Equilibria, *Proceedings of the Royal Society of London. Series A. Mathematical and Physical Sciences*, 300(1460), 1-24.
- Bastia, R., and P. K. Nayak (2006), Tectonostratigraphy and depositional patterns in Krishna offshore basin, Bay of Bengal, *The Leading Edge*, 25(7), 839-845.
- Basu, S. (1990), Clay mineralogy and pressure analysis from seismic information in Krishna-Godavari basin, India, *Geophysics*, 55(11), 1447-1454.
- Baxter, C. D. P., M. S. Ravi Sharma, K. Moran, H. Vaziri, and R. Narayanasamy (2011), Use of $A=0$ as a Failure Criterion for Weakly Cemented Soils, *Journal of Geotechnical & Geoenvironmental Engineering*, 137(2), 161-170.

- Beck, M., O. Dellwig, K. Kolditz, H. Freund, G. Liebezeit, B. Schnetger, and H.-J. Brumsack (2007), In situ pore water sampling in deep intertidal flat sediments, *Limnology and oceanography: Methods*, 5, 136-144.
- Berg, P., and K. J. McGlathery (2001), A high-resolution pore water sampler for sandy sediments, *Limnology and Oceanography*, 46(1), 203-210.
- Berge, P. A., B. P. Bonner, C. Aracne-Ruddle, C. Trombino, and J. G. Berryman (1999), Compressional and shear wave velocities of soils at low pressures; theoretical estimates, and comparison to laboratory and field data, Seismological Society of America, Eastern Section, [Berkeley, CA], United States (USA), United States (USA), April 1999.
- Berryman, J. G. (1980), Long wavelength propagation in composite elastic media I. Spherical inclusions, *The Journal of the Acoustical Society of America*, 68, 1809.
- Berryman, J. G. (1995), Mixture theories for rock properties, *Rock physics and phase relations*, 205-228.
- Bertolin, A., D. Rudello, and P. Ugo (1995), A new device for in-situ pore-water sampling, *Marine Chemistry*, 49(2), 233-239.
- Biot, M. A. (1941), General theory of three-dimensional consolidation, *Journal of Applied Physics*, 12(2), 155-164.
- Bird, K. J. (1981), Machine-generated displays of well logs and lithology from selected wells on the North Slope of Alaska; 7 wells from the east-central North Slope *Rep. 81-1036*, U.S. Geological Survey
- Bird, K. J. (1999), Geographic and Geologic Setting in The Oil and Gas Resource Potential of the Arctic National Wildlife Refuge 1002 Area, Alaska *Rep. 98-34*, ANWR Assessment Team: U.S. Geological Survey.
- Bischoff, J. L., R. E. Greer, and A. O. Luistro (1970), Composition of interstitial waters of marine sediments: temperature of squeezing effect, *Science*, 167(3922), 1245-1246.
- Bjerrum, L. (1973), Problems of soil mechanics and construction of soft clays: State-of-the-Art Report to Session 4, in *8th International Conference on Soil Mechanics and Foundation Engineering*, edited, pp. 111-159, Moscow.
- Blackwell, V. R. (1999), Formation processes of clathrate hydrates of carbon dioxide and methane, California Institute of Technology.
- Blunt, M. J. (2001), Flow in porous media—pore-network models and multiphase flow, *Current opinion in colloid & interface science*, 6(3), 197-207.
- Bolliger, R., H. Brandl, P. Höhener, K. W. Hanselmann, and R. Bachofen (1992), Squeeze-water analysis for the determination of microbial metabolites in lake sediments-- comparison of methods, *Limnology and Oceanography*, 37(2), 448-455.
- Boswell, R. (2009), Is Gas Hydrate Energy Within Reach?, *Science*, 325(5943), 957-958.
- Boswell, R., and T. S. Collett (2011), Current perspectives on gas hydrate resources, *Energy & environmental science*, 4(4), 1206-1215.
- Brady, N. C., and R. R. Weil (2007), *The Nature and Properties of Soils*, 14th ed., Pearson Prentice Hall.
- Brigham, K. K., and G. H. Miller (1983), Paleotemperature estimates of the Alaskan

- Arctic Coastal Plain during the last 125,000 years, paper presented at 4th International Conference on Permafrost, National Academy Press, Fairbanks, Alaska, 17-22 July.
- Brooks, R. H., and A. T. Corey (1964), Hydraulic properties of porous media, *Hydrology Papers, No.3, Colorado State University, Fort Collins, Co.* (March).
- Brown, R. J. E. (1970), *Permafrost in Canada*, University of Toronto Press, Toronto.
- Buffett, B., and D. Archer (2004), Global inventory of methane clathrate: sensitivity to changes in the deep ocean, *Earth and Planetary Science Letters*, 227(3-4), 185-199.
- BujakResearchInternational (2008), Palynological biostratigraphy of the interval 1990-2484ft Mount Elbert 01 well Northern Alaska *Rep.*, 23 pp.
- Burger, C. A., and C. D. Shackelford (2001), Evaluating dual porosity of pelletized diatomaceous earth using bimodal soil-water characteristic curve functions, *Canadian Geotechnical Journal*, 38(1), 53-66.
- Burland, J. B. (1990), On the compressibility and shear strength of natural clays, *Géotechnique*, 40(3), 329-378.
- Campanella, R., and Y. P. Vaid (1974), Triaxial and plane strain creep rupture of an undisturbed clay, *Canadian Geotechnical Journal*, 11(1), 1-10.
- Campbell, G. S. (1974), A simple method for determining unsaturated conductivity from moisture retention data, *Soil science*, 117(6), 311-314.
- Cao, P.-l., K. Yin, J.-m. Peng, and J.-l. Liu (2007), Optimization Design and Finite Element Analysis of Core Cutter, *Journal of China University of Mining and Technology*, 17(3), 399-402.
- Carman, G. J., and P. Hardwick (1983), Geology and regional setting of Kuparuk oil field, Alaska *AAPG Bulletin (American Association of Petroleum Geologists)*, 67(6), 1014-1031.
- Carslaw, H. S., and J. C. Jaeger (1959), *Conduction of heat in solids*, 2nd ed., 510 pp., Oxford, Clarendon Press.
- Casavant, R. R., et al. (2004), Reservoir-fluid characterization and reservoir modeling of potential gas hydrate resources, Alaska North Slope, *CSPG Annual Convention, 2004*.
- Cascante, G., and J. C. Santamarina (1996), Interparticle contact behavior and wave propagation, *Journal of Geotechnical Engineering*, 122(10), 831-839.
- Cha, S. B., H. Ouar, T. R. Wildeman, and E. D. Sloan (1988), A third-surface effect on hydrate formation, *The Journal of Physical Chemistry*, 92(23), 6492-6494.
- Chau, K. W. (1991), Correlation of sampling effect in Hong Kong, Publ by A.A. Balkema, Bangkok, Thailand.
- Chiu, C. F., W. M. Yan, and K.-V. Yuen (2012), Estimation of water retention curve of granular soils from particle-size distribution — a Bayesian probabilistic approach, *Canadian Geotechnical Journal*, 49(9), 1024-1035.
- Cho, G.-C., J. Dodds, and J. C. Santamarina (2006), Particle shape effects on packing density, stiffness, and strength; natural and crushed sands, *Journal of Geotechnical and Geoenvironmental Engineering*, 132(5), 591-602.
- Cho, G., J. Lee, and J. Santamarina (2004), Spatial Variability in Soils: High Resolution Assessment with Electrical Needle Probe, *Journal of Geotechnical and Geoenvironmental Engineering*, 130(8), 843-850.

- Cho, G. C., and J. C. Santamarina (2001), Unsaturated Particulate Materials---Particle-Level Studies, *Journal of Geotechnical and Geoenvironmental Engineering*, 127(1), 84-96.
- Chung, S. G., J. M. Kwag, P. H. Giao, S. H. Baek, and K. N. Prasad (2004), A study of soil disturbance of Pusan clays with reference to drilling, sampling and extruding, *Geotechnique*, 54(Compendex), 61-65.
- Clayton, C. R. I., and A. Siddique (1999), Tube sampling disturbance-forgotten truths and new perspectives, *Proceedings of the Institution of Civil Engineers: Geotechnical Engineering*, 137(Compendex), 127-135.
- Clayton, C. R. I., A. Siddique, and R. J. Hopper (1998), Effects of sampler design on tube sampling disturbance-numerical and analytical investigations, *Geotechnique*, 48(Compendex), 847-867.
- Clennell, B. M., M. Hovland, J. S. Booth, P. Henry, and W. J. Winters (1999), Formation of natural gas hydrates in marine sediments 1. Conceptual model of gas hydrate growth conditioned by host sediment properties, *J. Geophys. Res.*, 104(B10), 22985-23003.
- Clough, G. W., N. S. Rad, R. C. Bachus, and N. Sitar (1981), Cemented sands under static loading, *Journal of the Geotechnical Engineering Division*, 107(6), 799-817.
- Collett, T., M. Riedel, R. Boswell, J. Cochran, P. Kumar, A. Sethi, and A. Sathe (2006), International team completes landmark gas hydrate expedition in the offshore of India, *Fire in the Ice*, 1-4.
- Collett, T., M. Riedel, J. Cochran, R. Boswell, J. Presley, P. Kumar, A. Sathe, A. Sethi, M. Lall, and V. Sibal (2008a), Indian national gas hydrate program expedition 01 initial reports, *Gen. of Hydrocarbons, Noida, India*.
- Collett, T. S. (2002), Energy resource potential of natural gas hydrates, *AAPG Bulletin*, 86(11), 1971-1992.
- Collett, T. S., K. J. Bird, and L. B. Magoon (1993), Subsurface temperatures and geothermal gradients on the north slope of Alaska, *Cold Regions Science and Technology*, 21(3), 275-293.
- Collett, T. S., K. J. Bird, K. A. Kvenvolden, and L. B. Magoon (1988), Geologic interrelations relative to gas hydrates within the North Slope of Alaska *Rep. 88-389*, U.S. Geological Survey.
- Collett, T. S., K. J. Bird, K. A. Kvenvolden, and M. W. Lee (1990), Terrestrial gas hydrate occurrences. , paper presented at Proc. Nat. Gas. R. D. Contr. Rev. Meeting, DOE/METC-91/6117.
- Collett, T. S., A. H. Johnson, C. C. Knapp, and R. Boswell (2009), Natural gas hydrates: a review.
- Collett, T. S., M. W. Lee, W. F. Agena, D. J. Miller, D. J. Taylor, T. D. Lorenson, W. J. Winters, and W. F. Waite (2008b), Energy source potential of gas hydrates on the North Slope of Alaska-Project briefing, edited, BP-DOE Gas Hydrate Meeting presentation on March 08.
- Consoli, N. C., A. Viana da Fonseca, R. C. Cruz, and K. S. Heineck (2009), Fundamental Parameters for the Stiffness and Strength Control of Artificially Cemented Sand,

- Journal of Geotechnical & Geoenvironmental Engineering*, 135(9), 1347-1353.
- Consoli, N. C., R. C. Cruz, M. F. Floss, and L. Festugato (2010), Parameters Controlling Tensile and Compressive Strength of Artificially Cemented Sand, *Journal of Geotechnical & Geoenvironmental Engineering*, 136(5), 759-763.
- Cook, A. E., D. Goldberg, and R. L. Kleinberg (2008), Fracture-controlled gas hydrate systems in the northern Gulf of Mexico, *Marine and Petroleum Geology*, 25(9), 932-941.
- Corey, A. T. (1954), The interrelation between gas and oil relative permeabilities, *Producers Monthly*, 19(1), 38-41.
- Cosby, B., G. Hornberger, R. Clapp, and T. Ginn (1984), A statistical exploration of the relationships of soil moisture characteristics to the physical properties of soils, *Water Resources Research*, 20(6), 682-690.
- Coussy, O. (2011), *Mechanics and physics of porous solids*, Wiley.
- Cryer, C. W. (1963), A comparison of the three dimensional consolidation theories of Biot and Terzaghi, *The Quarterly Journal of Mechanics and Applied Mathematics*, 16(4), 401-412.
- Cui, L., and Y. Abousleiman (2001), Time-dependent poromechanical responses of saturated cylinders *Journal of Engineering Mechanics*, 127(4), 391-398.
- Dai, S., C. Lee, and J. Carlos Santamarina (2011), Formation history and physical properties of sediments from the Mount Elbert Gas Hydrate Stratigraphic Test Well, Alaska North Slope, *Marine and Petroleum Geology*, 28(2), 427-438.
- Dai, S., F. Wuttke, and J. C. Santamarina (2013), Coda wave analysis to monitor processes in soils, *Journal of Geotechnical and Geoenvironmental Engineering*.
- Dai, S., J. C. Santamarina, W. F. Waite, and T. J. Kneafsey (2012), Hydrate morphology: Physical properties of sands with patchy hydrate saturation, *Journal of Geophysical Research: Solid Earth*, 117(B11).
- Daigle, H., and B. Dugan (2010), Origin and evolution of fracture-hosted methane hydrate deposits, *J. Geophys. Res.*, 115(B11), B11103.
- Davidson, D. W., S. K. Garg, S. R. Gough, Y. P. Handa, C. I. Ratcliffe, J. A. Ripmeester, J. S. Tse, and W. F. Lawson (1986), Laboratory analysis of a naturally occurring gas hydrate from sediment of the Gulf of Mexico, *Geochimica et Cosmochimica Acta*, 50(4), 619-623.
- Day, R. W. (1990), Sample disturbance of collapsible soil, *Journal of Geotechnical Engineering*, 116(Compendex), 158-161.
- De Lange, G., R. Cranston, D. Hydes, and D. Boust (1992), Extraction of pore water from marine sediments: A review of possible artifacts with pertinent examples from the North Atlantic, *Marine Geology*, 109(1), 53-76.
- DeJong, J. T., M. B. Fritzges, and K. Nüsslein (2006), Microbially Induced Cementation to Control Sand Response to Undrained Shear, *Journal of Geotechnical & Geoenvironmental Engineering*, 132(11), 1381-1392.
- Delage, P., M. Howat, and Y. Cui (1998), The relationship between suction and swelling properties in a heavily compacted unsaturated clay, *Engineering Geology*, 50(1), 31-48.

- Delude, N. A. (1997), Effect of calcite cementation on permeability and heterogeneity Sierra Ladrones Formation, New Mexico, Monographic thesis, 159 pp, University of New Hampshire, Durham.
- Detournay, E., and A. H. D. Cheng (1993), *Fundamentals of poroelasticity*, 113-171 pp., Pergamon Press, Oxford, United Kingdom (GBR), United Kingdom (GBR).
- Dickens, G. R., D. Schroeder, K. U. Hinrichs, and the Leg201 Scientific Party (2003), The Pressure Core Sampler (PCS) on ODP Leg201: General operations and gas release, in *Proceedings of the Ocean Drilling Program, Initial Reports*, edited by S. L. D'Hondt, B. B. Jørgensen and D. J. e. a. Miller.
- Dickens, G. R., M. Koelling, D. C. Smith, and L. Schnieders (2007), Rhizon sampling of pore waters on scientific drilling expeditions: an example from the IODP Expedition 302, Arctic Coring Expedition (ACEX), *Sci Drill*, 4, 22-25.
- Dominguez, A., S. Bories, and M. Prat (2000), Gas cluster growth by solute diffusion in porous media. Experiments and automaton simulation on pore network, *International Journal of Multiphase Flow*, 26(12), 1951-1979.
- Downey, M. W. (1984), Evaluating seals for hydrocarbon accumulations *AAPG Bulletin*, 68(11), 1752-1763.
- Duan, Z., and S. Mao (2006), A thermodynamic model for calculating methane solubility, density and gas phase composition of methane-bearing aqueous fluids from 273 to 523 K and from 1 to 2000 bar, *Geochimica et Cosmochimica Acta*, 70(13), 3369-3386.
- Duan, Z., N. Møller, and J. H. Weare (1992), An equation of state for the CH₄-CO₂-H₂O system: I. Pure systems from 0 to 1000°C and 0 to 8000 bar, *Geochimica et Cosmochimica Acta*, 56(7), 2605-2617.
- Durham, W. B., S. H. Kirby, L. A. Stern, and W. Zhang (2003), The strength and rheology of methane clathrate hydrate, *J. Geophys. Res.*, 108(B4), 2182.
- Dutton, S. P. D., Timothy N (1992), Evolution of porosity and permeability in the Lower Cretaceous Travis Peak Formation, East Texas, *AAPG Bulletin*, 76(2), 252-269.
- Dvorkin, J., M. B. Helgerud, W. F. Waite, S. H. Kirby, and A. Nur (2003), Introduction to physical properties and elasticity models, in *Natural Gas Hydrate*, edited, pp. 245-260, Springer.
- Eberhardt, E., D. Stead, and B. Stimpson (1999), Effects of sample disturbance on the stress-induced microfracturing characteristics of brittle rock, *Canadian Geotechnical Journal*, 36(Compendex), 239-250.
- Elias, S. A., and J. V. Matthews Jr (2002), Arctic North American seasonal temperatures from the latest Miocene to the Early Pleistocene, based on mutual climatic range analysis of fossil beetle assemblages, *Canadian Journal of Earth Sciences*, 39(6), 911-920.
- Elsenbeer, H. (2001), Pedotransfer functions in hydrology, *Journal of Hydrology*, 251, 121-122.
- Englezos, P., and S. Hall (1994), Phase equilibrium data on carbon dioxide hydrate in the presence of electrolytes, water soluble polymers and montmorillonite, *The Canadian Journal of Chemical Engineering*, 72(5), 887-893.

- Ersland, G., J. Husebø, A. Graue, B. A. Baldwin, J. Howard, and J. Stevens (2010), Measuring gas hydrate formation and exchange with CO₂ in Bentheim sandstone using MRI tomography, *Chemical Engineering Journal*, 158(1), 25-31.
- Fanning, K. A., and M. E. Pilson (1971), Interstitial silica and pH in marine sediments: Some effects of sampling procedures, *Science*, 173(4003), 1228-1231.
- Farrell, D. A., and W. E. Larson (1972), Modeling the pore structure of porous media, *Water Resources Research*, 8(3), 699-706.
- Fatt, I. (1956), The network model of porous media I. Capillary pressure characteristics, *Trans. AIME*, 207(7), 144-159.
- Fernandez, A. L., and J. C. Santamarina (2001), Effect of cementation on the small-strain parameters of sands, *Can. Geotech. J.*, 38(1), 191-199.
- Fischer, U., and M. A. Celia (1999), Prediction of relative and absolute permeabilities for gas and water from soil water retention curves using a pore-scale network model, *Water Resources Research*, 35(4), 1089-1100.
- Fletcher, N. H. (1958), Size Effect in Heterogeneous Nucleation, *The Journal of Chemical Physics*, 29(3), 572-576.
- Francisca, F., and P. Arduino (2007), Immiscible Displacement Model for Anisotropic and Correlated Porous Media, *International Journal of Geomechanics*, 7(4), 311-317.
- Frederiksen, N. O., V. A. Andriele, T. P. Sheehan, T. A. Ager, T. S. Collett, T. D. Fouch, K. J. Franczyk, and J. M. J. (1998), Palynological dating of Upper Cretaceous to middle Eocene strata in the Sagavanirktok and Canning formations, North Slope of Alaska. *Rep. 98-471*, U.S. Geological Survey
- Fredlund, D., A. Xing, and S. Huang (1994), Predicting the permeability function for unsaturated soils using the soil-water characteristic curve, *Canadian Geotechnical Journal*, 31(4), 533-546.
- Fredlund, D. G., and H. Rahardjo (1993a), *Soil mechanics for unsaturated soils*, John Wiley & Sons.
- Fredlund, D. G., and H. Rahardjo (1993b), An overview of unsaturated soil behavior, *Geotechnical Special Publication*(39), 1.
- Fredlund, D. G., and A. Xing (1994), Equations for the soil-water characteristic curve, *Canadian Geotechnical Journal*, 31(4), 521-532.
- Fredlund, D. G., A. Xing, M. D. Fredlund, and S. L. Barbour (1996), The relationship of the unsaturated soil shear to the soil-water characteristic curve, *Canadian Geotechnical Journal*, 33(3), 440-448.
- Gardner, W. (1958), Some steady-state solutions of the unsaturated moisture flow equation with application to evaporation from a water table, *Soil science*, 85(4), 228-232.
- Gens, A., and E. Alonso (1992), A framework for the behaviour of unsaturated expansive clays, *Canadian Geotechnical Journal*, 29(6), 1013-1032.
- Ghanbarian-Alavijeh, B., and A. G. Hunt (2012), Estimation of soil-water retention from particle-size distribution: Fractal approaches, *Soil science*, 177(5), 321.
- Ghanbarian-Alavijeh, B., A. Liaghat, G.-H. Huang, and M. T. Van Genuchten (2010), Estimation of the van Genuchten soil water retention properties from soil textural

- data, *Pedosphere*, 20(4), 456-465.
- Giao, P. H., N. Phien-Wej, and H. Tanaka (2004), An assessment on soil disturbance of Bangkok clay samples in relation with the intrinsic compression behavior, *Lowland Technology International*, 6(Compendex), 21-31.
- Gornitz, V., and I. Fung (1994), Potential distribution of methane hydrates in the world's oceans, *Global Biogeochem. Cycles*, 8(3), 335-347.
- Grantz, A., M. L. Holmes, and B. A. Kososki (1975), Geologic framework of the Alaskan continental terrace in the Chukchi and Beaufort Sea in Canada's continental margins and offshore petroleum exploration., in *Canadian Society of Petroleum Geologists Memoir 4*, edited by Yorath, Parker and Glass, pp. 669-700.
- Grantz, A., S. Eittreim, and D. A. Dinter (1979), Geology and tectonic development of the continental margin north of Alaska, *Tectonophysics*, 59(1-4), 263-291.
- Gret, A. A. (2004), Time-lapse monitoring with coda wave interferometry, Ph.D. thesis, n/a pp.
- Grozic, J. L. H. (2010), Interplay between gas hydrates and submarine slope failure, in *Submarine Mass Movements and Their Consequences: Advances in Natural and Technological Hazards Research*, edited by D. C. Mosher, L. Moscardelli, C. D. P. Baxter, R. Urgeles, R. C. Shipp, J. D. Chaytor and H. J. Lee, pp. 11-30, Springer Netherlands.
- Gupta, S. (2006), Basin architecture and petroleum system of Krishna Godavari Basin, east coast of India, *The Leading Edge*, 25(7), 830-837.
- Handa, Y. P., and D. Y. Stupin (1992), Thermodynamic properties and dissociation characteristics of methane and propane hydrates in 70-Å-radius silica gel pores, *The Journal of Physical Chemistry*, 96(21), 8599-8603.
- Hashin, Z., and S. Shtrikman (1962), A variational approach to the theory of the effective magnetic permeability of multiphase materials, *Journal of Applied Physics*, 33(10), 3125-3131.
- Hashin, Z., and S. Shtrikman (1963), A variational approach to the theory of the elastic behaviour of multiphase materials, *Journal of the Mechanics and Physics of Solids*, 11(2), 127-140.
- Haverkamp, R., and J.-Y. Parlange (1986), Predicting the Water-Retention Curve From Particle-Size Distribution: 1. Sandy Soils Without Organic Matter, *Soil science*, 142(6), 325-339.
- Hemmingsen, B. B., and E. A. Hemmingsen (1980), Rupture of the cell envelope by induced intracellular gas phase expansion in gas vacuolate bacteria, *Journal of Bacteriology*, 143(2), 841-846.
- Hennes, A. (2004), Structural Constraints on Gas-hydrate Formation and Distribution in the Milne Point, North Slope of Alaska, M.S. Thesis, University of Arizona, Arizona.
- Henry, P., M. Thomas, and M. B. Clennell (1999), Formation of natural gas hydrates in marine sediments: 2. Thermodynamic calculations of stability conditions in porous sediments, *Journal of Geophysical Research: Solid Earth (1978-2012)*, 104(B10), 23005-23022.
- Hesslein, R. H. (1976), An in situ sampler for close interval pore water studies,

- Limnology and Oceanography*, 21(6).
- Hight, D. W., R. Boese, A. P. Butcher, C. R. I. Clayton, and P. R. Smith (1992), Disturbance of the Bothkennar clay prior to laboratory testing, *Geotechnique*, 42(Compendex), 199-217.
- Hird, C. C., and A. R. Hajj (1995), Simulation of tube sampling effects on the stiffness of clays, *Geotechnical Testing Journal*, 18(Compendex), 3-14.
- Hobbs, P. V. (1974), *Ice physics*, Clarendon Press.
- Holland, M., P. J. Schultheiss, J. Roberts, and M. Druce (2008), Observed gas hydrate morphologies in marine sediments, paper presented at the 6th International Conference on Gas Hydrates, Vancouver, Canada, July 6-10.
- Hong, H., and M. Pooladi-Darvish (2005), Simulation of depressurization for gas production from gas hydrate reservoirs, *Journal of Canadian Petroleum Technology*, 44(11).
- Hornbach, M. J., L. L. Lavier, and C. D. Ruppel (2007), Triggering mechanism and tsunamogenic potential of the Cape Fear Slide complex, U.S. Atlantic margin, *Geochem. Geophys. Geosyst.*, 8(12), Q12008.
- Howes, B. L., J. W. Dacey, and S. G. Wakeham (1985), Effects of sampling technique on measurements of porewater constituents in salt marsh sediments, *Limnology and Oceanography*, 221-227.
- Huang, G.-H., R.-D. Zhang, and Q.-Z. Huang (2006), Modeling soil water retention curve with a fractal method, *Pedosphere*, 16(2), 137-146.
- Hunter, R. B., S. L. Patil, R. R. Casavant, and T. S. Collet (2005), Resource Characterization and Quantification of Natural Gas-Hydrate and Associated Free-Gas Accumulations in the Prudhoe Bay – Kuparuk River Area on the North Slope of Alaska Rep. DE-FC-01NT41332, U.S. DOE/NETL.
- Hunter, R. B., T. S. Collett, R. Boswell, B. J. Anderson, S. A. Digert, G. Pospisil, R. Baker, and M. Weeks (2011), Mount Elbert Gas Hydrate Stratigraphic Test Well, Alaska North Slope: Overview of scientific and technical program, *Marine and Petroleum Geology*, 28(2), 295-310.
- Husowitz, B., and V. Talanquer (2004), Nucleation in cylindrical capillaries, *Journal of Chemical Physics*, 121(16), 8021-8028.
- Hvorslev, M. J. (1949), Subsurface exploration and sampling of soils for civil engineering purposes Rep., 521 pp, the Committee on Sampling and Testing, Soil Mechanics and Foundations Division, American Society of Civil Engineers.
- Inks, T. L., M. W. Lee, W. F. Agena, D. J. Taylor, T. S. Collett, M. V. Zyrianova, and R. B. Hunter (2008), Seismic prospecting for gas hydrate and associated free-gas prospects in the Milne Point area of northern Alaska, in *Natural gas hydrates—Energy resource potential and associated geologic hazards: AAPG Memoir 89*, edited by T. S. Collett, A. Johnson, C. Knapp and R. Boswell, pp. 1-29.
- Ismail, M. A., H. A. Joer, W. H. Sim, and M. F. Randolph (2002), Effect of Cement Type on Shear Behavior of Cemented Calcareous Soil, *Journal of Geotechnical & Geoenvironmental Engineering*, 128(6), 520.
- Iwasaki, H., K. Uchida, K. Nakamura, and T. Suzuki (2005), Continuous natural gas

- hydrate pellet production by process development unit, paper presented at the Fifth International Conference on Gas Hydrates, Trondheim, Norway, June 13-16.
- Jamison, H. C., L. D. Brockett, and R. A. McIntosh (1980), Prudhoe Bay - a 10 year perspective, in *Giant oil and gas fields of the decade 1986-1978: AAPG Memoir 30*, edited by M. T. Halbouty, pp. 289-314.
- Jang, J. (2011), Gas production from hydrate-bearing sediments, Georgia Institute of Technology, Atlanta.
- Jang, J., G. A. Narsilio, and J. C. Santamarina (2011), Hydraulic conductivity in spatially varying media—a pore-scale investigation, *Geophysical Journal International*, 184(3), 1167-1179.
- Jannasch, H. W., C. G. Wheat, J. N. Plant, M. Kastner, and D. S. Stakes (2004), Continuous chemical monitoring with osmotically pumped water samplers: OsmoSampler design and applications, *Limnol. Oceanogr. Methods*, 2, 102-113.
- Jin, S., J. Nagao, S. Takeya, Y. Jin, J. Hayashi, Y. Kamata, T. Ebinuma, and H. Narita (2006), Structural investigation of methane hydrate sediments by microfocus X-ray computed tomography technique under high-pressure conditions, *Japanese Journal of Applied Physics*, 45, L714-L716.
- Jung, J.-W., J. C. Santamarina, and K. Soga (2012), Stress-strain response of hydrate-bearing sands: Numerical study using discrete element method simulations, *J. Geophys. Res.*, 117(B4), B04202.
- Jung, J. W., and J. C. Santamarina (2011), Hydrate adhesive and tensile strengths, *Geochem. Geophys. Geosyst.*, 12(8), Q08003.
- Jung, J. W., D. N. Espinoza, and J. C. Santamarina (2010), Properties and phenomena relevant to CH₄-CO₂ replacement in hydrate-bearing sediments, *J. Geophys. Res.*, 115(B10), B10102.
- Jung, J. W., J. Jang, J. C. Santamarina, C. Tsouris, T. J. Phelps, and C. J. Rawn (2011), Gas Production from Hydrate-Bearing Sediments: The Role of Fine Particles, *Energy & Fuels*.
- Kalil, E. K., and M. Goldhaber (1973), A sediment squeezer for removal of pore waters without air contact, *Journal of Sedimentary Research*, 43(2).
- Kanj, M. Y., and Y. N. Abousleiman (2004), The generalized Lamé problem - Part I: coupled poromechanical solutions, *Transactions of the ASME*, 71, 168-179.
- Kaufman, D. S., et al. (2004), Holocene thermal maximum in the western Arctic (0–180°C), *Quaternary Science Reviews*, 23(5–6), 529-560.
- Kawasaki, M., S. Umezumi, and M. Yasuda (2006), Pressure temperature core sampler (PTCS), *Journal of the Japanese Association for Petroleum Technology*, 71(1), 139-147.
- Kennett, J. P., K. G. Cannariato, I. L. Hendy, and R. J. Behl (2000), Carbon isotopic evidence for methane hydrate instability during Quaternary interstadials, *Science*, 288(5463), 128-133.
- Kerker, P., K. W. Jones, R. Kleinberg, W. B. Lindquist, S. Tomov, H. Feng, and D. Mahajan (2009), Direct observations of three dimensional growth of hydrates hosted in porous media, *Applied Physics Letters*, 95(2), 3.

- Khan, Z., A. Majid, G. Cascante, D. J. Hutchinson, and P. Pezeshkpour (2006), Characterization of a cemented sand with the pulse-velocity method, *Canadian Geotechnical Journal*, 43(3), 294-309.
- Kimoto, S., F. Oka, T. Fushita, and M. Fujiwaki (2007), A chemo-thermo-mechanically coupled numerical simulation of the subsurface ground deformations due to methane hydrate dissociation, *Computers and Geotechnics*, 34(4), 216-228.
- Kimura, T., and K. Saitoh (1984), Effect of sampling disturbance on undrained strength of cohesive soils, *Geotechnical Engineering*, 15(Compendex), 37-57.
- Kleinberg, R. L., C. Flaum, D. D. Griffin, P. G. Brewer, G. E. Malby, E. T. Peltzer, and J. P. Yesinowski (2003), Deep sea NMR: Methane hydrate growth habit in porous media and its relationship to hydraulic permeability, deposit accumulation, and submarine slope stability, *J. Geophys. Res.*, 108(B10), 2508.
- Kneafsey, T. J. (2010), Analysis of core samples from the BPXA-DOE-USGS Mount Elbert gas hydrate stratigraphic test well: Insights into core disturbance and handling, edited.
- Knight, R., and R. Nolen-Hoeksema (1990), A laboratory study of the dependence of elastic wave velocities on pore scale fluid distribution, *Geophysical Research Letters*, 17(10), 1529-1532.
- Koh, C. A., A. K. Sum, and E. D. Sloan (2009), Gas hydrates: Unlocking the energy from icy cages, *Journal of Applied Physics*, 106(6), 061101-061114.
- Kosugi, K. i. (1994), Three-parameter lognormal distribution model for soil water retention, *Water Resour. Res.*, 30(4), 891-901.
- Kovács, G. (2011), *Seepage hydraulics*, Elsevier Science.
- Krinsley, D. H., and J. C. Doornkamp (1973), *Atlas of quartz sand surface textures*, Cambridge University Press, Cambridge.
- Krishna, M. R., S. Chand, and C. Subrahmanyam (2000), Gravity anomalies, sediment loading and lithospheric flexure associated with the Krishna–Godavari basin, eastern continental margin of India, *Earth and Planetary Science Letters*, 175(3–4), 223-232.
- Krumbein, W. C., and L. L. Sloss (1963), *Stratigraphy and Sedimentation*, 2nd ed., W. H. Freeman and Company, San Francisco.
- Kuhs, W. F., G. Genov, D. K. Staykova, and T. Hansen (2004), Ice perfection and onset of anomalous preservation of gas hydrates, *Physical Chemistry Chemical Physics*, 6(21), 4917-4920.
- Kuster, G. T., and M. N. Toksöz (1974), Velocity and attenuation of seismic waves in two-phase media: Part I. Theoretical formulations, *Geophysics*, 39(5), 587-606.
- Kvalstad, T. J., L. Andresen, C. F. Forsberg, K. Berg, P. Bryn, and M. Wangen (2005), The Storegga slide: evaluation of triggering sources and slide mechanics, *Marine and Petroleum Geology*, 22(1–2), 245-256.
- Kvenvolden, K. A. (1988), Methane hydrate—a major reservoir of carbon in the shallow geosphere?, *Chemical Geology*, 71(1), 41-51.
- Kvenvolden, K. A., and T. D. Lorenson (2001), The global occurrence of natural gas hydrate, in *Natural Gas Hydrates: Occurrence, Distribution, and Detection*, edited, pp. 3-18, AGU, Washington, DC.

- Kvenvolden, K. A., L. A. Barnard, and D. H. Cameron (1983), Pressure core barrel: application to the study of gas hydrates, in *Init. Repts. DSDP*, edited by R. E. Sheridan, F. M. Gradstein and et al., pp. 367-375, U.S. Govt. Printing Office, Washington.
- Kwon, T.-H., G.-C. Cho, and J. C. Santamarina (2008), Gas hydrate dissociation in sediments: Pressure-temperature evolution, *Geochem. Geophys. Geosyst.*, 9(3), Q03019.
- La Rochelle, P., J. Sarrailh, F. Tavenas, M. Roy, and S. Leroueil (1980), Causes of sampling disturbance and design of design of a new sampler for sensitive soils, paper presented at 33rd Canadian Geotechnical Conference: Problems and Progress in Geotechnical Engineering, Preprint Volume., Calgary, Alberta, Can.
- Lachenbruch, A. H., J. H. Sass, B. V. Marshall, and T. H. Moses, Jr. (1982), Permafrost, Heat Flow, and the Geothermal Regime at Prudhoe Bay, Alaska, *J. Geophys. Res.*, 87, 9301-9316.
- Ladd, C. C., and D. J. DeGroot (2003), Recommended practice for soft ground site characterization: Arthur Casagrande Lecture, paper presented at Proc. 12th Panamerican Conf. on Soil Mechanics and Geotechnical Engineering, MIT.
- Landon, M. M. (2007), Development of a non-destructive sample quality assessment method for soft clays, 3275806 thesis, University of Massachusetts Amherst, United States -- Massachusetts.
- Landon, M. M., D. J. DeGroot, and T. C. Sheahan (2007), Nondestructive sample quality assessment of a soft clay using shear wave velocity, *Journal of Geotechnical and Geoenvironmental Engineering*, 133(4), 424-432.
- Lapham, L. L., J. P. Chanton, C. S. Martens, P. D. Higley, H. W. Jannasch, and J. R. Woolsey (2008), Measuring Temporal Variability in Pore-Fluid Chemistry To Assess Gas Hydrate Stability: Development of a Continuous Pore-Fluid Array, *Environmental Science & Technology*, 42(19), 7368-7373.
- Lee, J.-S., and J. C. Santamarina (2005a), Bender elements: performance and signal interpretation, *Journal of Geotechnical and Geoenvironmental Engineering*, 131(9), 1063-1070.
- Lee, J.-S., and J. C. Santamarina (2005b), P-wave reflection imaging, *Geotechnical Testing Journal*, 28(2).
- Lee, J., J. C. Santamarina, and C. Ruppel (2010a), Parametric study of the physical properties of hydrate-bearing sand, silt, and clay sediments: 1. Electromagnetic properties, *Journal of Geophysical Research: Solid Earth (1978–2012)*, 115(B11).
- Lee, J. Y. (2007), Hydrate-bearing sediments: formation and geophysical properties, Georgia Institute of Technology, Atlanta, GA.
- Lee, J. Y., J. C. Santamarina, and C. Ruppel (2008), Mechanical and electromagnetic properties of northern Gulf of Mexico sediments with and without THF hydrates, *Marine and Petroleum Geology*, 25(9), 884-895.
- Lee, J. Y., J. C. Santamarina, and C. Ruppel (2010b), Volume change associated with formation and dissociation of hydrate in sediment, *Geochem. Geophys. Geosyst.*, 11(3), Q03007.

- Lee, J. Y., T. S. Yun, J. C. Santamarina, and C. Ruppel (2007), Observations related to tetrahydrofuran and methane hydrates for laboratory studies of hydrate-bearing sediments, *Geochem. Geophys. Geosyst.*, 8(6), Q06003.
- Lee, J. Y., P. J. Schultheiss, M. Druce, and J. Lee (2009a), Pressure core sub sampling for GH production tests at in situ effective stress, *Fire in the Ice Newsletter*, 9(4), 16-17.
- Lee, M.-J., S.-K. Choi, and W. Lee (2009b), Shear Strength of Artificially Cemented Sands, *Marine Georesources & Geotechnology*, 27(3), 201-216.
- Lee, M. W., and T. S. Collett (2009), Gas hydrate saturations estimated from fractured reservoir at Site NGHP-01-10, Krishna-Godavari Basin, India, *Journal of Geophysical Research: Solid Earth*, 114(B7), B07102.
- Lee, M. W., and T. S. Collett (2011), In-situ gas hydrate hydrate saturation estimated from various well logs at the Mount Elbert Gas Hydrate Stratigraphic Test Well, Alaska North Slope, *Marine and Petroleum Geology*, 28(2), 439-449.
- Lenormand, R. (1989), Flow through porous media: limits of fractal patterns, *Proceedings of the Royal Society of London. A. Mathematical and Physical Sciences*, 423(1864), 159-168.
- Lerand, M. (1973), Beaufort Sea, in *The Future Petroleum Provinces of Canada-Their Geology and Potential: Canadian Society of Petroleum Geologists Memoir 1*, edited by R. G. McCrossan, pp. 315-386.
- Levadoux, J.-N., and M. M. Baligh (1980), *Pore pressures during cone penetration in clays*, Massachusetts Institute of Technology, Sea Grant College Program, Cambridge.
- Li, X., L. Zhong, and L. J. Pyrak-Nolte (2001), Physics of partially saturated porous media: Residual saturation and seismic-wave propagation, *Annual Review of Earth and Planetary Sciences*, 29(1), 419-460.
- Li, X. S., J. Holland, G. Wang, and C. J. Roblee (1997), Analysis of stress-change disturbance caused by ideal drilling in clay, *Journal of Geotechnical and Geoenvironmental Engineering*, 123(Compendex), 626-634.
- Liang, K., G. White, D. Wilkinson, L. J. Ford, K. J. Roberts, and W. M. L. Wood (2004), Examination of the Process Scale Dependence of L-Glutamic Acid Batch Crystallized from Supersaturated Aqueous Solutions in Relation to Reactor Hydrodynamics, *Industrial & Engineering Chemistry Research*, 43(5), 1227-1234.
- Lin, W., G. J. Chen, C. Y. Sun, X. Q. Guo, Z. K. Wu, M. Y. Liang, L. T. Chen, and L. Y. Yang (2004), Effect of surfactant on the formation and dissociation kinetic behavior of methane hydrate, *Chemical Engineering Science*, 59(21), 4449-4455.
- Lo, K. Y., and M. Roy (1973), Response of particulate materials at high pressures, *Soils and Foundations*, 13(1), 61-76.
- Loder, T., W. Lyons, S. Murray, and H. McGuinness (1978), Silicate in anoxic pore waters and oxidation effects during sampling.
- Long, M. (2003), Sampling disturbance effects in soft laminated clays, *Proceedings of the Institution of Civil Engineers: Geotechnical Engineering*, 156(Compendex), 213-224.
- Looney, B. B., and R. W. Falta (2000), *Vadose zone science and technology solutions*,

- Battelle Press, Columbus, OH.
- Lorenson, T. D., T. S. Collett, and R. B. Hunter (2008), Preliminary Assessment of Hydrocarbon Gas Sources from the Mt. Elbert No.1 Gas Hydrate Test Well, Milne Pt. Alaska, in *6th International Conference on Gas Hydrate*, edited.
- Lu, N., and W. J. Likos (2004), *Unsaturated soil mechanics*, J. Wiley.
- Lunardini, V. J. (1995), Permafrost formation time. *Rep. CRREL 95-8*.
- Lunne, T., T. Berre, K. H. Andersen, S. Strandvik, and M. Sjørusen (2006), Effects of sample disturbance and consolidation procedures on measured shear strength of soft marine Norwegian clays, *Canadian Geotechnical Journal*, 43(7), 726-750.
- Mahaney, W. C. (2002), *Atlas of sand grain surface textures and applications*, Oxford University Press, Inc., New York.
- Mahaney, W. C., and V. Kalm (1996), Field guide, in *the International Conference on Quaternary Glaciation and Paleoclimate*, edited, Quaternary Survey, Toronto.
- Makemson, J. C. (1972), An interstitial water sampler for sandy beaches, *LIMNOLOGY AND OCEANOGRAPHY, VOL 17, NO 4, P 626-628, JULY 1972. 2 FIG, 3 REF.*
- Malinverno, A. (2010), Marine gas hydrates in thin sand layers that soak up microbial methane, *Earth and Planetary Science Letters*, 292(3), 399-408.
- Mandel, J. (1953), Consolidation des sols, *Geotechnique*, 3, 287-299.
- Marshall, T. J., J. W. Holmes, and C. W. Rose (1996), *Soil physics*, Cambridge University Press.
- Masterson, W. D., L. I. P. Dzou, A. G. Holba, A. L. Fincannon, and L. Ellis (2001), Evidence for biodegradation and evaporative fractionation in West Sak, Kuparuk and Prudhoe Bay field areas, North Slope, Alaska, *Organic Geochemistry*, 32(3), 411-441.
- Matheus, P., J. Begét, O. Mason, and C. Gelvin-Reymiller (2003), Late Pliocene to late Pleistocene environments preserved at the Palisades Site, central Yukon River, Alaska, *Quaternary Research*, 60(1), 33-43.
- Mavko, G., and T. Mukerji (1998), Bounds on low-frequency seismic velocities in partially saturated rocks, *Geophysics*, 63(3), 918-924.
- McCutcheon, S. C., J. L. Martin, and T. O. Barnwell, Jr. (1993), Water quality, in *Handbook of Hydrology*, edited by D. R. Maidment, p. 1424, McGraw-Hill.
- McDowell, G. R. (1999), Micromechanics of Clastic Soil, in *Proceedings of the International Workshop on Soil Crushability*, edited, pp. 138-157, Yamaguchi, Japan.
- McIver, R. D. (1981), Gas hydrates, in *Long term energy resources*, edited by R. F. Meyer and J. C. Olson, pp. 713-726, Pitman.
- Melia, T. P., and W. P. Moffitt (1964), Secondary Nucleation from Aqueous Solution, *Industrial & Engineering Chemistry Fundamentals*, 3(4), 313-317.
- Melnikov, V. P., A. N. Nesterov, A. M. Reshetnikov, and A. G. Zavodovsky (2009), Evidence of liquid water formation during methane hydrates dissociation below the ice point, *Chemical Engineering Science*, 64(6), 1160-1166.
- Melnikov, V. P., A. N. Nesterov, A. M. Reshetnikov, V. A. Istomin, and V. G. Kwon (2010), Stability and growth of gas hydrates below the ice-hydrate-gas equilibrium

- line on the P–T phase diagram, *Chemical Engineering Science*, 65(2), 906-914.
- Milkov, A. V. (2004), Global estimates of hydrate-bound gas in marine sediments: how much is really out there?, *Earth-Science Reviews*, 66(3-4), 183-197.
- Miller, C. J., N. Yesiller, K. Yaldo, and S. Merayyan (2002), Impact of soil type and compaction conditions on soil water characteristic, *Journal of Geotechnical and Geoenvironmental Engineering*, 128(9), 733-742.
- Mitchell, J. K., and K. Soga (2005), *Fundamentals of soil behavior*, 3rd ed., Wiley, New York.
- Montgomery, J. R., M. T. Price, J. Holt, and C. Zimmermann (1981), A close-interval sampler for collection of sediment pore waters for nutrient analyses, *Estuaries*, 4(1), 75-77.
- Moridis, G., S. Silpngarmert, M. Reagan, T. Collett, and K. Zhang (2011), Gas production from a cold, stratigraphically-bounded gas hydrate deposit at the Mount Elbert Gas Hydrate Stratigraphic Test Well, Alaska North Slope: Implications of uncertainties, *Marine and Petroleum Geology*, 28(2), 517-534.
- Moridis, G. J., and E. D. Sloan (2007), Gas production potential of disperse low-saturation hydrate accumulations in oceanic sediments, *Energy Conversion and Management*, 48(6), 1834-1849.
- Moridis, G. J., M. B. Kowalsky, and K. Pruess (2008), TOUGH+ HYDRATE v1. 0 user's manual: A code for the simulation of system behavior in hydrate-bearing geologic media, *Report LBNL-00149E*, Lawrence Berkeley National Laboratory, Berkeley, CA.
- Mualem, Y. (1986), Hydraulic conductivity of unsaturated soils: prediction and formulas, in *Methods of soil analysis. Part I. Physical and mineralogical methods*, edited by A. Klute, pp. 799-823.
- Mullin, J. W. (2001), *Crystallization*, Butterworth-Heinemann.
- Mullin, J. W., and K. D. Raven (1962), Influence of Mechanical Agitation on the Nucleation of Some Aqueous Salt Solutions, *Nature*, 195(4836), 35-38.
- Murray, B. J., and A. K. Bertram (2006), Formation and stability of cubic ice in water droplets, *Physical Chemistry Chemical Physics*, 8(1), 186-192.
- Myerson, A. (2002), *Handbook of industrial crystallization*, Butterworth-Heinemann.
- Nakata, Y., M. Hyodo, A. F. L. Hyde, Y. Kato, and H. Murata (2001), Microscopic Particle Crushing of Sand Subjected to One-Dimensional Compression, *Soils and Foundations*, 41(1), 69-82.
- Nayar, S., D. Miller, S. Bryars, and A. Cheshire (2006), A simple, inexpensive and large volume pore water sampler for sandy and muddy substrates, *Estuarine, Coastal and Shelf Science*, 66(1), 298-302.
- Nimblett, J., and C. Ruppel (2003), Permeability evolution during the formation of gas hydrates in marine sediments, *J. Geophys. Res.*, 108(B9), 2420.
- Nuth, M., and L. Laloui (2008), Advances in modelling hysteretic water retention curve in deformable soils, *Computers and Geotechnics*, 35(6), 835-844.
- Öberg, A.-L., and G. Sällfors (1997), Determination of shear strength parameters of unsaturated silts and sands based on the water retention curve, *ASTM geotechnical*

- testing journal*, 20(1), 40-48.
- Olague Caballero, R. I. (2008), Oedometric and shearing response of naturally cemented sands of southern New Mexico, 179 pp, New Mexico State University Las Cruces.
- Olivella, S., J. Carrera, A. Gens, and E. Alonso (1994), Nonisothermal multiphase flow of brine and gas through saline media, *Transport in Porous Media*, 15(3), 271-293.
- Olson, R., and D. Daniel (1981), Measurement of the hydraulic conductivity of fine-grained soils, *Permeability and groundwater contaminant transport, ASTM STP*, 746, 18-64.
- Østergaard, K. K., R. Anderson, M. Llamedo, and B. Tohidi (2002), Hydrate phase equilibria in porous media: effect of pore size and salinity, *Terra Nova*, 14(5), 307-312.
- Osterkamp, T. E., and J. P. Gosink (1991), Variations in Permafrost Thickness in Response to Changes in Paleoclimate, *J. Geophys. Res.*, 96.
- Otheim, T. L., L. Adam, K. van Wijk, M. L. Batzle, T. McLing, and R. Podgorney (2011), CO₂ sequestration in basalt: Carbonate mineralization and fluid substitution, *The Leading Edge*, 30(12), 1354-1359.
- Page, A. J., and R. P. Sear (2006), Heterogeneous nucleation in and out of pores, *Physical Review Letters*, 97(6).
- Parent, S.-É., A. Cabral, and J. G. Zornberg (2007), Water retention curve and hydraulic conductivity function of highly compressible materials, *Canadian Geotechnical Journal*, 44(10), 1200-1214.
- Park, C. B., and D. S. Clark (2002), Rupture of the Cell Envelope by Decompression of the Deep-Sea Methanogen *Methanococcus jannaschii*, *Applied and Environmental Microbiology*, 68(3), 1458-1463.
- Park, S.-H., and G. Sposito (2003), Do montmorillonite surfaces promote methane hydrate formation? Monte carlo and molecular dynamics simulations, *The Journal of Physical Chemistry B*, 107(10), 2281-2290.
- Parkes, R. J., G. Sellek, G. Webster, D. Martin, E. Anders, A. J. Weightman, and H. Sass (2009), Culturable prokaryotic diversity of deep, gas hydrate sediments: first use of a continuous high-pressure, anaerobic, enrichment and isolation system for seafloor sediments (DeepIsoBUG), *Environmental Microbiology*, 11(12), 3140-3153.
- Parrish, J. M., J. T. Parrish, J. H. Hutchison, and R. A. Spicer (1987), Late Cretaceous Vertebrate Fossils from the North Slope of Alaska and Implications for Dinosaur Ecology, *PALAIOS*, 2(4), 377-389.
- Peat, D. M. W., G. P. Matthews, P. J. Worsfold, and S. C. Jarvis (2000), Simulation of water retention and hydraulic conductivity in soil using a three-dimensional network, *European Journal of Soil Science*, 51(1), 65-79.
- Pedarla, A., A. Puppala, L. Hoyos, S. Vanapalli, and C. Zapata (2012), SWRC Modelling Framework for Evaluating Volume Change Behavior of Expansive Soils, in *Unsaturated Soils: Research and Applications*, edited by C. Mancuso, C. Jommi and F. D'Onza, pp. 221-228, Springer Berlin Heidelberg.
- Perrier, E., M. Rieu, G. Sposito, and G. Marsily (1996), Models of the water retention curve for soils with a fractal pore size distribution, *Water Resources Research*,

- 32(10), 3025-3031.
- Pestana, J. M., and L. A. Salvati (2006), Small-Strain Behavior of Granular Soils. I: Model for Cemented and Uncemented Sands and Gravels, *Journal of Geotechnical & Geoenvironmental Engineering*, 132(8), 1071-1081.
- Petrovic, J. J. (2003), Review Mechanical properties of ice and snow, *Journal of Materials Science*, 38(1), 1-6.
- Pettigrew, T. L. (1992), The design and operation of a wireline pressure core sampler (PCS)Rep., ODP Tech. Note, 17.
- Phadnis, H. S., and J. C. Santamarina (2011), Bacteria in sediments: pore size effects, *Géotechnique Letters*, Nov., 91-93.
- Pozdniakov, S., and C.-F. Tsang (2004), A self-consistent approach for calculating the effective hydraulic conductivity of a binary, heterogeneous medium, *Water Resour. Res.*, 40(5), W05105.
- Pratt, R. M. (1979), Gas hydrate evaluation and recommendations, National Petroleum Reserve, Alaska Rep. TC-7916, 27 pp, U.S. Geological Survey.
- Qin, H., L. Gu, S. Li, L. Zhu, and Y. Chen (2005), Pressure tight piston corere - a new approach on gas hydrate investigation, *China Ocean Engineering*, 19(1), 121-128.
- Quintal, B., M. Frehner, C. Madonna, N. Tisato, M. Kuteynikova, and E. H. Saenger (2011), Integrated numerical and laboratory rock physics applied to seismic characterization of reservoir rocks, *The Leading Edge*, 30(12), 1360-1367.
- Rao, G. (2001), Sedimentation, stratigraphy, and petroleum potential of Krishna-Godavari basin, East Coast of India, *AAPG Bulletin*, 85(9), 1623-1643.
- Rao, G., and K. Mani (1993), A study on generation of abnormal pressures in Krishna Godavari basin, *India: Indian Journal of Petroleum Geology*, 2(1), 20-30.
- Rawls, W., T. Gish, and D. Brakensiek (1991), Estimating soil water retention from soil physical properties and characteristics, in *Advances in soil science*, edited, pp. 213-234, Springer.
- Reagan, M. T., and G. J. Mordis (2008), Dynamic response of oceanic hydrate deposits to ocean temperature change, *Journal of Geophysical Research: Oceans*, 113(C12), C12023.
- Rees, E. V. L., J. A. Priest, and C. R. I. Clayton (2011), The structure of methane gas hydrate bearing sediments from the Krishna–Godavari Basin as seen from Micro-CT scanning, *Marine and Petroleum Geology*, 28(7), 1283-1293.
- Reimnitz, E., S. C. Wolf, and C. A. Rodeick (1972), Preliminary interpretation of seismic profiles in the Prudhoe Bay area, Beaufort Sea, Alaska. Rep. 72-312, U.S. Geological Survey.
- Reiser, H. N., W. P. Brosge, J. T. Dutro, and R. L. Dettman (1978), Geologic map of the Demarcation Point Quadrangle, Alaska. Rep. 72-312, U.S. Geological Survey.
- Restagno, F., L. Bocquet, and T. Biben (2000), Metastability and Nucleation in Capillary Condensation, *Physical Review Letters*, 84(11), 2433-2436.
- Rhoades, J. D. (1982), Soluble salts, in *Methods of Soil Analysis, Part 2. Chemical and Microbiological Properties*, edited by A. L. Page, p. 1159.
- Rice, J. R., and M. P. Cleary (1976), Some basic stress-diffusion solutions for fluid-

- saturated elastic porous media with compressible constituents, *Reviews of Geophysics and Space Physics*, 14(2), 227-241.
- Richart, F. E., J. R. Hall, and R. D. Woods (1970), Vibrations of soils and foundations.
- Ridley, A., and W. Wray (1996), Suction measurement: a review of current theory and practices, paper presented at Proceedings of the First International Conference on Unsaturated Soils, Unsat '95, Paris, France.
- Riesterberg, D., O. West, S. Lee, S. McCallum, and T. J. Phelps (2003), Sediment surface effects on methane hydrate formation and dissociation, *Marine Geology*, 198(1-2), 181-190.
- Rinaldi, V. A., and J. C. Santamarina (2008), Cemented soils: small strain stiffness, in *Deformational Characteristics of Geomaterials*, edited, pp. 267-273, Atlanta, GA.
- Risgaard-Petersen, N., A. M. Langezaal, S. Ingvarsen, M. C. Schmid, M. S. Jetten, H. J. O. den Camp, J. W. Derksen, E. Piña-Ochoa, S. P. Eriksson, and L. P. Nielsen (2006), Evidence for complete denitrification in a benthic foraminifer, *Nature*, 443(7107), 93-96.
- Robbins, J. A., and J. Gustinis (1976), A squeezer for efficient extraction of pore water from small volumes of anoxic sediment, *Limnology and Oceanography*, 905-909.
- Rose, K., R. Boswell, and T. Collett (2011), Mount Elbert Gas Hydrate Stratigraphic Test Well, Alaska North Slope: Coring operations, core sedimentology, and lithostratigraphy, *Marine and Petroleum Geology*, 28(2), 311-331.
- Rosenbaum, E. J., N. J. English, J. K. Johnson, D. W. Shaw, and R. P. Warzinski (2007), Thermal Conductivity of Methane Hydrate from Experiment and Molecular Simulation, *The Journal of Physical Chemistry B*, 111(46), 13194-13205.
- Ruppel, C., and J. W. Pohlman (2008), Climate change and the global carbon cycle: Perspectives and opportunities, in *Fire in the Ice*, edited, pp. 5-8, NETL, U.S. Dep. of Energy, Albany, Oreg.
- Safaqah, O. A., and M. F. Riemer (2006), Minimizing sampling disturbance using a new in situ device, *Soil Dynamics and Earthquake Engineering*, 26(Compendex), 153-161.
- Sain, K., and H. Gupta (2012), Gas hydrates in India: Potential and development, *Gondwana Research*, 22(2), 645-657.
- Sanchez, M., and J. C. Santamarina (2010), Analysis of Hydrate Bearing Sediments using a fully coupled THMC formulation, paper presented at Fifth International Conference on Unsaturated Soils, Barcelona, Spain, 6-8 September.
- Santagata, M., and J. T. Germaine (2005), Effect of OCR on sampling disturbance of cohesive soils and evaluation of laboratory reconsolidation procedures, *Canadian Geotechnical Journal*, 42(Compendex), 459-474.
- Santamarina, J., and J. Jang (2009), Gas production from hydrate bearing sediments: geomechanical implications, *NETL methane hydrate newsletter: Fire in the ice*, 9(4), 18-22.
- Santamarina, J., A. Klein, and M. Fam (2001), *Soils and waves*, 488 pp., John Wiley & Sons, New York.
- Santamarina, J. C., and G. Cho (2001), Determination of Critical State Parameters in

- Sandy Soils. , *ASTM Geotechnical Testing Journal*, 24(2), 185-192.
- Santamarina, J. C., and C. Ruppel (2010), The Impact of Hydrate Saturation on the Mechanical, Electrical, and Thermal Properties of Hydrate-Bearing Sand, Silts, and Clay. , in *Geophysical Characterization of Gas Hydrates*, edited by M. Riedel, E. C. Willoughby and S. Chopra, p. 373, Society of Exploration Geophysicists.
- Santamarina, J. C., S. Dai, J. Jang, and M. Terzariol (2012), Pressure Core Characterization Tools for Hydrate-Bearing Sediments, *Scientific Drilling*, 14, 44-48, doi:10.2204/iodp.sd.2214.2206.2012.
- Sayles, F., T. Wilson, D. Hume, and P. Mangelsdorf (1973), In situ sampler for marine sedimentary pore waters: evidence for potassium depletion and calcium enrichment, *Science*, 181(4095), 154-156.
- Schrum, H. N., R. W. Murray, and B. Gribsholt (2012), Comparison of Rhizon sampling and whole round squeezing for marine sediment porewater, *Scientific Drilling*, 13, 47-50.
- Schultheiss, P. J., M. Holland, and G. Humphrey (2009), Wireline coring and analysis under pressure: recent use and future developments of the HYACINTH system, *Scientific Drilling*, 7, 44-50.
- Schultheiss, P. J., et al. (2006), Pressure coring, logging and subsampling with the HYACINTH system, *Geological Society, London, Special Publications*, 267(1), 151-163.
- Schurr, D. P., J.-Y. Kim, K. G. Sabra, and L. J. Jacobs (2011), Damage detection in concrete using coda wave interferometry, *NDT & E International*, 44(8), 728-735.
- Seeberg-Elverfeldt, J., M. Schlüter, T. Feseker, and M. Kölling (2005), Rhizon sampling of pore waters near the sediment/water interface of aquatic systems, *Limnology and oceanography: Methods*, 3, 361-371.
- Sens-Schönfelder, C., and U. Wegler (2006), Passive image interferometry and seasonal variations of seismic velocities at Merapi Volcano, Indonesia, *Geophysical Research Letters*, 33(21).
- Shankar, U., and M. Riedel (2011), Gas hydrate saturation in the Krishna–Godavari basin from P-wave velocity and electrical resistivity logs, *Marine and Petroleum Geology*, 28(10), 1768-1778.
- Shapiro, N. M., M. Campillo, L. Stehly, and M. H. Ritzwoller (2005), High-Resolution Surface-Wave Tomography from Ambient Seismic Noise, *Science*, 307(5715), 1615-1618.
- Shin, H., and J. Santamarina (2011), Open-mode discontinuities in soils, *Géotechnique Letters*, 1(October-December), 95-99.
- Shogaki, T., and M. Kaneko (1994), Effects of sample disturbance on strength and consolidation parameters of soft clay, *Soils and Foundations*, 34(Compendex), 1-10.
- Siddique, A., C. R. I. Clayton, and R. J. Hopper (1999), The Effects of Varying Centerline Tube Sampling Disturbance on the Behavior of Reconstituted Clay, *Geotechnical Testing Journal*, 22(Compendex), 245-256.
- Singh, A., and J. K. Mitchell (1968), General Stress-strain-time Function for Soils, *Journal of Soil Mechanics and Foundation Engineering Division, ASCE*, 94(1), 21-

- 46.
- Singh, A., and J. K. Mitchell (1969), Creep potential and creep rupture of soils, paper presented at Soil Mech & Fdn Eng Conf Proc/Mexico/.
- Skempton, A. W. (1954), The pore pressure coefficients A and B, *Geotechnique*, 4, 143-147.
- Skovborg, P., H. J. Ng, P. Rasmussen, and U. Mohn (1993), Measurement of induction times for the formation of methane and ethane gas hydrates, *Chemical Engineering Science*, 48(3), 445-453.
- Sloan, E. D., and F. Fleyfel (1991), A molecular mechanism for gas hydrate nucleation from ice, *AIChE Journal*, 37(9), 1281-1292.
- Sloan, E. D., and C. A. Koh (2008), *Clathrate hydrates of natural gases*, 3rd ed., CRC Press, Boca Raton.
- Sloan, E. D., C. A. Koh, A. K. Sum, A. L. Ballard, G. J. Shoup, N. McMullen, J. L. Creek, and T. Palermo (2009), Hydrates: state of the art inside and outside flowlines, *Journal of Petroleum Technology*, 61(12), 89-94.
- Snieder, R. (2006), The Theory of Coda Wave Interferometry, *Pure and Applied Geophysics*, 163(2), 455-473.
- Snieder, R., A. Grêt, H. Douma, and J. Scales (2002), Coda wave interferometry for estimating nonlinear behavior in seismic velocity, *Science*, 295(5563), 2253-2255.
- Spangenberg, E. (2001), Modeling of the influence of gas hydrate content on the electrical properties of porous sediments, *J. Geophys. Res.*, 106(B4), 6535-6548.
- Spicer, R. A., and J. L. Chapman (1990), Climate change and the evolution of high-latitude terrestrial vegetation and floras, *Trends in Ecology & Evolution*, 5(9), 279-284.
- Stange, C. F., and R. Horn (2005), Modeling the Soil Water Retention Curve for Conditions of Variable Porosity, *Vadose Zone J.*, 4(3), 602-613.
- Stehfest, H. (1970), Algorithm 368: Numerical inversion of Laplace transforms, *Communications of the ACM*, 13(1), 47-49.
- Stern, L. A., S. Circone, S. H. Kirby, and W. B. Durham (2001), Anomalous Preservation of Pure Methane Hydrate at 1 atm, *The Journal of Physical Chemistry B*, 105(9), 1756-1762.
- Stern, L. A., S. H. Kirby, W. B. Durham, S. Circone, and W. F. Waite (2000), Laboratory synthesis of pure methane hydrate suitable for measurement of physical properties and decomposition behavior, *Coastal Systems and Continental Margins*, 5, 323-348.
- Stevens, J., B. Baldwin, A. Graue, G. Ersland, J. Husebo, and J. Howard (2008), Measurements of hydrate formation in sandstone, *Petrophysics*, 49(1), 67.
- Stokoe, K. H., and J. Santamarina (2000), Seismic-wave-based testing in geotechnical engineering, *GeoEng 2000*, 1490-1536.
- Sun, R., and Z. Duan (2005), Prediction of CH₄ and CO₂ hydrate phase equilibrium and cage occupancy from ab initio intermolecular potentials, *Geochimica et Cosmochimica Acta*, 69(18), 4411-4424.
- Sun, R., and Z. Duan (2007), An accurate model to predict the thermodynamic stability of methane hydrate and methane solubility in marine environments, *Chemical*

- Geology*, 244(1–2), 248-262.
- Sun, X., and K. K. Mohanty (2006), Kinetic simulation of methane hydrate formation and dissociation in porous media, *Chemical Engineering Science*, 61(11), 3476-3495.
- Tajima, H., A. Yamasaki, and F. Kiyono (2004), Continuous formation of CO₂ hydrate via a Kenics-type static mixer, *Energy and Fuels*, 18(5), 1451-1456.
- Takeya, S., W. Shimada, Y. Kamata, T. Ebinuma, T. Uchida, J. Nagao, and H. Narita (2001), In Situ X-ray Diffraction Measurements of the Self-Preservation Effect of CH₄ Hydrate, *The Journal of Physical Chemistry A*, 105(42), 9756-9759.
- Tanaka, H., J. Locat, S. Shibuya, T. T. Soon, and D. R. Shiwakoti (2001), Characterization of Singapore, Bangkok, and Ariake clays, *Canadian Geotechnical Journal*, 38(2), 378-400.
- Tatsuoka, F., and S. Shibuya (1991), Deformation characteristics of soils and rocks from field and laboratory tests, paper presented at Ninth regional conference on Soil mechanics and foundation engineering, Organizing Committee for the Asian Regional Conference on Soil Mechanics and Foundation Engineering, Singapore, Bangkok, Thailand, December 1991.
- Terzaghi, K. (1923), Die berechnung der durchlässigkeitsziffer des tones aus dem verlauf der hydrodynamischen spannungserscheinungen, *Sitz. Akad. Wissen., Wien Math*, 132, 105-124.
- Tietje, O., and M. Tapkenhinrichs (1993), Evaluation of pedo-transfer functions, *Soil Science Society of America Journal*, 57(4), 1088-1095.
- Ting, H. S. U. H., and W. L. McCabe (1934), Supersaturation and crystal formation in seeded solutions, *Industrial and Engineering Chemistry*, 26(11), 1201-1207.
- Tohidi, B., R. Anderson, M. B. Clennell, R. W. Burgass, and A. B. Biderkab (2001), Visual observation of gas-hydrate formation and dissociation in synthetic porous media by means of glass micromodels, *Geology*, 29(9), 867-870.
- Tohidi, B., J. Yang, M. Salehabadi, R. Anderson, and A. Chapoy (2010), CO₂ Hydrates Could Provide Secondary Safety Factor in Subsurface Sequestration of CO₂, *Environmental Science & Technology*, 44(4), 1509-1514.
- Torres, M. E., T. S. Collett, K. K. Rose, J. C. Sample, W. F. Agena, and E. J. Rosenbaum (2011), Pore fluid geochemistry from the Mount Elbert Gas Hydrate Stratigraphic Test Well, Alaska North Slope, *Marine and Petroleum Geology*, 28(2), 332-342.
- Trehu, A. M., C. Ruppel, M. Holland, G. R. Dickens, M. E. Torres, T. S. Collet, D. Goldberg, M. Riedel, and P. J. Schultheiss (2006), Gas hydrates in marine sediments: Lessons from scientific ocean drilling, *Oceanography*, 19(4), 124-142.
- Trehu, A. M., P. E. Long, M. Torres, G. Bohrmann, F. Rack, T. Collett, D. Goldberg, A. Milkov, M. Riedel, and P. Schultheiss (2004), Three-dimensional distribution of gas hydrate beneath southern Hydrate Ridge: constraints from ODP Leg 204, *Earth and Planetary Science Letters*, 222(3), 845-862.
- Trofimuk, A. A., N. V. Cherskiy, and V. P. Tsarev (1973), Accumulation of natural gases in zones of hydrate-formation in the hydrosphere, *Doklady Akademii Nauk SSSR*, 212, 931-934.
- Tse, J. S., and D. D. Klug (2002), Formation and decomposition mechanisms for clathrate

- hydrates, *Journal of Supramolecular Chemistry*, 2(4), 467-472.
- Turnbull, D., and B. Vonnegut (1952), Nucleation catalysis, *Industrial & Engineering Chemistry*, 44(6), 1292-1298.
- Tyler, S. W., and S. W. Wheatcraft (1989), Application of fractal mathematics to soil water retention estimation, *Soil Science Society of America Journal*, 53(4), 987-996.
- Uchida, T., T. Ebinuma, and T. Ishizaki (1999), Dissociation condition measurements of methane hydrate in confined small pores of porous glass, *The Journal of Physical Chemistry B*, 103(18), 3659-3662.
- Uddin, M., F. Wright, and D. Coombe (2011), Numerical Study of Gas Evolution and Transport Behaviours in Natural Gas-Hydrate Reservoirs, *Journal of Canadian Petroleum Technology*, 50(1), 70-89.
- Ussler III, W., and C. K. Paull (2001), Ion exclusion associated with marine gas hydrate deposits, *Geophysical Monograph Series*, 124, 41-51.
- Valdes, J. R., and J. C. Santamarina (2006), Particle clogging in radial flow: Microscale mechanisms, *SPE Journal*, 11(2), 193-198.
- Valdes, J. R., and J. C. Santamarina (2007), Particle transport in a nonuniform flow field: Retardation and clogging, *Applied Physics Letters*, 90(24), 244101.
- Valin, Z. C., and T. S. Collett (1992), Molecular and isotopic analyses of the hydrocarbon gases within gas hydrate-bearing rock units of the Prudhoe Bay-Kuparuk River area in Northern Alaska. *Rep. 92-299*, U.S. Geological Survey.
- van Genuchten, M. T. (1980), A Closed-form Equation for Predicting the Hydraulic Conductivity of Unsaturated Soils¹, *Soil Sci. Soc. Am. J.*, 44(5), 892-898.
- Vanapalli, S., and D. Fredlund (2000), Comparison of different procedures to predict unsaturated soil shear strength, *Geotechnical Special Publication*, 195-209.
- Vanapalli, S. K., D. G. Fredlund, D. E. Pufahl, and A. W. Clifton (1996), Model for the prediction of shear strength with respect to soil suction, *Canadian Geotechnical Journal*, 33(3), 379-392.
- Vogel, H. J. (2000), A numerical experiment on pore size, pore connectivity, water retention, permeability, and solute transport using network models, *European Journal of Soil Science*, 51(1), 99-105.
- Vogel, T., and M. Cislerova (1988), On the reliability of unsaturated hydraulic conductivity calculated from the moisture retention curve, *Transport in Porous Media*, 3(1), 1-15.
- Vogelaar, B., D. Smeulders, and J. Harris (2010), Exact expression for the effective acoustics of patchy-saturated rocks, *Geophysics*, 75(4), N87-N96.
- Vysniauskas, A., and P. R. Bishnoi (1983), A kinetic study of methane hydrate formation, *Chemical Engineering Science*, 38(7), 1061-1072.
- Wagner, B., V. Tarnawski, V. Hennings, U. Müller, G. Wessolek, and R. Plagge (2001), Evaluation of pedo-transfer functions for unsaturated soil hydraulic conductivity using an independent data set, *Geoderma*, 102(3), 275-297.
- Waite, W. F., W. J. Winters, and D. H. Mason (2004), Methane hydrate formation in partially water-saturated Ottawa sand, *American Mineralogist*, 89(8-9), 1202-1207.
- Waite, W. F., et al. (2009), Physical properties of hydrate-bearing sediments, *Rev.*

- Geophys.*, 47(4), RG4003.
- Walczak, R., F. Moreno, C. Sławiński, E. Fernandez, and J. Arrue (2006), Modeling of soil water retention curve using soil solid phase parameters, *Journal of Hydrology*, 329(3), 527-533.
- Wallace, P. J., G. R. Dickens, C. K. Paul, and W. Ussler III (2000), Effects of core retrieval and degassing on the carbon isotope composition of methane in gas hydrate - and free gas-bearing sediments from the Blake Ridge *Rep.*, College Station, TX.
- Wang, Y.-H., and S.-C. Leung (2008), A particulate-scale investigation of cemented sand behavior, *Can. Geotech. J.*, 45(1), 29-44.
- Watson, P. G., and T. E. Frickers (1990), A multilevel, in situ pore-water sampler for use in intertidal sediments and laboratory microcosms, *Limnology and Oceanography*, 35(6), 1381-1389.
- Weinberger, J. L., and K. M. Brown (2006), Fracture networks and hydrate distribution at Hydrate Ridge, Oregon, *Earth and Planetary Science Letters*, 245(1), 123-136.
- Williams, P. J. (1982), *The surface of the earth: An introduction to geotechnical science*, 212 pp., Longman, London and New York.
- Winters, W., M. Walker, R. Hunter, T. Collett, R. Boswell, K. Rose, W. Waite, M. Torres, S. Patil, and A. Dandekar (2011), Physical properties of sediment from the Mount Elbert Gas Hydrate Stratigraphic Test Well, Alaska North Slope, *Marine and Petroleum Geology*, 28(2), 361-380.
- Wolfe, J. A. (1980), Tertiary climates and floristic relationships at high latitudes in the northern hemisphere, *Palaeogeography, Palaeoclimatology, Palaeoecology*, 30(0), 313-323.
- Wolfe, J. A. (1994), Tertiary climatic changes at middle latitudes of western North America, *Palaeogeography, Palaeoclimatology, Palaeoecology*, 108(3-4), 195-205.
- Wolfe, J. A., and G. R. J. Upchurch (1987), North American nonmarine climates and vegetation during the Late Cretaceous, *Palaeogeography, Palaeoclimatology, Palaeoecology*, 61(0), 33-77.
- Wood, W. T., and W. Y. Jung (2008), Modeling the extent of Earth's marine methane hydrate cryosphere, paper presented at Proceedings of the 6th International Conference on Gas Hydrates, Vancouver, Canada, July 6-10.
- Wuttke, F., M. Asslan, and T. Schanz (2012), Time-lapse monitoring of fabric changes in granular materials by coda wave interferometry, *ASTM Geotechnical Testing Journal*, 35(2), 353-362.
- Xia, W., and M. Thorpe (1988), Percolation properties of random ellipses, *Physical Review A*, 38(5), 2650.
- Xu, W., and C. Ruppel (1999), Predicting the occurrence, distribution, and evolution of methane gas hydrate in porous marine sediments, *J. Geophys. Res.*, 104.
- Yakushev, V. S., and V. A. Istomin (1992), Gas-hydrate self-preservation effect, in *Physics and Chemistry of Ice*, edited by N. Maeno and T. Hondoh, pp. 136-139, Hokkaido University Press, Sapporo, Japan.
- Yamamuro, J. A., and P. V. Lade (1996), Drained sand behavior in axisymmetric tests at high pressures, *Journal of Geotechnical Engineering*, 122(2), 109-119.

- Youn, J.-U., Y.-W. Choo, and D.-S. Kim (2008), Measurement of small-strain shear modulus G_{max} of dry and saturated sands by bender element, resonant column, and torsional shear tests, *Canadian Geotechnical Journal*, 45(10), 1426-1438.
- Young, S. W. (1911), Mechanical stimulus to crystallization in supercooled liquids, *Journal of the American Chemical Society*, 33(2), 148-162.
- Young, S. W., and R. J. Cross (1911), The mechanical stimulus to crystallization, *Journal of the American Chemical Society*, 33(8), 1375-1388.
- Yun, T. S., and J. C. Santamarina (2005), Decementation, Softening, and Collapse: Changes in Small-Strain Shear Stiffness in k_0 Loading, *Journal of Geotechnical & Geoenvironmental Engineering*, 131(3), 350-358.
- Yun, T. S., J. C. Santamarina, and C. Ruppel (2007), Mechanical properties of sand, silt, and clay containing tetrahydrofuran hydrate, *J. Geophys. Res.*, 112(B4), B04106.
- Yun, T. S., D. Fratta, and J. C. Santamarina (2010), Hydrate-Bearing Sediments from the Krishna–Godavari Basin: Physical Characterization, Pressure Core Testing, and Scaled Production Monitoring, *Energy & Fuels*, 24(11), 5972-5983.
- Yun, T. S., F. M. Francisca, J. C. Santamarina, and C. Ruppel (2005), Compressional and shear wave velocities in uncemented sediment containing gas hydrate, *Geophys. Res. Lett.*, 32(10), L10609.
- Yun, T. S., G. A. Narsilio, J. C. Santamarina, and C. Ruppel (2006), Instrumented pressure testing chamber for characterizing sediment cores recovered at in situ hydrostatic pressure, *Marine Geology*, 229(3-4), 285-293.
- Yun, T. S., C. Lee, J.-S. Lee, J. J. Bahk, and J. C. Santamarina (2011), A pressure core based characterization of hydrate-bearing sediments in the Ulleung Basin, Sea of Japan (East Sea), *J. Geophys. Res.*, 116(B2), B02204.
- Zapata, C. E., W. N. Houston, S. L. Houston, and K. D. Walsh (2000), Soil–Water Characteristic Curve Variability, in *Geotech. Spec. Publ. 99, Advances in Unsaturated Geotechnics*, edited, pp. 84-124.
- Zhang, R., and T. Lunne (2002), Effect of sample disturbance on soft clay with low plasticity, *Yanshilixue Yu Gongcheng Xuebao/Chinese Journal of Rock Mechanics and Engineering*, 21(Compendex), 2350-2355.